ULM UNIVERSITY

DOCTORAL THESIS

Gaining control over three-body recombination in an ultracold rubidium gas

Dissertation

zur Erlangung des akademischen Grades
Doktor der Naturwissenschaften (Dr. rer. nat.)
eingereicht an der
Fakultät für Naturwissenschaften
der
Universität Ulm

von
Dominik Dorer
aus
Ehingen

2024

Amtierender Dekan der Fakultät für Naturwissenschaften: Prof. Dr. Kay-Eberhard Gottschalk
Erstgutachter und Betreuer: Prof. Dr. Johannes Hecker Denschlag
Zweitgutachter: apl. Prof. Dr. Maxim A. Efremov
Tag der mündlichen Prüfung: 02.05.2025

Die in dieser Dissertation beschriebenen Arbeiten wurden an der

Universität Ulm
Institut für Quantenmaterie
Albert-Einstein-Allee 45
89081 Ulm

durchgeführt.

Publications

The following articles were published during the course of this thesis:

- Shinsuke Haze, José P. D'Incao, Dominik Dorer, Paul S. Julienne, Eberhard Tiemann, Markus Deiß and Johannes Hecker Denschlag, "Spin-conservation propensity rule for three-body recombination of ultracold Rb atoms", *Phys. Rev. Lett.* **128**, 133401 (2022), DOI: `10.1103/PhysRevLett.128.133401`. Reprinted with permission from American Physical Society, Copyright © 2022 by American Physical Society

- Shinsuke Haze, Jinglun Li, Dominik Dorer, José P. D'Incao, Paul S. Julienne, Eberhard Tiemann, Markus Deiß and Johannes Hecker Denschlag "Energy-scaling of the product state distribution for three-body recombination of ultracold atoms", *Phys. Rev. Res.* **5**, 013161 (2023). DOI: `https://doi.org/10.1103/PhysRevResearch.5.013161`. This work is licensed under Creative Commons Attribution CC BY 4.0, `https://creativecommons.org/licenses/by/4.0/`

- Dorer, D. and Frosz, M. H. and Haze, S. and Deiß, M. and Schoch, W. and Hecker Denschlag, J. "Hollow-Core Fiber for Single-Mode, Low Loss Transmission of Broadband UV Light", *IEEE Journal of Selected Topics in Quantum Electronics* **30** (6) 4300106 (2024), DOI: `10.1109/JSTQE.2023.3299158`, © 2024 IEEE. Reprinted, with permission from the authors, "Hollow-Core Fiber for Single-Mode, Low Loss Transmission of Broadband UV Light", IEEE Journal of Selected Topics in Quantum Electronics, 2024.

- Shinsuke Haze, Jinglun Li, Dominik Dorer, José P. D'Incao, Paul S. Julienne, Eberhard Tiemann, Markus Deiß and Johannes Hecker Denschlag "Controlling few-body reaction pathways using a Feshbach resonance", DOI: `https://doi.org/10.48550/arXiv.2408.14922`, reprinted with permission from the authors.

Abstract

My doctoral thesis covers three areas: three-body recombination in ultracold gases, optical spectroscopy of molecules, and the characterization of a hollow-core fiber for the transmission of ultraviolet light.

Three-body recombination (TBR) is a chemical process in which three atoms collide, causing two of them to form a molecule while the third atom absorbs part of the binding energy. I studied this process in an ultracold cloud of rubidium atoms in a well-defined internal quantum state at temperatures around one microkelvin. This led to the following questions: Are there preferences in how this process occurs? In which quantum states do the resulting molecules reside, and how many are produced in each state? Is it possible to control this process, and if so, how can it be experimentally implemented? To answer these questions, I developed spectroscopic techniques and investigated the molecular states in a state-resolved manner. The key results of my work are as follows: we discovered that for three-body recombination of rubidium, the spin states of the atoms tend to be preserved. Furthermore, we identified two methods to control the reaction pathway and thus the molecular product distribution. We utilized magnetic fields to precisely control the spin composition of the atomic scattering state or molecular states.

For the state-resolved detection of molecules, our lab employs resonance-enhanced multiphoton ionization (REMPI). In this technique, a molecule is first excited into an intermediate state with a first photon and then ionized by a second photon. The ion can be detected with near 100% efficiency. The choice of intermediate state is crucial, as it directly affects ionization and therefore detection efficiency. To identify the optimal intermediate state, I conducted detailed optical molecular spectroscopy of excited states near the 5s + 4d asymptote. This allowed us to resolve the vibrational and rotational structure, as well as the fine structure, of the electronic states $(2)^1\Sigma_u^+$ and $(2)^3\Pi_g$ in an energy range from 493 to 503 THz x h. Based on these experimental results, new potential energy curves will be calculated in collaboration with Professor Tiemann from Hannover.

Additionally, in collaboration with the Max Planck Institute for the Physics of Light in Erlangen, I worked on a hollow-core fiber to efficiently and robustly transmit laser light in the 300 - 320 nm range. This wavelength range is particularly relevant for the spectroscopy of highly excited Rydberg molecules, opening new possibilities for precise investigations. We achieved a transmission efficiency of over 70% in single-mode operation with a fiber length of

approximately 10 m. The optical fiber showed no aging effects within the investigated time frame, which is an advantage compared to conventional fiber types that can be prone to degradation.

Zusammenfassung

Meine Doktorarbeit umfasst drei Themenbereiche: die Dreikörperrekombination in einem ultrakalten Gas, die optische Spektrokopie von Molekülen und die Charakterisierung einer Hohlkernfaser zur Übertragung von ultraviolettem Licht.

Die Dreikörperrekombination (TBR) ist ein chemischer Prozess, bei dem drei Atome miteinander kollidieren, wodurch zwei Atome ein Molekül bilden, während das dritte Atom einen Teil der Bindungsenergie aufnimmt. Diesen Prozess habe ich in einer ultrakalten Wolke aus Rubidiumatomen untersucht, die sich in einem wohldefinierten internen Quantenzustand bei Temperaturen von etwa einem Mikrokelvin befinden. Dabei stellten sich die folgenden Fragen: Gibt es Präferenzen, nach denen dieser Prozess abläuft? In welchen Quantenzuständen befinden sich die entstandenen Moleküle, und wie viele werden in den jeweiligen Zuständen erzeugt? Ist es möglich, diesen Prozess gezielt zu steuern, und falls ja, wie lässt sich dies im Experiment umsetzen? Um diese Fragen zu beantworten, habe ich spektroskopische Messmethoden weiterentwickelt und die Molekülzustände zustandsaufgelöst untersucht. Die Kernresultate meiner Arbeit sind wie folgt: wir haben herausgefunden, dass bei der Dreikörperrekombination von Rubidium Spin-Zustände der Atome die Tendenz haben, erhalten zu bleiben. Darüber hinaus konnten wir zwei Methoden finden, mit denen der Reaktionsweg und somit die molekulare Produktverteilung gesteuert werden konnten. Dabei nutzten wir, dass man mit Hilfe eines Magnetfeldes gezielt die Spinzusammensetzung des atomaren Streuzustandes oder von molekularen Zuständen kontrollieren kann.

Für den zustandsaufgelösten Nachweis der Moleküle verwenden wir in unserem Labor die resonanzverstärkte Mehrphotonenionisation (REMPI). Hierbei wird ein Molekül zunächst mit einem Photon in einen angeregten Zwischenzustand überführt und anschließend mit einem weiteren Photon ionisiert. Das Ion kann dann mit einer Effizienz von nahe 100% nachgewiesen werden. Die Wahl des Zwischenzustands spielt eine entscheidende Rolle, da sie die Ionisationseffizienz und damit direkt die Nachweiseffizienz beeinflusst. Um den optimalen Zwischenzustand zu identifizieren, habe ich eine detaillierte optische Molekülspektroskopie an angeregten Zuständen nahe der 5s + 4d Asymptote durchgeführt. Dabei konnte die Vibrations- und Rotationsstruktur sowie die Feinstruktur der elektronischen Zustände $(2)^1\Sigma_u^+$ und $(2)^3\Pi_g$ in einem Energiebereich von 493 bis 503 THz x h aufgeschlüsselt werden. Basierend auf den experimentellen Ergebnissen werden in Zukunft

neue Potentialenergiekurven in Zusammenarbeit mit Professor Tiemann aus Hannover berechnet.

Des Weiteren habe ich in Zusammenarbeit mit dem Max Planck Institut für die Physik des Lichts in Erlangen an einer Hohlkernfaser gearbeitet, um Laserlicht im Bereich von 300 - 320 nm effizient und robust zu übertragen. Dieser Bereich ist unter anderem relevant für z.B. die Spektroskopie hochangeregter Rydberg-Moleküle und eröffnet neue Möglichkeiten für präzise Untersuchungen. Wir erreichten eine Übertragungseffizienz von über 70% im Single-Mode Betrieb bei einer Faserlänge von $\sim$10 m. Die optische Faser zeigte in dem von uns untersuchten Rahmen keine Alterungseffekte, was bei herkömmlichen Fasertypen für Probleme sorgen kann.

Contents

Chapter 1

Introduction

The emergence of quantum mechanics revolutionized our understanding of the physical world, providing the fundamental framework to describe the behavior of atoms and molecules and the mechanisms of chemical reactions [15, 59, 113, 129]. With respect to chemistry, in particular, it allowed researchers to investigate molecular orbitals, analyze electron distributions and understand the dynamics of chemical interactions.

To investigate the quantum mechanical aspect of chemical reactions in more detail, early experimental studies often employed molecular beams [62, 83, 142]. In typical molecular beam experiments, two beams of atoms or molecules from thermal sources are crossed, leading to collisions and reactions of the particles where the two beams intersect. The resulting products are then analyzed using detectors such as quadrupole mass filters or hot metal filaments. Especially in the early phase of the molecular beam experiments, measurements have been conducted at thermal energies of 300 Kelvin or higher. However, high thermal velocities limit interaction times, and the broad velocity distribution of the particles prevents precise control over the angular momentum of the collisions. New inventions and technological advancements opened up the path to investigations of chemical reactions in dilute gases at ultracold temperatures. Such gases are typically created through laser cooling [100] followed by evaporative cooling [77]. At temperatures in the nanokelvin range and particle densities between 10^{12} and $10^{15}\,\mathrm{cm}^{-3}$, quantum-degenerate states of matter emerge when the atomic de Broglie wavelength becomes comparable to or exceeds the average interparticle distance, causing quantum statistics to govern the system's behavior.

Ultracold temperatures ensure that collisions between atoms predominantly occur in low partial waves (often only s-waves are considered). There are chemical reactions that involve two colliding particles and others are based on three colliding particles. One fundamental two-body reaction is the photoassociation. Photoassociation is a process in which two colliding atoms are bound together by the absorption of a photon. It was the first successful approach to create a gas of molecules in the electronic ground state at temperatures in the microkelvin range. There were also developments where scientists employed magnetic fields to ramp over a Feshbach resonance which leads to the formation of Feshbach molecules [24]. At a Feshbach resonance, a molecular bound state becomes energetically degenerate with the scattering state of two atoms. Although a Feshbach resonance is fundamentally a two-body phenomenon, it also affects other chemical reactions. A well-known example of such a reaction is three-body recombination (TBR). In this chemical process, three atoms collide, resulting in two atoms forming a molecule, while the third atom absorbs part of the binding energy and remains unbound. Ultracold quantum gases offer an ideal environment to study this reaction in detail. Numerous studies — both experimental and theoretical — have focused on three-body recombination in ultracold gases (see e.g.[71, 122, 149, 151, 153]). In the BaRbI experiment in Ulm, we investigate the process of three-body recombination [51, 157, 158]. In our laboratory, we use a hybrid setup that allows us to work with ultracold neutral atoms and molecules as well as charged particles. We can trap a large number of atoms ($\approx 10^6$) with adjustable particle density and temperature in an optical dipole trap and prepare them in a well-defined internal quantum state. Our group employs the resonance-enhanced multiphoton ionization (REMPI) technique to achieve state-resolved detection of the reaction products from three-body recombination. Since the internal quantum states of the atoms in the entrance channel of the reaction can be precisely prepared, and the quantum states of the resulting molecules can be fully resolved, these projects fall within the field of state-to-state chemistry.

Within my doctoral thesis, I conducted new experiments to investigate three-body recombination in greater detail. My work focused on addressing the following key questions: Are there specific tendencies or propensities governing the three-body recombination process? Specifically, what are the possible reaction channels on the exit of the reaction, and is the reaction flux (into the molecular states) evenly distributed, or are there parameters that influence the probability of molecule formation? In how far can the reaction pathway be controlled, and if so, how can this be implemented experimentally?

An essential initial step in my work was optimizing the molecular detection scheme using REMPI. With REMPI, we aim to state-selectively drive transitions between molecular states resonantly to ionize molecules and subsequently count them. I searched for optimized REMPI-based detection schemes for our experiments and for that, I performed high-resolution molecular spectroscopy of the two electronic states $(2)^1\Sigma_u^+$ and $(2)^3\Pi_g$ near the 5s + 4d asymptote (see Chapter 4). The high-resolution spectroscopic experiments yielded two main results: The REMPI efficiency was improved by nearly two orders of magnitude compared to previously employed schemes in our laboratory by using an intermediate molecular level of either $(2)^1\Sigma_u^+$ or $(2)^3\Pi_g$. Additionally, we achieved to get a deeper understanding of the molecular structure of the investigated excited states, enabling a detailed study of interactions such as spin-orbit coupling in the $(2)^3\Pi_g$ system.

This optimized REMPI pathway allows us to detect more molecular states which are formed by three-body recombination. In subsequent experiments, we analyzed the molecular product distributions using the improved REMPI scheme and discovered that three-body recombination tends to preserve the initial spin state of the atoms involved in the reaction. The results and interpretation are discussed in Chapter 5. Further, we used this spin conservation propensity rule for a demonstration of different control methods for a chemical reaction.

We demonstrate two distinct methods to steer the reaction flux of three-body recombination into different pathways. In the experiments described in Chapter 6, we demonstrated that modifying the spin composition of a reaction channel at the exit of the reaction allows for control over the reaction flux into that channel. For this purpose, we used two molecular states exhibiting an avoided energy level crossing. By applying an external magnetic field, the spin composition of the molecular states could be manipulated. This allows us to selectively steer the reaction flux from one reaction channel to another. In Chapter 7, we present a method where we employ a magnetically-tunable Feshbach resonance to admix a specific spin state on the entrance of the reaction. Experimentally, we observed that this allows for a control of the reaction flux into the admixed spin channel. We were able to observe molecular product states that would be very rarely produced without the controlled spin mixing in the input channel of the reaction, and which could not be experimentally detected otherwise.

Our team in the laboratory has also carried out spectroscopy of highly excited Rydberg molecules [31, 32, 58], although this is not a main topic for my thesis. We typically employ photoassociation spectroscopy of Rydberg molecules with a single photon at around 300 nm. This wavelength lies in the UV range and cannot be efficiently transmitted through conventional solid-core optical fibers, as they degrade over time and lose their ability to guide light effectively. For our laboratory, robust and efficient light transmission was crucial for the spectroscopy. As part of my doctoral work — conducted in collaboration with the Max Planck Institute for the Science of Light in Erlangen — I worked on characterizing and testing an optical hollow-core fiber for the single-mode transmission of light at a wavelength of 300 - 320 nm. The fiber samples were produced in Erlangen, and the characterization was carried out in Ulm. Our results demonstrated that hollow-core fibers exhibit excellent properties for UV light transmission, including a high-quality beam profile and high transmission efficiency.

In the following, I will present a short outline of my thesis.

Chapter 2 provides an overview of the experimental setup used for the investigation of three-body recombination and high-resolution molecular spectroscopy.

Chapter 3 introduces some theoretical aspects for the description of diatomic molecules. It also contains information about molecular interactions and symmetries.

In Chapter 4, I present high-resolution spectroscopy of the molecular states $(2)^1\Sigma_u^+$ and $(2)^3\Pi_g$ near the 5s + 4d asymptote for both isotopes ^{85}Rb and ^{87}Rb.

Chapters 5 to 7 focus on the study of three-body recombination. Chapter 5 presents experimental data showing that a spin conservation propensity rule applies in rubidium. The different methods for controlling the reaction path in three-body recombination are discussed in Chapters 6 and 7.

Chapter 8 addresses the characterization of a hollow-core fiber for the transmission of ultraviolet light.

In Chapter 9, I provide a summary of my research and give an outlook on future topics in my field of study.

Chapter 2

Experimental apparatus

The focus of this thesis is the experimental investigation on the production and detection of ultracold atoms and molecules. The hybrid apparatus used in the experiments consists of several vacuum chambers designed to maintain ultra-high vacuum conditions which is essential for trapping atoms and ions and their manipulation. The setup has been discussed extensively in previous publications [52, 126, 127]. Here, I will provide a brief overview of the key components in Section 2.1 and I discuss modifications relevant to this work in subsequent Sections 2.2 - 2.3.
A critical improvement made to the system involves the calibration of the absorption imaging technique, see Section 2.2. Absorption imaging is a crucial tool that allows for precise measurement of atomic properties as temperature, density and spatial distribution. For experiments involving chemical reactions controlled by an external magnetic field, precise calibration of the magnetic field is a key aspect. We exploited the Zeeman shift of energy levels to characterize the magnetic field coils and additionally determined the background B-field which is covered in Section 2.3. For high-resolution spectroscopy of molecules in different quantum states, stable and tunable laser sources are essential. The operation principles and specifications of these lasers are given in Section 2.4. Signal detection in ultracold chemistry experiments relies heavily on elastic collisions between atoms and ions. An important factor is to achieve optimal spatial overlap between charged particles and neutral particles. Previous work has already dealt with this [80], so it is only briefly mentioned in the description of the vacuum setup. These improvements and calibrations ensure the reliability and accuracy of the experimental results, paving the way for detailed investigations into state-to-state chemistry and controlled chemical reactions.

2.1 Description of the vacuum chamber

The Barium Rubidium Ion Experiment (BaRbIE) in Ulm is one of the few hybrid apparatuses that combines an ion trap for charged particles with an optical trap for neutral atoms. In Ulm, we work with the neutral isotopes ^{85}Rb or ^{87}Rb and with charged atoms or molecules such as Rb^+, Rb_2^+, BaRb^+

and Ba^+. The apparatus can essentially be divided into three different sections, see Fig. 2.1. Two chambers (MOT, BEC) are used to prepare atomic clouds of rubidium with adjustable temperatures and densities. The third chamber (science chamber) contains the linear Paul trap in the center where chemical reactions take place and are detected. The whole experiment is fully automated and controlled via home-built Labview software.

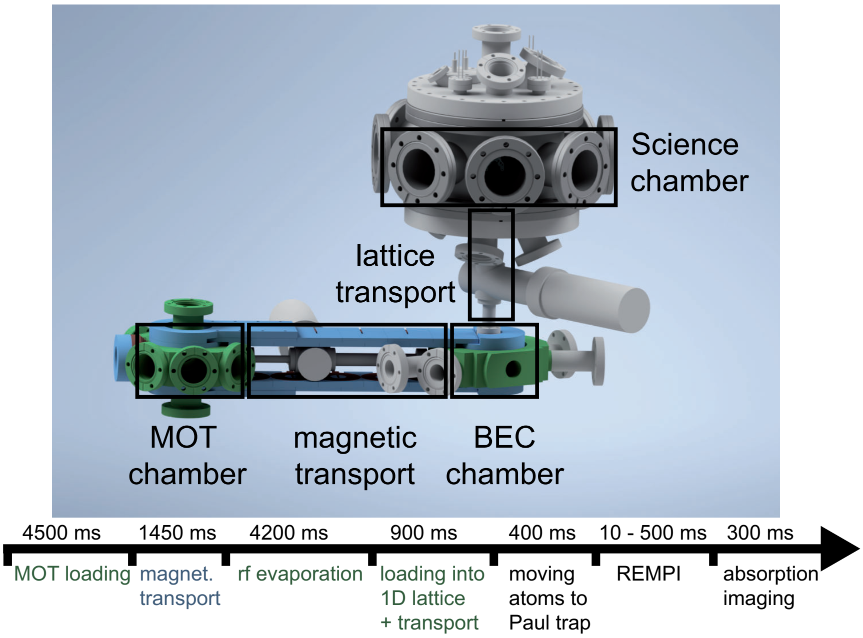

FIGURE 2.1: Drawing of the three-chamber vacuum system of the Ulm experiment. In the science chamber, three-body recombinations happens including the detection of molecules. A rough outline of a typical experimental sequence is also shown below the drawing which shows that most of the sequence is used to prepare the atomic sample and only a short amount of time is used for three-body recombination studies.

MOT and BEC chamber

As a first step, Rb atoms are loaded into a magneto-optical trap in the MOT chamber. Currently, this process takes 4.5 seconds to trap about 5×10^9 atoms at a temperature of $\approx 120\ \mu\text{K}$ using a power of 400 mW distributed over 6 laser beams. Before the atoms are transported into the BEC chamber by magnetic transport, they are cooled to a few µK by polarization gradient cooling [30] and subsequently spin-polarized to a desired spin state (e.g. for ^{87}Rb, $f = 1, m_f = -1$ state or $f = 2, m_f = 2$ for ^{85}Rb) and magnetically trapped in the MOT chamber for a few milliseconds.

Through a sequential circuit of 13 different coils, a spatially moving magnetic potential is generated, which the atoms follow because of their magnetic moment and are thus brought into the BEC chamber within 1.45 seconds. In this chamber, the atoms are first trapped by a combination of magnetic trap and optical dipole trap. Through radio frequency evaporation combined with simultaneous reduction of the laser intensity, temperatures of a few hundred nK are finally reached in this chamber. The science chamber is positioned above the BEC chamber. The final transport step consists of an optical transport along 305 mm using a moving 1D optical lattice in vertical direction. The vertical lattice beam propagating from top to bottom (further named upper lattice) can be spatially displaced via piezo actuators to ensure maximum precision when loading atoms from the optical dipole trap into the 1D optical lattice.

Science chamber

After the optical lattice transport, the atom cloud is loaded into a crossed optical dipole trap generated by the upper lattice beam and an additional laser beam (horizonal dipole trap) with a wavelength of 1064 nm. The additional horizontal beam in this chamber can also be shifted by piezo actuators, allowing the atomic cloud to be precisely positioned in 3 dimensions. The horizontal dipole trap beam can be shifted in vertical (z) and horizontal (x) direction. The vertical upper lattice beam can be shifted in both horizontal (x,y) directions, see Fig. 2.2. In a typical experiment, the atom cloud is positioned at the center of the Paul trap (see Fig. 2.3) where the detection of chemical reactions takes place. A general description of the Paul trap is not given here but there is a nice review by Leibfried et. al [87]. In our case, the positioning of the ions is an important step in making detection as efficient as possible. We can position the ion with sub micrometer precision inside our linear Paul trap by applying static voltages to the endcaps. Signals are mainly detected via particle losses in the atomic cloud, for which we use absorption imaging of the atom cloud. During this work, improvements were achieved in absorption imaging methods in the science chamber to precisely

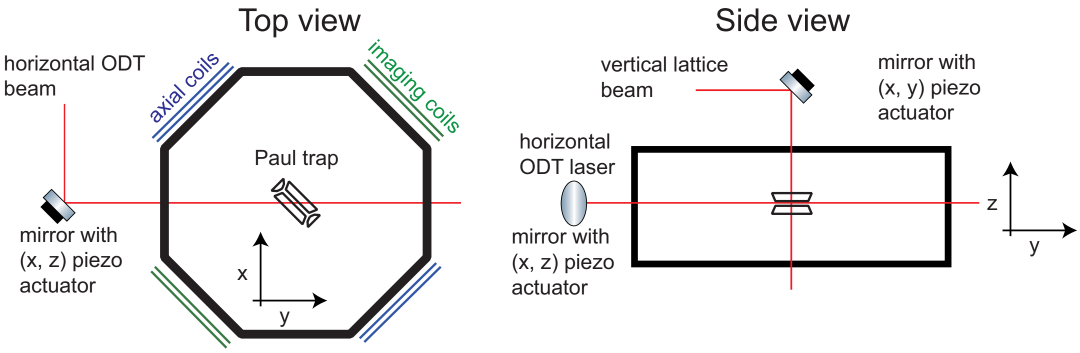

FIGURE 2.2: Schematic of the laser beams for optically trapping the atoms. The horizontal optical dipole trap beam can be shifted vertically (z) and horizontally (x) direction, see left top view. The upper lattice beam can be shifted in both horizontal directions (x,y), see right side view. In total, we have full three-dimensional position control of the atomic cloud.

measure the absolute number of particles. A detailed description of the methods can be found in Section 2.2. Furthermore, precise knowledge of the applied magnetic fields is crucial for spectroscopic measurements as it enables accurate control of chemical reactions during three-body-recombination. The Feshbach coils which are part of the science chamber are calibrated and adjustments are made to compensate for any background magnetic fields, see Section 2.3.

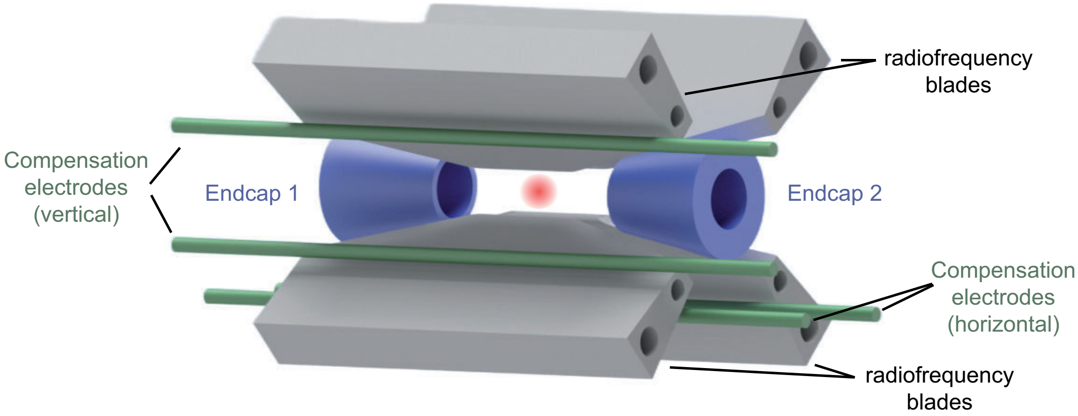

FIGURE 2.3: Schematic of the linear Paul trap. The radiofrequency blades generate an oscillating electric field for (time-averaged) radial confinement. The endcaps 1 and 2 are used for axial confinement and also for positioning the ion with respect to the atomic cloud. The compensation electrodes are used for compensation of any residual electric fields which would lead to excess micromotion of the ion.

2.2 Absorption imaging

Our main motivation in calibrating the atom numbers is to measure rate coefficients for three-body recombination as precisely as possible. Existing literature contains experimental results on these coefficients obtained through various methodologies [19, 118, 154]. Through the calibration of our imaging system, we aim to quantitatively determine rate coefficients for three-body recombination for a thermal Rb cloud confined in a crossed optical dipole trap. The following section describes how to calibrate the number of particles in an absorption image in absolute terms. It mainly involves a compensation of the background magnetic field in the science chamber and a measurement of the probe laser intensity as accurately as possible. There are several methods in the literature for calibrating the measured particle number for imaging in an absolute way [67, 116, 148]. One possibility is to calibrate the particle number by varying the intensity of the probe beam [116] which is also used in our setup. This method is based on the Lambert-Beer law, which describes how the intensity of light exponentially decreases as it passes through a medium. We give a short summary of the theory of resonant absorption imaging and provide detailed information about the calibration method and important parameters. The starting point is a modified Lambert-Beer law which also takes saturation effects into account

$$\frac{dI\left(x,y,z\right)}{dz}=-n\left(x,y,z\right)\sigma_0\frac{1}{1+I\left(x,y,z\right)/I_s^0}I\left(x,y,z\right) \tag{2.1}$$

where n is the atomic density and $I\left(x,y,z\right)$ the intensity at position $\left(x,y\right)$ of the imaging light [116] in propagation direction z. For an ideal two-level system, the cross section is given by $\sigma_0=\frac{3\lambda^2}{2\pi}$ and the saturation intensity $I_s^0=\frac{\pi}{3}\frac{hc\Gamma}{\lambda^3}$ [137] with Planck's constant h, c the speed of light, λ the wavelength and Γ the natural linewidth of the transition used for imaging. In a real system, however, effects such as imperfect polarization of the imaging light and not perfectly prepared quantum states of the system as well as an imperfectly aligned magnetic field vector must be taken into account. Therefore, a dimensionless correction factor α is introduced, which leads to a rescaling of the cross section of the optical transition and the associated saturation intensity. Because only two-dimensional information is available with a single camera, Eq. (2.1) is integrated over z, so we obtain an optical column density $od_c\left(x,y\right)$ of the atomic cloud

$$od_c(x,y)=\frac{\alpha}{\sigma_0}\left[-\left(1+4\left(\frac{\delta}{\Gamma}\right)^2\right)\ln\left(\frac{I_a}{I_r}\right)+\frac{I_r-I_a}{I_s^0\alpha}\right]. \tag{2.2}$$

Here, a term for a laser detuning δ is already included, but typically resonant light is used for imaging as long as the optical density of the cloud is not too high and weak probe beam intensities are used (for our setup OD < 2, $I/I_s^0<0.05$). I_r is the reference intensity and I_a is the intensity after the light has been absorbed by the atoms. For small intensities compared to the saturation intensity, the linear term in (2.2) is neglected and leads to the simple Lambert-Beer law. Equation (2.2) is evaluated for each pixel of the camera sensor, which then provides a full image of the atom cloud and its optical column density od_c for each individual pixel. The calibration of the absolute particle number is based on the idea that the laser intensity is varied and the density or particle number of the atomic cloud must not change as a result. The logarithmic term alone would converge to 0 for high intensities because the difference between reference intensity I_r and intensity after absorption I_a becomes small and therefore $I_r/I_a\rightarrow 1$. The linear term becomes increasingly dominant in the limit of high intensities and compensates the decrease of the logarithmic component. Experimentally, the better the absolute intensity of the laser beam at the location of the atoms is known, the better the subsequent calibration method works.

2.2.1 Camera system and optical path

This section briefly describes the optical path with all relevant components and then discusses the specifications of the camera. Our imaging path (see Fig. 2.4) is used for two purposes: on the one hand it is possible to image atomic clouds via absorption imaging, on the other hand fluorescence imaging for Ba^+ is also used. The HALO (high-aperture laser objective) used in the setup is specially anti-reflection coated for the fluorescence light of Ba^+ at around 493 nm and absorbs about a half of the light for absorption imaging at 780 nm. In order to be able to estimate the intensity of the light at the position of the atoms, the transmission of each individual optical component in the beam path is measured. The transmission of the HALO can only be measured indirectly, as it is installed inside the vacuum. Experimentally, the transmission of one viewport is $T_{1V} = 98.4\%$. The transmission through the whole chamber (2 viewports and the HALO) is $T_{ch} = 59\%$ and the transmission through the dichroic mirror is $T_{dc} = 84.6\%$. With this information, it is possible to draw conclusions about the intensity of the light at the location of the atoms from the intensity measured by the camera. $T_{eff} = T_{1V} + T_{Halo} + T_{dc} \approx 50\%$. This means that the camera perceives a factor of two less light intensity than it should be the location of the atoms. This of course has to be included in the calibration routine for absorption imaging.

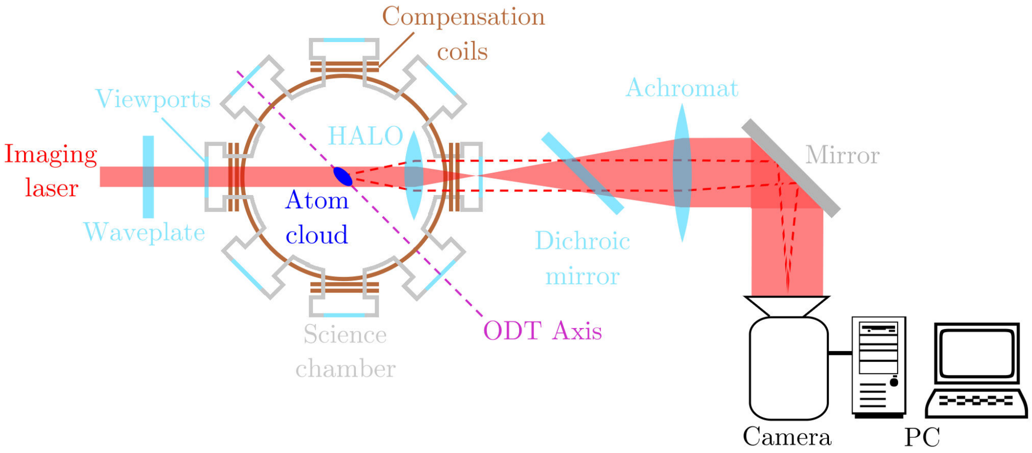

FIGURE 2.4: Imaging setup of the science chamber. A slightly focused laser beam runs directly from a fiber through the viewports into the chamber onto the atoms and propagates through the HALO, another viewport and via the dichroid mirror onto the CCD sensor of the camera. Schematic from [68].

Stingray F145-B camera

The installed camera model is a Stingray F145-B from Allied vision. The size of a single pixel is 6.45 µm x 6.45 µm and the quantum efficiency is 15% [138]

at 780 nm. The quantum efficiency indicates how many electrons are generated in the CCD sensor by an incident photon. The camera itself further converts the electrons into counts which are readout by a Labview software automatically. This conversion parameter is not known. Instead, the conversion factor G from photons to counts is experimentally determined by an independent measurement. For this, laser pulses of different lengths and powers are sent through the imaging system and measured before the science chamber and also detected afterwards by the camera. The power meter used here is a Thorlabs PM160 with an optical sensor, which can also measure powers of down to 10 nW with an uncertainty of ±3% according to the manufacturer. The number of photons N_{ph} in the pulse is then calculated using the power meter and the pulse length which can be precisely set by our experimental control software (the shortest pulse width is 2 µs) and the photon energy E_{ph}. We then compare this photon number with the counts N_c measured by the CCD sensor of the camera. If the transmission of the imaging optics is taken into account, a value of $G = \frac{N_{ph}}{N_c} = 2.15 \pm 0.08$ is obtained. It is important to note that for powers below 1µW or pulse durations below 5 µs, the system is subject to fluctuations and the pulse shape is not stable. The pulses themselves are generated by an acousto-optical modulator and for very low RF power the diffraction efficiency varies (probably due to thermal effects). The PM160 optical power meter is not able to measure these short-term differences, but with a photodetector this was possible and the pulse height is consistently to low at very low power levels or short pulse duration. This leads to an overestimation of the gain factor in the area of low total counts of the camera. It is possible to correct this effect slightly, but it has not been possible to eliminate it completely. We have decided to define an operating point for our system under which these fluctuations do not occur. It is an area in which the gain factor is almost constant and the signal-to-noise ratio of the images is also significantly better in this area.

Final image processing

To generate the final image of the atom cloud, three distinct images are taken sequentially. The first image depicts the atoms, providing the most important data. The second image serves as a reference which only captures laser light without any atoms. The third image is used for corrections of the background without any laser illumination. The images are taken at intervals of about 100 ms and directly processed by a Labview software which calculates the particle number automatically. In order to obtain directly particle numbers as a result, Eq. (2.2), which only describes the optical density $od_c(x,y)$ for a pixel at the position (x,y), must be further adapted and modified. The camera itself only produces counts per pixel $C(x,y)$ as a quantity. For the linear term, a conversion must be made from counts per pixel to absolute intensity per

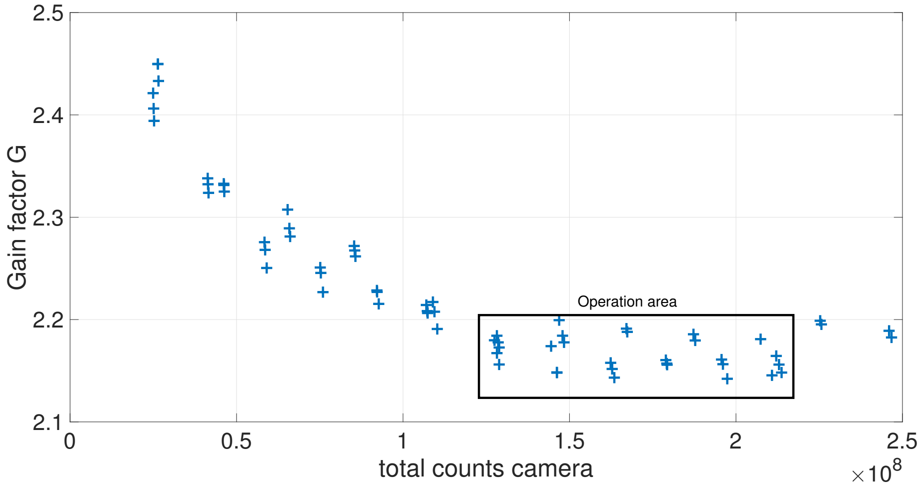

FIGURE 2.5: Measurement of the inverse gain G of the Stingray camera. The CCD sensor of the camera is illuminated by an precisely adjusted laser pulse. The camera itself provides counts per pixel, which are summed over the entire sensor to give the total counts. From a precise power and pulse length measurement, the photon number N_{ph} of the pulse is calculated. The ratio between photon number and total count rate gives the inverse gain factor G.

pixel for which the previously determined gain G of the camera is required

$$N_c(x,y) = \frac{\alpha p^2 M^2}{\sigma_0}\left[-\left(1+4\left(\frac{\delta}{\Gamma}\right)^2\right)\ln\left(\frac{C_a}{C_r}\right) + \frac{E_{ph}G}{p^2M^2T}\frac{C_r - C_a}{I_s^0\alpha}\right]. \quad (2.3)$$

Additional parameters are the pixel size p, the magnification factor M, the photon energy E_{ph} and the camera gain G and the transmission of the system T. This formula gives the atoms per pixel, see Fig. 2.6 for a cloud of ^{87}Rb atoms. To quantify the atom number within the cloud, two approaches are commonly used: summation over all pixels across the entire image to directly obtain the particle number or first sum up columns or rows and fit a Gaussian profile to it. From the fitting parameters, the particle number is calculated. Important for the second approach is that this method provides additional insights (spatial distribution, position) of the atom cloud which can further be used to derive thermodynamic properties such as the temperature.

2.2.2 Calibration and discussion

As described above, the calibration of the particle number can be achieved by varying the probe laser intensity. The methodology follows the work in [116] quite closely and also provides information on how the calibration factor in the system can be optimized as far as possible and which factors play a role. In the following, the level scheme for ^{87}Rb is used, but the explanations

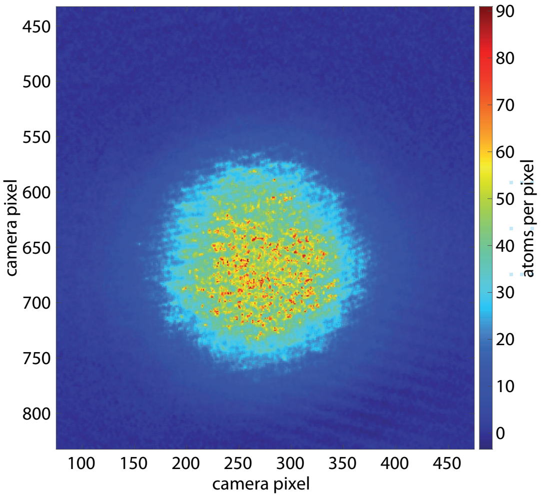

FIGURE 2.6: Image of a Rubidium atom cloud after 15 ms time of flight. These images can be used to determine typical parameters such as the number of particles and density of an atomic cloud. In this image, the color is a measure of how many atoms accumulate on a camera pixel. For this example, the cloud consists of about 1.6×10^6 particles and has a density of $1 \times 10^{13}\text{cm}^{-3}$.

are analogous to the isotope ^{85}Rb, only the frequencies of the imaging light change and different hyperfine states are used in a first order approximation. In the main experiment, typically we work with the hyperfine state (F = 1, $m_F = -1$), see Fig. 2.7. For absorption imaging, it is convenient to use the light which is previously used for the magneto-optical trap. This laser is resonant to the F = 2 to F′ = 3 transition. Therefore, it is necessary to repump our atoms from the F = 1 state into the F = 2 state before the actual absorption imaging happens. The corresponding laser is called imaging repumper and it is linearly polarized, parallel to the magnetic field vector in the science chamber.

The atoms can decay from the excited state F′ = 2 to the ground state F = 2, which gives us a distribution of the atoms at different m_f levels. For a given circular polarization of our imaging light, σ-transitions are optimally driven as soon as the magnetic field vector $\vec{B}$ and the propagation axis $\vec{k}$ are parallel. This can now be used to determine the background magnetic fields of the system in more detail. If the alignment deviates from a parallel setting, one gets a smaller effective cross section and the saturation intensity of the transition increases and the atoms absorb less light at a fixed laser power. Or in other words, the calibration factor α increases. The result is a cloud of atoms that only appears more dilute due to the absorption imaging. It is important to understand that one has to assume that we can drive transitions fast enough to reach a steady-state of the system very fast within a few scattered photons. In order to optimize the calibration, the background magnetic field has to be compensated as precisely as possible, as this can change

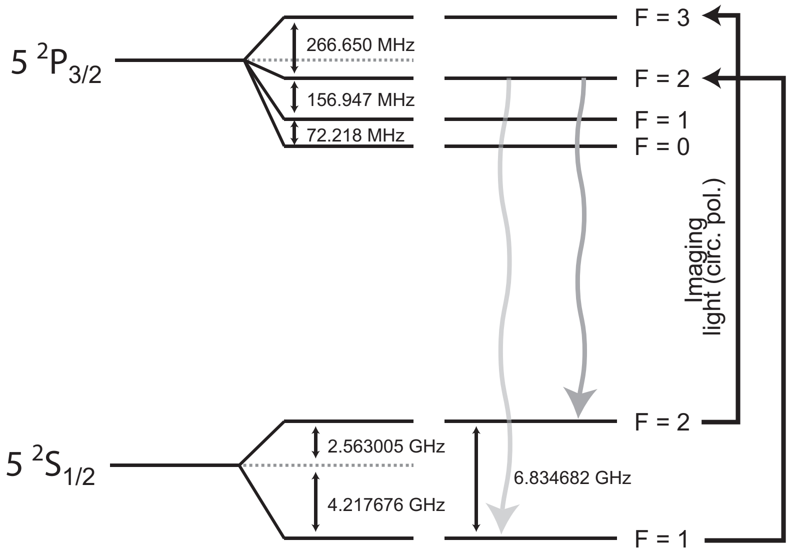

FIGURE 2.7: Energy level structure of ^{87}Rb for absorption imaging. To optically pump the atoms into the right hyperfine state F = 2 for absorption imaging, an imaging repumper laser is used which is resonant to the transition F = 1 to F′ = 2. For the absorption imaging itself the master laser is used which is frequency-stabilized to the F = 2 to F′ = 3 transition.

the probability of a σ-transition. The determination of the background field might also belong to the chapter on magnetic field coils, but it is essential for the calibration of the absorption imaging. Therefore, the determination of the background field is discussed in more detail here. We use three different coils (in Helmholtz configuration) in three perpendicular spatial directions (see Fig. 2.4). For the directions that are approximately perpendicular to the beam axis, the magnetic field is varied and the measured optical density or the measured particle number is maximized. The idea here is to align the beam axis as parallel as possible to the vector of the applied magnetic field, because this increases the probability of the transition which is effectively a compensation of the background field in the corresponding axes. For the coil which is parallel to the light propagation axis, one notices a different behavior. As soon as the background field in the propagation axis is nearly compensated, a drop in particle number fraction is observed (see Fig. 2.8, right). In the ideal case, the light propagation vector $\vec{k}$ and the magnetic field vector $\vec{B}$ are parallel and therefore σ^+ transitions are optically driven. As the magnetic field along the beam axis is reduced, it can no longer be assumed that the magnetic field vector and the k-vector are parallel. This can lead to admixtures of other transitions (such as σ^-), which decreases the cross-section, causing the atoms to scatter less light. As a result, the observed particle count decreases. From the measurements, we can determine the background magnetic field. The background magnetic field has the direction $\vec{B} = (\text{axial}, \text{imaging}, \text{vertical}) = (0.08, 0.51, 0.51)\,\text{G}$. With the compensated background field and an additional B-field $\approx 1\,\text{G}$ along the laser beam

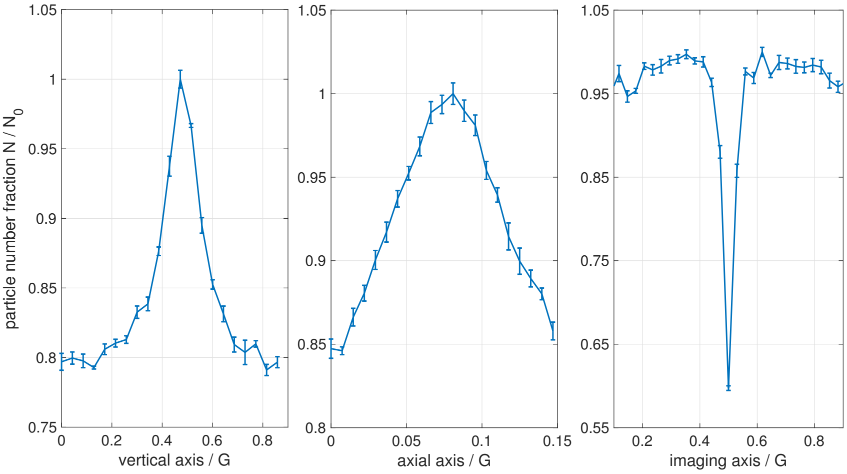

FIGURE 2.8: Determination of the background magnetic field in the science chamber. All three figures show scans of the compensation coils in different axis. Where the vertical and axial axis (which are perpendicular to the imaging axis) show a maximum at certain applied fields, the imaging axis features a sharp dip. For the two axes in the left and the middle, the position of the maximum particle number corresponds to a compensation of the background field in the respective axes. The right figure shows what happens if the background magnetic field is almost fully compensated by the coils: the particle number fraction drops. An explanation for this is given in the text.

direction, we measure the particle number as a function of the laser intensity. As a reminder, our initial assumption is that the number of particles may not change with imaging laser intensity. When analyzing the images, we now vary the correction factor α (see Eq. (2.3)) until the experimental data fits to our assumption. We consider the value for α as optimal where the particle number varies least with intensity, see Fig. 2.9 (cf. [116]). In the experiment, we vary the intensity from $0.03 \times I_s^0$ to about $3 \times I_s^0$ and keep the photon number per imaging pulse constant at a low level as this reduces momentum transfer to the atoms [67]. Our experimental lower limit in pulse length is 2 µs limited by the clock frequency of the control system. For shorter pulses, additional devices can be installed which is typically for absorption imaging not necessary. The final result for the calibration is $\alpha = 1.06 \pm 0.03$. This implies that the particle numbers obtained from the camera image, without any post-correction, is approximately 6% lower than the actual value and needs to be adjusted upwards. The physics of this correction lies in the fact that neither the light polarization nor the orientation of the magnetic field can be set perfectly. Both effects directly influence the cross section of the transition. Additionally, during the repumper process prior to the absorption imaging, the magnetic quantum numbers m_F of the atoms could be mixed due to spontaneous decay. This further reduces the effective cross section for the entire atom cloud.

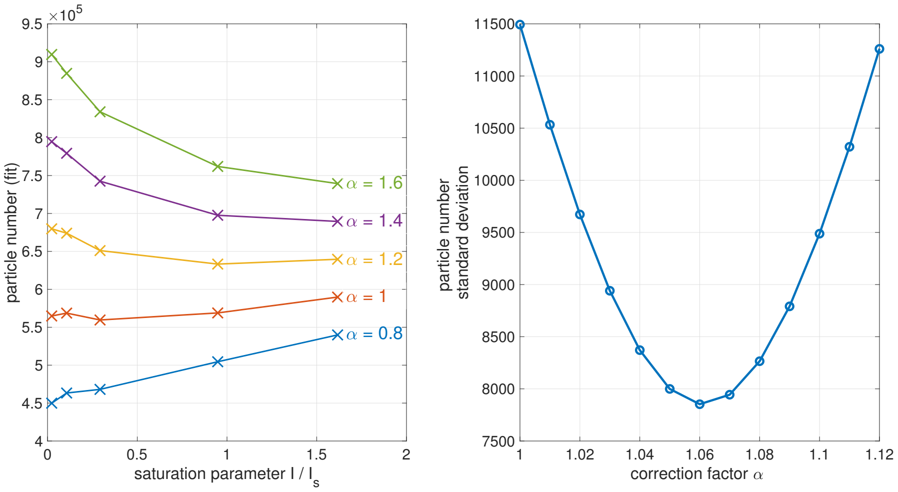

FIGURE 2.9: Determination of the correction factor α. Left: Measurement of the particle number with varying probe laser intensity (from 0.02 to $1.8 I_s$). The camera pictures are evaluated using different correction factors. Ideally, the particle number should not scale with the laser intensity. Right: Detailed analysis to determine α. For each setting of α, the standard deviation of the particle number for the intensity scan is calculated. We define the minimum in the standard deviation as the optimal correction factor for our system.

2.3 Coil system of the science chamber

The main coil system in the science chamber consists of a pair of copper coils (in the further course they are named Feshbach coils) which were previously described in [127]. Each coil has two layers of 15 winding each. The inner diameter is 130 mm and the outer 147 mm. The distance of the two coils is 126 mm with respect to the center of the Paul trap. We operate the coils in a Helmholtz configuration to generate a homogeneous magnetic field in the center where the Paul trap is located. The Feshbach coils are operated with a Delta 60-100 power supply from Delta Electronika. These can deliver up to 6 kW of power and have switching times (rise and fall) of around 2 ms. Another customization option for this system is to switch between a Helmholtz configuration and an Anti-Helmholtz configuration. Possible applications, first test measurements and the setup are presented in the Appendix A.1.

The Biot-Savart law is used to approximately estimate what B-field is produced for a specific electric current. The Biot-Savart law is first applied for one loop and then simply added for all other loops. The results are shown in Fig. 2.11. As expected from an Helmholtz configuration, the calculated magnetic field is approximately homogeneous around the geometrical center of

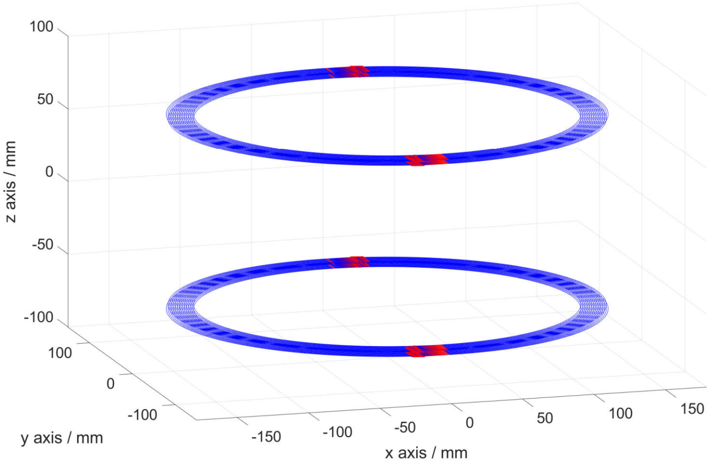

FIGURE 2.10: Schematic of the Feshbach coils which is used for the simulation. The geometric parameters are given in the text.

the setup within a range of 40 mm. This is an order of magnitude bigger than typical atomic cloud sizes in our science chamber. From the calculation, the coils produce

$$\frac{B}{I} = 2.01\,\frac{G}{A}. \tag{2.4}$$

in the center of the Paul trap (z = x = 0).

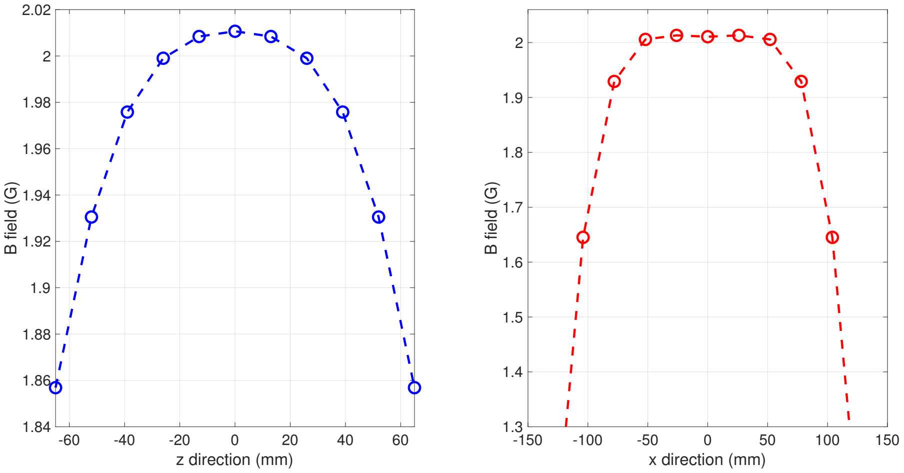

FIGURE 2.11: Simulation of the magnetic field for the Feshbach coils using the Biot-Savart law. Left: Calculated absolute magnetic field as a function of the z-direction (x = y = 0). In the center, the field strength exhibits a maximum and a minor dependence on the position. Right: Calculation for the absolute magnetic field of the x-direction (y = z = 0). In the center region, the magnetic field is approximately constant which shows the homogeneous properties of a Helmholtz configuration.

2.3.1 Calibration via photoassociation spectroscopy

We want to determine experimentally what B-field our coils generate at the location of the atomic cloud for a certain applied current. Here we do this using photoassociation (PA) spectroscopy. The spectroscopic technique is explained in further detail in Chapter 4.1. We use the molecular excited state $A^1\Sigma_u^+$ of $^{87}\mathrm{Rb}_2$ in the vibrational level $\nu = 66$. At nearly zero magnetic field, we observe a photoassociation signal at 281.444950(10) THz. By increasing the magnetic field, we observe that the photoassociation signal shifts in frequency due to the Zeeman effect. It is well known in the literature how the hyperfine levels of rubidium ground state $F = 1, m_F = -1$ shift in a magnetic field [137]. As a very good approximation, the shift turns out to be $2 \times 0.7\,\mathrm{MHz/G}$ and is further used for our calibration. The experimentally determined value for the Feshbach coils is then

$$\frac{B_{\mathrm{exp}}}{I} = 2.09 \pm 0.04\,\frac{G}{A}. \tag{2.5}$$

There is a slight discrepancy between the experimental results and the previous calculation. This could be due to the fact that the experimental setup does not exactly match the dimensions used in the calculations and technical drawings. For example, if the distance between the pair of coils is 125 mm instead of the intended 130 mm, this difference alone could explain the observed discrepancy. The magnetic fields that can currently be achieved are 200 G.

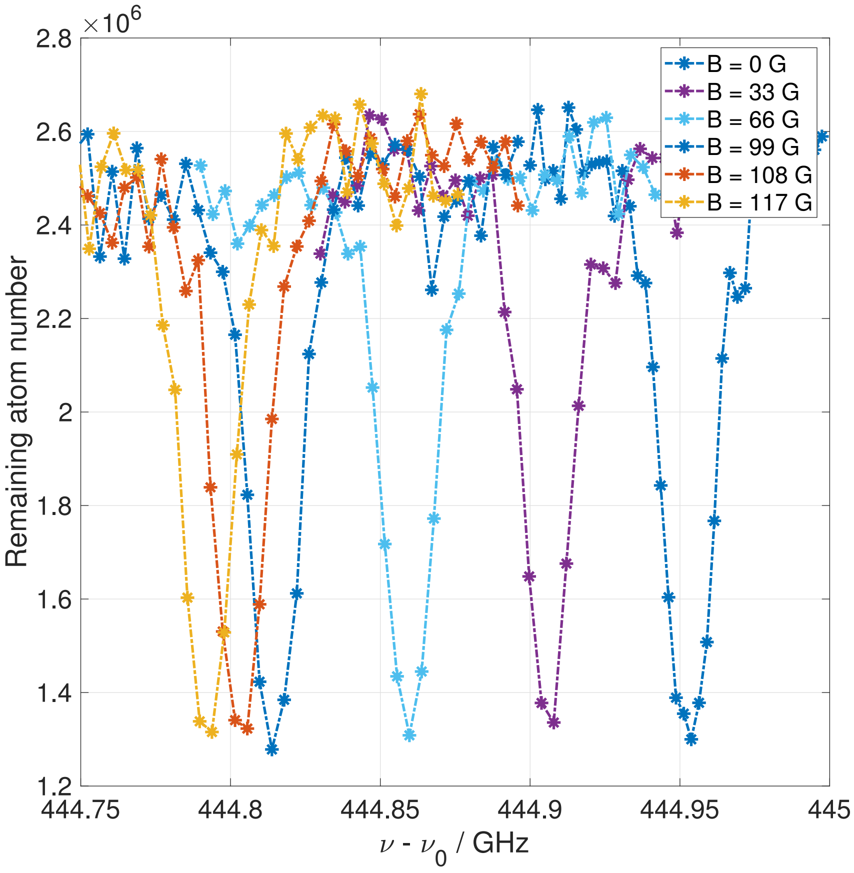

FIGURE 2.12: Photoassociation spectroscopy for various externally applied magnetic fields. Each color represents a different applied magnetic field. The spectra exhibit a minimum in the remaining atom number if two unbound atoms are associated by a photoassociation laser. Due to the Zeeman effect of the rubidium atomic ground state $F = 1, m_F = -1$, the resonance positions shifts with higher magnetic field to lower excitation frequency ν.

2.4 Laser systems for the spectroscopy of ultracold molecules

Molecular spectroscopy demands laser sources that are not only highly stable but also offer broad frequency tunability. A nice review about cold and ultracold molecules and spectroscopic techniques can be found in [20]. The main interest in this work is the precise study of three-body recombination in a state-to-state fashion. Techniques as photoassociation (PA) and resonance enhanced multiphoton ionization (REMPI) are routinely used to examine ultracold molecules which is explained in more detail later in Chapter 4.2. In the following section we will focus on the technical requirements that our laser systems have to fulfill in order to successfully carry out molecular spectroscopy. For instance, the excited molecular levels of ^{87}Rb corresponding to the 5s + 4d asymptote span a spectral region from 518 nm to 710 nm. Laser systems that can offer such wide tunability are based on OPO (optical parametric oscillator) technology or a dye laser. Another important parameter is the linewidth of the laser system. We expect the molecules to be ultracold, so velocity induced Doppler broadening of the natural linewidth is neglected here. Theoretically, the natural linewidth of a molecular state is difficult to predict and calculate and can vary significantly depending on factors such as interactions between molecular levels. Our experimental observations have shown that the smallest linewidth observed in our studies, using low laser intensities of less than $I = 20\frac{\mathrm{mW}}{\mathrm{cm}^2}$, is approximately 12 - 15 MHz. At higher power levels, the linewidth can broaden to several hundred MHz. There is a variation of the linewidth for fixed powers between different molecular levels, see Fig. 4.20 and Fig. 4.19 which have been recorded at 100 mW. Ideally, the linewidth of the laser systems should be smaller than the natural linewidth of the molecules. In this thesis, three distinct laser systems are used for the molecular spectroscopy, each described in detail in the following sections.

2.4.1 Hübner Photonics C-WAVE

The C-WAVE system is a commercial system built and designed by the company Hübner Photonics. A general overview is given in [136]. The system provides large frequency tunability in the visible region (from 450 nm to 650 nm with a gap at 532± 10 nm) and in the infrared (from 900 nm to 1300 nm, with a gap around 1064± 20 nm). The system mainly consists of three optical cavities (see Fig. 2.13) which are described in the following sections in more detail. The supplied C-WAVE CONTROL software makes operation fully automatic. Within a precision of 100 GHz the laser output can be generated automatically. More precise settings can then be made manually and the frequency can be stabilized to an external reference, (see Section 2.17) to achieve the accuracy necessary for molecular spectroscopy. The manufacturer states that the linewidth of the entire system should be below 500 kHz for the VIS output.

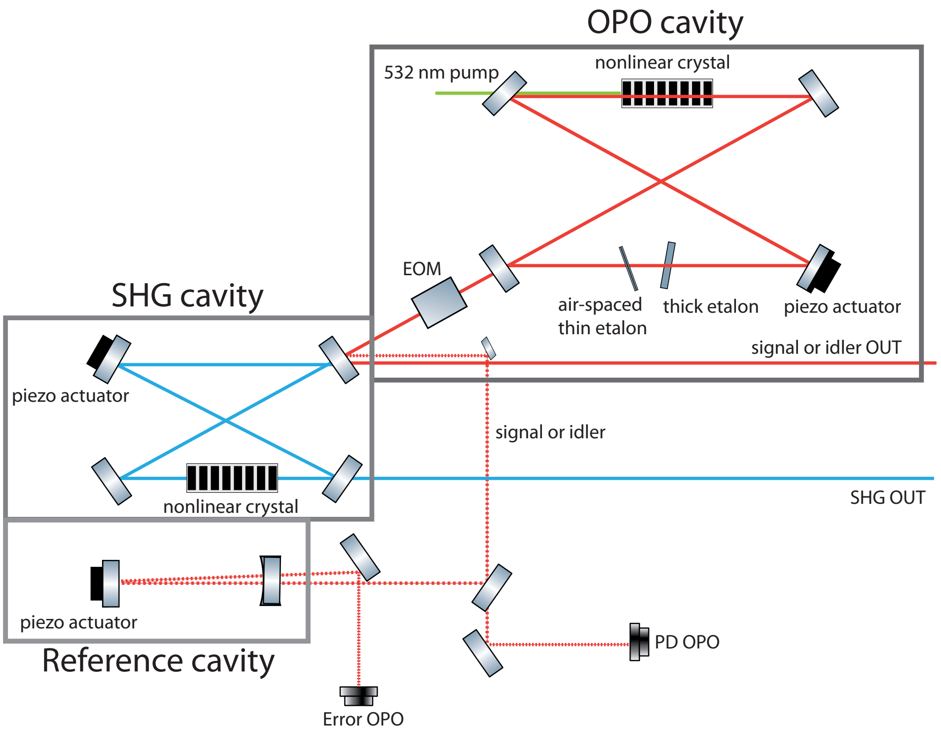

FIGURE 2.13: Schematic beam path and overview of the C-WAVE system. In a first step, a 532 nm pumps a nonlinear crystal to generate photons in the near infrared spectral range (OPO). To reach the visible spectrum (450 - 650 nm), the photons are frequency-doubled in a SHG cavity. The whole system is frequency-stabilized to a reference cavity which can possibly be stabilized to a wavelength meter (not shown).

OPO cavity

The operation principle is based on OPO technology. A nonlinear optical crystal is pumped with a strong (up to 5 W) fiber laser at 532 nm. The crystal itself converts the incoming photon w_p into two photons (down conversion), called signal w_s and idler w_i. This process adheres to energy conservation and quasi-phase-matching. This essentially means a visible photon is down-converted into two photons in the infrared. To achieve sufficient conversion efficiency, the nonlinear crystal is operated inside a resonator cavity. The resonator is operated at either a particular idler wavelength (1080 - 1300 nm) or a particular signal wavelength (900 - 1040 nm). The coarse frequency tuning in the order of hundreds of Gigahertz is done using the temperature of the nonlinear crystal and choosing a suitable poling period and a very thin turnable etalon. An additional thick air-spaced etalon then also enables fine frequency tuning over a few GHz, but is mainly used for automatized power optimization of the system. For precise tunability, the OPO cavity length is tuned using a piezo actuator connected to one of the cavity mirrors, see OPO cavity in Fig. 2.13. This complex setup allows us to achieve stable and broad tunability necessary for molecular spectroscopy.

Reference cavity

Additionally, the system includes a reference cavity that enables stabilization of the OPO resonator's frequency. A small fraction of light is outcoupled from the OPO and modulated by an electro-optical modulator (EOM), operating at around 10 MHz. This modulated light is then coupled into the reference cavity. Unfortunately, the manufacturer does not specify specifications as free spectral range (FSR) or linewidth. Some portion of the light is reflected back from the reference cavity and directed onto a photodetector. The signal from the photodetector is demodulated, resulting in an error signal with which the system can be stabilized to a specific set point. To control frequencies more precisely on an absolute scale, we use a wavelength meter WS7 from the company High Finesse. The technique of laser frequency stabilization by using a wavelength meter is explained in Section 2.17 and can be used for other laser systems as well. We achieve long-term (> 8 hours) stability in the order of a few MHz.

SHG cavity

To produce frequencies in the visible range, a further nonlinear crystal (SHG crystal) is necessary. The process for wavelength conversion takes place in another separate cavity. It has a similar design as the OPO cavity. Dependent on the wavelength (whether we operate the OPO cavity resonantly for signal or idler wavelength), the system automatically chooses a suitable poling period and performs a temperature tuning to automatically optimize the conversion efficiency and thereby the output power in the visible regime. The stabilization of the cavity is done by another piezo actuator which enables to achieve power stability better than 2 % over several hours. To the majority of measurements presented in this work, the SHG output is used for the molecular spectroscopy.

Maintenance of the C-WAVE system

The C-WAVE system needs generally an average amount of maintenance. It is advisable to periodically check the output power of the seed laser (NKT fiber laser) for the pump amplifier, ideally every few weeks. This output should be around 11 mW and has remained stable for several years. Additionally, the ALS pump laser should also be checked on a daily basis if operated. It is operated in a constant power mode, so it is important to monitor the pump diode current regularly. According to the manufacturer ALS (now TOPTICA), fluctuations of ±10% are normal and have been observed in our setup as well.

The base-plate of the C-WAVE is water-cooled. Although it is a closed system, the cooling water tends to become contaminated over time, so it is recommended to replace it with fresh distilled water every 6 months. Maintenance of the optical system itself typically involves aligning the pump laser into the OPO cavity. This should be checked every 1-2 months and handled with great care. Any additional alignment work as well as cleaning the optical components has so far been conducted in consultation with and under the guidance of a service engineer of Hübner.

2.4.2 Sirah Matisse 2 DX

A dye laser Matisse 2DX from the company Sirah was used additionally to the C-WAVE system. Most of the measured data for the spectroscopy in Chapter 4 was recorded using the dye laser due to a repair of the C-WAVE system. The dye laser may be preferred for measurements requiring very high power. However, its tunability depends on the dye employed. In the studies of this thesis, the dye laser was operated with Rhodamine 6G (which has spectral emission maximum at approx. 590 nm) dissolved in ethylene glycol and pumped by a 20 W laser from Spectra Physics at 532 nm. To resonantly enhance the emission of narrow frequencies, the dye beam is placed in a bow-tie configured optical cavity. Similar to the C-Wave system, various optical components (a thick etalon with 20 GHz free spectral range (FSR), a thin etalon with a 250 GHz FSR, and a birefringent filter with a 130 nm FSR) and electronic components (piezo actuator) are used to adjust the optical length of the cavity and thereby tune the resonant frequency of the system.

The system can then be stabilized to an external high-finesse cavity (linewidth of the cavity according to manufacturer $\approx$ 100 kHz). Analogous to the C-WAVE system, the length of this cavity is adjusted and stabilized using a wavelength meter lock. For additional details and operational guidance, the company Sirah provides a comprehensive manual to help users to understand and operate the laser system.

The laser output can then be frequency-doubled using a SHG cavity (Matisse Wavetrain) to produce UV light at around 300 nm. This has been used in previous work to investigate neutral long-range Rydberg molecules in our group [32] but will not be covered within this thesis.

Maintenance of the Sirah Matisse

The Matisse system requires more maintenance than the C-WAVE system. Over time, the dye used in the Matisse system ages and becomes less efficient and needs to be replaced. According to my experience, the dye has to be replaced every two to three months if operated full-time (8-10 hours per day). In practice, the issue is not the degrading output power but rather the increasing difficulty in stabilizing the frequency of the fundamental bow-tie cavity. Optical alignment of the laser is rarely needed - less than once a year

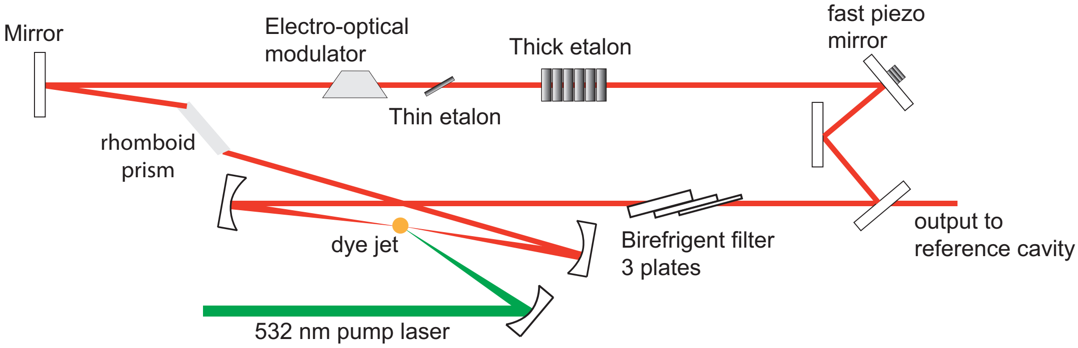

FIGURE 2.14: Simplified schematic of the Matisse bow-tie cavity. Several optical components (birefrigent filter, thick etalon, thin etalon, fast piezo mirror are used for optical path length adjustment. A fraction of the output power is coupled into a reference cavity for external frequency stabilization (not shown here). A more detailed illustration can be found online: https://www.sirah.com/lasers/cw/matisse-2/matisse-2-d/.

under our laboratory conditions - and should only be performed if, for example, the system needs to optimized for a different wavelength (a change of $\approx 10\,\mathrm{nm}$ with the same dye needs adjustment). Water-cooling of the Spectra physics pump laser has to be checked on a daily basis and also the water-cooling of pump for the dye jet.

2.4.3 Sirah Credo

The Credo system is another dye laser from Sirah, differing from the Matisse system by being operated with a pulsed pump laser at 532 nm. This system generates average powers up to 28 W with repetition rates up to 100 kHz and pulse lengths of 10 ns. The laser's linewidth is approximately 1.8 GHz, determined by the resonator design of the system and the tuning range is 588 - 632 nm for Rhodamine B. The pulsed operation allows for the measurement of larger frequency ranges nearly 100 times faster but with reduced resolution. In this work, the Credo laser was primarily used to measure the molecular states related to the 5s + 4d asymptotic level for both rubidium isotopes. Since we typically work with ultracold molecules and low rotational angular momenta ($J = 0, 1, 2$ ..), it is difficult to resolve rotational structures of the molecules but vibrational levels can be identified quite fast. Here, we give more information about the setup and the frequency adjustment. Measurement data and its interpretation are presented in Chapter 4 and further analyzed in the Appendix B.
The system consists of a resonator unit which is pumped with a relatively low amount of 532 nm light. The pump beam hits the dye flowing through a glass cell (Brewster Dye cell). Typically, Rhodamine B solved in Ethanol is used for emission at around 600 nm. The resonance frequency of the resonator is adjusted by using a grating and a motorized rotating mirror similar

to a Littrow configuration. The resonator output is then used to seed an (optional) amplifier unit which is pumped by a high amount of laser light (in our case up to 90 W). In our setup, we use the fundamental light and no additional frequency conversion unit.

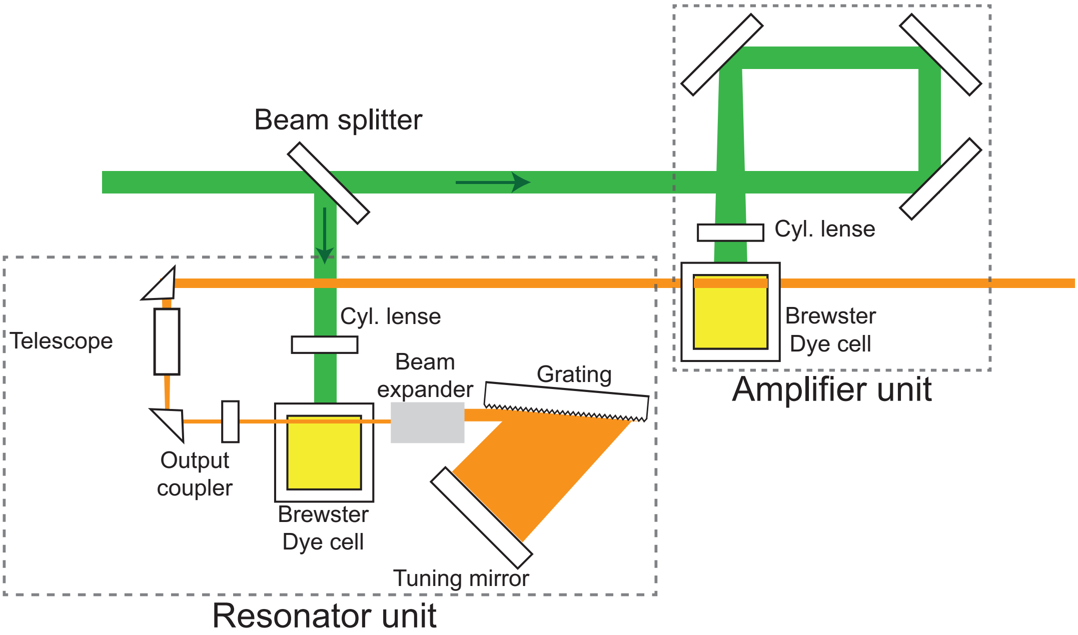

FIGURE 2.15: Overview of the Credo system. It consists of two main units: the resonator unit and the amplifier unit. The resonator unit is used to adjust the frequency by a tuning mirror and the resonator output seeds the amplifier unit to amplify the laser output power.

The frequency can be set in a Sirah software by controlling the motor and its position. Sirah also provides additional tools that allow direct integration with a high-precision wavemeter, enabling the stabilization of the laser frequency at a defined setpoint (see Sec. 2.4.4). However, this process proved to be extremely slow in practice, achieving active frequency stabilization only within more than 2 seconds. Given that the extreme high pump power leads to a fast degradation of the dye (typical working hours are only 4 hours at maximum pump power), we could not keep the laser turned on for extended periods. An active frequency-stabilization which is very slow would require almost a permanently running pumplaser which would result in a daily exchange of the dye. Instead, we opted for a simpler, non-actively stabilized method to tune the frequency. We calibrated the system to determine the number of motor steps required per 2 GHz frequency steps. In the experiments then, we adjusted the motor position with turned off pump laser, then briefly generate laser pulses for about 0.5 seconds and hit the atoms with the laser output. In parallel, we measured the frequency of the emitted laser pulse with a wavelength meter. This method allowed for reproducible scanning and significantly extended the dye's lifetime by a factor of more than

20 and is recommended until a faster automated frequency stabilization is available.

Maintenance of the Credo system

The Credo system require the most maintenance among our setups, primarily due to the high laser power which is used to pump the dye. According to the manufacturer, the typical lifespan of the dye is around 400 - 500 Wh, meaning the laser can operate at full power (100 W) for about 4 to 5 hours before the output power and stability drops significantly. Changing the dye is considerably more time consuming than with the Matisse system, as the Credo is a closed system with the dye circulating through glass cells. There, a cleaning step with pure ethanol is required before new dye can be refilled. While removing the glass cells is not particularly difficult, it ideally requires at least two people to do it.

The manufacturer claims that the glass cells can be removed and reinstalled without requiring laser realignment but this has not been our experience. After replacing the dye, the laser needs to be re-optimized with both output power and beam profile being affected by the alignment. The alignment process itself is not complex, as the resonator path generally does not need to be readjusted. Only the in-coupling and the beam path (beam shaping optics) which passes the amplifier cell needs more care.

During a three-week period of operation (not full-time), we had to replace the dye twice. This matches the recommended operation of approximately 400 Wh. Another critical aspect is the cooling cycle of the pump laser. We use a Termotek chiller which is a water-water cooling system. Due to the poor quality of our cooling water of the facility, it is necessary to clean or replace the filter in the external water circuit every four weeks. If the filter becomes too dirty and restrict the water flow, the pump laser cannot reach its operating temperature of 25°C.

2.4.4 Frequency stabilization by using a wavelength meter

For the molecular spectroscopy presented in this thesis, a wavelength meter lock was employed for active frequency stabilization of our used laser sources. In the following section, the operating principle of a wavelength meter lock is presented, along with an explanation why this method is suitable and sufficient for the measurements presented in this work.

The most crucial aspect of this method is the reliable determination of the actual laser frequencies. In our laboratory, we use a High finesse wavelength meter WS7-60. The manufacturer specifies a relative frequency uncertainty of 2 MHz and an absolute frequency uncertainty of 60 MHz. The frequency uncertainty varies depending on the exact frequency range used. Typically, our wavelength meters (WS7-60 VIS/Standard) cover a spectral range of 400 - 1100 nm and can determine the frequency within 2 ms using enough laser power (200 - 1000 µW). The basic idea of a wavelength meter lock is quite simple. A target frequency is defined as a set point and compared with the measured frequency. Depending on the deviation from set point and actual laser frequency, a computer software (e.g. LabView) generates a feedback signal. This feedback signal is converted into an analog voltage and then fed back to the laser. In our case (C-WAVE, Matisse), the feedback is used to change the length of the reference cavity of the respective system (see Fig. 2.14 and 2.13). The corresponding systems follow the change in length automatically and the frequency shifts. The simple scheme is given in Fig. 2.17. The really big advantage of this method is the flexibility. As long as we use laser frequencies which can be measured by the wavelength meter and we have a feedback option, it is possible to use this method. This covers a range of more than 700 nm for our WS7-60 which is very difficult to achieve with a self-built cavity due to the lack of high-quality broadband coatings. However, the method itself also has some important parameters which are discussed in the following paragraphs.

Digital-analog conversion is one crucial aspect which can directly affect the performance of the wavelength meter lock. In general, the wavelength meter lock calculates a feedback by a computer software. The user can adjust the calculated feedback by changing the controller settings, in case of a steady linear regulator there are P, I and D controller. In our setup, the feedback for adjusting the cavity length of the respective reference cavity is an analog voltage from 0 to 100 V. The link between the computer and the reference cavity is a digital-analog converter and a high-voltage amplifier. We can use two different digital-analog converter systems in the BaRbIE laboratory.

- NI USB 6001 with 14-bit resolution and ±10 V output range. The maximal update rate is 5 kS/s and the slew rate is 3 V per µs. There are a lot of packages in different programming languages to correctly access and program the NI USB 6001 device, we use Labview or Python.
- Home-built analog-box included in the Bus system of the BaRbIE experiment with an output range of ±10 V and 16-bit resolution. The maximal update rate is given by the clock frequency of the BaRbIE system which is experimentally limited to 2µs and additionally the update rate of the integrated circuit which corresponds to 100 kS/s. The slew rate is similar to the NI USB 6001 with about 2 V per µs. The integrated circuit is the following: DAC7744 from the company Texas Instruments. The programming is done via LabView software.

The high-voltage amplifier is produced in the electronic workshop of Ulm University, currently P341 Version 2. Typically, by using the maximum range of the DAC, we set a gain around 10. The intrinsic noise level of the amplifier is smaller compared to the amplified noise level of the input from the DAC. Typically values are in the range of 20 mV.

Knowing the experimental resolution of WS7-60 is very important to judge the performance of the wavelength meter lock. The typical relative resolution specified by the company High Finesse is around 2 MHz in the wavelength range of 400 nm to 1100 nm. Experimentally, however, we found the relative resolution to be better by almost one order of magnitude. For confirming this, we used a narrow linewidth laser (< 10 kHz) which is externally frequency stabilized to a high-finesse ($F \approx 150000$) cavity [156]. The cavity's linewidth was independently measured in a cavity ring-down measurement to be smaller than 10 kHz. We monitor the frequency of the stabilized laser on the wavelength meter with an exposure time of 50 ms. The exposure time used for the wavelength meter heavily affects the recorded frequency of the laser, shorter exposure time gives worse results with more fluctuation in the frequency. For an exposure time of 50 ms the standard deviation for 100 samples was 250 kHz. By extending the exposure time to 500 ms, the recorded standard deviation decreased to about 30 kHz. This behavior is probably connected to a CCD sensor inside the wavelength meter which performs better with respect to the signal-to-noise ratio for longer exposure times. This demonstrates one of the disadvantages of the wavelength meter lock: in order to measure the frequency very precisely, long exposure times are necessary but for the actual wavelength meter lock, a high bandwidth (and low exposure times) is desired. This means basically, that the wavelength meter lock should be adjusted for the specific task and wavelength of the laser.

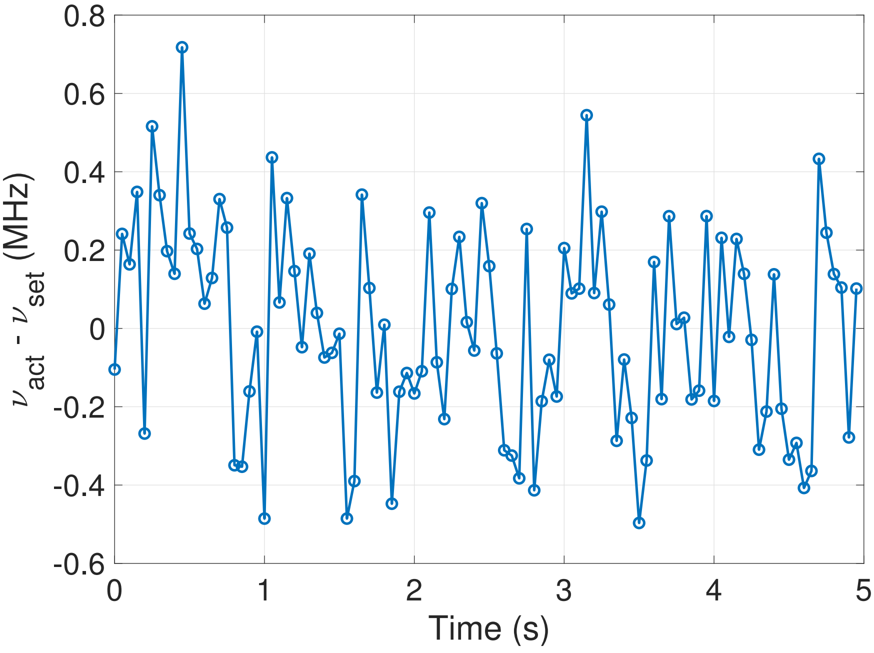

FIGURE 2.16: Recorded frequency of the 1762 nm laser system. This laser is locked to an external high-finesse cavity and used as a reference to test the wavelength meter specifications. The standard deviation of the recorded sample is 250 kHz, 100 samples are recorded in total and every 50 ms one sample is taken.

Experimental timings play an important role for the performance of the wavelength meter lock. Here, I give just a few ideas about the individual timings which matter for the experiment.

- Software bandwidth (computational time) can also limit the bandwidth of the whole wavelength meter lock. Typical bandwidths of our LabView programs are about 15-20 Hz. Higher bandwidths (more than 500 Hz) can be achieved by replacing the Labview software with Python based scripts or further optimizing the home-built LabView software.
- Whenever a fiber-switcher comes in operation, this drastically reduces performance of the wavelength meter lock. A fiber-switch operates up to 8 input fibers and combines them into one fiber which is directly connected to the wavelength meter. The fiber-switch mechanically switches the laser light which extends the time between frequency measurements depending on the number of channels used. For example, by using 8 channels with 2 ms exposure time each, each frequency is measured every 18 ms once. But if one channel needs more exposure time, this extends the overall time between frequency measurements of individual channels.

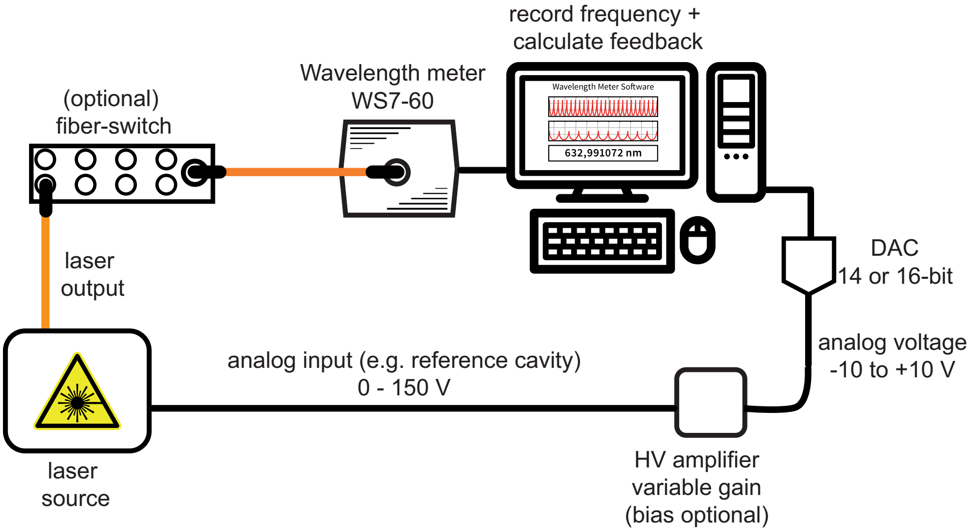

FIGURE 2.17: Schematic of the wavelength meter locking setup. The frequency of the emitted light of the C-WAVE is measured by the wavelength meter. The PC frequently reads the current frequency with 100 Hz repetition rate and calculates a feedback using an target and current frequency value. The feedback is first send to a DAQ device (NI USB 6001 or BaRbIE DAQ) and converted into a voltage in the range 0 - 10 V. To drive the piezo actuator of the reference cavity, the voltage has to be amplified further to change the length of the reference cavity.

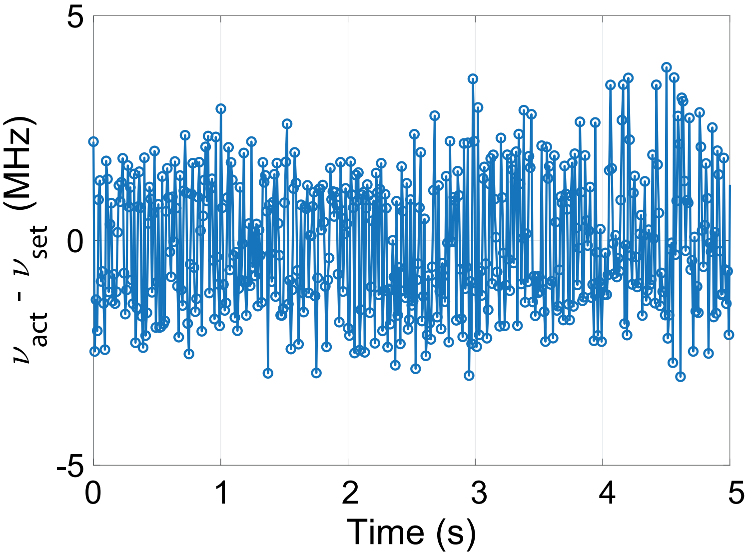

FIGURE 2.18: Stability measurement of C-WAVE locked by the wavelength meter stabilization. It shows the deviation between actual (measured) frequency ν_{act} and a set point ν_{set} in MHz. The standard deviation over 5 seconds is approximately 1 MHz and the peak-to-peak value is about 5 MHz. This stabilization is sufficient enough for us to probe ultracold molecules.

Chapter 3

Ultracold diatomic molecules

In the following chapter, I will provide a brief discussion of some aspects of ultracold diatomic molecules, focusing on rubidium as used in our experiments. Instead of presenting a general overview, I will tailor the discussion to the particular conditions relevant to our experimental setup. First, an explanation of the Born-Oppenheimer approximation is given and how potential energy curves can be derived from it. This will be supplemented by an introduction to Hund's coupling cases, which provide a simplified framework for describing the coupling of various angular momenta within a molecule and allow for classification of the molecular states according to symmetries and couplings of angular momenta.
Further, in Section 3.1.4, I will introduce the concept of coupled-channel analysis and discuss the couplings that are particularly relevant to our specific case (here: spin-orbit coupling and rotational coupling). This will be essential for the later discussion and understanding of the spectroscopic recordings in Chapter 4.

3.1 Theory of diatomic molecules

This section covers some theoretical concepts for the description of diatomic molecules. This is an abbreviated presentation and the interested reader can refer to a more complete and detailed description in textbooks [5, 17, 33, 63, 85]. In simple systems such as the hydrogen atom, the Schrödinger equation can be solved analytically and it provides a description of the eigenstates of the system. In the case of complex molecules as rubidium, however, this is no longer possible and approximations have to be made. In the following, I introduce the basic concept of the Born-Oppenheimer approximation.

3.1.1 Born-Oppenheimer approximation

The Born-Oppenheimer approximation treats the nuclei and electrons of the molecule separately. This is based on the different time scales that are relevant for electrons and nuclei. Due to their different masses, the state of the (heavy) nuclei can be described as rigid and that of the (light) electrons are considered as dynamic. This assumption allows the electronic wave function of the molecules to be calculated for any fixed internuclear distance R. The set of solutions for the eigenenergies for different R obtained by this approach are molecular potential energy curves (PEC) for diatomic molecules. For the mathematical description of the Born-Oppenheimer approximation, the interested reader may refer to a textbook of their choice (e.g. [5, 17, 63]). In the following thesis, we mainly deal with potential energy curves as a function of the internuclear separation. Fig. 3.1 shows potential energy curves for the rubidium dimer as a function of the internuclear separation calculated by an ab initio approach [95]. The two energetically lowest potential energy curves $X^1\Sigma_g$ and $a^3\Sigma_u$ belong to the case when two rubidium atoms approach each other in their atomic ground state $5s_{1/2}$ and are therefore assigned to the 5s + 5s asymptote. Analogously, excited states can be summarized with respect to their asymptotic atomic states for large internuclear distances. The notation used for the individual molecular states and interactions is explained in more detail below using Hund's cases.

3.1.2 Hund's coupling cases

The situation described above in the Born-Oppenheimer approximation is complicated by the fact that there are several angular momenta in molecules. The angular momenta lead to couplings that can be classified according to their strength. In the 1920s Friedrich Hund proposed various cases of coupling, which are called Hund's cases [69, 70]. Molecular term symbols are used to describe the molecules and their couplings. These also give information about the symmetry of the wavefunction. Similar to the atomic case, selection rules for spectroscopic transitions between molecular states are derived from that. If we neglect the nuclear spin, there are three sources of angular momentum in a molecule: the sum of the spin of the electrons $\boldsymbol{S}$, the sum of the orbital angular momenta $\boldsymbol{L}$ of the electrons and the purely mechanical rotation of the molecule $\boldsymbol{R}$. Hund has considered a total of five different coupling cases which are then labelled Hund's case a) to e). For the purpose of understanding the spectra and their analysis later on, I will only refer to three of Hund's cases here: case a), b) and c). Table 3.1 summarizes the angular momenta and their projections. The projections of the electronic angular momenta appear as quantum numbers because the molecular axis is a quantization axis for the electronic system.

In Hund's coupling case (a), the orbital angular momenta $\boldsymbol{L}$ is strongly coupled to the molecular axis because of Coulomb interaction and the spin S is coupled to the internuclear axis of the molecule. The projections onto the internuclear axis define the quantum numbers Λ and Σ. The sum of the projections gives the total electronic angular momentum $\Omega = |\Sigma + \Lambda|$ along the molecular axis. The resultant angular momentum then combines with the rotational angular momentum $\boldsymbol{R}$ to give a total angular momentum $\boldsymbol{J}$ (exclusive of nuclear spin). In this case, Λ, Σ, Ω, J are good quantum numbers. The

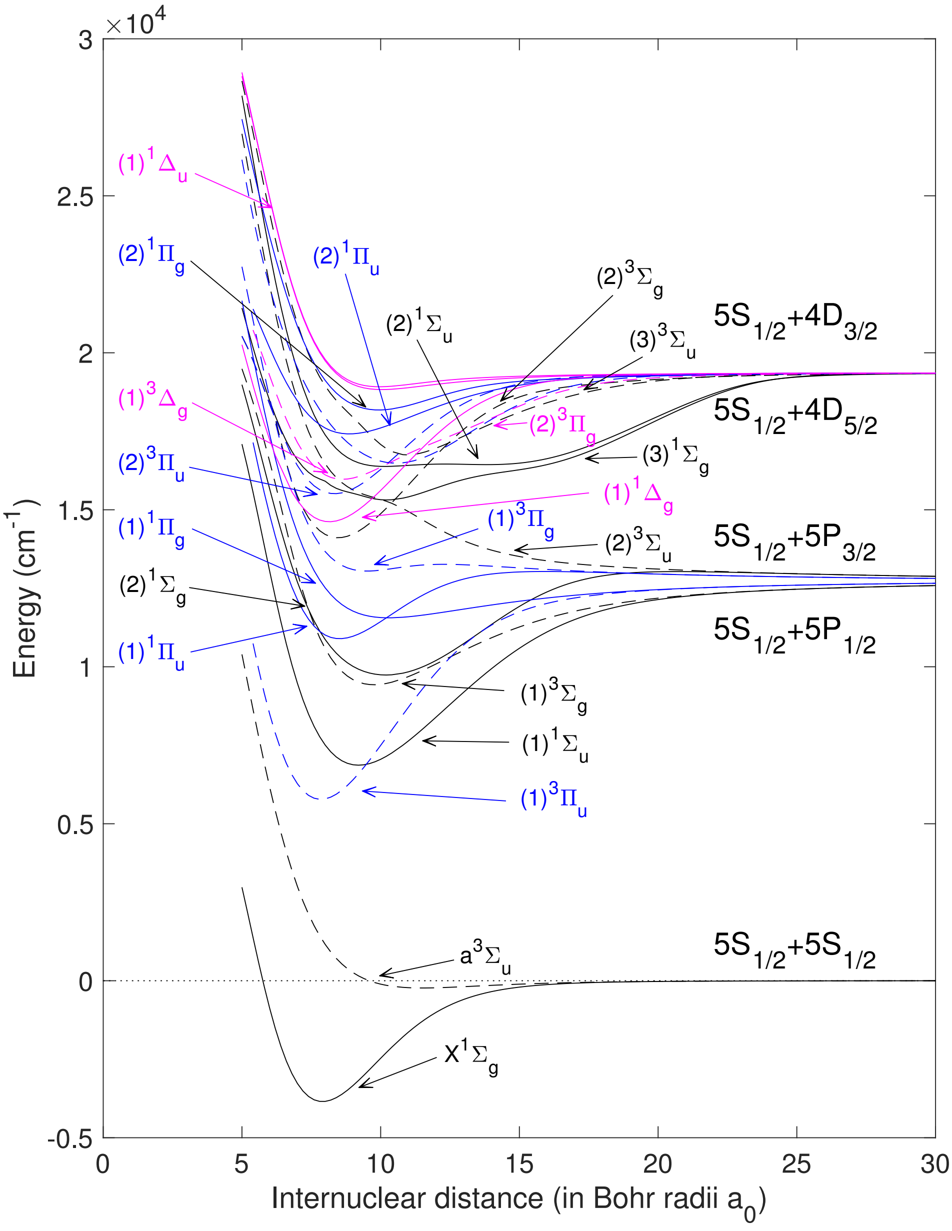

FIGURE 3.1: Potential energy curves (PEC) of the rubidium dimer Rb_2 according to Lozeille [95]. The solid lines correspond to molecular singlet states and the dashed lines are triplet states. Different color schemes refer to states with different Λ-projections on the intermolecular axis (Σ, Π, Δ-states).

nomenclature used in Fig. 3.1 in the basis of Hund's coupling case a) is given by

$$^{2S+1}\Lambda^{(+/-)}_{\Omega,(g/u)} \tag{3.1}$$

where g/u denotes the parity of the state under inversion of the electronic spatial coordinates, typically refered to as "gerade" (symmetric, g) or "ungerade" (antisymmetric, u). This applies only if both nuclei have the same nuclear charge Z. The +/- superscript indicates the reflection symmetry of the electronic wavefunction with respect to any plane containing both nuclei which applies only for Σ states. For states with $\Lambda > 0$, the +/- notation is omitted. This is because for such states, there is always one component that is symmetric with respect to reflection through this plane and another that is antisymmetric. It is also important to clarify the convention for labelling states: states with $\Lambda = 0$ are denoted as Σ states, $\Lambda = 1$ as Π states, and $\Lambda = 2$ as Δ states, and so forth. Here, Λ refers to the projection of the orbital angular momentum onto the internuclear axis.

Hund's coupling case b) differs from case a), since the spin is decoupled from the intermolecular axis. The nuclear rotation $\boldsymbol{R}$ couples with $\boldsymbol{L}$ and produces $\boldsymbol{N}$. $\boldsymbol{N}$ couples then to $\boldsymbol{S}$ to form $\boldsymbol{J}$. Good quantum numbers are Λ, N, S and J and Λ is not only the projection of $\boldsymbol{L}$ which does not appear as a quantum number , but also from $\boldsymbol{N}$. Later I will describe the molecules which are formed by three-body recombination by Hund's case b) and motivate the selection rules and derive what optical transitions to the excited states are allowed.

In Hund's coupling case c) the total electronic orbital momentum and the total electronic spin are strongly coupled. The consequence is that Λ and Σ are no good quantum numbers. The projection Ω, however, is still a good quantum number. The typically used notation in Hund's case (c) is

$$\Omega^{+/-}_{g/u} \tag{3.2}$$

with the corresponding g/u gerade / ungerade and $+/-$ reflection symmetry (for $\Omega = 0$ states).

In the following spectroscopic analysis, I will mainly use Hund's case a) for the description of the excited states. Here, one essential aspect is that the rotational structure for molecules described in Hund's case a) (and e.g. c)) is expressed by the rotational energy ladder $E_R = B_v J(J+1)$ with the rotational constant B_v. The analysis of the rotational states can therefore be carried out in the same way, only different rotational constants are used for the different electronic states.

TABLE 3.1: Relevant angular momenta for Hund's coupling cases. The projection is always referred to the molecular internuclear axis. The projection for $\boldsymbol{R}$ is zero since the internuclear axis and the nuclear rotation vector are perpendicular.

Type of angular momentum	Operator	Quantum number	Projection
Nuclear rotation	$\boldsymbol{R}$	R - case e) only	-
Electronic orbital	$\boldsymbol{L}$	L	Λ
Total angular momentum without spin	$\boldsymbol{N} = \boldsymbol{R} + \boldsymbol{L}$	N	Λ
Electronic spin	$\boldsymbol{S}$	S	Σ
Total angular momentum with spin	$\boldsymbol{J} = \boldsymbol{R} + \boldsymbol{L} + \boldsymbol{S}$	J	Ω

3.1.3 Molecular symmetries

For a deeper understanding of molecular spectra, knowledge of the basic symmetry operations in the molecules can be helpful. There are several types of symmetries which will be described in the following paragraphs. Later in Chapter 4.2, symmetries are used to specify selection rules for photoassociation (PA) of atoms and molecular bound-to-bound transitions using laser light.

The total parity describes the inversion of the coordinates of nuclei and electrons. The molecular states have either a positive parity (+) or a negative parity (-) which is different from the +/- reflection symmetry of the electronic state and also of the u/g symmetry. The corresponding operator does not change the vibrational part of the wavefunction since it is only a function of the internuclear distance. However, the behavior on the rotational part of the wavefunction, i.e. the rotation of the nuclei complicates the situation because it depends on the total angular momentum J.

The rotationless parity Since the total parity changes with J, for a more convenient treatment, the rotationless parity e / f is introduced. The alternation of the total parity is factored out.

Gerade / ungerade (g/u) parity for equal Z describes inversion of the electron coordinates with respect to the center of the molecular frame by the operator $\hat{\boldsymbol{\imath}}$. The positive eigenvalue refers to gerade states and the negative sign refers to ungerade states. In the molecular term symbol, g/u is used as a subscript.

Symmetric / antisymmetric (s/a) parity is a symmetry in homonuclear systems which describes the exchange of the two nuclei by the operator $\hat{\boldsymbol{P}}_{\mathbf{12}}$. For bosons, the wavefunction is symmetric with respect to the $\hat{P}_{12}$ operator and the eigenvalue is +1 whereas for fermions the eigenvalue would be -1 and the corresponding wavefunction asymmetric with respect to the operator $\hat{P}_{12}$. This is a consequence of the Pauli exclusion principle and the distinction gives rise to classifications such as ortho and para dihydrogen, which, however, will not be discussed in detail here.

3.1.4 Coupled-channel analysis and couplings

Our investigation of the excited molecular states near the 5s + 4d asymptote (see Fig. 3.1) takes place in a close collaboration between our experimental group and theory group. While the spectra shown in this thesis (see Chapter 4.4) have been recorded in Ulm and preliminarily assigned in their quantum numbers, the theoretical analysis to obtain refined potentials is carried out by Prof. Eberhard Tiemann at the University of Hannover. A coupled-channel model is fitted to our new measurement data and improved Born-Oppenheimer potentials and coupling functions are constructed specifically for the states $(2)^1\Sigma_u$ and $(2)^3\Pi_g$. We are mainly interested in two coupling mechanisms and their strength: The spin-orbit coupling and the rotational coupling. Fig. 3.2 shows colored tables that are generally the same for g and u symmetry and show which couplings are taken into account between which states. These states are given in the Hund's case (a) basis. In the following, I would like to briefly discuss the idea and procedure of a coupled-channel analysis from a practical perspective. The starting point of this analysis is a set of undisturbed Hund's case (a) Born-Oppenheimer potentials given as functions of internuclear separation, which are then coupled accordingly using an interaction Hamiltonian described by coupling functions. From the newly generated potentials, bound states and their binding energies can be calculated and compared with the experimental observations. In an iterative procedure, coupling parameters and coupling functions are now further adjusted until theory and experiment are in agreement within the experimental uncertainty. The final potentials and coupling functions obtained can then be used to calculate wave functions of the states represented by the channel functions for the molecular states defining the Hamiltonian matrix. From these wave functions, Franck-Condon factors and transition dipole matrix elements can be calculated which provides important information for future work. The two main contributions to couplings considered are summarized in the following paragraphs.

The spin-orbit coupling describes the coupling between the total spin $\boldsymbol{S}$ of the electrons and their orbital momentum $\boldsymbol{L}$. The spin-orbit operator in the molecular coordinate system has the following form

$$\begin{aligned}\hat{\boldsymbol{H}}_{so} &= A\hat{\boldsymbol{L}}\cdot\hat{\boldsymbol{S}} \\ &= A\hat{L}_z\hat{S}_z + \frac{1}{2}A\left(\hat{L}^+\hat{S}^- - \hat{L}^-\hat{S}^+\right)\end{aligned} \tag{3.3}$$

in which $\hat{L}^\pm = \hat{L}_x \pm i\cdot\hat{L}_y$, $\hat{S}^\pm = \hat{S}_x \pm i\cdot\hat{S}_y$ are raising or lowering operators. Please note that A depends on the internuclear distance of the system. Spin-orbit coupling does not only mediate interactions between states of different Λ and Σ (which is described by the second term in Eq. (3.3)) but also leads to splitting of the term energies (first term in Eq. (3.3)). In Fig. 3.2, couplings based on spin-orbit interactions are highlighted with green color in the upper right triangle (off-diagonal elements corresponding to the second term in Eq. (3.3)) and orange color (diagonal elements corresponding to the first term in Eq. (3.3)). Please note that the color itself just indicates the type of interaction and not anything about coupling strengths. In fact, these can be different for the different matrix elements. The amplitude A for the right and left part of the interaction is not necessarily of the same magnitude.

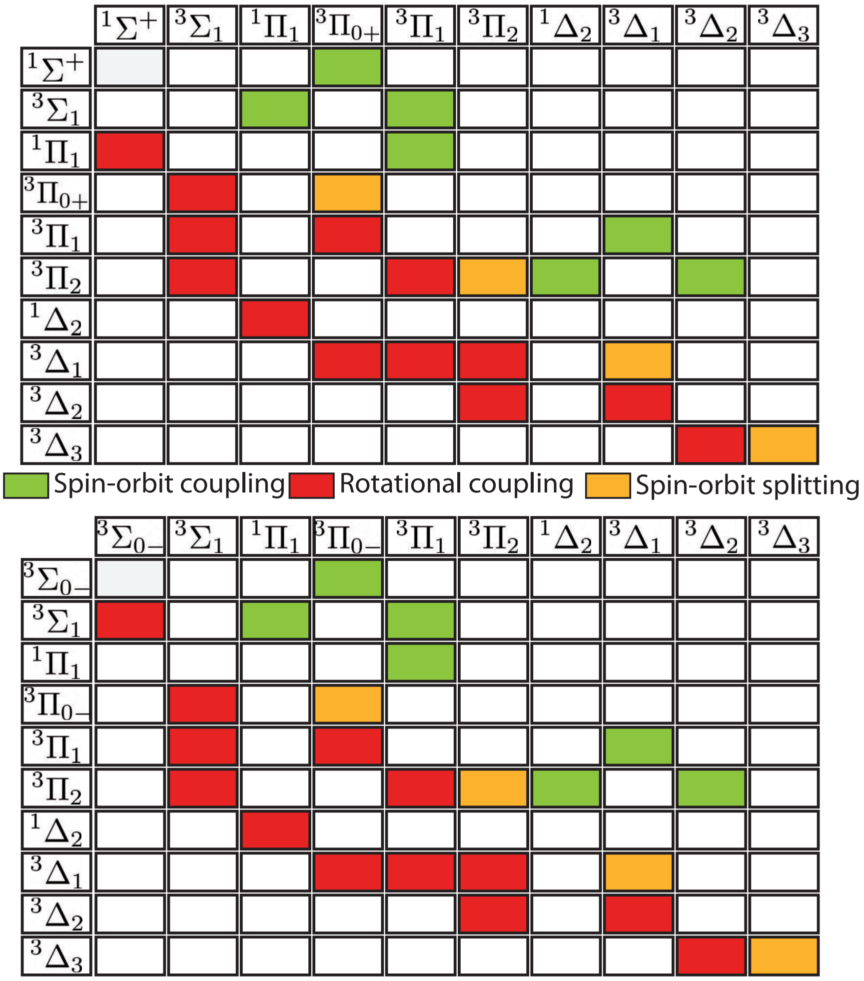

	$^1\Sigma^+$	$^3\Sigma_1$	$^1\Pi_1$	$^3\Pi_{0+}$	$^3\Pi_1$	$^3\Pi_2$	$^1\Delta_2$	$^3\Delta_1$	$^3\Delta_2$	$^3\Delta_3$
$^1\Sigma^+$				🟩						
$^3\Sigma_1$			🟩		🟩					
$^1\Pi_1$	🟥				🟩					
$^3\Pi_{0+}$		🟥		🟧						
$^3\Pi_1$		🟥		🟥				🟩		
$^3\Pi_2$		🟥			🟥	🟧	🟩		🟩	
$^1\Delta_2$			🟥							
$^3\Delta_1$				🟥	🟥	🟥		🟧		
$^3\Delta_2$						🟥		🟥		
$^3\Delta_3$									🟥	🟧

🟩 Spin-orbit coupling 🟥 Rotational coupling 🟧 Spin-orbit splitting

	$^3\Sigma_{0-}$	$^3\Sigma_1$	$^1\Pi_1$	$^3\Pi_{0-}$	$^3\Pi_1$	$^3\Pi_2$	$^1\Delta_2$	$^3\Delta_1$	$^3\Delta_2$	$^3\Delta_3$
$^3\Sigma_{0-}$				🟩						
$^3\Sigma_1$	🟥		🟩		🟩					
$^1\Pi_1$					🟩					
$^3\Pi_{0-}$		🟥		🟧						
$^3\Pi_1$		🟥		🟥				🟩		
$^3\Pi_2$		🟥			🟥	🟧	🟩		🟩	
$^1\Delta_2$			🟥							
$^3\Delta_1$				🟥	🟥	🟥		🟧		
$^3\Delta_2$						🟥		🟥		
$^3\Delta_3$									🟥	🟧

FIGURE 3.2: Overview of the various coupling mechanisms taken into account for the coupled-channel analysis. Only contributions by spin-orbit (green, orange shown in the upper triangles) and non-diagonal rotation energy (red shown in the lower triangles) are indicated. The upper grid corresponds to e states and the lower grid corresponds to f states. Differences appear only in the upper left corner between the different grids. Colours are only intended to represent the type of interaction and tell nothing about the strength of the interaction. This content can be found in a similar way in many textbooks, e.g. [85].

The rotational coupling can be expressed by the rotational Hamiltonian of a diatomic molecule in the molecular frame with rotational angular momentum $\boldsymbol{R}$ perpendicular to the molecular axis

$$\begin{aligned}\hat{\boldsymbol{H}}_{rot} &= B\left(\hat{\boldsymbol{R}}\right)^2 = B\left(\hat{\boldsymbol{J}} - \hat{\boldsymbol{L}} - \hat{\boldsymbol{S}}\right)^2 \\ &= B\left(\hat{J}^2 - \hat{J}_z^2\right) + B\left(\hat{S}^2 - \hat{S}_z^2\right) + B\left(\hat{L}^2 - \hat{L}_z^2\right) \\ &\quad - B\left(\hat{J}^+\hat{L}^- - \hat{J}^-\hat{L}^+\right) - B\left(\hat{J}^+\hat{S}^- - \hat{J}^-\hat{S}^+\right) - B\left(\hat{L}^+\hat{S}^- - \hat{L}^-\hat{S}^+\right).\end{aligned} \tag{3.4}$$

In this simplified expression, we call B the rotational constant. This contains the nuclear separation R and the reduced mass of the molecule. To derive the terms in the second and third line of Eq. (3.4), again lowering and raising operators (e.g. $\hat{L}^{\pm} = \hat{L}_x \pm i \cdot \hat{L}_y$ for L) are needed and additionally commutator relations (e.g. $\left[\hat{L}_x, \hat{L}_y\right] = i\hbar\hat{L}_z$) are used. The calculation is quite lengthy but can be found in textbooks such as [9, 85]. The first three terms in Eq. (3.4) correspond to unperturbed rotational energy levels. Two terms of them are independent of specific rotational states as they only contain contributions from orbital momentum and spin. The last line in Eq. (3.4) describes perturbations between different levels. The third term is effectively like spin-orbit coupling which leads to perturbations between two electronic with the same Ω but is typically lower in magnitude than the spin-orbit coupling. The second term is the so called spin-rotation coupling which connects states with the same Λ but with different Σ and $\Omega = \pm 1$. The first term describes rotational coupling between states with different Λ and $\Omega = \pm 1$ which leads to Λ doubling of rotational states. All the different contributions of the rotational coupling are included in Fig. 3.2 and are highlighted with the same red color. Here again, color only indicates the type of interaction and nothing about the coupling strength. Rotational couplings are highlighted in the lower left side of the grid. Any possible couplings different from the ones mentioned, are not considered in the coupled-channel analysis so far.

Chapter 4

Spectroscopy of molecular states near 5s + 4d asymptote

The following chapter focuses on the spectroscopy of molecular states near the 5s + 4d asymptote. Primarily, we concentrate on molecular states belonging to $(2)^1\Sigma_u^+$ and the $(2)^3\Pi_g$ system. In Section 4.1, we present previous studies [4, 50, 66, 112, 165] that have already investigated these states using spectroscopic methods. Subsequently, in Section 4.2, we introduce the spectroscopic techniques employed in our experiments. Section 4.3 covers our initial investigations conducted with the pulsed laser system Credo (for a description of the laser system, see 2.4.3) and we compare our results with pulsed recordings from the Stwalley group [4]. Following that, we provide high-resolution spectroscopic recordings of the vibrational and rotational states belonging to $(2)^1\Sigma_u^+$ and $(2)^3\Pi_g$ using the Matisse system (for details of the laser system, see 2.4.2).

We further explain the observed rotational structures and show how this can be used for precise identification of the molecular states. In Section 4.5, we summarize the experiments and discuss how future projects can build on this work.

4.1 Previous work by other groups

In this section, I briefly present previous investigations of molecular states near the 5s + 4d asymptote. Table 4.1 gives an overview of the previous studies.

Initial investigations date back to the 1990s. In Amiot's work [1], many spectral lines, including those corresponding to the 5s + 4d asymptote, were measured using Fourier-transform spectroscopy. This study provided potential energy curves, molecular constants and dissociation energies which later served as the foundation for further research in the 2000s.

In 2006, a study [66] from the Stwalley group was published, primarily focused on the electronic state $X^1\Sigma_g$, which corresponds to the 5s + 5s asymptote. The detection was performed using a REMPI scheme with a pulsed laser (see Section 4.2.2 for a description of the method) via the $(2)^1\Sigma_u^+$ state as an intermediate state, similar to the measurements we conducted and present in Section 4.4.2.

In 2013, Guan et al. [50] reported new experimental data for the $(2)^3\Pi_{0g^+}$ states using the Facilitated Infrared–Infrared Double Resonance (PFIIDR) technique. This work is of particular value to us because they were able to identify vibrational states starting from $\nu = 0$, which will be important for our analysis later in Section 4.4.3.

In 2015, another study by M. Ascoli [4] from the Stwalley group was published. Similar to Huang's work [66], REMPI was used with a pulsed laser system to detect molecules, employing the $(2)^1\Sigma_u^+$ or $(2)^3\Pi_g$ states as intermediate steps. Many resonant transitions were spectroscopically analyzed, and the states were assigned accordingly by comparison with ab initio calculations and analyzing the ladder structure of the recordings. The spectroscopic data from this study forms the basis for comparisons with our pulsed data in Section 4.3. Unlike our high-resolution spectroscopy presented in 4.4, however, this method did not allow for the unambiguous identification of the molecular states through their rotational structure.

A study by Yang et al. [165] focused on the $(2)^3\Pi_{1g}$ state. They compared their experimental observations with those of the $(2)^3\Pi_{0g^+}$ state and found an average difference of 83.1 ± 0.3 cm^{-1} between the $\Omega = 0_g^+$ and $\Omega = 1_g$ states. If the vibrational assingnment is undoubtedly known for both components, this splitting corresponds to the spin-orbit splitting of the $(2)^3\Pi_g$ states. We will later compare this result with our analysis in Section 4.4.3, as our measurements also allow for the determination of the spin-orbit interaction in the $(2)^3\Pi_g$ state.

A more recent publication on molecular states of the ungerade symmetry group the 5s + 4d asymptote comes from A. Pashov [112]. In Pashov's work, transitions between $X^1\Sigma_g$ and $(2)^1\Pi_u$ were observed using polarization labelling spectroscopy. By comparing their results with earlier predictions [1], they concluded that the $(2)^1\Pi_u$ state is strongly perturbed by the nearby states $(2)^1\Sigma_u^+$, $(2)^3\Pi_u$, and $(3)^3\Sigma_u$. Through these experiments, they were able to indirectly generate a potential energy curve for $(2)^1\Sigma_u^+$ and fit it to their experimental observations of $(2)^1\Pi_u$.

4.2 Spectroscopic methods

For the investigation of the molecular states below the 5s + 4d asymptote, we prepare ultracold atomic clouds of the isotope ^{85}Rb or ^{87}Rb at magnetic fields of 4 G typically at temperatures around 800 - 900 nK. The atoms are spin polarized in the hyperfine ground state (f = 1, m_f = -1 for ^{87}Rb, f = 2, m_f = -2 for ^{85}Rb) and trapped in a far-detuned crossed optical dipole trap with a depth of about 15µK, see Section 2 for a general description of the apparatus. The process of three-body recombination takes place in our ultracold atomic cloud: this process leads to the formation of molecules in various quantum states corresponding to the coupled molecular state $X^1\Sigma_g^+ - a^3\Sigma_u^+$ below the

TABLE 4.1: Overview of the previous studies connected to molecular states near to the 5s + 4d asymptote. Here, I give a chronological order of the previous studies and briefly mention the molecular states under investigation. This list might not be complete and just presents the work we used for our own analysis.

Year	Reference	molecular states investigated
1990	[1]	$(1)^1\Sigma_g(X)$,$(1)^1\Sigma_u(A)$ $(2)^1\Sigma_g$, $(1)^1\Pi_u(B)$, $(1)^1\Pi_g$, $(2)^1\Pi_u(C)$
2006	[66]	$(2)^1\Sigma_u$
2013	[50]	$(2)^3\Pi_{0g}$
2015	[4]	$(2)^3\Pi_g, \Omega = 0^+, 0^-, 1$ $(2)^1\Sigma_u$
2017	[165]	$(2)^3\Pi_g, \Omega = 0^+, 1$
2022	[112]	$(2)^1\Pi_u$

$5S_{1/2} + 5S_{1/2}$ atomic asymptote [41, 103, 134]. The produced molecules are subsequently analyzed and characterized using spectroscopic methods. Two of these techniques, photoassociation spectroscopy and resonance-enhanced multiphoton ionization (REMPI), are described and discussed in the following paragraphs. Both methods can be employed with either a cw laser system or with a pulsed laser system.

4.2.1 Photoassociation

Photoassociation is a process in which two colliding atoms - such as rubidium - absorb one or multiple photons, leading to the formation of an excited molecular state.

$$\mathrm{Rb} + \mathrm{Rb} + h\nu_1 \rightarrow \mathrm{Rb}_2^* \left(\mathrm{v}', \mathrm{J}'\right) \tag{4.1}$$

Since ultracold atoms can be produced by laser cooling in atom traps, it has been a common method to produce ultracold ground-state molecules. Due to the low kinetic energy, photoassociation spectra are often simple because only a few partial waves contribute. A good review on the subject of ultracold photoassociation spectroscopy can be found in [72]. Here I will focus on how to observe photoassociation in our experiments. Either the cw laser or the pulsed dye at wavelength around 595 - 605 nm is used as a probe laser to combine the free ultracold atoms into molecules. Once formed, the molecules have a finite lifetime and can decay radiatively by emitting a photon. It is possible for the molecule to decay into two atoms with a higher kinetic energy (shown in Fig. 4.1), but it is also possible to decay to a lower kinetic energy or to a bound state. Regardless of which process takes place in detail, typically the particles can no longer be detected by absorption imaging.

$$\begin{aligned} Rb_2^*\left(v',J'\right) &\rightarrow Rb_2\left(v'',J''\right)+h\nu_2 \\ Rb_2^*\left(v',J'\right) &\rightarrow Rb+Rb+h\nu_3 \end{aligned} \tag{4.2}$$

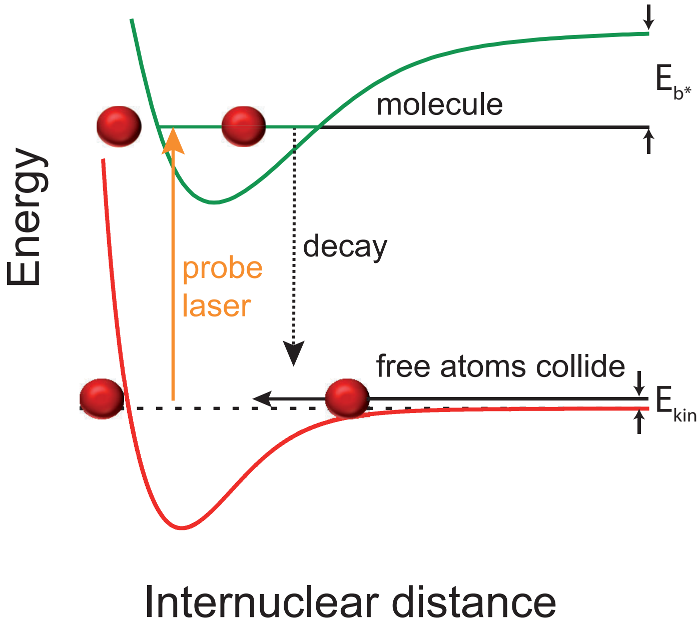

FIGURE 4.1: An illustration of the photoassociation process (PA). Two potential energy curves are shown as a function of internuclear distance. Free atoms can form a molecule when exposed to a laser. Molecules in the excited state can then radiatively decay which is indicated with the dashed arrow downwards. Typically this results in loss of atoms in the optical dipole trap.

4.2.2 Resonance enhanced multi-photon ionization (REMPI)

Resonance enhanced multi-photon ionization (REMPI) is an experimental technique to state-selectively ionize molecules (or atoms). In the following, REMPI is used in the context of molecules, although the principle can also be applied to atoms. Tunable laser sources are used to bring either atoms or molecules to an excited energy level with one or more photons in a first step. The excited molecule can be ionized by absorption of further photons.

$$\begin{aligned} Rb+Rb+h\nu_1 &\rightarrow Rb_2^*\left(v',J'\right) \\ Rb_2^*\left(v',J'\right)+h\nu_2 &\rightarrow {Rb_2}^+ + e^- \end{aligned} \tag{4.3}$$

or

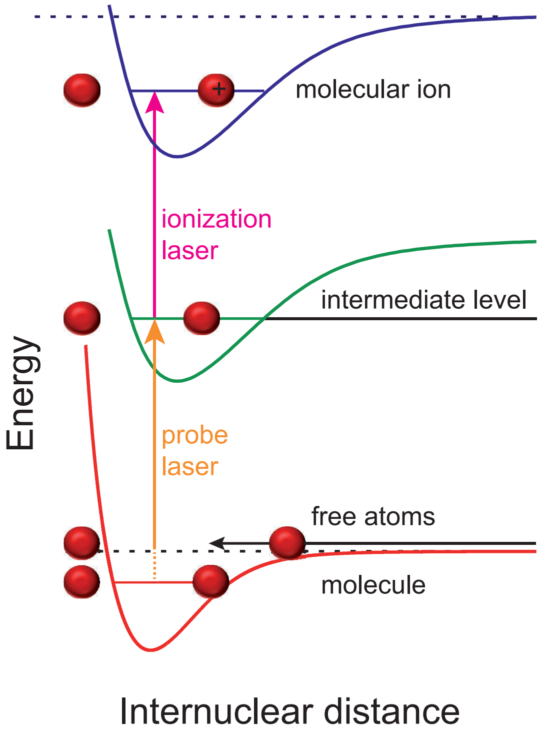

FIGURE 4.2: Illustration of a two-step resonance-enhanced multiphoton ionization (REMPI). In a first step, the probe laser either photoassociates unbound atoms or excites molecules into an intermediate state. Subsequently, the intermediate molecule is ionized into ionic molecular state by an ionization laser. In our experiment, two identical photons are used for the two different steps, so a one-color two-photon REMPI is used.

$$\begin{aligned} \mathrm{Rb_2} + h\nu_1 &\rightarrow \mathrm{Rb_2^*}\left(\mathrm{v}',\mathrm{J}'\right) \\ \mathrm{Rb_2^*}\left(\mathrm{v}',\mathrm{J}'\right) + h\nu_2 &\rightarrow \mathrm{Rb_2}^+ + e^- \end{aligned} \tag{4.4}$$

Compared to photoassociation spectroscopy, this method has the advantage that potentially additional information about the rotational structure of the excited molecules can be obtained. The produced ions are then detected with an efficiency of almost 100% using a linear Paul trap to store the produced ions and subsequently count them. In Ulm, currently, we count the number of ions indirectly via elastic collisions with neutral atoms. Fig. 4.2 shows a simplified illustration of the REMPI process. In our experiments, two identical photons are used for REMPI. The intermediate level is an electronic molecular state that belongs to the 5s + 4d asymptote: $(2)^1\Sigma_u^+$ or $(2)^3\Pi_g$ whose vibrational and rotational structure will be discussed in Sections 4.4.2 and 4.4.3. It is not entirely clear how the final ionization step works in our experiments. Energetically, it is possible that there is a direct ionization to the $(1)1/2_g$ level with a single photon (e.g. see [76]). Another less likely alternative would be to go via a low-lying Rydberg state, which then proceeds via a third step (another photon, auto-ionization) to an ionic state. It is important to demonstrate the difference in the data between PA spectroscopy and REMPI spectroscopy. This is shown in Fig. 4.3. Here, a REMPI spectrum is obtained by using the $(2)^1\Sigma_u^+, \nu = 33$ as an intermediate state with the Paul trap turned on (blue data) for the isotope ^{87}Rb. The photoassociation transition is identified by a photoassociation measurement (orange) at a frequency of ν_0 = 499754.027 GHz while the Paul trap is turned off. It can clearly be seen that the transitions between bound molecule from the three-body recombination can only be detected by the REMPI technique combined with the linear Paul trap to store the produced ions. It can also be seen that the signal strength in terms of atom number loss is significantly higher in the REMPI process than in pure PA spectroscopy. For the 5s + 4d potential in particular, the PA signals are weak and sometimes even undetectable. The two measurements were taken under different conditions: the exposure time for photoassociation was 900 ms, while the exposure time for REMPI spectroscopy was 300 ms, which makes the difference in signal strength even clearer. The REMPI method is used to assign the excited electronic state because the information of several bound-bound transitions is required. The experimental techniques are similar for both isotopes and there are no significant differences in the observation from a technical point of view. For clear

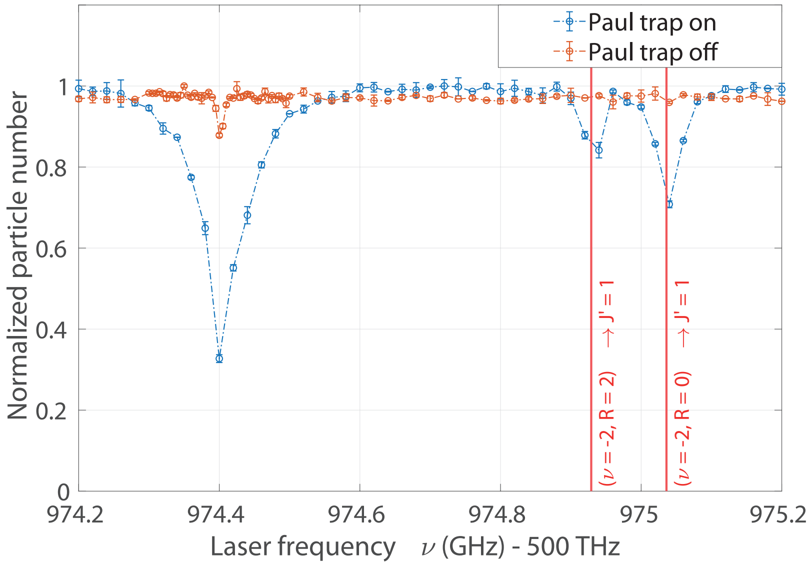

FIGURE 4.3: REMPI vs. PA spectroscopy using the intermediate state $(2)^1\Sigma_u^+(\nu = 33)$ for ^{87}Rb. The blue data shows a REMPI spectrum. Bound-to-bound transitions become visible and the signal at the PA frequency becomes stronger by using the REMPI technique. The most weakly-bound state $(\nu = -1, R = 0)$ is not visible due to its small binding energy of 24 MHz. It strongly overlaps with the photoassociation signal in the REMPI recordings. The pure PA signal (orange) shows a small peak at the resonance frequency of the photoassociation.

identification of the bound-to-bound transitions, selection rules are necessary which are described in the following.

4.2.3 Selection rules for dipole transitions

Instead of a general treatment, I will explain the selection rules on the basis of the situation in the experiment. These rules apply for bound-to-bound transitions which are part of the REMPI and also for photoassociation. From basic symmetry arguments, we know that a photon couples g states to u states and vice versa. In our case for Rubidium (both isotopes) the hyperfine structure leads to the fact that a collision in the 5S+5S ground-state has no clear g/u symmetry, so transitions to u/g are both allowed starting from asymptotic ground state levels. In addition, there is no well-defined singlet or triplet character, so both types of transitions are allowed. After the strict symmetry selection rules (which apply to all Hund's cases), the angular momentum selection rules must be defined. For Hund's case a) (which is used to describe the excited molecules in our study here), the following transition rules apply: $\Delta\Lambda = 0, \pm 1$, $\Delta S = 0$, $\Delta\Sigma = 0$, $\Delta\Omega = 0, \pm 1$ and $\Delta J = 0, \pm 1$ with exclusion of transitions between $J = J' = 0$. The weakly bound molecules produced via three-body recombination (TBR) can be described within Hund's case (b). In this scenario, R is a good quantum number, while J is not, due to hyperfine interactions leading to mixing. To assess the excited states that the molecules can be optically excited to, we refer to Table 4.2. This table illustrates how to assign the states from Hund's case (b) to Ω (Hund's case (a)) based on the J quantum number and parity. The table should be read from left to right for various values of $R = 0, 2, 4$. It is crucial to keep in mind that the parity of the molecule remains unchanged when transforming between different Hund's cases. In Hund's case b) the parity is given by $(-1)^R$ and therefore always positive for even R. For Hund's case a), the parity for $\Omega = 0^-$ states is given by $(-1)^{J+1}$ and thus alternate with J. For $\Omega = 1$, there is always a state with positive and negative parity for $J \geq 1$. Table 4.2 shows for a given rotational quantum number R what Ω quantum number composition is possible for the triplet (S = 1) case. Crossed out elements are not possible due to different parity (e.g. $\Omega = 0^-$, J = 2 has negative parity).

Using the selection rules above, it is possible to identify the excited molecular states that are produced by photoassociation or bound-to-bound transitions. The expected transitions for photoassociation are relatively straightforward because we can assume that $R = 0$ applies in the case of two unbound atoms. Consequently, the J quantum numbers for the system corresponding to the 5S + 5S asymptote are limited to $J = 0$ (singlet) and $J = 1$ (triplet, see Tab. 4.2). The selection rule $\Delta J = 0, \pm 1$ must then be applied to determine the quantum number J' of the excited state. For the transitions between bound molecules, considerably more transitions are expected because the molecular states of the $X^1\Sigma_g^+ - a^3\Sigma_u^+$ manifold must be taken into account. The binding energy for the respective states is given in Table 4.4 for both rubidium isotopes with the R quantum number according to Hund's case b) and

TABLE 4.2: Assignment of molecular states Hund's case a) starting from Hund's case b) basis. The parity depends on J for $\Omega = 0^-$ states and alternates $(-1)^{J+1}$. We know that the molecules produced by TBR have positive parity which already limits the allowed J states for $\Omega = 0^-$ and thus, only even R are shown in the table. For example, the J = 3 state consists of a superposition of $\Omega = 0^-$ and $\Omega = 1$, whereas the J = 4 state contains only the $\Omega = 1$ component.

Hund's case b)			Hund's case a)	
for Σ-states, N = R			$\Omega = 0^-$	$\Omega = 1$
R	parity $(-1)^R$	J =R, R±1 for S = 1	parity $(-1)^{J+1}$	both possible
0	+1	1	+1	+1
2	+1	1	+1	+1
2		2	~~-1~~	+1
2		3	+1	+1
4	+1	3	+1	+1
4		4	~~-1~~	+1
4		5	+1	+1

TABLE 4.3: Electronic states connected to the 5s + 4d asymptote that can be produced by photoassociation of an ultracold rubidium gas starting from the asymptotic ground state 5s + 5s. Ω and J' are the corresponding quantum numbers for the excited molecules according to Hund's case a).

	Ω	J'
$(2)^1\Sigma_u^+$	0^+	1
$(2)^3\Pi_g$	0^+	1
	0^-	0,2
	1	1,2
	2	2
$(2)^3\Sigma_g$	0^-	0,2
	1	1,2

the vibrational quantum number ν. An important note: the description presented here is highly simplified, as it neglects the hyperfine interaction. In most cases, this simplification is not generally feasible.

TABLE 4.4: Binding energies of weakly bound molecules of the molecular complex $X^1\Sigma_g^+ - a^3\Sigma_u^+$ which correlates to the 5s + 5s asymptote at zero magnetic field and have the largest multichannel component with the hyperfine quantum numbers $f_a = f_b = 2$, F = 4, m_F = -4 for ^{85}Rb and $f_a = f_b = 1$, F = 2, $m_F = -2$ for ^{87}Rb. Binding energies up to about 3 GHz are typically sufficient for our spectroscopy and analysis. Note that the vibrational quantum number ν is counted from the most weakly bound state ν = -1 downwards.

ν	R	E_b (GHz)	
		^{85}Rb	^{87}Rb
-1	2	0.144	-
-1	0	0.221	0.024
-2	6	0.621	-
-2	4	1.136	0.291
-2	2	1.478	0.529
-2	0	1.682	0.636
-3	6	3.825	1.711
-3	4	4.617	2.301
-3	2	5.130	2.717
-3	0	5.352	2.896

4.3 Pulsed spectroscopy

In our initial study, we conducted a spectroscopic investigation of the 16400 - 16800 cm^{-1} region using the pulsed dye laser system Credo. The details of the laser system and its frequency tuning methods are described in Chapter 2.4. Given the system's linewidth of approximately 1.8 GHz, we did not expect to resolve the rotational structure of the excited molecular levels since we can only address low rotational quantum numbers J' in our experiment. However, we were able to scan over 13 THz for each rubidium isotope in a relatively short time, providing preliminary insights into the vibrational structure of the excited molecular complex associated with the 5s + 4d asymptote. We compare the recordings with previous recordings by M. Ascoli [4] in Section 4.3.2 and discuss and compare selected structures more carefully with additional high-resolution cw recordings.

4.3.1 Pulsed spectroscopic recordings

In the following section, we present and discuss the pulsed recordings for both isotopes. The measurements for ^{87}Rb are particularly interesting because most previous experimental data have been obtained with the isotope ^{85}Rb [4, 66]. The experimental parameters were as follows: 5000 pulses (10 ns pulse duration) over 500 ms (10 kHz repetition rate) with an average power of 100 - 200 mW. The recorded spectra are shown in Figs. 4.4 and 4.5. The experiments were conducted with turned-on linear Paul trap. The spectrum reveals not only the molecular transitions, which are our primary interest, but also excitations corresponding to atomic Rydberg states with high principal quantum number n. The black dashed lines in the spectrum were calculated using the Alkali-Rydberg calculator [131]. Additionally, based on the analysis of the cw recordings in following Chapter 4.4, including the analysis of the rotational structure, the positions for $(2)^1\Sigma_u^+$ (red) and $(2)^3\Pi_g$ (green) have been labeled. Signals which could not be assigned were labeled with magenta arrows and we discuss some of these structures in the Appendix B.1.1. The measurements for ^{85}Rb were performed in a similar way than the measurements for ^{87}Rb. One remarkable difference of the recorded spectra is the signal-to-noise ratio. For the measurements in ^{85}Rb, the noise level was about 5 times larger than for the case of ^{87}Rb. This might be connected to the larger scattering length and a larger three-body recombination loss rate.

The pulsed measurements significantly simplified the subsequent cw measurements by allowing us to narrow down the regions where relevant molecular transitions were expected.

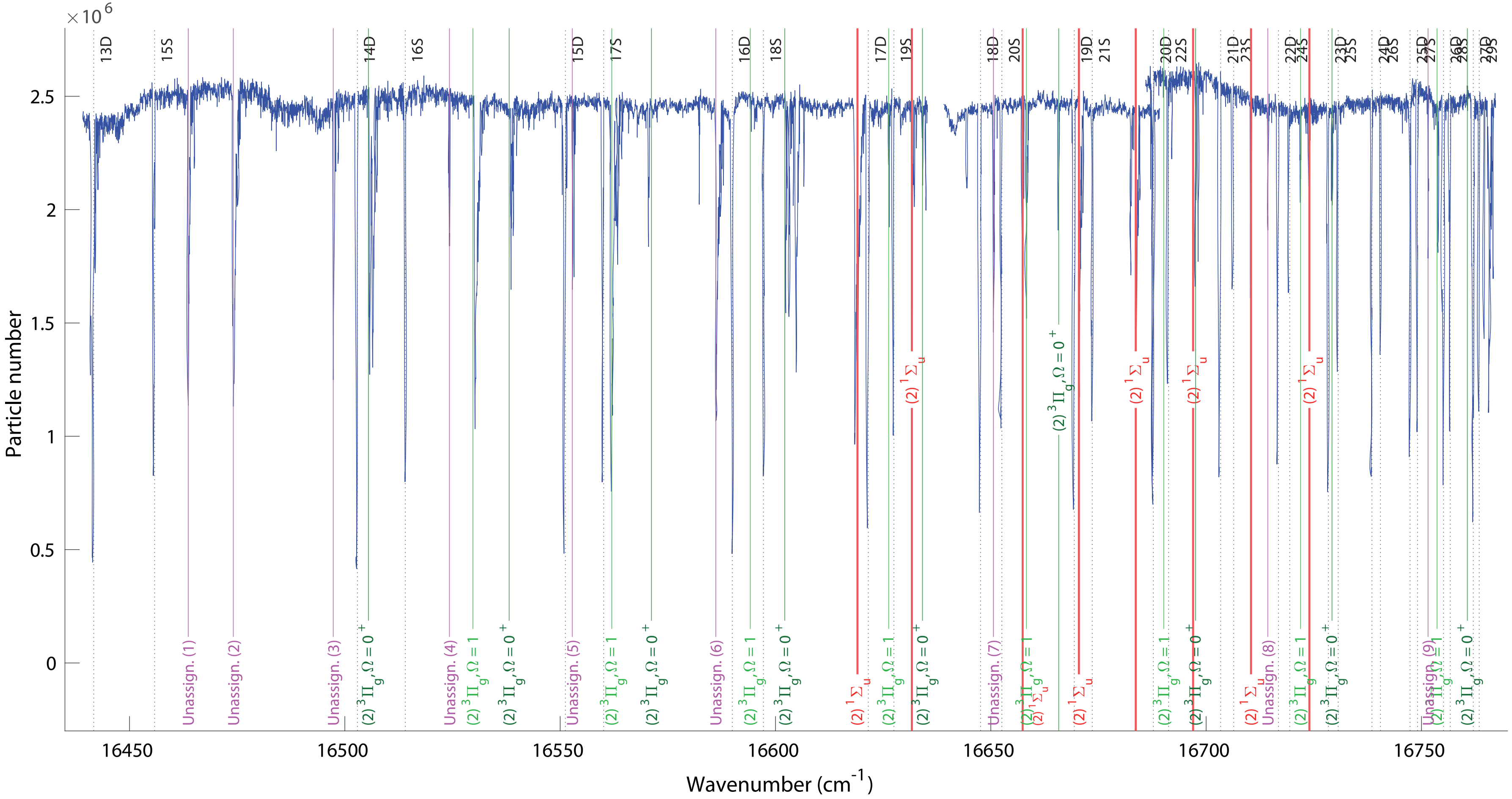

FIGURE 4.4: The spectrum for ^{87}Rb was recorded in the range of 16450 - 16770 cm^{-1} using the pulsed dye laser system. The spectrum shows both molecular and atomic transitions, the latter correspond to atomic Rydberg states. The annotated lines indicate the principal quantum number n along with the orbital quantum number l, such as 15S. According to the selection rules, this is a two-photon dipole transition, allowing transitions to S or D states since the atoms were initially prepared in the ground-state with l = 0 (S). Molecular excitations are $(2)^3\Pi_g$, $\Omega = 1, 0^+$ labeled with green color and $(2)^1\Sigma_u^+$ with red color and are further discussed in Chapter 4.4. Due to overlap of signals, the labels were shifted to the top or bottom to ensure more readability. Unidentified lines were marked in magenta and labeled with numbers. These signals will be further discussed in Section B.1.1.

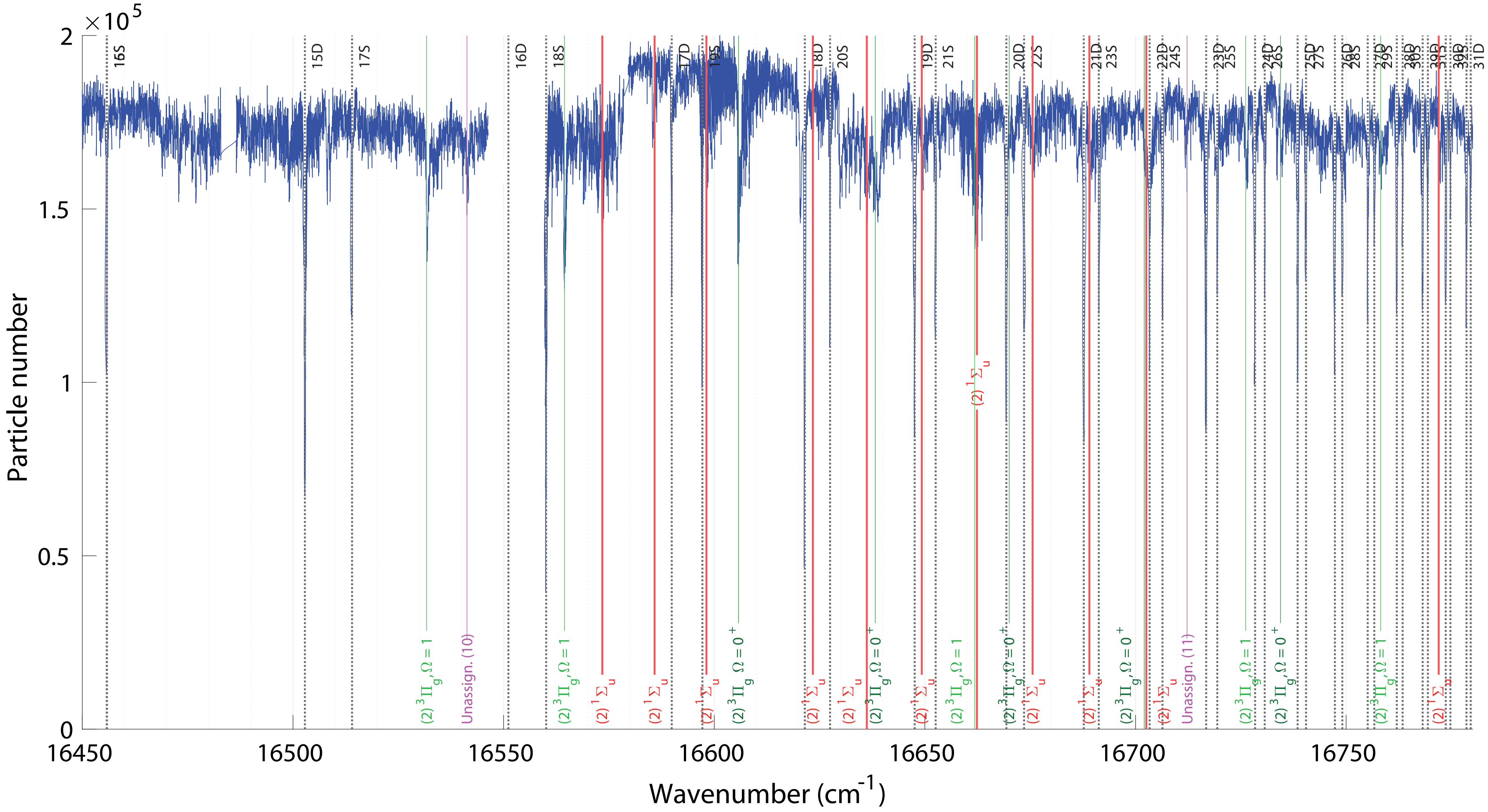

FIGURE 4.5: The spectrum for ^{85}Rb was recorded in the range of 16450 - 16780 cm^{-1} using the pulsed dye laser system. The spectrum shows both molecular and atomic transitions, the latter of which correspond closely to Rydberg states. The annotated lines indicate the principal quantum number n along with the orbital quantum number l, such as 15S. According to the selection rules, this is a two-photon dipole transition, allowing transitions to S or D states since the atoms were initially prepared in the ground-state with l = 0 (S). Molecular excitations are labeled $(2)^3\Pi_g$, $\Omega = 1, 0^+$ in green color and $(2)^1\Sigma_u^+$ are labeled in red color. Due to overlap of signals, the labels were shifted to the top or bottom to ensure most readability. Unassigned line were marked in magenta and labeled with numbers. These signals will be further discussed in Section B.1.1.

4.3.2 Comparison with another spectroscopic study

In this section, we compare the observations and assignments for ^{85}Rb from M. Ascoli's work (see Appendix of [4]) with the assignments we made in Ulm using high-resolution spectroscopy (see Sections 4.4.2 and 4.4.3). For better visibility, the full spectrum has been divided into four sections, shown in Figures 4.6 to 4.9. These figures display the pulsed dataset from Ulm with the measured Rydberg lines (labels at the top) and Ascoli's assignments (labels also at the top in black). The labels for the assignments we made in Ulm, confirmed by rotationally resolved spectroscopy, are shown at the bottom of the spectra. Ascoli's dataset includes an assignment of the $(2)^1\Sigma_u^+$ state, along with the vibrational quantum number assignment. However, for the $(2)^3\Pi_g$ state, Ascoli provides no assignments to the $\Omega = 0^+, 0^-, 1$ states, instead grouping the data into A, B, and C series. In the following, I list notable findings from the comparison of the two datasets:

- a striking observation is that in the Ulm dataset, no transitions could be identified between 16450 and 16530 cm^{-1} using high-resolution spectroscopy. However, in the pulsed dataset, there are weak coincidences with Ascoli's observations in this range, though they are comparable to the background noise of the spectrum. We could not observe and identify any molecular states there which could be a consequence of the Franck-Condon principle. Our cw spectroscopy could be simply not efficient enough for the excitation of molecules in this region.

- while there are many spectroscopic matches, there are also cases where the Ulm assignments contradict Ascoli's original assignments. For example, the transitions at 16574 cm^{-1} and 16702 cm^{-1}, which Ascoli identified as belonging to the $(2)^3\Pi_g$ state (B series), were clearly identified in Ulm as $(2)^1\Sigma_u^+$.

- from the comparison with the Ulm results, we can assign the A series to the $\Omega = 1$ state and the B series to the $\Omega = 0^+$ state. The C series remains unclear. If it corresponds to the $\Omega = 0^-$ state, these lines should always appear near the B series, as the typical splitting is expected to be approximately between 0.2 and 1.2 cm^{-1}. Theoretically, it would be possible that the recorded C series from Ascoli belongs to $\Omega = 2$, but we could not confirm this hypothesis since we did not find any $\Omega = 2$ levels in our recordings so far.

Some of the conclusions drawn here are based on the explanations and assignments from subsequent sections. However, since our dataset shown above and Ascoli's observations come from REMPI spectroscopy with pulsed laser systems, we have made the comparison here. The process of identifying individual states using high-resolution cw spectroscopy is explained in Section 4.4.

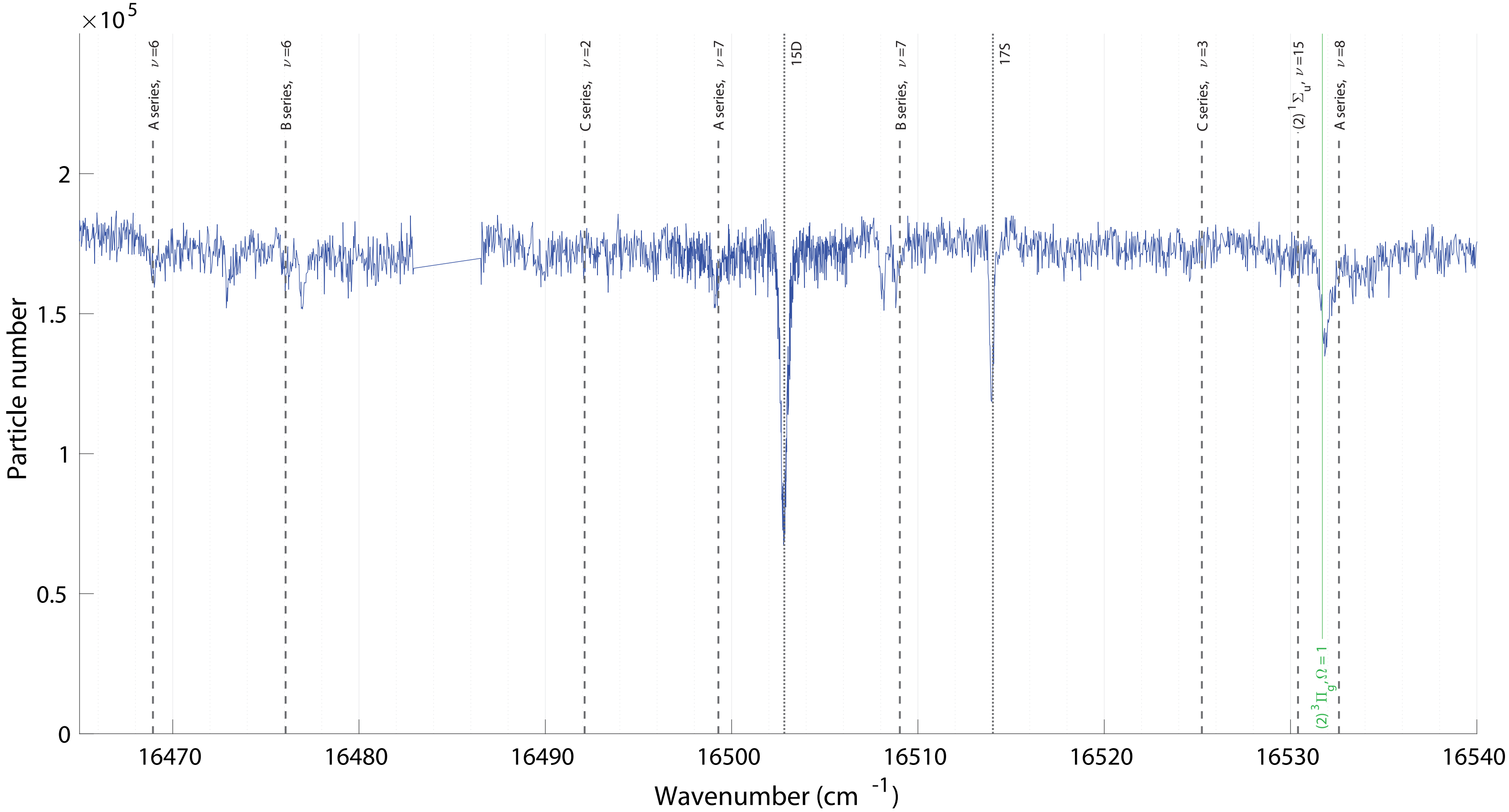

FIGURE 4.6: Pulsed dataset comparison with Ascoli's observations (1). Black dashed vertical lines are assignments by Ascoli, see [4] Appendix. Green or red vertical lines are assignments based on cw spectroscopy. In this particular energy range, we could barely identify molecular transitions in Ulm which could be connected to a small Franck-Condon overlap. Ascoli, however, still observed many transitions of his A, B, C series which could be a consequence of his different preparation sequence for creating molecules in the 5s + 5s asymptote.

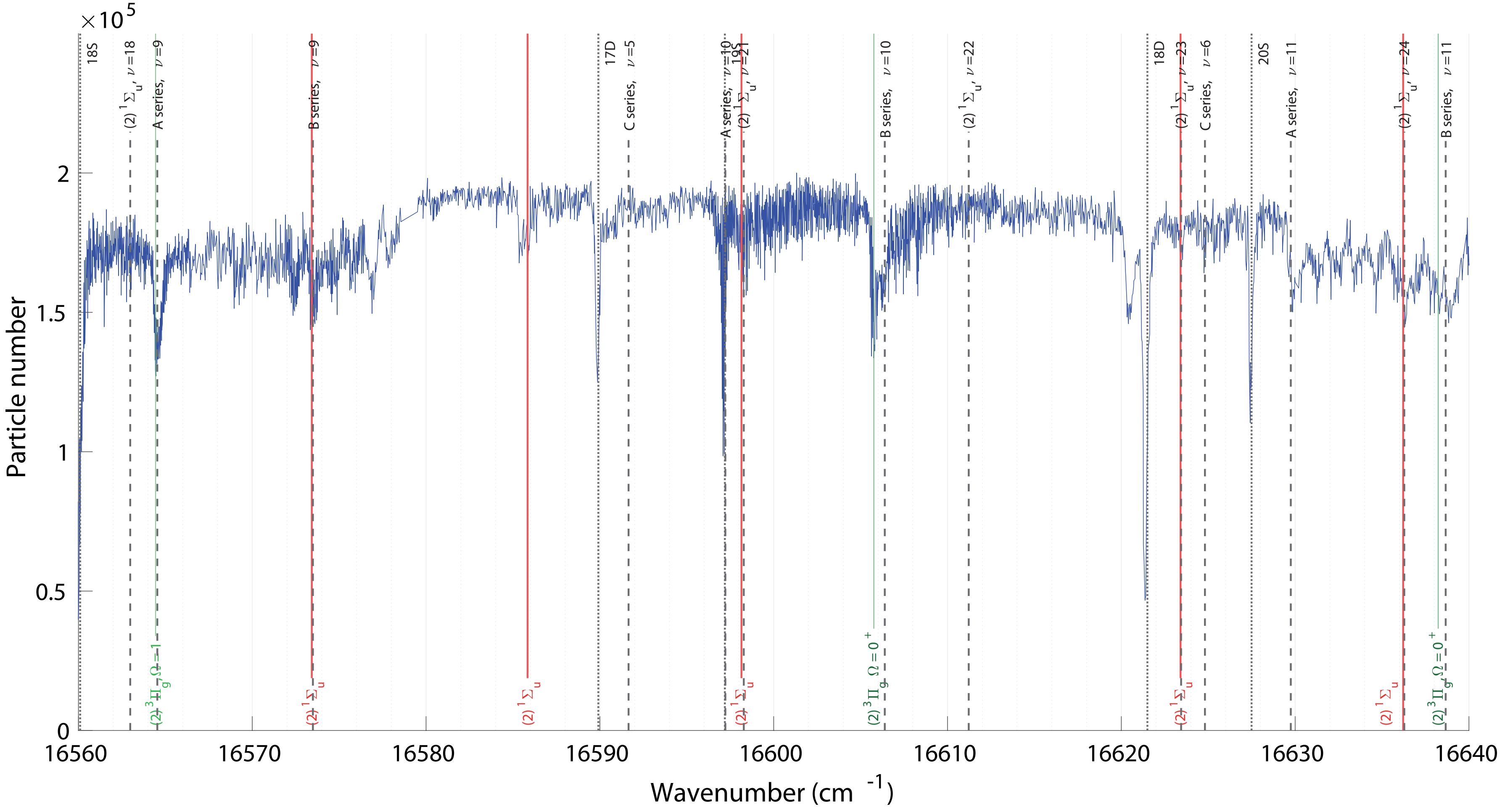

FIGURE 4.7: Pulsed dataset comparison with Ascoli's observations (2). Black dashed vertical lines are assignments by Ascoli, see [4]. Here, we could mainly confirm observations of Ascoli's A and B series. Interestingly, Ascoli falsely assigned some transitions to $(2)^1\Sigma_u^+$ as belonging to the B series which we checked with our cw spectroscopy.

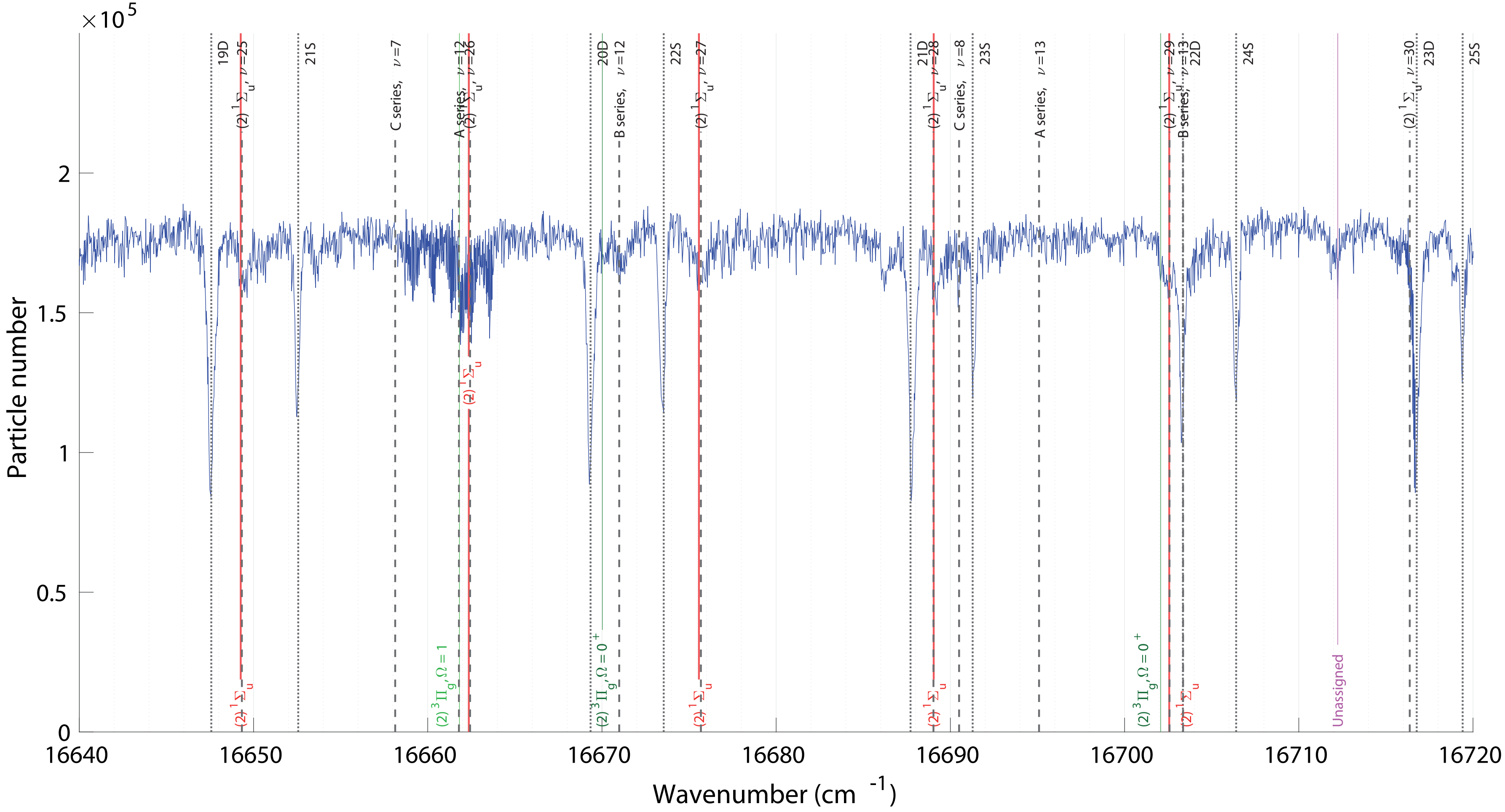

FIGURE 4.8: Pulsed dataset comparison with Ascoli's observations (3). Black dashed vertical lines are assignments by Ascoli, see Appendix of [4]. In our experiments in Ulm, we were not able to observe any of this recordings belonging to the C series.

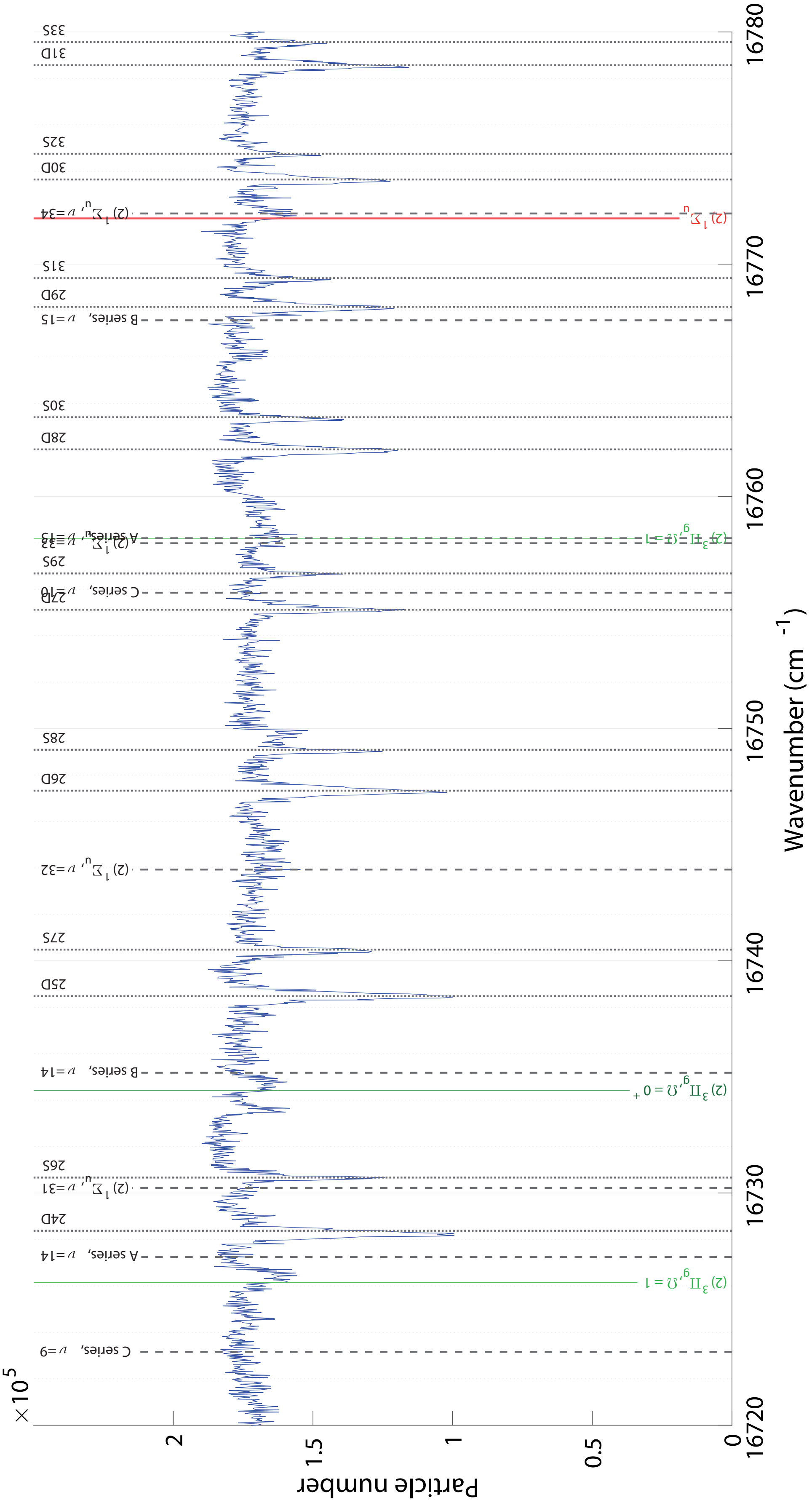

FIGURE 4.9: Pulsed dataset comparison with Ascoli's observations (4). Black dashed vertical lines are assignments by Ascoli, see [4] Appendix. Similar to other spectroscopic regions, the C series remains unclear in our assignment approach as we were not able to observe any signals near to Ascoli's observations. For more information, please read the text.

4.4 Continuous-wave (cw) spectroscopy

The following section presents spectroscopic recordings for the isotopes ^{85}Rb and ^{87}Rb within the range of 16450 to 16800 cm^{-1}. Primarily, we used the REMPI method in combination with our Paul trap for detection of the molecular states. For a more detailed description of the method, see Section 4.2.2. The dye laser Matisse was used for the spectroscopy, see Section 2.4.2. The analysis of the measurement data is divided into two subsections, each independently examining the states from $(2)^1\Sigma_u^+$ and $(2)^3\Pi_g$. For an overview of the potential energy curves of the investigated molecular states, see Fig. 4.10. Detected signals which could not be assigned so far, are discussed in the Appendix B.1.1.

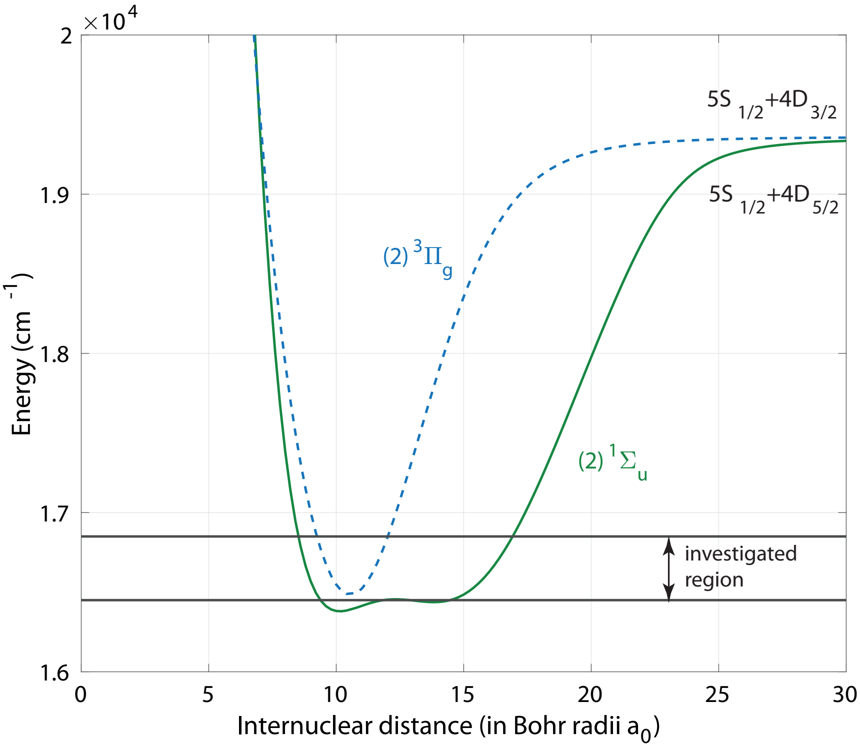

FIGURE 4.10: Potential energy curves of $(2)^1\Sigma_u^+$ and $(2)^3\Pi_g$ [95]. The region we investigated with the high-resolution spectroscopy is from 16450 to 16800 cm^{-1}.

4.4.1 Identification by using the rotational structure

The following chapter describes the rotational structure of the excited states $(2)^1\Sigma_u^+$, $(2)^3\Pi_g$ and $(2)^3\Sigma_g$. Already from the ab initio potentials (see Fig. 3.1) it can be estimated that the rotational constant differs for each of the electronic molecular states. In the following, I calculate the rotational constant B_ν for each vibrational level ν by solving the Schrödinger Equation using Lozeille's ab initio potentials including a term for rotational energy. The calculation shows that the values of the rotational constants for the different states differ significantly, see Fig. 4.11. The energies for the rotational structure of the excited states can be calculated according to Hund's coupling case a) using the rotational constant B_ν. The energy splitting between two rotational states with J_1 and J_2 is then given by $\Delta E = B_\nu(J_1(J_1+1) - J_2(J_2+1))$. Examples of the expected molecular structures are shown in the diagrams below for the different molecular states, see Fig. 4.12 and Fig. 4.14. In our work, we typically compare the measured recordings with the predicted structures and extract a rotational constant B_v from the experimental observation.

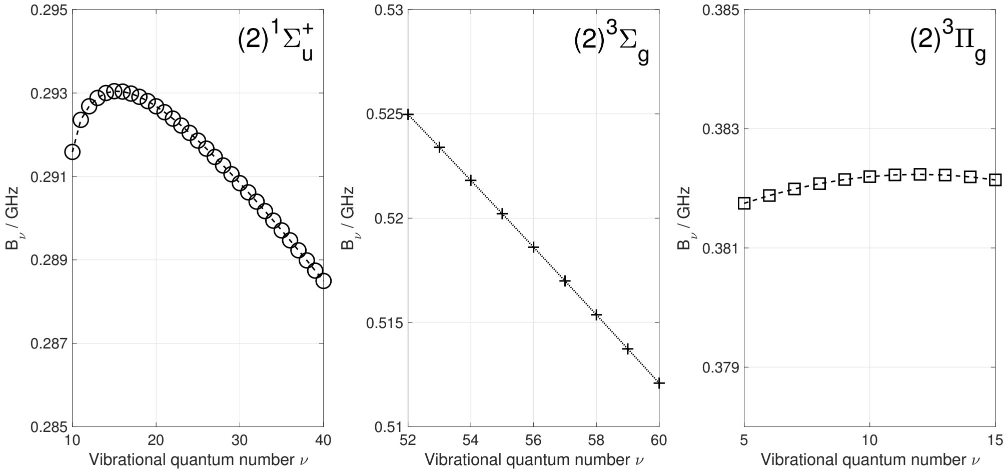

FIGURE 4.11: Rotational constants derived from ab initio potentials [95]. The calculations cover the vibrational quantum numbers we could spectroscopically adress with our laser systems. For each state of our interest, the rotational constant is significantly different which allows a clear spectroscopic assignment of the rotational structure.

Rotational structure of $(2)^1\Sigma_u^+$

By taking into account the selection rules, it is possible to determine which rotational states can be accessed by photoassociation and which molecules can be converted into electronically excited rotational states. For a given vibrational quantum number ν of the excited state, the recordings begin with the photoassociation line, whose position is used as the reference frequency ν_0. For the case ^{85}Rb $(2)^1\Sigma_u^+$ the photoassociation leads to the excited rotational state $J' = 1$, see Fig. 4.13. If the spectroscopy laser is tuned to higher frequencies, the most weakly-bound molecular state $(\nu = -1, R = 2)$ of the molecular complex $X^1\Sigma_g^+ - a^3\Sigma_u^+$ can be excited to the state $J' = 1$ at a relative frequency of 0.144 GHz. The transition $(\nu = -2, R = 0)$ to $J' = 1$ appears at 0.221 GHz. More bound-to-bound transitions to $J' = 1$ appear until about 3 GHz when also transition to the higher rotational state $J' = 3$ become possible. As there is no PA to $J' = 3$, this spectrum then starts with the transition (ν = -2, R = 2) $\rightarrow$ J' = 3 at $\nu - \nu_0 = 0.144\,\text{GHz} + 10B_v = 3.044\,\text{GHz}$. The state

$(\nu = -2, R = 0)$ cannot be excited due to selection rules and therefore no longer appears as soon as $J' > 1$ is used as an intermediate state.

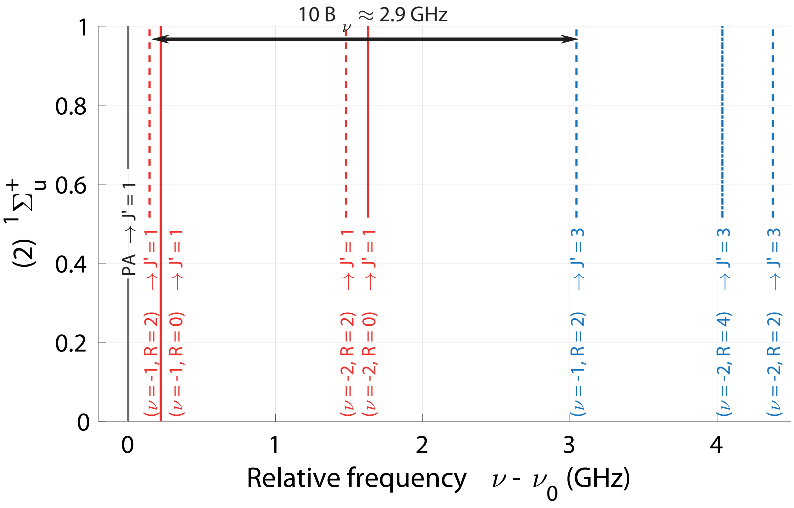

FIGURE 4.12: Estimated frequency spectrum for transitions to the excited molecular state $(2)^1\Sigma_u^+$ (^{85}Rb) by REMPI. The structure starts with the photoassociation to J′ = 1 of unbound atoms at a laser frequency of ν_0 and is followed by bound-to-bound transitions. Higher rotational states can be excited at relative frequencies of ≈ 3 GHz. This means for identification, typically measuring a frequency range of 5 GHz is sufficient.

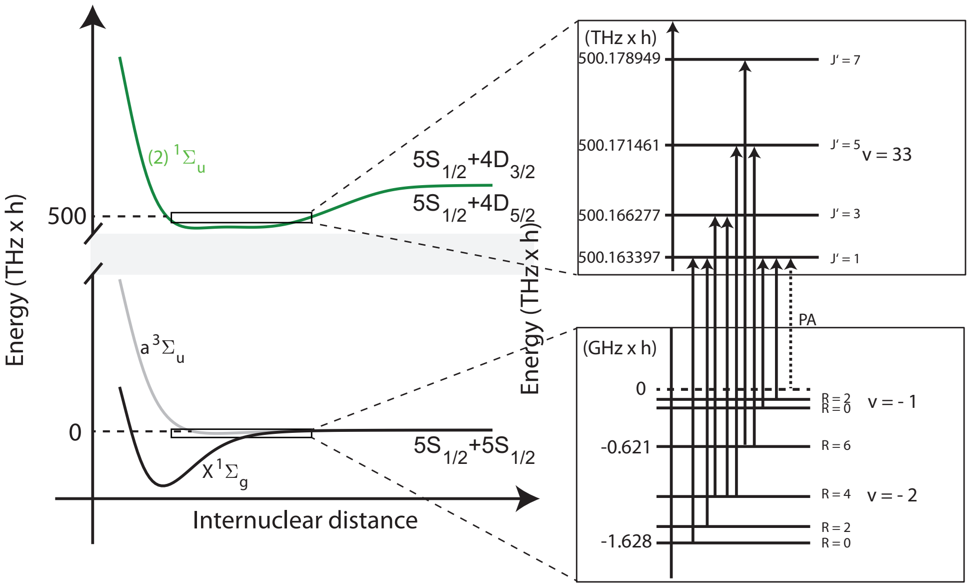

FIGURE 4.13: Illustration of the potential energy curves and the allowed molecular transitions to the $(2)^1\Sigma_u^+$ state (here for ^{85}Rb). The binding energies of the states for different v and R are given in Table 4.4 and are depicted in the lower right box of the diagram. The excited molecules are characterized by J', the positions for different J′ are shown in the upper right box. Solid vertical arrows indicate allowed bound-to-bound transitions, while the dashed arrow represents the photoassociation.

Rotational structure of $(2)^3\Pi_g$

Similar to the explanations for $(2)^1\Sigma_u^+$, the structure for the states of $(2)^3\Pi_g$ can also be estimated. $(2)^3\Pi_g$ occurs in different states $\Omega = 0^+, 0^-, 1, 2$ which have approximately the same rotational constant B_ν for the same vibrational quantum number ν. The difference is which quantum numbers J' are possible for the different Ω states. This is already indicated in Table 4.3 for the photoassociation and is shown graphically in Fig. 4.14 including bound-to-bound transitions. It is possible to distinguish between different Ω states once several transitions to different J' states are measured. For $\Omega = 0^+$ or $\Omega = 1$ the lowest rotational level belongs to $J' = 1$ but $\Omega = 1$ additionally exhibits a second PA signal for $J' = 2$. The energetic difference between $J' = 1$ and $J' = 2$ is $4B_\nu$. The case $\Omega = 0^-$ has $J' = 0$ as the lowest rotational level and shows a second PA line for $J' = 2$ at a energetic difference of about $6B_\nu$ relative to $J' = 0$. The electronic state $\Omega = 2$ has $J' = 2$ as the lowest rotational level and no further PA transition.

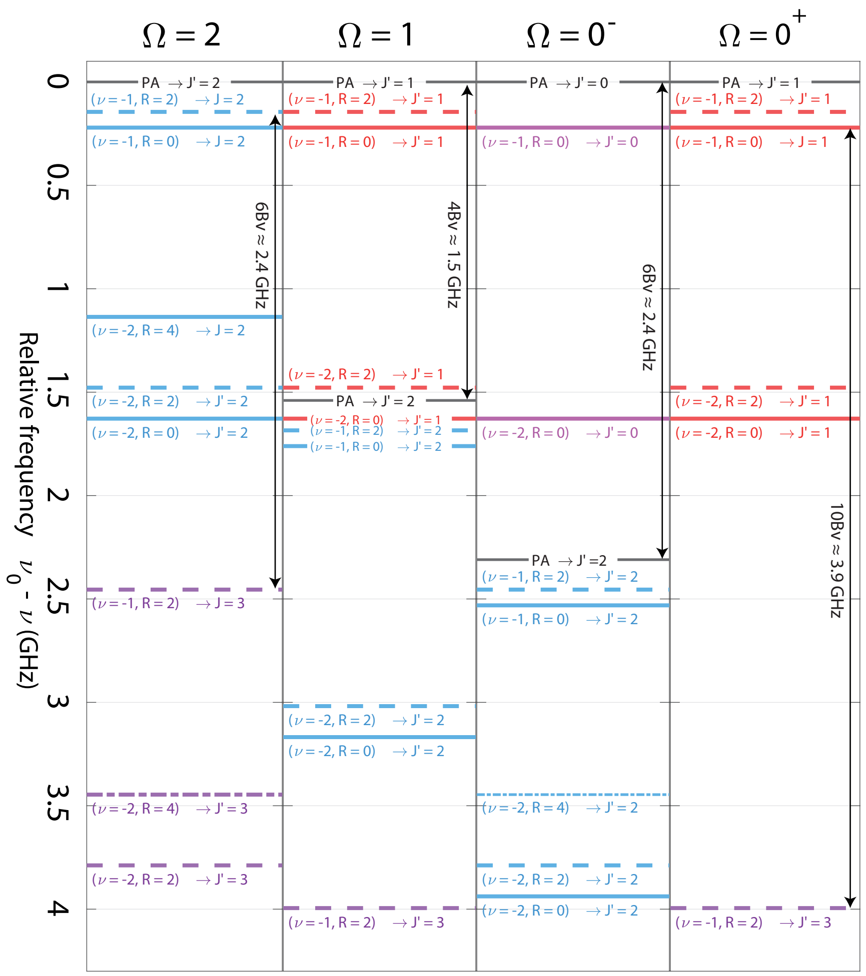

FIGURE 4.14: Visualisation of the expected spectroscopic structures for the $(2)^3\Pi_g$ states calculated for ^{85}Rb. Due to the spin-orbit coupling, several $\Omega = 0^+, 0^-, 1, 2$ states are expected, all of which differ in their rotational structure. The splittings between different J′ shown here were calculated using a rotational constant B_v = 390 MHz. In the later analysis, this is a fit variable given by the experimentally determined positions. Characteristic splittings are shown for the respective Ω states (black vertical arrows). Different rotational states J′ of the excited molecules are indicated by colors (red, blue, purple) whereas the line style (solid, dashed, dashed dotted) indicates the rotational state R of the molecule initially formed by TBR.

4.4.2 Recordings and results of $(2)^1\Sigma_u^+$

Recordings and analysis

Our high-resolution cw recordings cover vibrational states from $\nu = 25$ to 40 for ^{85}Rb and $\nu = 29$ to 37 for ^{87}Rb and including up to 3 rotational levels J' for each vibrational quantum number. We show a comparison of $(2)^1\Sigma_u^+$ using the vibrational states $\nu = 32, 33, 34$, see Fig. 4.5. The recordings are all very similar and the assignment of the transitions allows a determination of the rotational constant B_v of about $283 \pm 10\,\text{MHz}$ for ^{87}Rb. The relative experimental frequency uncertainty is about 10 MHz and is mainly due to the performance of the frequency stabilisation and additional power broadening. A frequency range of at least 4 GHz was measured for each vibrational state. To assign a rotational constant, it is necessary to detect at least two rotational states with different values of J′. Typically, we choose the two lowest rotational states for determining the rotational constant. It is also possible to measure even higher rotational states (e.g. J′ = 5, 7), but the splitting of the states becomes increasingly larger, making the measurements more time-consuming. All signals in the recorded data set which could be assigned through rotational analysis are summarized in Table 4.5. The vibrational quantum numbers given in Table 4.5 are not experimentally assigned. Instead, the assignment is done by comparison with theoretical analysis.

TABLE 4.5: Recorded transitions to $(2)^1\Sigma_u^+$ for ^{87}Rb and ^{85}Rb. Shown are the level energies in units of cm^{-1} for different rotational states J′ with respect to the 5s+5s asymptote. We extract the rotational constant from the energy difference. Here, the rotational constant is $B_\nu = 0.283 \pm 0.010$ GHz for ^{87}Rb and $B_\nu = 0.288 \pm 0.010$ GHz for ^{85}Rb. The assignment of the vibrational quantum numbers ν are according to the coupled-channel model and not experimentally confirmed.

ν	J′ = 1	J′ = 3	J′ = 5
		^{87}Rb	
29	16619.0350	16619.1297	16619.3002
30	16631.6718	16631.7658	-
32	16657.3959	16657.4900	16657.6600
33	16670.4599	16670.5503	16670.7244
34	16683.6551	16683.7495	16683.9195
35	16696.9729	16697.0643	16697.2354
36	16710.4229	16710.5180	16710.6871
37	16723.9776	16724.0713	-
		^{85}Rb	
25	16573.4262	16573.5223	-
26	16585.8391	16585.9352	-
27	16598.1447	16598.2408	-
29	16623.3998	16623.4959	-
30	16636.2077	16636.3038	-
31	16649.2624	16649.3585	-
32	16662.3578	16662.4539	-
33	16675.5655	-	-
34	16689.0422	16689.1386	-
35	16702.5622	16702.6589	-
40	16771.8034	16771.8994	-

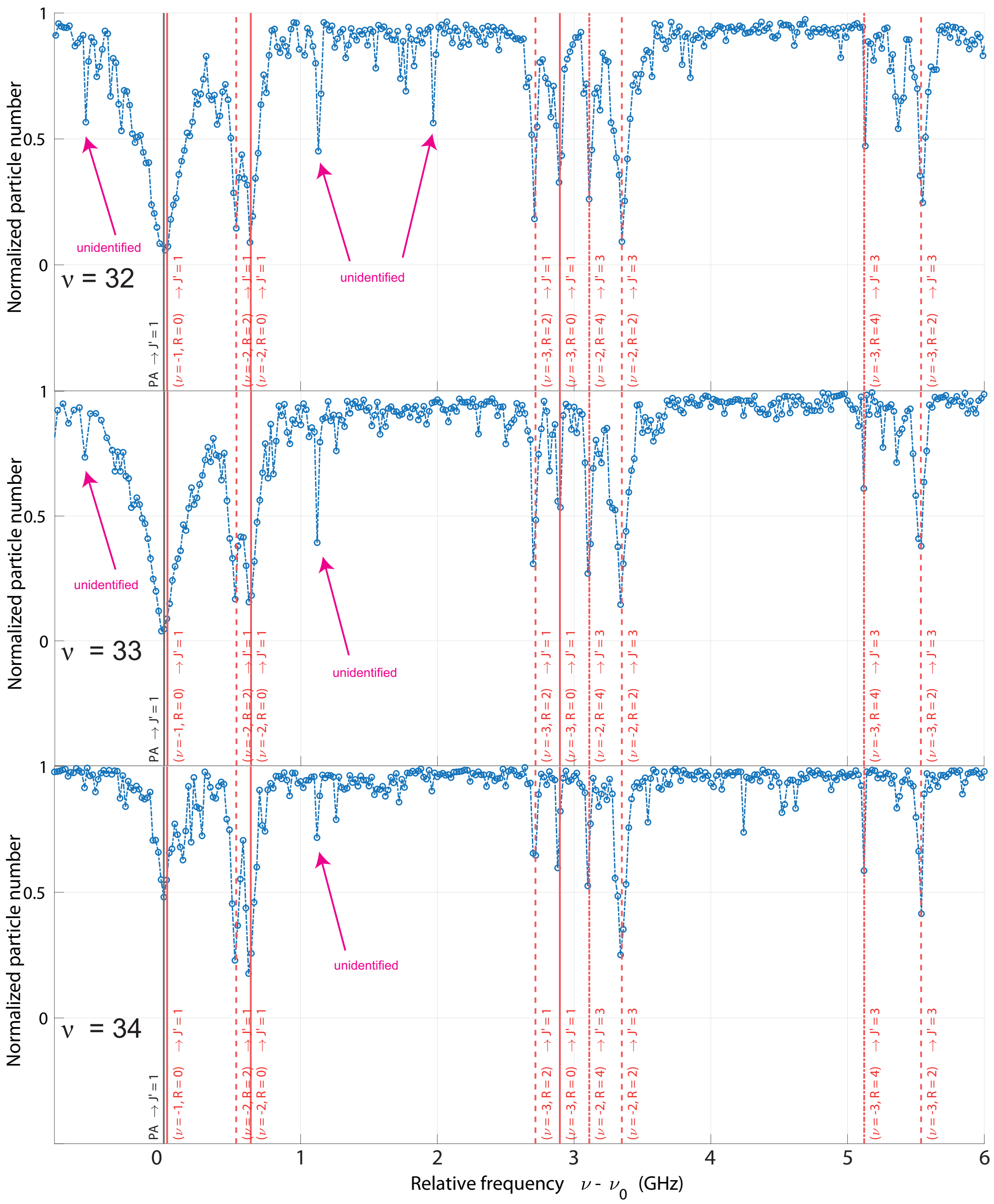

FIGURE 4.15: Spectroscopic recordings using REMPI. The vibrational states ν = 32,33,34 of $(2)^1\Sigma_u^+$ for ^{87}Rb were used as intermediate state. The reference frequencies are as follows: $\nu_0(v = 34)$ = 500.163397(10) THz, $\nu_0(v = 33)$ = 499.767815(10) THz and $\nu_0(v = 32)$ = 499.376166(10) THz. The assigned transitions have the same relative frequency positions within our measurement uncertainty and the experiments were executed under similar conditions. The signal strength for v = 34 and its photoassociation deviates slightly from the other two vibrational states which could already show the impact of the Franck-Condon principle.

Results and comparison with other studies

The spectroscopic measurements for the $(2)^1\Sigma_u^+$ state conducted in Ulm include more than 60 molecular transitions, which could be assigned through rotational analysis. The relative spectroscopic accuracy of these measurements is 10 MHz ($\approx 3.3 \cdot 10^{-4}\text{cm}^{-1}$), while the absolute accuracy is around 100 MHz ($\approx 3.3 \cdot 10^{-3}\text{cm}^{-1}$). In recent years, several research groups have worked on the electronic states near the 5s + 4d asymptote [4, 50, 66, 112], see Section 4.1.

In the following, we compare our spectroscopic results with those from the Stwalley group [4, 66], specifically the more recent work from M. Ascoli [4]. A key difference between their measurements and ours lies in the laser sources used and Ascoli's preparation of the molecular samples. While we use a cw laser for detection, their previous work employed pulsed lasers, which exhibit typically a significantly bigger linewidth (they specify it as approximately 0.1 - 0.2 cm^{-1}). Additionally, they prepare various molecular states associated to the 5s + 5s asymptotic level by photoassociation to a molecular level of the 5s + 5p asymptote which subsequently decay back to molecular levels of the 5s + 5s asymptote. The resulting molecules are then ionized using a REMPI scheme. Their studies also included an analysis of the vibrational progression and assignment of vibrational quantum numbers by comparison with ab initio calculations from [111]. The data from Huang [66] and Ascoli [4] show good agreement with each other within their measurement uncertainties. In Fig. 4.16 on the right, we directly compare our recordings with the results from Ascoli. In the spectroscopic regions where the data sets overlap, both data sets and also the analysis of the vibrational spacing show good agreement. The spacing of vibrational levels increases with higher vibrational quantum numbers and the progression is well described by a linear function. Irregularities in the smooth trend could indicate possible interactions to other electronic molecular states or issues with the measurement and identification. For example, the energy difference between $\Delta\nu = 27 - 26$ in our recordings deviates from the linear trend, suggesting that this should be revisited for further interpretation in the future. Unfortunately, there is a gap in our data set where no signal could be detected, while the Ascoli data set reveals a significant irregularity. Ascoli's and also Huang's work suggest that this irregularity could be caused by spin-orbit interaction to the electronic molecular state $(2)^3\Pi_u$, see Fig. 3.2. However, a deeper analysis, such as calculating updated potential energy curves, was not carried out in these studies.

Another indirect investigation was recently carried out and published in a study by A. Pashov [112]. In Pashov's work transitions between $X^1\Sigma_g^+$ and $(2)^1\Pi_u$ are observed in a polarisation labelling spectroscopy experiment. Through their experiments, they were able to indirectly generate a potential energy curve for $(2)^1\Sigma_u^+$ and fit it to their experimental observations of $(2)^1\Pi_u$. By comparison with predictions from previous work [1], they concluded that the state $(2)^1\Pi_u$ is strongly perturbed by the surrounding states

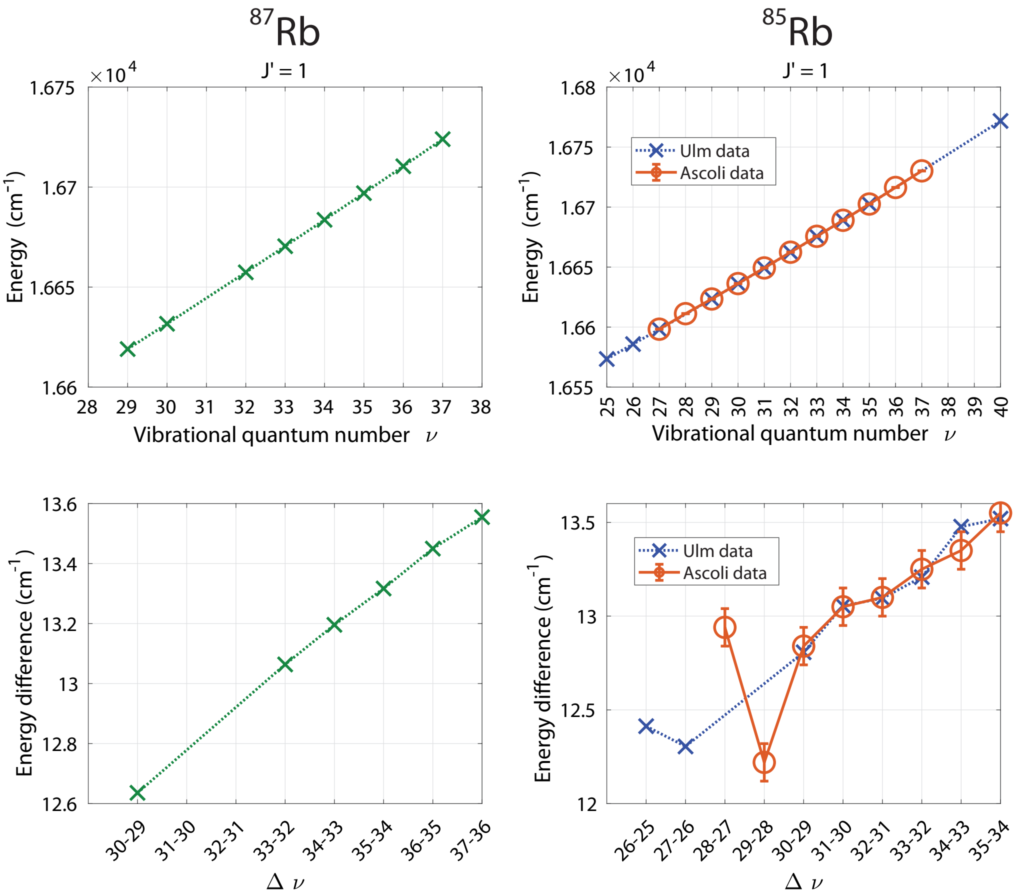

FIGURE 4.16: Results of the measured vibrational states of the $(2)^1\Sigma_u^+$ state for ^{87}Rb and ^{85}Rb for J′ = 1. On the upper left side, the energy levels from Table 4.5 for ^{87}Rb are presented (green), and on the right side, the corresponding data for ^{85}Rb are shown (blue) with respect to the 5s+5s asymptote. Examining the energy differences $E(\nu_i) - E(\nu_i - 1)$ between adjacent vibrational states (bottom plots) reveals that the vibrational spacing increases with higher vibrational states. Any irregularities in this representation could indicate possible couplings to other electronic molecular states. For the case of ^{85}Rb, we compare our data with data from [4] and discuss it further in Section 4.4.2.

$(2)^1\Sigma_u^+$, $(2)^3\Pi_u$ and $(3)^3\Sigma_u^+$. The rotational levels for the e symmetry of $(2)^1\Pi_u$ interact with the $(2)^1\Sigma_u^+$ by rotational coupling (see Fig. 3.2). For unknown reasons, they could not observe any transitions to $(2)^1\Sigma_u^+$ although in principle it should be allowed in their spectroscopy. Nevertheless, the theoretical analysis provides indirectly a refined potential energy curve of $(2)^1\Sigma_u^+$ (see [112] Supplementary material) which is used in Fig. 4.17 as a comparison to the results of the experiments and preliminary analysis from Ulm. However, Pashov's result for the PEC of $(2)^1\Sigma_u^+$ was not unambiguous, as it was still possible to describe their observations of $(2)^1\Pi_u$ sufficiently well with a different PEC of the $(2)^1\Sigma_u^+$ state. But now, it might be possible to calculate a refined potential energy curve based on our current measurements combined with the previously published data sets. The measured energy range from Ulm covers the range 16400 - 16800 cm^{-1} which energetically has only a small overlap with $(2)^1\Pi_u$ so only minor pertubations are expected to a first approximation. In Fig. 4.17, we compare two different analyses: Solid lines represent the PEC by the analysis of A. Pashov whereas the dashed lines show refined potentials obtained by taking the new Ulm data into account. The calculations and theoretical analysis has been done by Prof. E. Tiemann from the University of Hannover and is still ongoing. The addition of our new data has already had a visible effect on the potential energy curves of $(2)^1\Sigma_u^+$. The potential well seems to shift towards larger internuclear distances. In the future, it is planned to further use the dataset from Pashov's work together with the new data from Ulm in a complete coupled channel model of all ungerade states correlating to the asymptote 5s+4d.

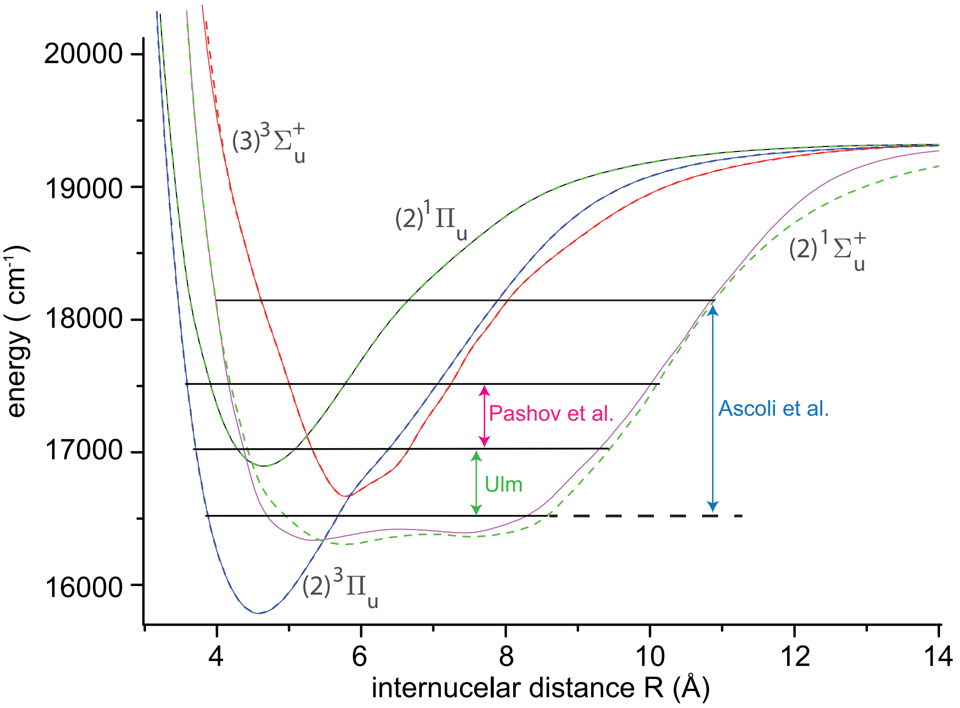

FIGURE 4.17: Overview of the potential energy curves corresponding to $(2)^1\Sigma_u^+$ and the states with relevant coupling to it (current status). The solid lines represent the potential energy curves according to A. Pashov's analysis [112]. The dashed lines are updated PEC including Ulm data. The green dashed line is the $(2)^1\Sigma_u^+$ state which already changed significantly from the previous result (magenta). Vertical arrows indicate the regions which were experimentally investigated.

4.4.3 Recordings and results for $(2)^3\Pi_g$

Recordings and analysis

The following section provides a presentation of the recorded spectra and the analysis of the $(2)^3\Pi_g$ system. It contains several electronic molecular states with $\Omega = 0, 1$. Here, electronic states with different Ω exhibit a different rotational structure as described in Section 4.4.1 and illustrated in Fig. 4.14. Currently, the Ulm data set contains transitions to the $\Omega = 0_g^+$, 0_g^- and 1_g states for the isotopes ^{85}Rb and ^{87}Rb including several vibrational and rotational levels. Figures 4.18, 4.19 and 4.20 show the recorded spectra, including assignments of the signals for the vibrational quantum number (ν = 9 for $(2)^3\Pi_{0g^+}$, ν = 13 for $(2)^3\Pi_{0g^-}$ and ν = 9 for $(2)^3\Pi_{1g}$). In general, the spectra reveal that the observed lines are approximately three times broader at the same laser power compared to the $(2)^1\Sigma_u^+$ state. This broadening causes partial overlap of the lines, making a clear separation challenging. This effect is particularly pronounced for $\Omega = 1$, where the rotational structure is less spread out than for $\Omega = 0^+$ or $\Omega = 0^-$. The analysis for other vibrational states was performed similarly, the whole recorded data set is summarized in Tables 4.6 and 4.7 for the respective isotopes. The splitting between $\Omega = 0^+$ and $\Omega = 0^-$ typically ranges between 10 and 30 GHz which makes a search quite easy but it was not possible to find all corresponding pairs belonging to the same vibrational quantum number (e.g. $\nu = 7$ or $\nu = 11$ for ^{87}Rb) as in these cases no measurable signal could be detected. Experimentally, we attempted to measure complete vibrational ladders without gaps.

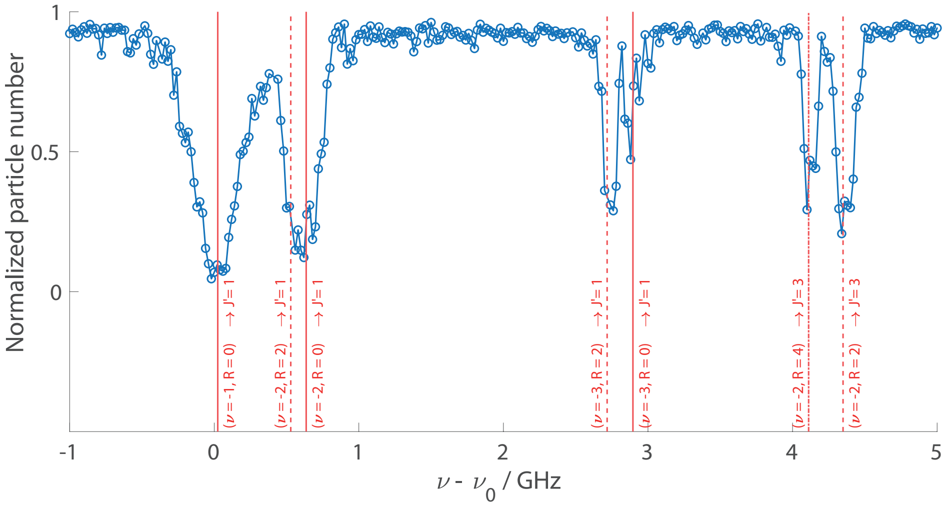

FIGURE 4.18: Recorded spectrum for $(2)^3\Pi_{0g+}$, ν = 13 for ^{87}Rb. Each data point is a single measurement. We use the position of the photoassociation line ν_0 = 501.528916(10) GHz as reference frequency. The frequency positions for the assigned transitions are marked vertically in red. From the distance between (ν = -2, R = 2, J′ = 1 and ν = -2, R = 2, J′ = 3 a rotational constant of B_v = 0.383 GHz can be extracted.

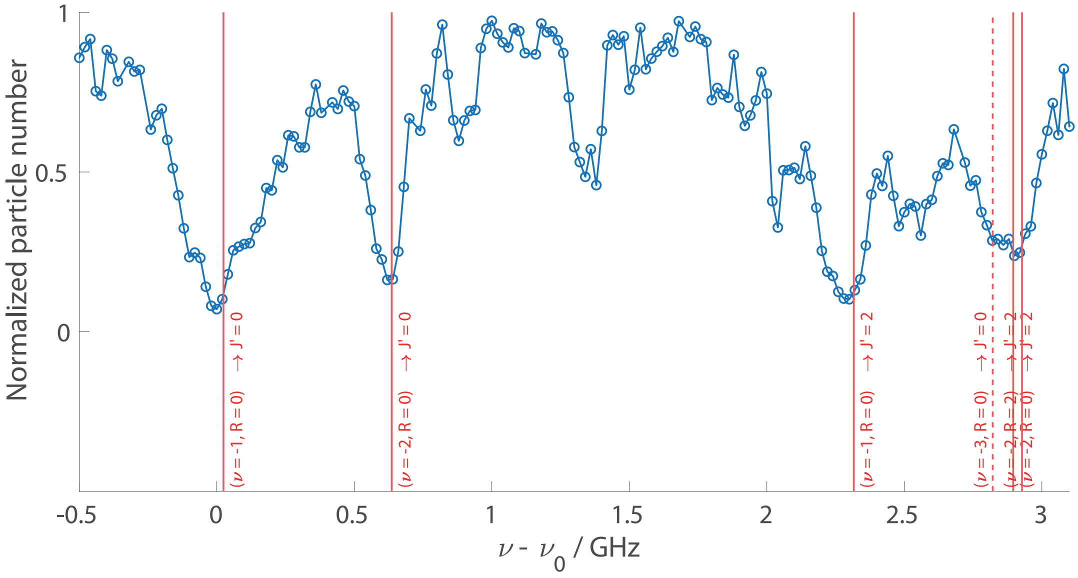

FIGURE 4.19: Recorded spectrum for $(2)^3\Pi_{0g-}$, $\nu = 13$ for ^{87}Rb. Each data point is a single measurement. We use the position of the photoassociation line $\nu_0 = 501.553175(10)$ GHz as reference frequency. The frequency positions for the assigned transitions are marked vertically in red. From the distance between (ν = -1, R = 0, J′ = 0 and ν = -1, R = 0, J′ = 2 a rotational constant of B_v = 0.381 GHz can be extracted. Higher transitions (>= J′ = 6) were not recorded and J′ = 4 is not shown here for visibility. Please note that in this region, additional (not labeled) signals appear because of an overlap with $(2)^3\Pi_{0g+}$, $\nu = 13$.

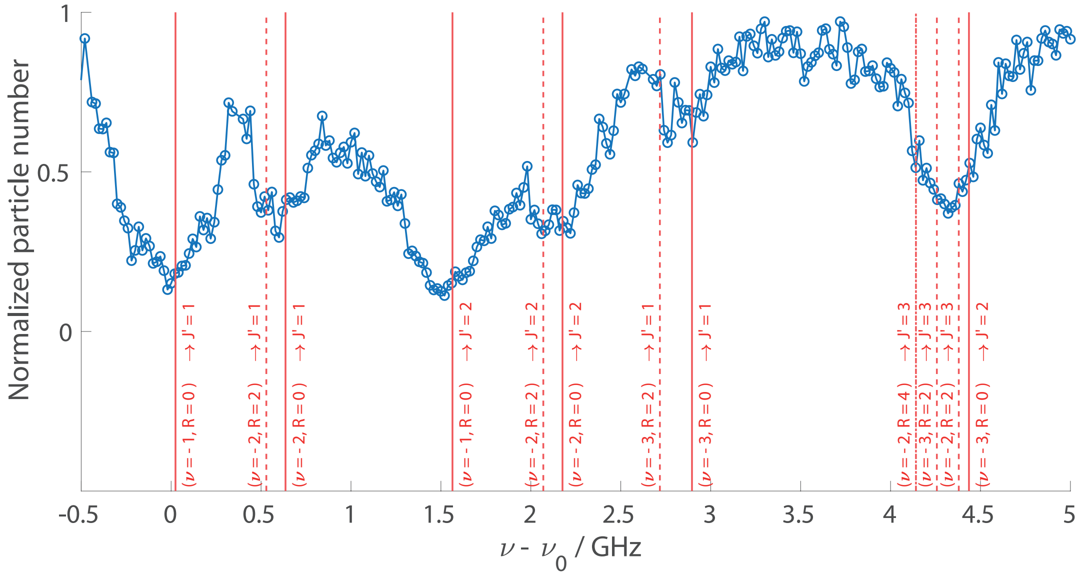

FIGURE 4.20: Recorded spectrum for $(2)^3\Pi_{1g}$, $\nu = 12$ for ^{87}Rb. Each data point is a single measurement. We use the position of the photoassociation line $\nu_0 = 502.264816(10)$ GHz as a reference frequency. The positions for the assigned transitions are marked vertically in red. From the distance between (ν = -1, R = 0, J′ = 1 and ν = -1, R = 0, J′ = 2) a rotational constant of B_v = 0.381 GHz can be extracted. Higher transitions (>= J′ = 4) were not recorded

TABLE 4.6: $(2)^3\Pi_g$ measurements of ^{85}Rb for $\Omega = 0^+, 0^-, 1$. Shown are the level energies in units of cm^{-1} for different rotational states J′ with respect to the 5s+5s asymptote. We extract the rotational constant from the energy difference $B_\nu = 0.385 \pm 0.010\,$GHz.

		$\Omega = 0^+$		
ν	J′ = 1	J′ = 3	J′ = 5	
9	16605.7615	16605.8909	-	
10	16638.2297	16638.3597	16638.5950	
11	16670.0250	16670.1547	-	
12	16702.0712	-	-	
13	16734.4175	16734.5466	16734.7792	
		$\Omega = 0^-$		
ν	J′ = 0	J′ = 2	J′ = 4	
9	16606.2703	16606.3479	16606.5295	
10	16638.6710	16638.7495	16638.9305	
11	16670.9540	16671.0310	16671.2133	
		$\Omega = 1$		
ν	J′ = 1	J′ = 2	J′ = 3	J′ = 4
5	16531.7066	16531.7573	16531.8337	-
6	16564.4394	16564.4908	16564.5648	-
9	16661.8266	16661.8773	16661.9541	16662.0587
11	16726.1492	16726.1999	16726.2789	16726.3833
12	16758.1925	16758.2444	16758.3216	16758.4244

TABLE 4.7: $(2)^3\Pi_g$ measurements of ^{87}Rb for $\Omega = 0^+, 0^-, 1$. Shown are the level energies in units of cm^{-1} for different rotational states J′ with respect to the 5s+5s asymptote. We extract the rotational constant from the energy difference $B_\nu = 0.383 \pm 0.010$ GHz.

		$\Omega = 0^+$	
ν	J′ = 1	J′ = 3	J′ = 5
9	16602.1520	16602.2770	-
10	16634.0984	16634.2252	16634.4563
11	16665.7810	16665.9064	-
12	16697.5587	16697.6848	-
13	16729.20390	16729.3310	16729.55910
		$\Omega = 0^-$	
ν	J′ = 0	J′ = 2	J′ = 4
7	16538.58070	16538.65580	-
9	16602.83310	16602.9095	16603.09803
10	16634.81660	16634.89230	16635.07040
12	16698.21980	16698.29520	-
13	16730.01310	16730.08820	16730.26620
		$\Omega = 1$	
ν	J′ = 1	J′ = 2	J′ = 3
5	16529.81260	16529.86330	-
6	16561.96790	16562.01860	-
8	16626.32230	16626.37230	16626.44870
11	16721.90550	16721.95690	16722.0319
12	16753.75090	16753.80230	16753.8780

Results and comparison with other studies

Table 4.6 and 4.7 shows all measured transitions that can be assigned via the analysis of the rotational structure. Both isotopes ^{85}Rb and ^{87}Rb are included, a total of over 20 vibrational transitions were measured and successfully assigned with an absolute spectroscopic accuracy of less than 100 MHz.
Previous studies on the analysis of the $(2)^3\Pi_g$ system have been published [4, 50, 165] (experiments), along with a theoretical study [114] performing ab initio calculations. For a brief overview of previous experimental work, see Section 4.1. The work of M. Ascoli which we discussed for the $(2)^1\Sigma_u^+$ states in Section 4.4.2 also includes recordings of the $(2)^3\Pi_g$ system. And there as well, the assignment of the vibrational quantum numbers was based on comparisons with their measured vibrational ladders and ab initio calculations. A possible uncertainty with this approach is that the assignment of the absolute vibrational quantum number is not unambiguous and additionally, the electronic states $\Omega = 0^+, 0^-, 1$ were not directly identified, unlike in our study, where the rotational structure was resolved and therefore allowed a clear identification of the electronic state. As already mentioned in Section 4.3.2, it seems that in the assignment of Ascoli et. al, signals of $(2)^1\Sigma_u^+$ were assigned to the B series which would belong to the $(2)^3\Pi_g$ system.
In another study by Yang et al. [165] cw lasers were used and also transitions to different rotational states for $\Omega = 1$ were observed but the assignment of vibrational quantum numbers is not clearly explained. As a main result of their study, they reported an average energy splitting between $\Omega = 0^+$ and $\Omega = 1$ of $83\,\mathrm{cm}^{-1}$ which corresponds to the spin-orbit splitting. Figure 4.21 provides a brief explanation of the spin-orbit splitting in the $(2)^3\Pi_g$ system. Ab initio calculations [114] estimate the spin-orbit coupling to be about 30 - $40\,\mathrm{cm}^{-1}$, strongly depending on the internuclear distance.
In principle, we can extract the spin-orbit splitting from our dataset as well because we have recordings from all Ω-states. One essential point is the identification of the absolute vibrational quantum numbers of our recorded transitions. For the state $\Omega = 0^+$, the work of [50] provided absolute vibrational quantum numbers. So the only remaining question is the identification of the vibrational quantum numbers of the $\Omega = 1$ states. We analyzed our data further and we use the fact that our dataset contains both isotopes of rubidium. More specifically, we investigated the isotope shift between the two rubidium isotopes. Due to the different masses of ^{85}Rb and ^{87}Rb, we expect the transitions to molecular states with identical vibrational quantum number to be slightly shifted relative to each other. The isotope shift itself depends on the absolute vibrational quantum number and increases with the vibrational quantum number for the $(2)^3\Pi_g$ system. In our spectroscopic observation range, an isotope shift between 2 and 5 cm^{-1} is expected. In Fig. 4.22, we compare the isotope shift of the $\Omega = 0^+$ with that of the $\Omega = 1$, considering two possible scenarios: one where the assignment of vibrational quantum numbers corresponds to the spin-orbit splitting of $\approx 83\,\mathrm{cm}^{-1}$ (red) reported by Yang et. al, and another where it corresponds to a spin-orbit coupling of

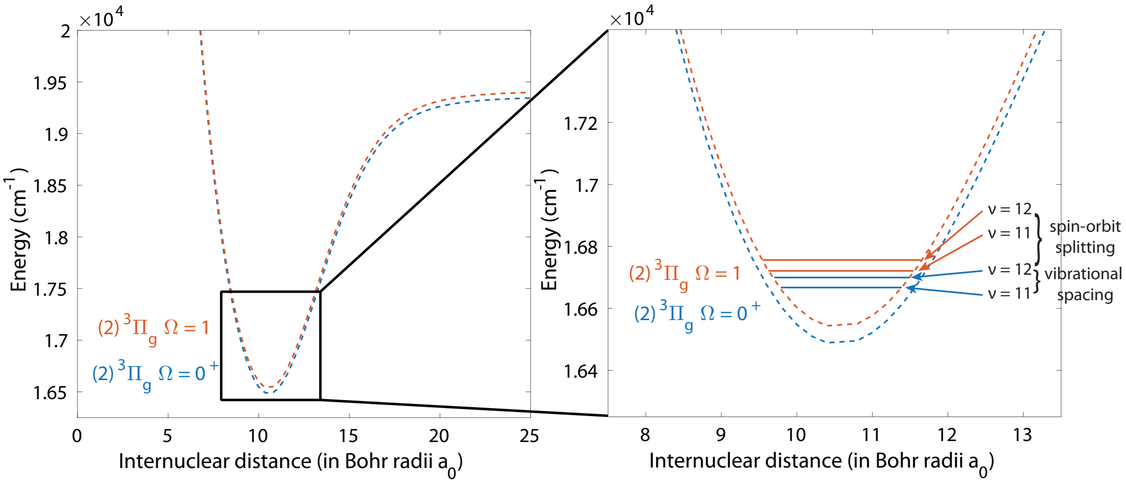

FIGURE 4.21: Illustration of the spin-orbit splitting between $\Omega = 0^+$ and $\Omega = 1$ for ^{87}Rb. On the right, we show the vibrational states $\nu = 11, 12$ for $\Omega = 0^+$ and $\Omega = 1$. The vibrational spacing is approximately 31.8 cm^{-1} in this case. The splitting between states with the same vibrational quantum number ν but different Ω is about 55 cm^{-1} here and corresponds to the spin-orbit splitting.

$\approx 55\,\text{cm}^{-1}$. To determine which spin-orbit splitting and vibrational quantum number assignment of $\Omega = 1$ is correct, we assume that the isotope shift for $\Omega = 0^+$ and $\Omega = 1$ should be approximately equal assuming that the R-dependence of spin-orbit coupling is not significant in this studied range for the same vibrational quantum number. In Fig. 4.22, the orange curve (representing $\Omega = 1$ with $55\,\text{cm}^{-1}$ spin-orbit coupling) aligns much better with the isotope shift of $\Omega = 0^+$. This strongly suggests that the value for spin-orbit splitting is around $55 \pm 10\,\text{cm}^{-1}$. Our experimental frequency uncertainty is small enough to clearly distinguish the two cases. Unfortunately, we have not yet been able to observe any transitions to $\Omega = 2$, which would be additionally helpful for the analysis of spin-orbit coupling and would make the analysis statistically more reliable.

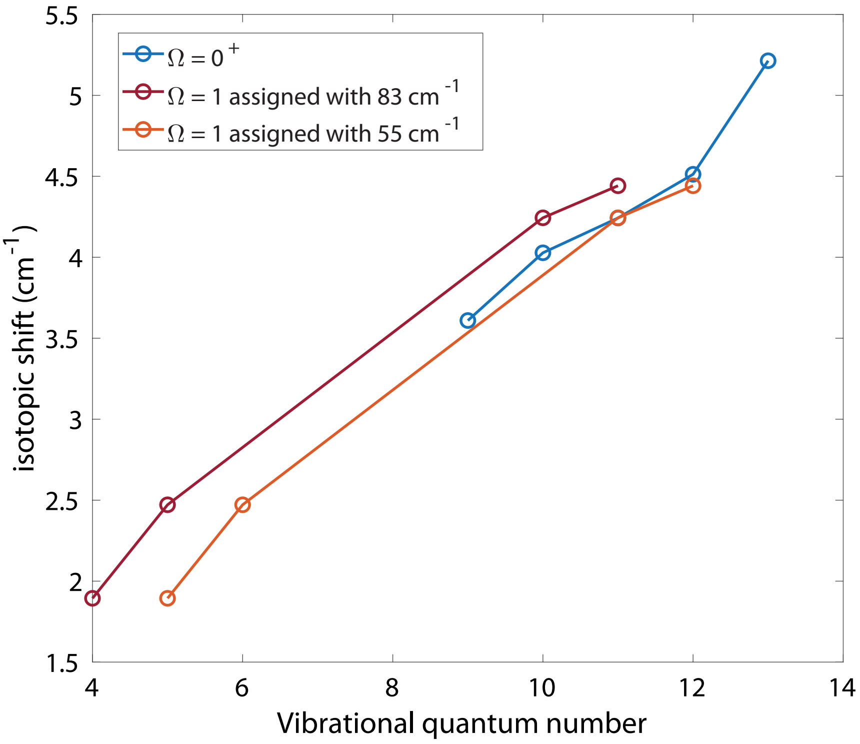

FIGURE 4.22: Isotope shift for $\Omega = 0_g^+$ (blue) where the vibrational quantum number is known from [50] and isotope shifts for $\Omega = 1_g$ (orange, red) where we test two different scenarios (which belong to two cases of spin-orbit interaction). The red vibrational assignment (spin-orbit splitting of 55 cm^{-1}) fits better to the blue data than the red (spin-orbit splitting of 83 cm^{-1} according to [165]) which makes a vibrational quantum number assignment for $\Omega = 1_g$ possible. The vibrational quantum numbers for the $\Omega = 1_g$ given in Tab. 4.7 and 4.6 were assigned accordingly.

4.5 Summary and outlook

In Ulm, precise measurements of the excited electronic molecular states $(2)^3\Pi_g$, $\Omega = 0^+, 0^-, 1$ and $(2)^1\Sigma_u^+$ associated with the 5s + 4 d asymptote, were carried out. More than 100 molecular states were successfully assigned in their respective quantum numbers. While the experimental work has been completed, further analysis of the observations, particularly through coupled-channel model calculations, is currently ongoing.
Our recordings for $(2)^1\Sigma_u^+$ show good agreement with previously reported studies [4] with improved spectroscopic precision by almost two orders of magnitude. A preliminary potential energy curve for the electronic state $(2)^1\Sigma_u^+$ is shown in Fig. 4.17, already indicating significant deviations from previous calculations. Similarly, for the electronic states $(2)^3\Pi_g, \Omega = 0^+, 0^-, 1$, we could experimentally extract a value for the spin-orbit splitting of about $55\,\mathrm{cm}^{-1}$. Once the theoretical analysis is finalized, both results will be published. Our spectroscopic measurements and analysis for the molecular transitions are key to gain a better understanding of the investigated excited molecular states. New calculations for potential energy curves will allow for more accurate predictions of molecular transitions in frequency position and also in terms of transition probabilities. This knowledge is expected to be useful in future three-body recombination experiments to optimize REMPI detection pathways.

Chapter 5

Spin-conservation propensity rule for three-body recombination of ultracold Rb atoms

The observations and analysis presented in the following chapter reveal an important principle in ultracold three-body recombination (TBR): the spin conservation propensity rule. This rule dictates that TBR preferentially produces molecules with the same spin character as the reacting atom pair. It enables control over ultracold reactions by allowing manipulation of reactant or product spin states. This principle motivates the experiments in Chapters 6 and 7 and serves as their theoretical foundation. In turn, the corresponding experiments validate the spin conservation propensity rule and broaden its scope and applicability.

In the following Chapter 5, we analyze mainly the observations about the conservation of the hyperfine spin in the reaction and discuss the physical origin. In Chapters 6 and 7, we apply this concept in two distinct approaches to influence chemical reactions in three-body recombination:

Product Channel manipulation using an avoided energy level crossing

In this approach, we aim to manipulate the outgoing product channels of the reaction by utilizing an avoided energy level crossing in the ^{87}Rb isotope. This involves coupling of two specific molecular states that exhibit barely any mixing at low magnetic fields. This results in the fact, that the molecular state which initially has a different spin character than the incoming channel is rarely produced. By applying an external magnetic field, however, the superposition of these states changes, allowing more of the incoming channel's spin character to mix in. We observed that this adjustment leads to a higher rate of molecule formation via three-body recombination for that initially rarely product molecular state. This scheme therefore enables the tuning of production rates of two specific molecular levels by using external magnetic fields.

Mixing of the incoming channel by using a magnetic feshbach resonance

In this method, the incoming channels are mixed through a magnetic Feshbach resonance, allowing the formation and detection of entire families of product molecules. In contrast to the approach above, this technique produces a significantly broader population distribution of molecules by mixing the incoming channel rather than focusing on just two specific product states.

The spin-conservation propensity rule provided critical insights for subsequent controlled chemistry experiments, laying the foundation for a further series of experiments in which various control mechanisms can be combined.

The content of this chapter is published in Ref. [57]. The experimental part of this work was conducted in the BaRbIE lab under the supervision of postdoctoral researcher Shinsuke Haze. My contribution to this publication involved supporting lab work and assisting in the execution of the experiments.

Shinsuke Haze, José P. D'Incao, Dominik Dorer, Paul S. Julienne, Eberhard Tiemann, Markus Deiß and Johannes Hecker Denschlag

"Spin-conservation propensity rule for three-body recombination of ultracold Rb atoms", *Phys. Rev. Lett.* **128**, 133401 (2022).
DOI: `10.1103/PhysRevLett.128.133401`
Reprinted with permission from American Physical Society

5.1 Abstract

We explore the physical origin and the general validity of a propensity rule for the conservation of the hyperfine spin state in three-body recombination. This rule was recently discovered for the special case of ^{87}Rb with its nearly equal singlet and triplet scattering lengths. Here, we test the propensity rule for ^{85}Rb for which the scattering properties are very different from ^{87}Rb. The Rb_2 molecular product distribution is mapped out in a state-to-state fashion using REMPI detection schemes which fully cover all possible molecular spin states. Interestingly, for the experimentally investigated range of binding energies from zero to $\sim 13\,\mathrm{GHz} \times h$ we observe that the spin-conservation propensity rule also holds for ^{85}Rb. From these observations and a theoretical analysis we derive an understanding for the conservation of the hyperfine spin state. We identify several criteria to judge whether the propensity rule will also hold for other elements and collision channels.

5.2 Introduction

The particular mechanisms of chemical reactions often give rise to selection and propensity rules. While selection rules express strict exclusion principles for product channels, propensity rules specify which product channels are more likely to be populated than others [10, 40]. Since the early days of quantum mechanics a central question in reaction dynamics is whether composite spins are conserved. Wigner's spin-conservation rule, e.g., states that the total electronic spin has a propensity to be conserved [61, 82, 105]. The recent progress in the quantum state-resolved preparation and detection of ultracold atoms and molecules has now made it possible to experimentally explore spin conservation rules that also involve nuclear spins. In a recent study of bimolecular reactions of ultracold KRb molecules the conservation of the total nuclear spin was found [65, 94]. In a study on the final state distribution of three-body recombination of ultracold ^{87}Rb atoms our group found a propensity for the conservation of the hyperfine state of the atom pair forming the molecule [157, 158]. More precisely, this spin propensity rule states that the angular momentum quantum numbers F, f_a, f_b and $m_F = m_{fa} + m_{fb}$ are conserved in the reaction. Here, f_a, f_b correspond to the total angular momenta of the two atoms (a, b) forming the molecule, and $\vec{F} = \vec{f}_a + \vec{f}_b$.

Formally, there is no selection rule that forbids spin exchange between all three atoms in the recombination process, and a corresponding change in the quantum numbers. In fact, recent calculations predict spin exchange to occur in three-body recombination of ^{7}Li [89] and ^{39}K [21, 160], although being suppressed for ^{87}Rb [89]. In order to explain the observed spin propensity rule for ^{87}Rb one can justifiably argue that ^{87}Rb is special since here the singlet (a_s) and triplet (a_t) scattering lengths are nearly identical ($a_s \approx 90a_0, a_t \approx 99a_0$, where a_0 is the Bohr radius). This leads to a strong suppression of two-atom spin exchange reactions [18, 75, 79].

In order to explore the validity of the spin propensity rule further, we investigate here, both experimentally and theoretically, three-body recombination of ultracold ^{85}Rb atoms which have very different two-body scattering properties from ^{87}Rb atoms. The singlet and triplet scattering lengths for ^{85}Rb atoms are $a_s = 2720a_0$ and $a_t = -386.9a_0$ [139], respectively, and the three-body recombination rate constant L_3 for ^{85}Rb is about four orders of magnitude larger than for ^{87}Rb. Nevertheless, as a central result of our work, we find the spin propensity rule to also hold for ^{85}Rb, within the investigated range of binding energies from zero to 13 GHz $\times\, h$ and the resolution of our experiment. This result is corroborated by the fact that our measured product distributions are well reproduced by numerical three-body calculations based on a single-spin channel. The spin propensity rule that we find for ^{87}Rb and ^{85}Rb will also hold for other elements if certain conditions are met, which are formulated in the present work.

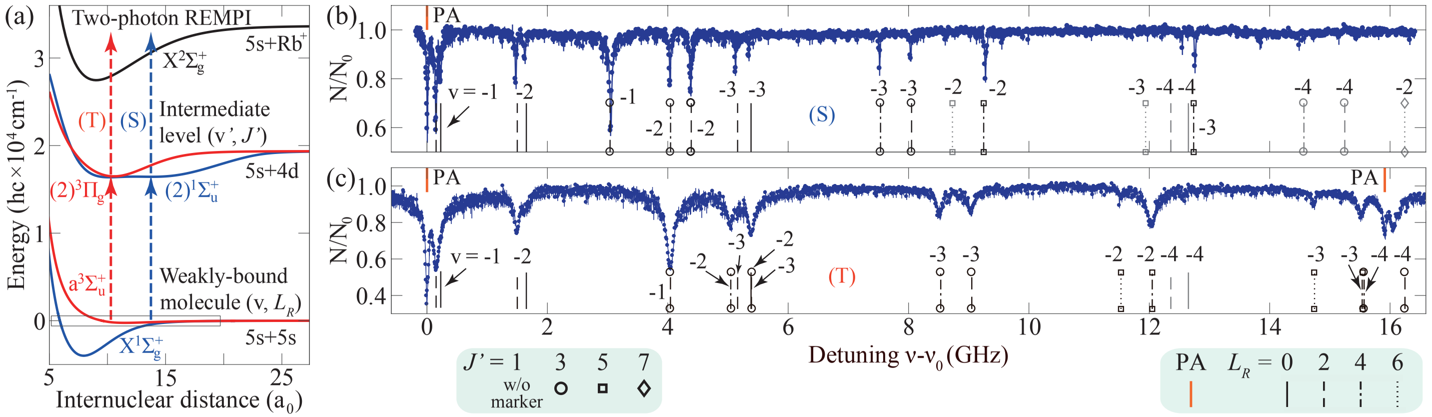

FIGURE 5.1: (a) REMPI pathways for detecting molecules with singlet $X^1\Sigma_g^+$ and/or triplet $a^3\Sigma_u^+$ character via the intermediate states $(2)^1\Sigma_u^+$, v′ = 22 [4] (path (S)) and $(2)^3\Pi_g$, 0_g^+, v′ = 10 [4] (path (T)), respectively (see blue (red) dashed vertical arrows). The potential energy curves are derived from [8, 95, 139]. (b,c) REMPI spectra of product molecules using path (S) for (b) and path (T) for (c). Shown is the normalized remaining atom number N/N_0 as a function of the REMPI laser frequency ν, where $\nu_0 = 497603.591$ GHz (b), $\nu_0 = 497831.928$ GHz (c), are the resonance positions of the photoassociation signals (PA) of the intermediate levels with $J' = 1$. J' is the total angular momentum excluding nuclear spin. The vertical lines represent calculated resonance positions, where black (gray) color indicates experimentally observed (unobserved) states. Each line is marked with the vibrational quantum number v. L_R and J' are given by the linestyle and the plot symbols, respectively (see legends).

5.3 Measurements and results

We carry out the measurements with an ultracold cloud of 2.5×10^5 ^{85}Rb ground state atoms at a temperature of 860 nK and at near-zero magnetic field B. The atoms have spin $f = 2, m_f = -2$ and are trapped in a far-detuned optical dipole trap. Three-body recombination produces weakly-bound molecules in the mixed singlet $X^1\Sigma_g^+$ and triplet $a^3\Sigma_u^+$ states, see Fig. 5.1(a), which are coupled by hyperfine interaction [139]. We measure the yields of molecular products, observing a range of rovibrational states with vibrational and rotational quantum numbers v, L_R, respectively, from v $= -1$ to -4 and from $L_R = 0$ to 6. A main result of our experiments is that we only find population in molecular states which are in the same spin state $F = 4, f_a = 2, f_b = 2$ (in short $F f_a f_b = 422$) as the reacting atom pair, although the investigated range of binding energies covers many bound states with different spin states. Because the two ^{85}Rb atoms (a, b) are identical bosons, the state $F f_a f_b = 422$ goes along with only having even angular momenta L_R and a positive total parity.

We have extended our previous state-selective detection scheme [158] so that it now covers all symmetries of the dimer product state space, including spin triplet and singlet states with their respective u/g symmetry. We apply two-step resonance-enhanced multiphoton ionization (REMPI), similar to [46, 66, 76, 95, 96], but with a cw-laser. By two different REMPI pathways, (S) or (T), we probe product molecules via singlet or triplet character [see Fig. 5.1(a)]. Both schemes use identical photons for the two REMPI steps at wavelengths around 602.2 nm. The intermediate states are deeply-bound levels of $(2)^1\Sigma_u^+$ and $(2)^3\Pi_g$ for REMPI (S) and (T), respectively. When ions are produced via REMPI, they are directly trapped and detected in an eV-deep Paul trap which is centered on the atom cloud. Subsequently, elastic atom-ion collisions inflict tell-tale atom loss while the ions remain trapped. From the atom loss which is measured via absorption imaging of the atom cloud [51, 158] the ion number can be inferred.

Figures 5.1(b) and (c) show REMPI spectra of Rb_2 product molecules following three-body recombination, using path (S) and (T), respectively. Apart from three signals stemming from the photoassociation of two atoms (indicated by PA) [72], each resonance line of loss corresponds to a molecular product state. The photoassociation lines serve as references for the $|f = 2, m_f = -2\rangle + |f = 2, m_f = -2\rangle$ asymptote corresponding to zero binding energy at about zero magnetic field. The vertical lines in Figs. 5.1(b) and (c) are predicted frequency positions for product states for the spin state $F f_a f_b = 422$. These predictions are obtained from coupled-channel calculations for the $X^1\Sigma_g^+ - a^3\Sigma_u^+$ complex [139]. Coincidences of predicted and observed lines allow for an assignment. As a consistency check for the assignment of signals in Figs. 5.1(b) and (c) we make use of product states with $L_R > 0$ since these give rise to two resonance lines corresponding to the transitions towards $J' = L_R \pm 1$. Indeed, the data in Figs. 5.1(b) and (c) confirm this consistency. Inspection clearly shows, that all experimentally observed spectral lines in Figs. 5.1(b) and (c) can be explained as signals from product molecules with the spin $Ff_af_b = 422$. As an additional check for the line assignment, we show in the Supplementary material that our experimental spectra do not match up with molecular spin states other than $Ff_af_b = 422$. This clearly indicates that the same spin propensity rule previously observed for ^{87}Rb also holds for ^{85}Rb.

For each product signal in the singlet REMPI path (S) we obtain a corresponding signal in the triplet REMPI path (T). This is because the spin state $Ff_af_b = 422$, $m_F = -4$ has sizeable singlet ($\approx 15\%$) and triplet ($\approx 85\%$) admixtures. The spectra of Figs. 5.1(b) and (c) generally look different since the rotational constants differ for $(2)^1\Sigma_u^+$ ($B_{\mathrm{v}'} = 289(1)$ MHz) and for $(2)^3\Pi_g, 0_g^+$ ($B_{\mathrm{v}'} = 389(2)$ MHz), see, e.g., [50]. The linewidths in Fig. 5.1(c) are typically on the order of 100 MHz (FWHM) which is larger than the typical linewidths in Fig. 5.1(b) of about 30 MHz. This is a consequence of the larger hyperfine splitting of the $(2)^3\Pi_g$ state, which is not resolved in our measurements. In Fig. 5.1(c) at $\nu - \nu_0 = 15.90$ GHz there is a photoassociation signal which belongs to the 0_g^- component of $(2)^3\Pi_g$. We show the corresponding REMPI spectrum in the Supplementary material. It exhibits the same molecular states as in Figs. 5.1(b) and (c).

We now carry out a more quantitative analysis where we compare the experimental signal strengths of the various REMPI paths and also compare them to theoretical calculations. For this, we measure the ion production rate for each assigned resonance line in Fig. 5.1 and Fig. 5.4 in the Supplementary material. For a given REMPI path, the ion rate signal is expected to be proportional to the product molecule population rate, if we assume equal REMPI ionization efficiencies for the states. Our data show that this assumption is indeed fulfilled for most data points within the uncertainty limits of the recordings. Figure 5.2 shows the extracted ion production rates γ_i of each molecular product state for the three REMPI paths (via $(2)^1\Sigma_u^+$, $(2)^3\Pi_g\ 0_g^+$, and $(2)^3\Pi_g\ 0_g^-$). If a state is observed via two or three different J' levels for a given path, we plot the average of the rates and mark the standard deviation from the mean with an error bar. In order to ease the comparison between the three data sets we have globally scaled the ion signals for the $(2)^3\Pi_g\ 0_g^-$ and $(2)^1\Sigma_u^+$ paths by a factor of 7.3 and 3.2, respectively, so that the signal bars for all REMPI paths in Fig. 5.2 are the same height for the state ($\mathrm{v} = -2$, $L_R = 4$), see black arrow. These scaling factors compensate the differences in the ionization efficiencies of the different REMPI paths, which are due to the different singlet and triplet components of the product molecule as well as differences in the electric dipole transition moments, which are generally not very well known yet. After the scaling the signals of the three paths for a given bound state are consistent over the set of detected product states.

In addition to the experimental data, we plot in Fig. 5.2 calculated channel rate constants $L_3(\mathrm{v}, L_R)$ for a temperature of 0.8 μK. The calculations use a

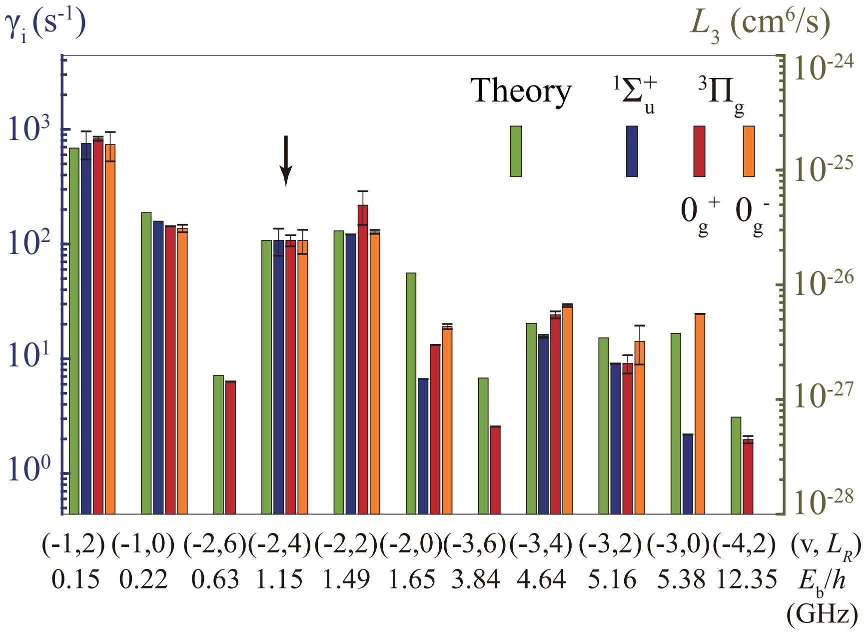

FIGURE 5.2: Comparison of calculations and experiments. Measured (scaled) ion production rates γ_i for the product states (v, L_R) with binding energies E_b are given for the three REMPI paths together with calculations for the three-body recombination channel rate constants $L_3(\mathrm{v}, L_R)$ (see the legend for the color coding). The ion signals for the $(2)^3\Pi_g\ 0_g^-$ and $(2)^1\Sigma_u^+$ paths have been scaled (see text).

single-spin model (see Supplementary material 5.4) which is similar to the one used in Ref. [158] in order to solve the three-body Schrödinger equation in an adiabatic hyperspherical representation [29, 149]. For this, we use pairwise additive long range van der Waals potentials with a scattering length of $-443a_0$ [25] for ^{85}Rb and with a truncated number Z of $L_R = 0$ bound states ($Z = 9$ for Fig. 5.2). The calculated total recombination rate constant at 0.8 μK (including thermal averaging) is $L_3 = 3.07 \times 10^{-25}$ cm^6/s and is consistent with the values found in Ref. [120].

All data sets in Fig. 5.2 display the trend that the population of a molecular state due to three-body recombination typically decreases with increasing binding energy E_b of the product state, which is consistent with the work for ^{87}Rb [158]. The overall agreement between theory and experiment in Fig. 5.2 is good, as the experimentally observed relative strengths of the signals for low L_R are in general well reproduced by the calculated recombination rates. This suggests that our single-spin model fully captures the characteristics of the three-body chemical reaction in the given parameter regime, which can be viewed as additional evidence for the spin propensity rule.

Based on our theoretical analysis, we conclude that the spin propensity rule in our experiment is a consequence of the following scenario. a) The reaction takes place at interparticle distances where the interactions of particles a and

b (forming the molecule) with particle c are nearly spin-independent. b) In the investigated range all possible product molecules have quantum states with good quantum numbers F, f_a, f_b. c) In the reaction region, the spin composition of the reacting pair a, b is essentially given by $F f_a f_b = 422$. As a consequence of conditions a), b) and c) the molecule formation is driven by mechanical forces from atom c while the spin state of the reacting pair is not affected.

To show that this scenario holds for our experiments, we first analyze the typical interparticle distances where the reaction occurs. Our numerical calculations (see Supplementary material 5.4) show that the formation of $^{85}\mathrm{Rb}_2$ molecules mainly takes place near a hyperradius $R \approx 1.5 r_{\mathrm{vdW}}$, extending from $R \approx 1.1 r_{\mathrm{vdW}}$ to $2 r_{\mathrm{vdW}}$. Here, $r_{\mathrm{vdW}} = (2\mu C_6/\hbar^2)^{1/4} = 82 a_0$ denotes the van der Waals length for Rb, and μ and C_6 are the reduced mass and the van der Waals coefficient of the two-particle system, respectively. The hyperradius R describes the characteristic size of the three-body system and is given by $R^2 = (\vec{r}_b - \vec{r}_a)^2/d^2 + d^2(\vec{r}_c - (\vec{r}_a + \vec{r}_b)/2)^2$, where $\vec{r}_i$ is the location of particle i and $d^2 = 2/\sqrt{3}$ [29]. The fact that the reactions occur at these large R can be understood within the framework of the adiabatic hyperspherical representation, where an effective repulsive barrier for the three-body entrance channel forms at a hyperradius of about $R = 1.7 r_{\mathrm{vdW}}$ [150].

We now consider the formation of a molecule state with a size $\lesssim r_{\mathrm{hf}} \approx 0.6 r_{\mathrm{vdW}}$. Only for such a state can spin components other than $F f_a f_b = 422$ be substantial (for more details see Supplementary material). Here, $r_{\mathrm{hf}} = (C_6/E_{\mathrm{hf}})^{1/6}$ is the hyperfine radius and $E_{\mathrm{hf}} = 3.04\,\mathrm{GHz} \times h$ is the atomic hyperfine splitting. Given the hyperradius $R > 1.1 r_{\mathrm{vdW}}$ and the interparticle distance $r_{ab} \equiv |\vec{r}_a - \vec{r}_b| < r_{\mathrm{hf}}$, the distances of particle c to the others must be $r_{ca}, r_{cb} > 0.6 r_{\mathrm{vdW}}$. Since the interaction between two Rb atoms is essentially spin-independent for distances $\gtrsim 0.25 r_{\mathrm{vdW}}$, this validates point a) of the scenario described above. Concerning point b), our coupled-channel calculations show that the weakly-bound molecular states up to a binding energy of about $50\,\mathrm{GHz} \times h$ have almost pure spin states $F f_a f_b$. This can be explained by the fact that the ^{85}Rb triplet and singlet scattering lengths are large in magnitude. For ^{85}Rb, where these scattering lengths are of opposite sign, this leads to a near energetical degeneracy of the triplet vibrational levels v_T with the singlet vibrational levels $\mathrm{v}_S = \mathrm{v}_T - 1$ [73, 74]. Since, in addition, the singlet and triplet vibrational wavefunctions are very similar at long range, the interaction between the two atoms is effectively spin-independent. As a consequence the atomic hyperfine interaction of each atom is essentially unperturbed, which leads to the atomic hyperfine structure with the quantum numbers f_a, f_b for the molecule. Subsequent coupling of $\vec{f}_a, \vec{f}_b$ in the molecule forms a total $\vec{F}$.

To show point c), we first note that due to the magnitude of R the three-body system can be effectively decomposed (with respect to spin) into a two-body collision of two $f = 2, m_f = -2$ atoms (a and b) and a third atom (c) which is spin-wise only a spectator, see also Supplementary material. During the two-body collision of atoms a and b, spin admixtures to the original 422 state can occur at close distance. However, these admixtures are only on the % level for ^{85}Rb even for short atomic distances $r_{ij} \sim 0.25 r_{\text{vdW}}$, and therefore negligible. That this admixture is small can be derived from the fact, that the two-body scattering wavefunction is very similar to the one of the corresponding last molecular bound state at short distance. The scattering state therefore shares the relatively pure Ff_af_b spin state character of the weakly-bound molecular states, as discussed before.

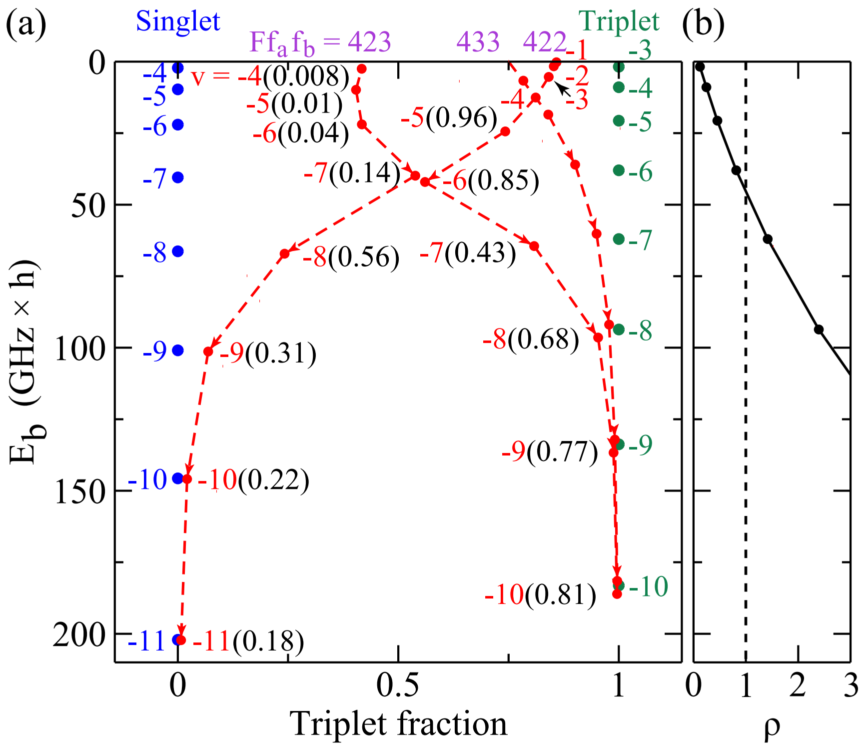

FIGURE 5.3: (a) Binding energy and spin character of weakly-bound ^{85}Rb$_2$ molecules for various vibrational quantum numbers v $= -1$ to -11 at $B = 0$ (red circles). Here, $L_R = 0$, $F = 4$, and $m_F = -4$. Zero energy corresponds to two separated atoms in state $f_a f_b = 22$. The spin character is given as the norm of the spin triplet component. Shown are the three spin families with $F = 4$ which correlate with the states $Ff_af_b = 422, 423, 433$ at the $E_b = 0$ threshold. Red dashed arrows are guides to the eye and indicate the change of each family's spin character with increasing binding energy. The norm of the 422 spin component is presented in parentheses for the 423 and 422 families. For the 433 family the 422 norm is about 1% for the shown bound states. Blue and green circles are the bound state levels of the pure singlet and triplet potentials, respectively, the dissociation limit of which is at $E = +3.542\,\text{GHz} \times h$ above $E_b = 0$. (b) Ratio ρ for various binding energies (see text).

Our coupled-channel calculations using the potentials of [139] show that for molecular bound states with a binding energy larger than 50 GHz × h the spin decomposition changes, because the splitting of adjacent singlet and triplet vibrational levels becomes larger than the hyperfine splitting. This is shown in Fig. 5.3(a). In our experiment we only observe product states down to the $\mathrm{v} = -4$ level in the 422 family, for which the norm of the 422 entrance channel remains between 0.99 and unity. All other unobserved spin families have a norm of the 422 channel much less than unity. In Fig. 5.3(b) we plot the ratio ρ of the triplet and singlet level splitting and the hyperfine splitting, $\rho = |E_\mathrm{T}(\mathrm{v}) - E_\mathrm{S}(\mathrm{v}-1)|/E_\mathrm{hf}$. For $\rho > 1$ hyperfine mixing is increasingly suppressed and the propensity rule is expected to break down.

Similar arguments can be used to also explain the spin propensity rule for ^{87}Rb as observed in [157, 158]. Here, the singlet and triplet scattering lengths are almost equal, leading to a near degeneracy of the singlet and triplet vibrational states for $\mathrm{v}_T = \mathrm{v}_S$. Furthermore, the atomic hyperfine splitting in ^{87}Rb is larger by a factor of ≈ 2.4 than in ^{85}Rb. As a consequence the spin propensity rule holds for even larger binding energies of up to 100 GHz × h (see Fig S5 in the Supplementary material).

In the future, it will be interesting to investigate the breakdown of the spin propensity rule for ^{85}Rb by studying product molecules with binding energies larger than $\sim$ 50 GHz × h. For these measurements the ability to state-selectively detect singlet and triplet product molecules as demonstrated here, will be essential. The spin propensity rule will also break down when F is not a good quantum number anymore, e.g., by applying strong magnetic fields. ^{85}Rb features a broad Feshbach resonance at 153.3 [13] where spin-mixing in the incoming channel naturally becomes important [21, 130, 160]. Besides for Rb the spin-conservation propensity rule may hold for other elements. Cs, e.g., might be a good candidate when working in a regime where dipolar relaxation processes are negligible.

Acknowledgements

This work was financed by the Baden-Württemberg Stiftung through the Internationale Spitzenforschung program (contract BWST ISF2017-061) and by the German Research Foundation (DFG, Deutsche Forschungsgemeinschaft) within contract 399903135. J. P. D. also acknowledges partial support from the U.S. National Science Foundation, Grant No. PHY-2012125, and NASA/JPL 1502690. The authors would like to thank Jinglun Li for helpful discussions. J. P. D. thanks Timur Tscherbul for stimulating discussions.

5.4 Supplemental Material

Ultracold atoms - setup

The ultracold ^{85}Rb atoms are initially prepared in the spin state $f = 2, m_f = -2$ of the electronic ground state. This state is stable in two-body collisions due to energetic closure of other atomic exit channels and due to small dipolar relaxation rates. Indeed, our coupled-channel calculations have verified that the two-body spin-relaxation rate constants for ^{85}Rb remain below 10^{-14} cm^3/s when the magnetic field is not near a Feshbach resonance. The scattering length for the collision of two $f = 2, m_f = -2$ atoms is $a = -460a_0$.

In our set-up the atoms are trapped in a far-detuned optical dipole trap with trapping frequencies $\omega_{x,y,z} = 2\pi \times (156, 148, 18)$ Hz. The optical dipole trap operates at a wavelength of about 1064 nm.

REMPI

For REMPI we use a laser wavelength around 602.2 nm. The laser light is either provided by a cw dye laser (Matisse, Sirah Lasertechnik GmbH) or an optical parametric oscillator (C-Wave, Hübner GmbH). Each laser is stabilized to a cavity and has a short-term linewidth of less than 1 MHz. Longer term drifts are compensated by a lock to a wavelength meter and we have a shot-to-shot frequency stability on the order of ±5 MHz. The laser beam has a power of 100 mW and a beam waist ($1/e^2$ radius) of 1 mm at the location of the molecules. It has a mixture of σ- and π-polarization and can be essentially considered as unpolarized. REMPI produces Rb$_2^+$ molecules with binding energies larger than 479 cm^{-1} in the $X^2\Sigma_g^+$ state. We have no indication of a resonance structure for the ionization transition, in agreement with [46, 115] where the ionization range is referred to as a diffuse band. Coincidences of predicted and observed lines in REMPI spectra allow for an assignment of the observed lines. The precision of coincidences was typically around 10 MHz, as mainly determined by slight drifts of the wavemeter. We note that besides the triplet and singlet paths discussed in detail in this publication we also have tested a REMPI path via the $A^1\Sigma_u^+$ state (associated with the $5s + 5p$ asymptote) similar to the one described in [158], however, the overall detection efficiencies are much lower in that case. Furthermore, the spectra of Figs. 1(b) and (c) and Fig. 5.4 are very clean in a sense that essentially no unidentified resonance signals are visible which represents a significant improvement as compared to [158].

The $(2)^3\Pi_g$, 0_g^- intermediate state

Figure 5.4 shows the REMPI spectrum using the intermediate state $(2)^3\Pi_g$, 0_g^-. For 0_g^- the total parity is given by $(-1)^{J'+1}$. Therefore, since the initial product molecules have positive total parity, only transitions towards intermediate states with even quantum number J' are possible. Concerning photoassociation we now observe two lines, one for $J' = 0$ and the other one for $J' = 2$. The vertical lines are calculations for the expected REMPI signals, where we use the same rotational constant of $B_{v'} = 389(2)$ MHz for the intermediate state as for $(2)^3\Pi_g$, 0_g^+. The calculated resonance positions agree well with the measurements. As a consistency check for the assignment of signals in Fig. 5.4 we use that product states can give rise to up to three resonance lines corresponding to the transitions towards $J' = L_R$ and $J' = |L_R \pm 2|$. The data in Fig. 5.4 confirm this consistency.

Ion number calibration

For each molecular resonance line in the spectra of Fig. 5.1 and Fig. 5.4 we have measured the ion production rate in our experiment. For this, we tune the ionization laser onto a given resonance and turn it on for a short enough pulse time so that only a few ions (< 20) are produced. We are then in a regime where the ion number grows linearly with time (see inset of Fig. 5.5 for a typical measurement). Afterwards we count the number of ions by inserting them into a fresh atom cloud with 2.5×10^5 atoms. After an interaction time of 500 ms, during which the ions inflict atom loss due to (mostly) elastic atom-ion collisions [51], we measure the remaining number of atoms with absorption imaging. Using the calibration curve in Fig. 5.5 we can convert the measured atom fraction into an ion number. Dividing the ion number by the pulse time we obtain the ion production rate. The calibration curve was obtained as follows. Initially, the ion trap and the optical dipole trap are spatially separated from each other so that the atoms cannot collide with the ions. A known number of laser-cooled $^{138}\mathrm{Ba}^+$ ions in a range between 1 to about 40 is prepared in the Paul trap. The cold ions form an ion crystal in the trap and are counted with single-particle resolution after fluorescence imaging. In parallel, we prepare a $^{85}\mathrm{Rb}$ atom cloud in the crossed optical dipole trap. Next, the centers of the ion and atom traps are overlaid, immersing the Ba^+ ions into the atom cloud. Subsequently, the Ba^+ ions can undergo reactions with the Rb atoms, such as, e.g., charge exchange [104]. After a long interaction time of 2s we are predominantly left with Rb^+ ions, as confirmed by mass spectrometry. Although these ions can have high kinetic energy they are still confined in the eV-deep Paul trap, i.e., the initial number of trapped ions is conserved. Afterwards, the ion trap and the optical dipole trap are separated again from each other, the old atom cloud is discarded and a new atom cloud (with 2.5×10^5 atoms) is prepared. The ions are immersed into the new atom cloud for 500 ms and atom-ion collisions inflict again atom loss. Figure 5.5 shows the remaining atom fraction N/N_0 as a function of initial ion number N_i. The dashed line is a fit with the empirically-found function $N/N_0 = (\frac{N_\mathrm{i}}{\alpha} + 1)^\beta$. Here, α and β are fit coefficients.

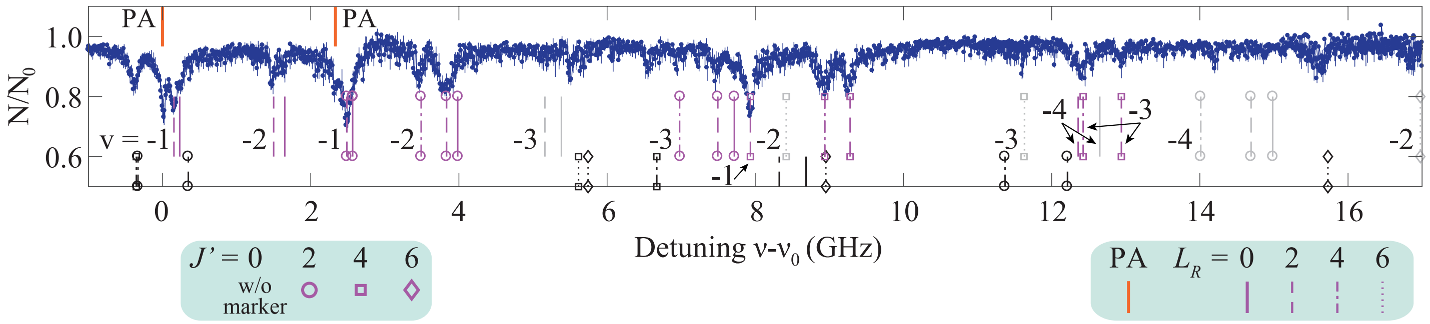

FIGURE 5.4: REMPI spectrum via the triplet path (T) with intermediate state $(2)^3\Pi_g$, 0_g^-, $\mathrm{v}' = 10$. The remaining atom fraction N/N_0 is plotted as a function of the REMPI laser frequency ν. $\nu_0 = 497847.828\,\mathrm{GHz}$ is the resonance frequency for photoassociation (PA) towards $(2)^3\Pi_g$, 0_g^- $(J' = 0)$. A second photoassociation line for a transition towards $(2)^3\Pi_g$, 0_g^- $(J' = 2)$ is located at around $\nu - \nu_0 = 2.4\,\mathrm{GHz}$. The vertical lines are predicted possible line positions of molecular states. If observed they are purple (0_g^-) or black (0_g^+), if unobserved they are gray. The lines involving 0_g^- are marked with the vibrational quantum number v. The rotational quantum number L_R and the intermediate level J' are given by the linestyle and the plot symbols, respectively (see legends).

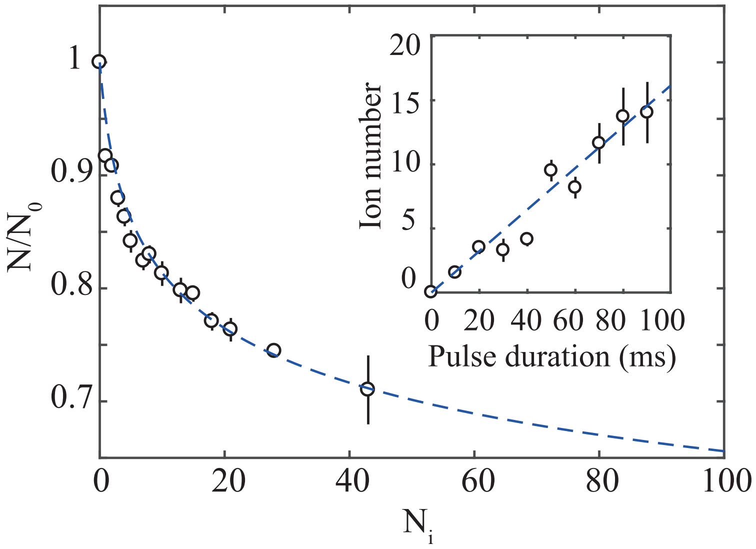

FIGURE 5.5: Atom loss due to elastic collisions with N_i ions (predominantly Rb^+). Shown is the remaining atom fraction N/N_0 of the atom cloud after 500 ms of atom-ion collisions with N_i ions previously prepared in the Paul trap. The dashed line is the fit function $N/N_0 = (\frac{N_\mathrm{i}+\alpha}{\alpha})^\beta$ with the fit parameters $\alpha = 1.4$ and $\beta = -10.1$. The inset is a typical measurement of the ion number as a function of the REMPI laser pulse duration. For the given example, the REMPI laser frequency is set to resonantly excite the molecular state $(\mathrm{v}, L_R) = (-1, 2)$ towards the $(2)^3\Pi_g$, 0_g^-, $\mathrm{v}' = 10$, $J' = 2$ intermediate state. The dashed line is a linear fit to the data.

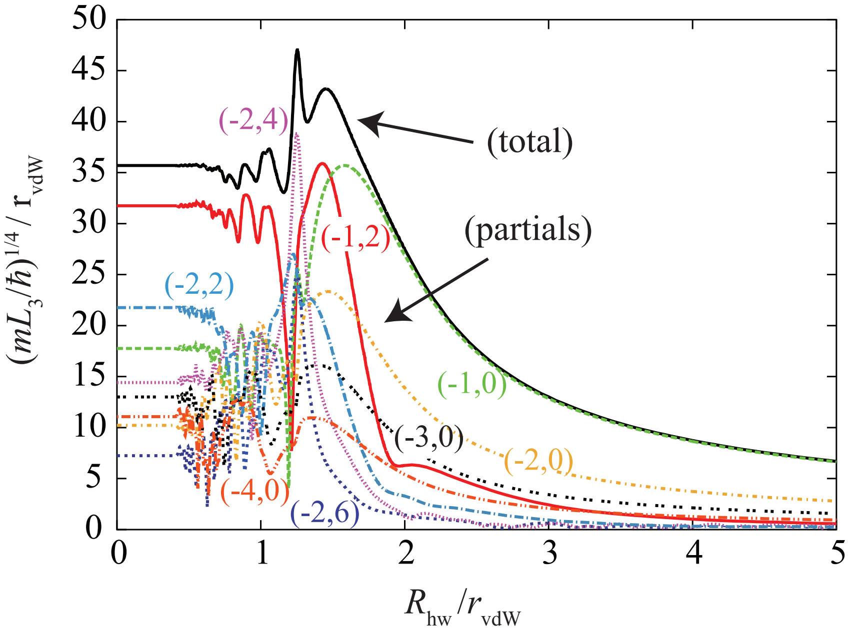

FIGURE 5.6: Total three-body recombination rate L_3 (black solid line) and corresponding partial rates for the six most weakly-bound molecular states currently observed, (v, L_R) = (-1,2), (-1,0), (-2,6), (-2,4), (-2,2) and (-2,0), as well as (-3,0) and (-4,0), calculated with a two-body interaction model supporting 5 s-wave bound states. These results indicate that recombination is likely to occur at $R \approx 1.5 r_{\text{vdW}}$, while it is increasingly suppressed for $R < 1.5 r_{\text{vdW}}$ likely due to the presence of a repulsive barrier on the income collision channel (see text) and for $R > 1.5 r_{\text{vdW}}$ due to the decrease of the hyperradial inelastic couplings with R [27].

Three-body model for ^{85}Rb atoms

Our three-body calculations for ^{85}Rb atoms were performed using the adiabatic hyperspherical representation [29, 149] where the hyperradius R determines the overall size of the system, while all other degrees of freedom are represented by a set of hyperangles Ω. Within this framework, the three-body adiabatic potentials U_α and channel functions Φ_α are determined from the solutions of the hyperangular adiabatic equation:

$$\left[\frac{\Lambda^2(\Omega)+15/4}{2\mu R^2}\hbar^2+\sum_{i<j}v(r_{ij})\right]\Phi_\alpha(R;\Omega)=U_\alpha(R)\Phi_\alpha(R;\Omega), \tag{5.1}$$

which contains the hyperangular part of the kinetic energy, expressed through the grand-angular momentum operator Λ^2 and the three-body reduced mass $\mu = m/\sqrt{3}$. To calculate the three-body recombination rate we solve the hyperradial Schrödinger equation [149],

$$\begin{aligned}\left[-\frac{\hbar^2}{2\mu}\frac{d^2}{dR^2}+U_\alpha(R)\right]F_\alpha(R)&\\ +\sum_{\alpha'}W_{\alpha\alpha'}(R)F_{\alpha'}(R)&=EF_\alpha(R),\end{aligned} \tag{5.2}$$

where α is an index that labels all necessary quantum numbers to characterize each channel, and E is the total energy. From Eq. (5.2) we determine the S-matrix and the recombination rate L_3 [149]. In this present study, the interaction between ^{85}Rb atoms is modeled by a potential similar to that used in Ref. [158], and given by a modified Lenard-Jones potential,

$$v(r)=-\frac{C_6}{r^6}\left(1-\frac{\lambda^6}{r^6}\right)-\left(\frac{C_8}{r^8}+\frac{C_{10}}{r^{10}}[f_\lambda(r)]^2\right)[f_\lambda(r)]^{12}, \tag{5.3}$$

where $C_6 = 4710.431E_h a_0^6$, $C_8 = 576722.7E_h a_0^8$, and $C_{10} = 75916271E_h a_0^{10}$, are the van der Waals dispersion coefficients from Ref. [139]. Here, $f_\lambda(r) = \tanh(2r/\lambda)$ is a cut-off function that suppresses the divergence of the C_8 and C_{10} interaction terms for vanishing interatomic distance r. We can adjust the value of λ to have different numbers of diatomic bound states supported by the interaction, while still reproducing the value of the background scattering length $a_{\rm bg} = -443a_0$ [25]. Our calculations were performed using $\lambda = 20.72577414766491a_0$, producing 9 s-wave ($L_R = 0$) bound states, and a total of 101 bound states including higher partial-wave states, $L_R > 0$. Our numerical calculations for three-body recombination through the solutions of Eq. (7.1) have included up to 200 hyperspherical channels leading to a total rate converged within a few percent. The calculated total recombination rate constant at 0.8 μK (including thermal averaging) is $L_3 = 3.07 \times 10^{-25}$ cm^6/s and is consistent with the values found in Ref. [120].

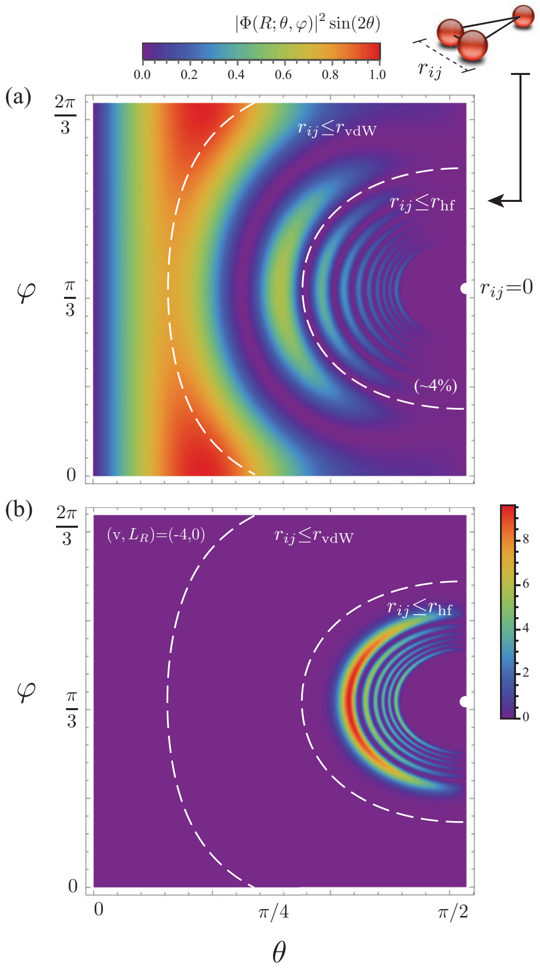

FIGURE 5.7: Hyperangular probability density, $|\Phi_\alpha(R;\theta,\varphi)|^2\sin(2\theta)$ [150], at $R = 1.593r_{\rm vdW}$ for the initial collision channel (a) and the molecular product state $(\mathrm{v},L_R) = (-4,0)$ (b). A point on the θ-φ hyperangular plane specifies the geometry of the three-atom system. The regions within the circles marked by dashed lines, correspond to geometries for which two of the atoms are found at distances $r_{ij} \leq r_{\rm vdW}$ and $r_{ij} \leq r_{\rm hf}$, respectively, while the third atom is further away.

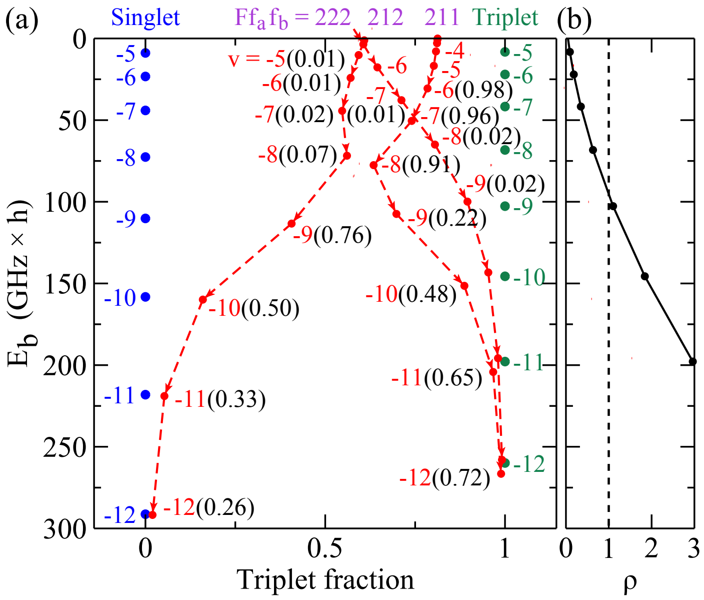

FIGURE 5.8: (a) Binding energy and spin character of weakly-bound ^{87}Rb$_2$ molecules for various vibrational quantum numbers v $= -1$ to -12 at $B = 0$ (red circles). Here, $L_R = 0$, $F = 2$, and $m_F = -2$. Zero energy corresponds to two separated atoms in state $f_a f_b = 11$. The spin character is given as the norm of the spin triplet component. Shown are the three spin families with $F = 2$ which correlate with the states $F f_a f_b = 222, 212, 211$ at the $E_b = 0$ threshold. Red dashed arrows are guides to the eye and indicate the change of each family's spin character with increasing binding energy. The norm of the 211 spin component is presented in parentheses. Blue and green circles are the bound state levels of the pure singlet and triplet potentials, respectively. The dissociation limit of these two potentials is at $E = +8.543\,\text{GHz} \times h$ above $E_b = 0$. (b) shows the ratio ρ for various binding energies.

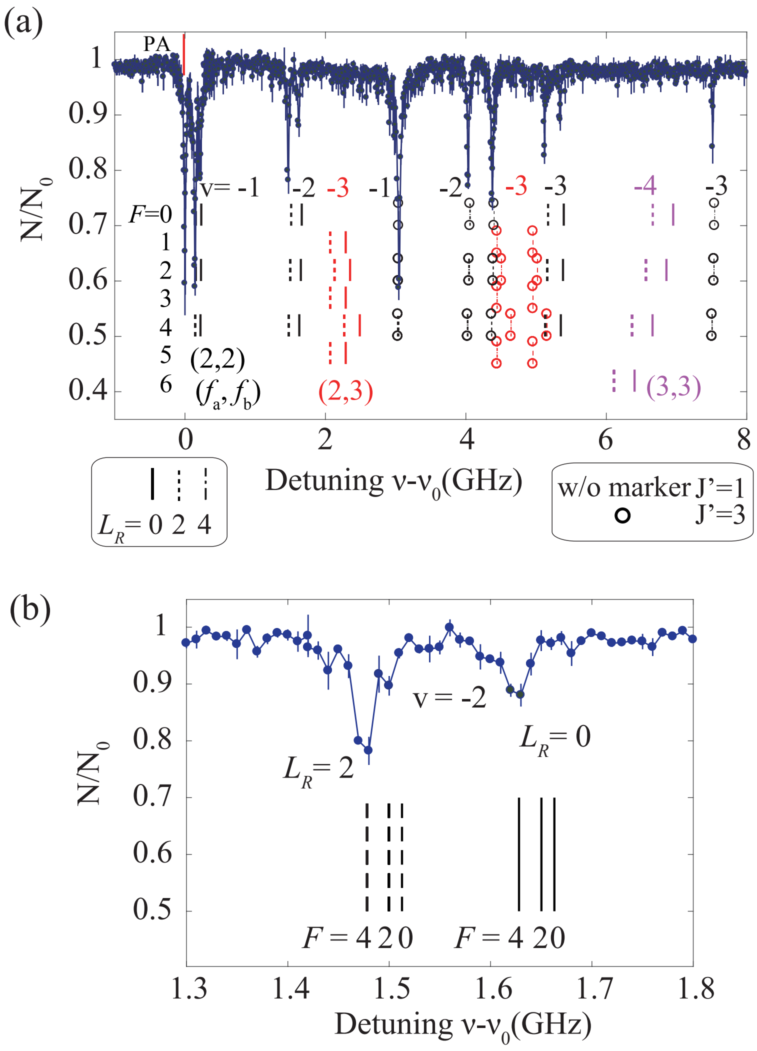

FIGURE 5.9: (a) REMPI spectrum of Fig. 5.1(b) for small REMPI laser detunings $\nu - \nu_0$ between about zero and 8 GHz (path (S) via intermediate state $(2)^1\Sigma_u^+$, v$' = 22$). Vertical lines represent calculated resonance positions for product molecules of spin families with $f_a f_b = 22$ (black), $f_a f_b = 23$ (red) and $f_a f_b = 33$ (purple). Each of the bound states with different F (from 0 to 6) is separately plotted in the vertical direction. Negative numbers above the calculated bound state positions indicate vibrational quantum numbers. (b) Further zoom into the spectrum for REMPI laser detunings $\nu - \nu_0$ between 1.3 and 1.8 GHz. Here, the black vertical lines correspond to the predicted resonance positions for product molecules characterized by $F, f_a = 2, f_b = 2$ with $F = 0, 2, 4$.

In order to gain more insight on how three-body recombination occurs within the hyperspherical representation we introduced an artificial hyper-radial hard-wall at $R = R_{\mathrm{hw}}$ and performed recombination calculations for various values of R_{hw}. The hard-wall prevents any flux into the range $R < R_{\mathrm{hw}}$ and therefore reactions in this range are not possible. By analyzing how the total and partial reaction rates change as a function of R_{hw} one can infer at what hyperradii R reactions dominantly occur. Figure 5.6 shows the total rate L_3 (black solid line) and the partial rates for some of the currently observed molecular states, (v, L_R) = (-1,2), (-1,0), (-2,6), (-2,4), (-2,2) and (-2,0). This particular calculation was performed with a two-body interaction model (Eq. 5.3) supporting 5 s-wave bound states in order to reduce some numerical instabilities associated with the hard-wall interaction. The figure clearly indicates that recombination is most likely to occur at $R \approx 1.5 r_{\mathrm{vdW}}$. For $R_{\mathrm{hw}} < 1.5 r_{\mathrm{vdW}}$ the partial rates are affected by interference effects related to the different collision pathways three atoms can follow to form a molecule [29]. Interference effects can be seen as the fast oscillations on the partial rates in Fig. 5.6. For $R > 1.5 r_{\mathrm{vdW}}$ partial rates are increasingly suppressed due to the decrease of the inelastic couplings with R [27]. The peaking of the reaction rates at around $R \approx 1.5\, r_{\mathrm{vdW}}$ in Fig. 5.6 can be explained as a consequence of a repulsive barrier in the hyperspherical effective potential of the entrance channel at $R \approx 1.7 r_{\mathrm{vdW}}$. Such a barrier was first identified in Ref. [150] where it occurred at $R \approx 2 r_{\mathrm{vdW}}$ for $a = \pm\infty$.

We now analyze the geometric characteristics of the three-atom system near the region where recombination is most likely to occur in order to identify which type of coupling is dominating the inelastic transitions. Figure 5.7 shows the hyperangular probability density at $R = 1.593 r_{\mathrm{vdW}}$ in terms of the hyperspherical channel functions Φ_α and hyperangles θ and φ as: $|\Phi_\alpha(R;\theta,\varphi)|^2 \sin(2\theta)$ (see Ref. [150]). Each point in the θ-φ hyperangular plane corresponds to a specific geometry of the three-atom system. In particular, the regions within the dashed half-circles represent geometries where two of the atoms are found at a distance $r_{ab} \leq r_{\mathrm{vdW}}$ and $r_{ab} \leq r_{\mathrm{hf}}$, respectively, and the third atom remains at distances $r_{ca}, r_{cb} > r_{\mathrm{hf}}$ (i.e., $r_{ci} \geq 0.71 r_{\mathrm{vdW}}$ and $r_{ci} \geq 1.2 r_{\mathrm{vdW}}$, respectively). In Fig. 5.7(a) we show the probability density for the initial collision channel, which indicates that the most likely configuration is where all three atoms are located at distances typically larger than r_{hf}. In contrast, the probability density for the target molecular states is pronounced inside the small circle. As an example, Fig. 5.7(b) shows the probability density for $(\mathrm{v}, L_R) = (-4, 0)$. In order to produce this state, the two atoms forming the bound state obviously need to be closer than r_{hf} and the third atom is at interparticle distances $r_{ci} > r_{\mathrm{hf}}$. For a spin flip to happen during the reaction, the two atoms forming the molecule must be at a distance $r_{ab} < r_{\mathrm{hf}}$ and the wavefunctions of either the two-body scattering state or the two-body target bound state must have a sizeable spin admixture. In the range of binding energies discussed here for ^{85}Rb these admixtures are on the %-level and therefore quite small. The admixtures are not shown in

Fig. 5.7.

Characteristics of collisions at large distance

The interaction between two Rb atoms is effectively spin-independent for interparticle distances $r_{ij} \equiv |\vec{r}_i - \vec{r}_j| \gtrsim 0.25 r_{\mathrm{vdW}}$. This is because at these distances the exchange splitting between the electronic singlet and triplet ground state potentials is smaller than the atomic hyperfine splitting $E_{\mathrm{hf}} = 3.04\,\mathrm{GHz} \times h$. As a consequence the atomic hyperfine states are only weakly perturbed by the exchange interaction and therefore essentially remain eigenstates in this realm. In other words the exchange interaction is not strong enough to decouple the atomic hyperfine spins and flip them.

Next, we consider the low-energy collision of two $f = 2, m_f = -2$ Rb atoms, corresponding to the channel $F f_a f_b = 422$. At vanishing magnetic field and neglecting dipolar relaxation processes, F and m_F are conserved throughout the collision. At a close enough distance $< 0.25 r_{\mathrm{vdW}}$ spin exchange interaction, however, can admix the spin states $F f_a f_b = 423, 433$ (For an overview of all spin channels of two colliding ground state ^{85}Rb atoms see [78].). Interestingly, this admixture is restricted to distances $r_{ab} < r_{\mathrm{hf}} \approx 0.6 r_{\mathrm{vdW}}$ due to energetic closure of the $f_a f_b = 23, 33$ scattering channels at larger distances. For $m_F = -4$, the channel $F f_a f_b = 422$ is the lowest in energy. The hyperfine distance $r_{\mathrm{hf}} = (C_6/E_{\mathrm{hf}})^{1/6}$ is the distance at which the potential curve of channel $f_a f_b = 23$ crosses the collision energy (which approximately corresponds to the asymptotic energy of the 422 channel). This crossing is also relevant in another regard. It effectively limits the size of molecular bound states of the spin channels $f_a f_b = 23, 33$ which are energetically located below the $F f_a f_b = 422$ entrance channel to be $\lesssim r_{\mathrm{hf}} \approx 0.6 r_{\mathrm{vdW}}$.

We now consider a three-body collision of three $f = 2, m_f = -2$ atoms and assume the hyperradius to be $R > 1.1 r_{\mathrm{vdW}}$. Using the expression $R^2 = (\vec{r}_b - \vec{r}_a)^2/d^2 + d^2(\vec{r}_c - (\vec{r}_a + \vec{r}_b)/2)^2$, where $\vec{r}_i$ is the location of particle i and $d^2 = 2/\sqrt{3}$ [29], we calculate that for $R > 1.1 r_{\mathrm{vdW}}$ at least one of the three atoms, say c, has distances r_{ca}, $r_{cb} > 0.6 r_{\mathrm{vdW}}$ from both other atoms. This is outside the distance range $r_{ca}, r_{cb} < r_{\mathrm{hf}} \approx 0.6 r_{\mathrm{vdW}}$ for atom c to exhibit a spin admixture. Therefore, atom c should have a pure spin state $f = 2, m_f = -2$, even if it had possibly undergone spin exchange interaction in a previous collision with one of the other two atoms. Reciprocally, we can conclude that the two other colliding atoms a and b must be in the collision channel $F f_a f_b = 422$. Thus, at a hyperradius $R > 1.1 r_{\mathrm{vdW}}$ the three-body system can be effectively decomposed (with respect to spin) into a two-body collision of two $f = 2, m_f = -2$ atoms and a third atom which is spin-wise only a spectator.

Spin composition of ^{87}Rb$_2$ molecules

Figure 5.8 shows the binding energy and the spin composition of weakly-bound ^{87}Rb$_2$ molecules. For ^{87}Rb$_2$ the ratio ρ is given by $\rho = |E_\mathrm{T}(\mathrm{v}) - E_\mathrm{S}(\mathrm{v})|/E_\mathrm{hf}$. It becomes > 1 for binding energies $E_b \gtrsim 100\,\mathrm{GHz} \times h$. Around $\rho = 1$ a major change in the spin composition of the spin families occurs.

Tests of the spin propensity rule

In the spectra of Fig. 5.1 and Fig. 5.4 we showed that our observed lines match with the calculated positions of molecular states with $Ff_af_b = 422$. For the sake of completeness we show here with a few examples, that our data do not match with the calculated spectra of other spin families. Figure 5.9(a) shows a section of the spectrum in Fig. 5.1(b) together with calculated positions for product molecules with $f_af_b = 23$ and 33. The positions are indicated by vertical red and purple lines, respectively. Each of the bound states with different F (from 0 to 6) is plotted separately in vertical direction. Clearly, there is no convincing match between these and the experimental lines within the detection limit. The observed lines only match calculated resonance frequency positions for molecules with $Ff_af_b = 422$. In Fig. 5.9(b) we zoom in further into the spectrum shown in Fig. 5.9(a) and check for molecules with $Ff_af_b = 022$ and $Ff_af_b = 222$. Again, the observed signals only match in a convincing way for $Ff_af_b = 422$.

Chapter 6

Controlling reaction pathways by coupling of product channels

6.1 Introduction

Controlling chemical reactions at the quantum level has been a central goal in quantum chemistry. In cold chemical reactions, reactants evolve into product states through quantum dynamical processes, often exhibiting remarkable complexity even in the simplest systems. During a typical collision, the collision complexes experience quantum interference effects which can significantly influence the reaction pathways and determine the resulting product channels. Recent advancements in the manipulation and detection of ultracold molecules have elevated the field to the realm of state-to-state chemistry, enabling precise experimental investigations and unlocking new possibilities for steering chemical reaction outcomes [6, 20, 56, 61, 93, 94, 108, 135]. In Figure 6.1, we schematically illustrate a chemical reaction. In this simplified scheme, the chemical reaction starts with a single incoming entrance channel and can possibly end in many exit channels. Each exit channel is then assigned a reaction flux, which indicates how often the chemical reaction ends in that particular exit channel. Entrance and exit channels correspond to eigenstates at large distances. To actively control the chemical reaction, one must find ways to steer the reaction flux between the exit channels or to open (close) exit channels. In 6.1(a), we consider the case of independent exit channels which means that there are no links between exit channels. One possible idea now to redirect the reaction flux is to couple reaction exit channels. This implies that the reaction flux can be diverted or split between the channels which is illustrated in Fig. 6.1(b). In this example, the coupling can lead to reaction flux to an exit channel which was not connected to the entrance channel by any pathway without coupling, see Fig. 6.1(a). Exit channels can be coupled due to a variety of different interactions: states can be coupled optically using laser light or via a RF field and there are couplings such as the spin-orbit interaction in molecules.

In this chapter, I present a novel approach for controlling the outcome of chemical few-body reactions. In particular, we manipulate the distribution

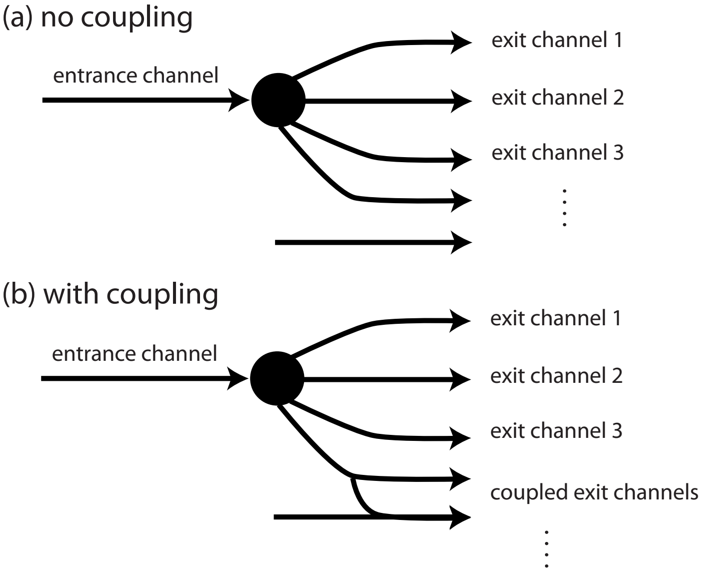

FIGURE 6.1: Schematic of a chemical reaction. In this simplified picture, the chemical reaction begins with an entrance channel and can end in many possible exit channels. Each of these reaction pathways can be associated with a reaction flux, which indicates with what probability the chemical reaction concludes in a specific exit channel. We consider no coupling between exit channel e.g. there are no links between the exit channels in (a). However, if we consider couplings between the exit channels, it would correspond to paths between exit channels.

of reaction flux between two distinct diatomic molecular product states during the recombination of three ultracold atoms. We exploit the fact that the two product states are coupled via an electronic exchange interaction. The coupling can be tuned onto resonance so that the degree of coherent mixing of the two states can be precisely tuned over a large range.
In the following part, I explain the experimental methods which have been used. The applied control scheme is further explained in Sec. 6.3 and in Sec. 6.4 we present experimental data which demonstrates the control scheme and compare it with numerical calculations.

6.2 Experimental methods

Preparation of atomic samples

The experiments are carried out with an ultracold gas of ^{87}Rb atoms which are spin-polarized in the hyperfine state $f = 1, m_f = -1$ of the electronic ground state $5S_{1/2}$ and trapped in a far-detuned optical dipole trap at 1065 nm. Typically, we prepare around 3×10^6 atoms with a density of $7-9\times10^{13}\text{cm}^{-3}$ and a temperature of approximately 800nK by using common techniques such as laser cooling and evaporative cooling. The trap frequencies of our optical dipole trap are $(w_x, w_y, w_z) = 2\pi \times (156, 148, 30)$ Hz.

Three-body recombination

In the atomic cloud, three-body recombination spontaneously occurs, preferentially producing weakly bound molecules within the coupled $X^1\Sigma_g^+ - a^3\Sigma_u^+$ molecular complex [56, 158]. This reaction is characterized by a broad product population distribution, meaning that a wide range of molecular states are populated [51, 56, 57, 158].

Detection of molecules by using REMPI

After the reaction, we state-selectively detect the produced molecular states by using resonance-enhanced multiphoton ionization (REMPI). A continuous-wave (cw) laser with a wavelength of 598 nm is used for the one-color two-photon REMPI process. The typical power is around 110 mW with a beam diameter of approximately 100 μm, the laser frequency uncertainty is estimated to be about $\pm$ 5 MHz. In the first step, molecules are excited to the intermediate molecular level $(2)^1\Sigma_u^+$, $\nu = 36$, $J' = 3$ or 5 via a first photon. Subsequently, a second identical photon ionizes the molecule which is trapped in a linear Paul trap. Once an ion is stored in our linear Paul trap, we can detect it with nearly 100% efficiency. When ions are produced and detected within the same atomic cloud, the signals exhibit larger particle number fluctuations due to the highly dynamic and complex nature of simultaneous ion production and detection. To mitigate this, we prepare a fresh atomic cloud with a low average density ($\bar{n} \sim 1 \times 10^{13}\,\mathrm{cm}^{-3}$), spatially overlapping it with the previously produced ions for 500 ms. Elastic collisions between ions and neutral atoms cause characteristic atom losses, which are measured via absorption imaging. Using an independent calibration, these atom losses are converted into ion numbers. This method reliably measures ion numbers up to 5 and is explained in the following section.

Calibration of ion numbers

In an independent measurement, a well-defined number of laser-cooled $^{138}\mathrm{Ba}^+$ ions are loaded into the Paul trap. The number of ions can be precisely counted using fluorescence imaging. In the next step, the ions are immersed into a rubidium cloud. Due to chemical reactions such as charge exchange, Barium ions are converted almost exclusively to Rb^+ or Rb_2^+ ions but the total number of ions remains constant. Next, a dilute detection cloud is prepared and atoms and ions are overlapped in the center of the Paul trap. Atomic losses due to elastic collisions are measured via absorption imaging as a function of the collision time t_c and for different number of initially prepared ions, see Fig. 6.2(a). From this figure, it becomes clear that different ion numbers can be distinctly differentiated as long as the number of ions is not significantly higher than 5. Using an empirical fitting curve, the relationship between ion count and remaining atom number after $t_c = 500\,\mathrm{ms}$ is described by the function $N_a = (N_i/a + b)^c$, where $a = 0.5055$, $b = 1.324$, and $c = -0.2093$. This function is later used in the experiment to convert the remaining particle numbers into the corresponding number of ions.

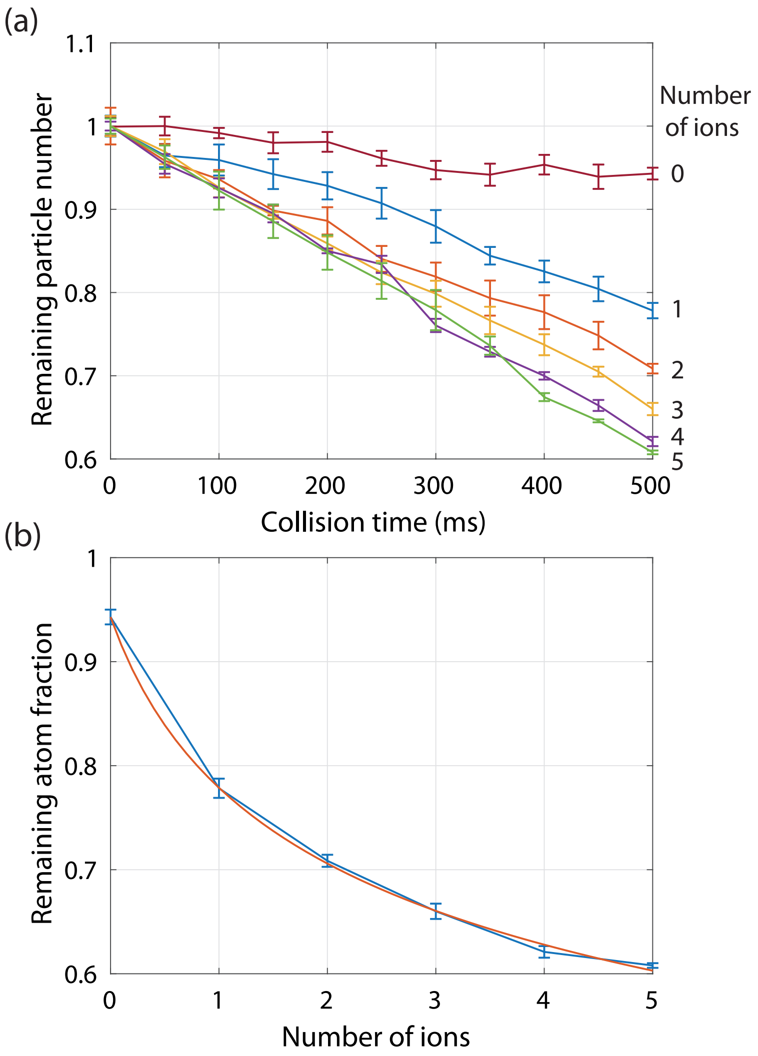

FIGURE 6.2: (a) The remaining atom fraction in the detection cloud after a collision time t_c for different number of ions. It enables a clear discrimination of the number of ions according to the remaining atom fraction after $t_c = 500\,\mathrm{ms}$. (b) The remaining atom fraction after $t_c = 500\,\mathrm{ms}$ for different number of ions. Our detection primarily uses the regime between 2 and 5 ions. For numbers higher than 5, the sensitivity of ion counting becomes lower which leads to larger uncertainties of the extracted ion numbers.

6.3 Control scheme for product channel mixing

Three-body recombination in our atomic cloud leads to the formation of molecules. We show a bound state spectrum for the most weakly bound molecular states in Fig. 6.3 up to a binding energy of 3 GHz x h. The figure presents the binding energy of the molecular states as a function of the magnetic field, with the asymptotic energy of the atomic scattering state ($f_a = 1, m_{fa} = -1 + f_b = 1, m_{fb} = -1$) chosen as the reference. The black lines correspond to molecular states that are dominantly populated by three-body recombination in our system which correspond to the $(F, f_a, f_b) = (2, 1, 1)$ molecular spin state. The reason for this is that the spin of the atoms forming the molecule tends to be conserved during the chemical reaction. We examined this in detail in Chapter 5 and we could observe this effect experimentally for rubidium [57]. The state depicted in gray, however, is practically not produced. The spin character of the gray molecular state is quite different from the spin of the entrance channel. Therefore, we expect a negligible reaction flux into this exit channel. The two molecular states highlighted in color (blue, orange) are special here because both molecular states are coupled, a mixing of the molecular spin state occurs. The mixing originates from the electronic exchange interaction and is enhanced by the nearly degenerate energy levels. In the experiment, we can tune this mixing by applying an external magnetic field which brings the molecular energy levels closer together. The relative reaction flux of both molecular product channels (orange, blue) at B = 0 G goes mainly to the blue molecular product state because of the strong overlap with the entrance channel of the reaction. This changes by applying the external magnetic field which decreases the spin overlap of the blue molecular product state with the entrance channel. Similarly, the orange product state can also be discussed. At $B = 0\,\mathrm{G}$, it exhibits a mainly a $(F, f_a, f_b) = (2, 2, 2)$ spin character, resulting in minimal overlap with the entrance channel. This can be modified via the magnetic field, such that at $B = 160\,\mathrm{G}$, the orange product state predominantly features a $(F, f_a, f_b) = (2, 1, 1)$ spin character. As a result, according to the spin conservation propensity rule, this state should become strongly populated.

The scheme allows control of the reaction flux between two exit channels. We experimentally demonstrate this control over the spin composition of the two molecular product channels using our state-selectively molecular detection methods. The results are discussed in the following section.

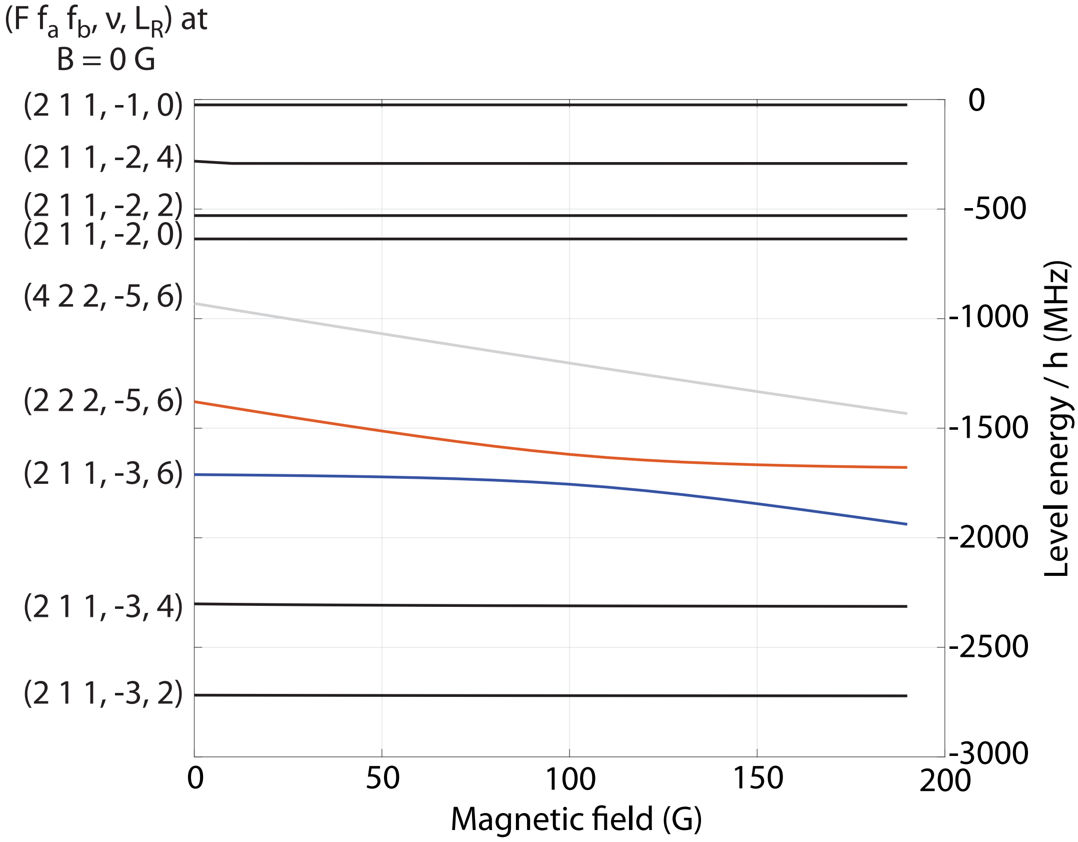

FIGURE 6.3: Molecular energy levels of molecules up to 3 GHz x h binding energy. The black lines represent molecular states predominantly populated after three-body recombination. The colored lines indicate the two molecular energy levels that are coupled and form an avoided crossing. For comparison, a gray energy level is also shown, which belongs to a different molecular spin-state and cannot be observed in our experiment.

6.4 Results and comparison with numerical calculations

We conducted REMPI spectroscopy of the two molecular states as a function of the magnetic field. Figure 6.4(a) presents coupled-channel two-body calculations (solid lines) with experimental data (symbols) showing the energy level positions of the two molecular product channels of the avoided crossing as a function of the magnetic field. The corresponding binding energy is extracted from the recorded spectra relative to the asymptotic level $(f_a = 1, m_{fa} = -1 + f_a = 1, m_{fa} = -1)$. In the following part, we will use the following labels for the molecular states: We name the state which is more deeply bound in the low magnetic field as lower state. The other - less deeply bound state - is called upper state. In Figure 6.4(b), we show spectroscopic recordings for B = 4, 80, 120, and 150 G. Each dip in a trace corresponds to a signal from a distinct molecular level. The REMPI signals are normalized, ranging from 0 to 1, as indicated by the vertical bar and additionally, the signals are vertically shifted for better visibility. The horizontal axis shows the relative frequency $\nu - \nu_0$ where ν is the frequency of the REMPI laser, ν_0 is the photoassociation transition frequency towards the intermediate state $(2)^1\Sigma_u^+$, v = 36, J′ = 1 at B = 4 G. For higher magnetic fields, we compensate for the Zeeman shift $(\nu_z = 1.4\frac{\text{MHz}}{\text{G}} \times B)$ of the reference state (which also corresponds to the Zeeman shift of the photoassociation line) to allow a better comparison of the spectra. The experimentally determined energy level positions have an uncertainty of approximately ±5 MHz, primarily due to the uncertainty of the laser frequency. In Fig. 6.4(b), the spectral range is selected to include possible signals from molecules in the two coupled product states and another state characterized by $(F, f_a, f_b = 2, 1, 1, v = -4, L_R = 4)$. We call this state in the following reference state which has a binding energy of approximately 7.1 GHz x h. In Fig. 6.4(a), the lower branch is well characterized by the state $(F, f_a, f_b = 2, 1, 1, v = -3, L_R = 6)$ in the low magnetic field limit. As already explained in Sec. 6.3, in the low-field regime, and in accordance with the spin-conservation propensity rule, we expect product molecules to be primarily formed in this molecular state. The upper state should remain essentially unpopulated. Our experiments at a magnetic field of $B = 4\,\text{G}$ (Fig. 6.4(b), lowest trace) clearly confirm this expectation. Additionally, we observe significant population in the reference state, which is also consistent with the spin conservation propensity rule because it exhibits a large overlap with the entrance channel. As the magnetic field is increased, and with it the spin mixing between the two product channels, molecular detection signals for the upper branch of the avoided crossing begin to appear, while the signal strength for the lower branch decreases (see the trace for $B = 80$ G in Fig. 6.4(b)). The mixing increases gradually as the resonance of the avoided crossing is approached (around $B = 110$ G). As the magnetic field is increased further, beyond the coupling resonance of the avoided crossing, the signal strength for the upper branch surpasses that of the lower branch.

This aligns with our expectations, as in the high-field limit, the upper state predominantly retains the spin characteristics of the initial scattering state. For all REMPI spectra in Fig. 6.4(b) across various magnetic fields, the signal strength of the reference state remains nearly constant. Notably, the reference state was detected via a different rotational level $J' = 3$ of the intermediate state, compared to $J' = 5$ for the avoided crossing branches. We also independently examined the reference state using the $J' = 5$ REMPI pathway and consistently observed similar signal strengths across various magnetic fields, see Fig. 6.5. We now proceed with a more quantitative analysis. Here, we conducted an additional set of experiments measuring the ion production rate for individual molecular states at the resonant REMPI laser frequencies (center positions of the dips in Fig. 6.4(b)). For this, we used the methods previously in Sections 6.2 and 6.2 discussed. Our results for the molecular-state-dependent ion production rates at different magnetic fields are presented in Fig. 6.6(a). The ion production rates of the ions are directly proportional to the number of molecules formed by TBR. The rates of the upper and lower strongly depend on the magnetic field and can be tuned by approximately an order of magnitude. In Fig. 6.6(b) we show numerical two-body calculations from Jinglun Li in our group based on coupled-channel Schrödinger equations and full Born-Oppenheimer potentials. Here P_{211} is the $|211\rangle$ spin-state component of a given molecular state $|\Psi_m\rangle$, defined by

$$P_{211} = \int |\langle 211|\Psi_m(\vec{r})\rangle|^2 \, d\vec{r}. \tag{6.1}$$

where the molecular wavefunction $\Psi_m(\vec{r})$ is normalized. The spin component P_{211} of the upper branch of the avoided crossing increases from nearly zero at low magnetic fields to over 0.8 at $B = 160\,\mathrm{G}$, while it decreases from approximately one to below 0.2 for the lower branch. The slopes of the corresponding ion production rates in Fig. 6.6(a) closely follow these trends qualitatively. This suggests that the product flux into the two branches of the avoided crossing is linked to the spin character of the individual branches.

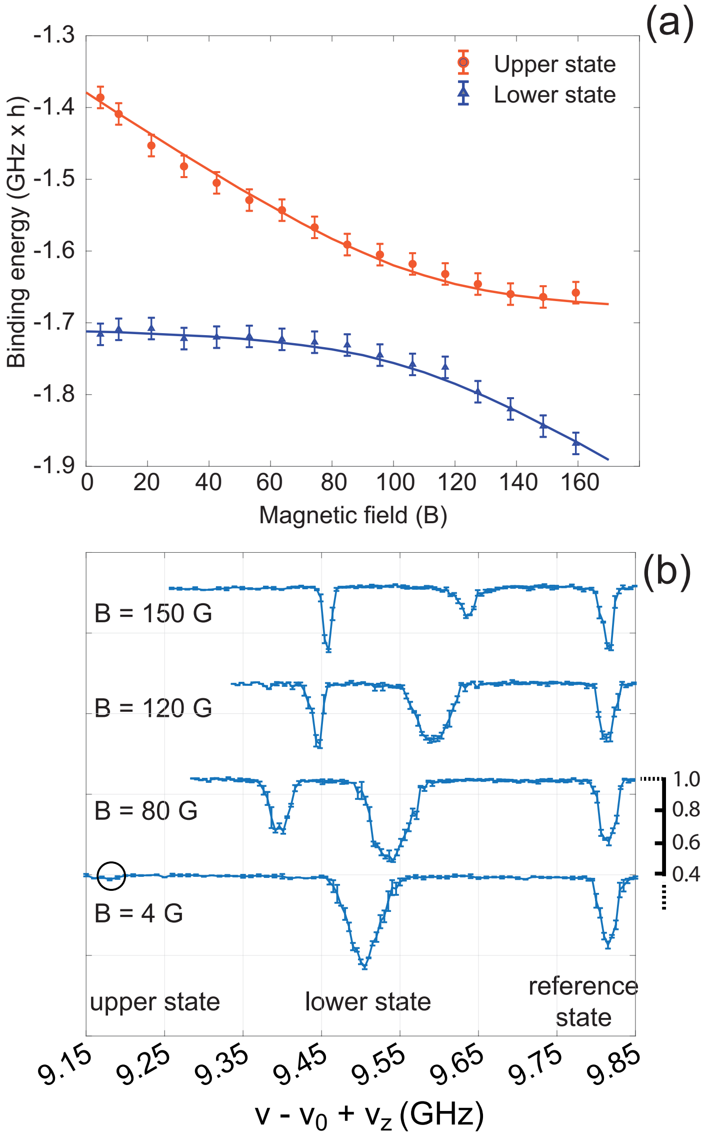

FIGURE 6.4: (a) Determination of the binding energy as a function of the magnetic field. The solid lines are calculated binding energies from the coupled-channel calculation and show a good agreement to the experiment. (b) REMPI spectra for four different magnetic fields. We show the normalized particle number as a function of the relative frequency $\nu - \nu_0 + \nu_z$ where $\nu_0 =$ 500.974420(30) THz is the position of the photoassociation transition towards the intermediate state $(2)^1\Sigma_u^+$, ν = 36, J′ = 1 at B = 4 G. For the spectra at higher magnetic field, we compensate the Zeeman shift $\nu_z = 1.4\frac{\mathrm{MHz}}{\mathrm{G}} \times B$ of the reference state (which also corresponds to the Zeeman shift of the photoassociation transition) allowing for a better comparison of the spectra. Three different molecular states are visible. The upper state belongs to $(F, f_a, f_b) = 2, 2, 2, v = -5, L_R = 6$ with $E_b \approx 1.38$ GHz x h at B = 4G and is barely visible (see black circle). The lower state $(F, f_a, f_b) = 2, 1, 1, v = -3, L_R = 6.$ with $E_b \approx 1.71$ GHz x h at B = 4 G is strongly populated.

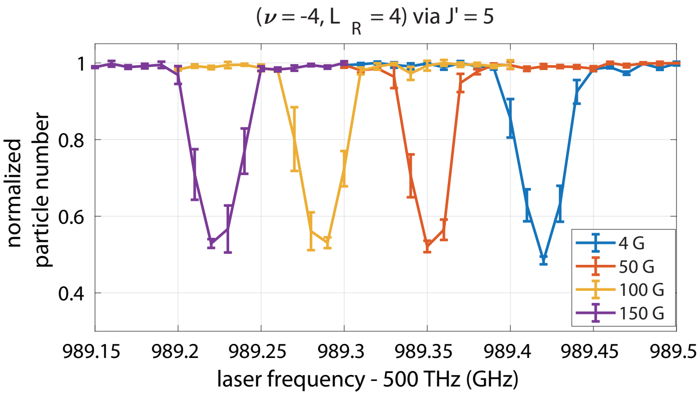

FIGURE 6.5: Detection of the reference state via different intermediate state J′ = 5 for different magnetic field B. Different colors indicate B = 0, 50, 100, 150 G. There is no significant change in the signal strength (particle loss) for different magnetic fields.

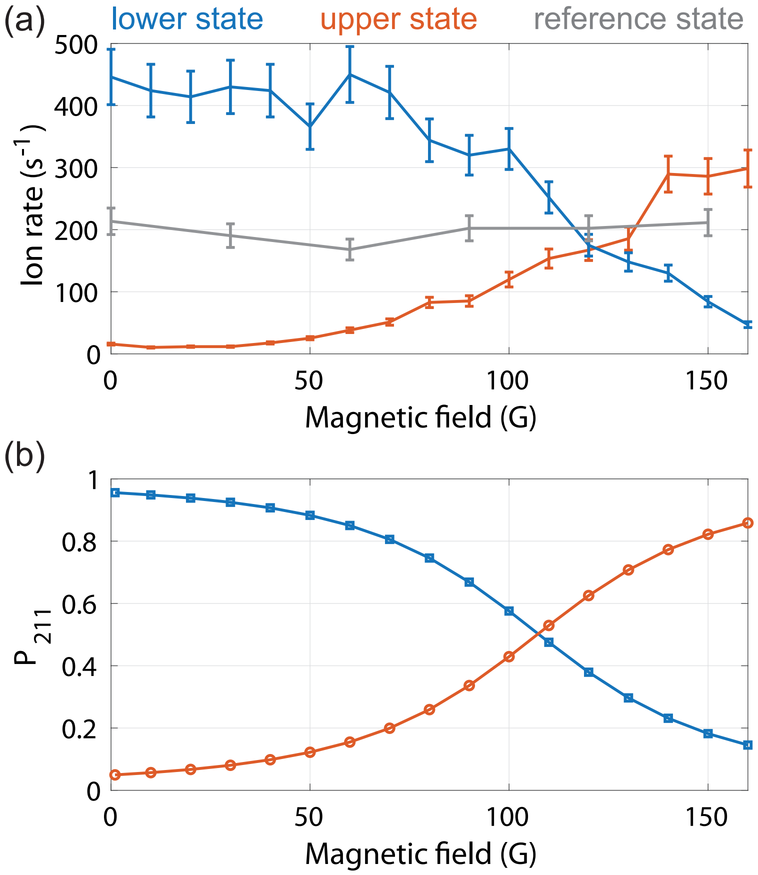

FIGURE 6.6: (a) Measured ion production rates for the three product states referred as upper state, lower state and reference. (b) Calculated molecular spin-component P_{211} on the (211) spin state for the upper and lower molecular state using two-body coupled channel Schrödinger equation with full molecular potentials.

6.4.1 Numerical three-body calculations

Furthermore, our theory collaborators José D'Incao and Jinglun Li conducted preliminary numerical three-body calculations, incorporating pairwise two-body interactions including spin effects and a limited number of bound states. The theoretical recombination partial rate coefficients L_3 in Fig. 6.7 are obtained by numerically solving the three-body Schrödinger equation in a hyperspherical coordinate representation [140, 149]. To properly describe the essential molecular spin mixing between the avoided crossing levels and its role in three-body recombination, the model contains the exact atomic spin structure as in our previous works [54, 90]. The interatomic interactions are taken as the pairwise singlet and triplet Born-Oppenheimer (BO) potentials from [139] with, however, the depth being restricted by adding a term of $C_6\lambda^6/r^{12}$. Here C_6 is the van der Waal dispersion coefficient and r denotes the internuclear distance. The short-range parameter λ is tuned to limit the number of s-wave bound states to 6 for both BO potentials and reproduce the low-energy scattering and bound-state properties of the original potentials [91]. The tuning procedure requires a slight shift of atomic hyperfine coupling as well. The construction of the shallower singlet and triplet potentials and their implementation in the three-body model in hyperspherical coordinate representation have been detailed in Ref. [91] and Refs. [54, 90], respectively. To briefly summarize, we use $\lambda = 25.89676a_0$ and $\lambda = 25.95295a_0$ for singlet and triplet potential respectively, while the atomic hyperfine coupling strength is reduced by a factor of 0.9026 [91]. The rest atomic and interaction parameters of the system shall take the realistic physical values. In our simulation, we restrict the spin state of the third atom in its initial state ($|f = 1, m_f = -1\rangle$) when the other two forming a molecule. This has been proved to be a very good approximation for Rb atoms in previous works [54, 56, 57, 90]. The calculated state-specific three-body recombination rate coefficients (see Fig. 6.7) for the two states of the avoided level crossing show qualitative agreement with the experimental results in Fig. 6.6(a). However, there is a notable quantitative deviation when comparing the ratios of the product fluxes between the two states. The relative variation of signal strength is more pronounced in the experiment (e.g. a increase in rate by a factor of 30 for the upper state) than predicted by the theory (here the upper state increases by a factor of 11). Interestingly, also the position where the molecular production rates cross, is shifted to higher magnetic fields in the experimental observation compared to the three-body calculations. However, for the two-body calculations using full potentials (see Fig. 6.6(b)), the position where the molecular states have a similar P_{211} component, fits better to the experimental results. It could be possible that this is one consequence of using potentials which are restricted in their depth.

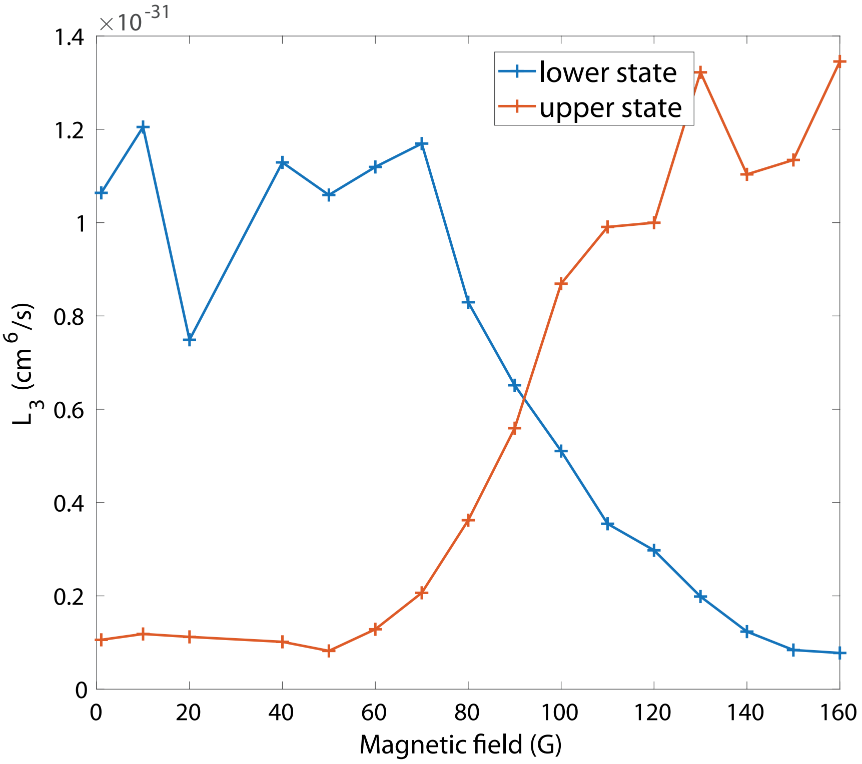

FIGURE 6.7: Calculated three-body recombination rate coefficients. The orange (blue) line corresponds to the upper (lower) state. The ratio of the production rates at B = 0 G is about 11 whereas we experimentally observed a ratio of about 30.

Chapter 7

Controlling few-body reaction pathways using a Feshbach resonance

The content of this chapter is published on the preprint server arXiv [54] and has been accepted for publication in Nature Physics.

The experimental part of this work was conducted in the BaRbIE lab under the supervision of postdoctoral researcher Shinsuke Haze. My contribution to this publication involved supporting lab work and assisting in the execution of the experiments as well as contributions to the writing of the manuscript.

Shinsuke Haze, Jinglun Li, Dominik Dorer, José P. D'Incao, Paul S. Julienne,
Eberhard Tiemann, Markus Deiß and Johannes Hecker Denschlag

"Controlling few-body reaction pathways using a Feshbach resonance",
DOI: https://doi.org/10.48550/arXiv.2408.14922, , reprinted with
permission from the authors.

This reprinted version of the work was adjusted to match the style of this doctoral thesis. Hence a consecutive numbering of figures and references for the whole thesis was applied as well.

Abstract

Gaining control over chemical reactions on the quantum level is a central goal of the modern field of cold and ultracold chemistry. Here, we demonstrate a novel method to coherently steer reaction flux of a three-body recombination process across different product spin channels. For this, we employ a magnetically-tunable Feshbach resonance to admix, in a controlled way, a

specific spin state to the reacting collision complex. This allows for the control of the reaction flux into the admixed spin channel, which can be used to significantly change the reaction products. Furthermore, we also investigate the influence of an Efimov resonance on the reaction dynamics. We find that while the Efimov resonance can be used to globally enhance three-body recombination, the relative flux between the reaction channels remains unchanged. Our control scheme is general and can be extended to other reaction processes. It also provides new opportunities in combination with other control schemes, such as quantum interference of reaction paths.

7.1 Introduction

A chemical reaction in a low-density gas phase is typically well-described by a fully coherent quantum mechanical evolution. Therefore, such a gas is a promising testbed for quantum control of chemical processes. In fact, recent platforms based on ensembles of ultracold atoms or molecules have paved the way for extended quantum mechanical steering of reactions. Demonstrated control schemes include the use of photoassociation [72, 88, 101], Feshbach resonances [24, 35, 60, 110, 153, 164], microwave-engineered collisions [2, 12, 22, 92, 163], electric-field-controlled reactions [99], relative positioning of traps [23, 118, 124, 167], confinement-induced effects [38, 49, 84, 102, 125, 145], quantum interference [93, 135], or rely on propensity rules and conservation laws [57, 65]. This progress has been further promoted by emerging technologies that enable state-to-state measurements (e.g. [64, 94, 122, 157, 158]).

A prominent tool for controlling chemical reactions is a tunable Feshbach resonance. A Feshbach resonance in atomic gases occurs when the energy of the scattering state of two colliding atoms is tuned into degeneracy with that of a molecular state, leading to the mixing of two such states [24]. As they offer unique control over the interparticle interaction, tunable Feshbach resonances have been essential for the development of the field of ultracold quantum gases. An established application of Feshbach resonances for chemical reactions is the controlled production of ultracold molecules. By magnetically ramping over a Feshbach resonance, ultracold pairs of atoms can be converted into an extremely weakly-bound molecule, the Feshbach molecule [24, 35, 39, 60, 143, 161]. In three-body recombination where three free atoms collide to form a diatomic molecule, Feshbach resonances have been used to tune the total molecular production rate and specifically to suppress atom loss [16, 71, 152, 160], and to demonstrate the Efimov effect [16, 29, 42]. Feshbach resonances and resonant scattering have also been proposed for controlling complex few-body reactions, see e.g. [61, 146].

7.2 Measurements and discussion

Here, we demonstrate the use of a Feshbach resonance in a three-body recombination process to steer reaction flux between families of molecular product channels with different spin states. More specifically, by tuning the magnetic field towards a Feshbach resonance we can gradually increase the initially negligible reaction rate into a specific spin channel, so that it becomes close to the total rate into all channels. The process is coherent and represents a novel tool for state-selective controlling of molecular production rates, using the applied magnetic field as a precisely tunable control knob.

The experiments are carried out with a 860 nK-cold cloud of about 2.5×10^5 ^{85}Rb atoms where each atom i is in the hyperfine state $(f_i, m_{f_i}) = (2, -2)$ of the electronic ground state. The atoms are confined in a far-detuned crossed optical dipole trap, for more details see Methods and [56]. In the atom cloud, three-body recombination spontaneously occurs, predominantly producing weakly-bound molecules in states of the coupled molecular complex $X^1\Sigma_g^+ - a^3\Sigma_u^+$. By tuning the magnetic field B in the vicinity of the s-wave Feshbach resonance at $B = 155\,\mathrm{G}$ [13, 78] we can control the product distribution of the molecules. For the details of the Feshbach resonance, see also Supplemental Materials. The molecules are state-selectively detected via resonance-enhanced multiphoton ionization (REMPI), see Methods for details.

Our scheme for controlling the reaction flux into different spin channels is illustrated in Fig. 7.1. In the three-body recombination process, the Rb atoms (a, b, c) collide and (a, b) form a molecule, see Fig. 7.1(a). In the particular reactions we study here, the third atom (c) is far enough away, so that it interacts with the atoms (a, b) merely mechanically and no spin flip between (c) and the pair (a, b) occurs [57]. Therefore, spin physics aspects of the reaction can be understood to a large extent in a two-body picture, where atom (a) collides with atom (b). At large internuclear distances the (a, b) scattering state has the hyperfine spin quantum numbers $(F, f_a, f_b, m_F) = (4, 2, 2, -4)$, where F denotes the total angular momentum of the molecule excluding rotation, and $m_F = m_{f_a} + m_{f_b}$ represents its projection. We denote this spin state by $|\uparrow\rangle$. At short internuclear distances the scattering state couples to an energetically near-by molecular bound level, giving rise to the Feshbach resonance. This level has the spin state $(F, f_a, f_b, m_F) = (4, 3, 3, -4)$ which we denote by $|\downarrow\rangle$ [1]. The coupling leads to an admixture of the $|\downarrow\rangle$ state to the initial scattering state with spin $|\uparrow\rangle$, and the strength of this admixture can be magnetically controlled. Next, in the mechanical collision with atom (c), the scattering state of (a, b) can transition into a molecular bound state. Due to angular momentum conservation, the spin state of the newly formed molecule must, however, have overlap either with the spin state $|\uparrow\rangle$ or with

---

[1] The level has the vibrational quantum number $\mathrm{v} = -3$ (counting down from the $f_a = f_b = 3$ atomic threshold, starting with $\mathrm{v} = -1$ for the last vibrational bound state) and has rotational angular momentum $L_R = 0$.

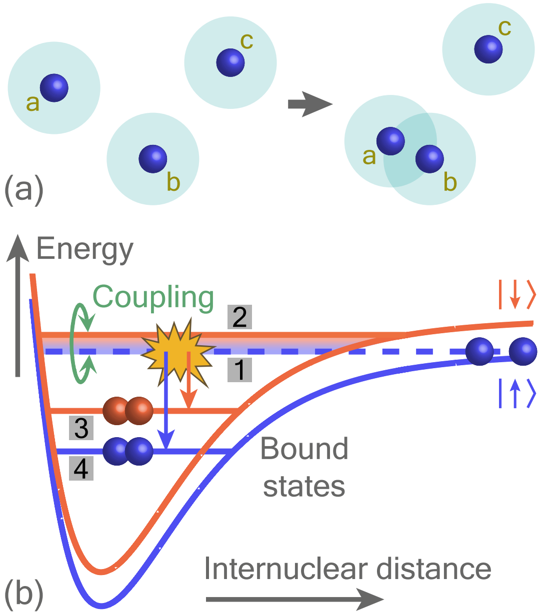

FIGURE 7.1: Scheme for controlling the reaction flux into different spin channels using a two-body Feshbach resonance. (a) Atoms (a, b, c) undergo three-body recombination, where (a, b) form a molecule. During this process, atom (c) is outside the ranges (cyan areas) for spin-exchange interaction with the other atoms. (b) Schematic representation of the Born-Oppenheimer potential energy curves for the atom pair (a, b). At close distance, the incoming scattering state (1) with spin $|\uparrow\rangle$ experiences admixing of the bound state (2) which has spin $|\downarrow\rangle$. Upon collision with the third atom (c) (not shown here) the scattering state can then relax into molecular bound states (3) or (4), with their respective spin states $|\downarrow\rangle$ and $|\uparrow\rangle$.

$|\downarrow\rangle$. In fact, by tuning the $|\downarrow\rangle$ admixture of the (a, b) scattering state we can control the reaction flux into molecular product channels with spin $|\downarrow\rangle$.

We now demonstrate this control scheme experimentally. Figure 7.2 presents REMPI spectra in a selected frequency range, showing signals from three different molecular product states. The spectra have been taken within a range of magnetic fields B between 4.6 G and 159.3 G. (Note the nonuniform step size of B.) ν represents the REMPI laser frequency and ν_0 is a frequency reference, see Methods. Each dip in a trace for a chosen B-field corresponds to a state-specific product molecule signal. Colored diamonds mark the known resonance positions predicted from coupled-channel calculations.

The molecular levels are labeled by their spin states ($|\uparrow\rangle$ or $|\downarrow\rangle$), and by their vibrational (v) and rotational (L_R) quantum numbers [78]. In Fig. 7.2 we observe one molecular state with spin $|\uparrow\rangle$ and two molecular states with spin $|\downarrow\rangle$. The resonance positions change in a characteristic way with the B-field due to the Zeeman effect. We use this as fingerprint information for identifying the molecular levels. The strength of each signal roughly reflects the

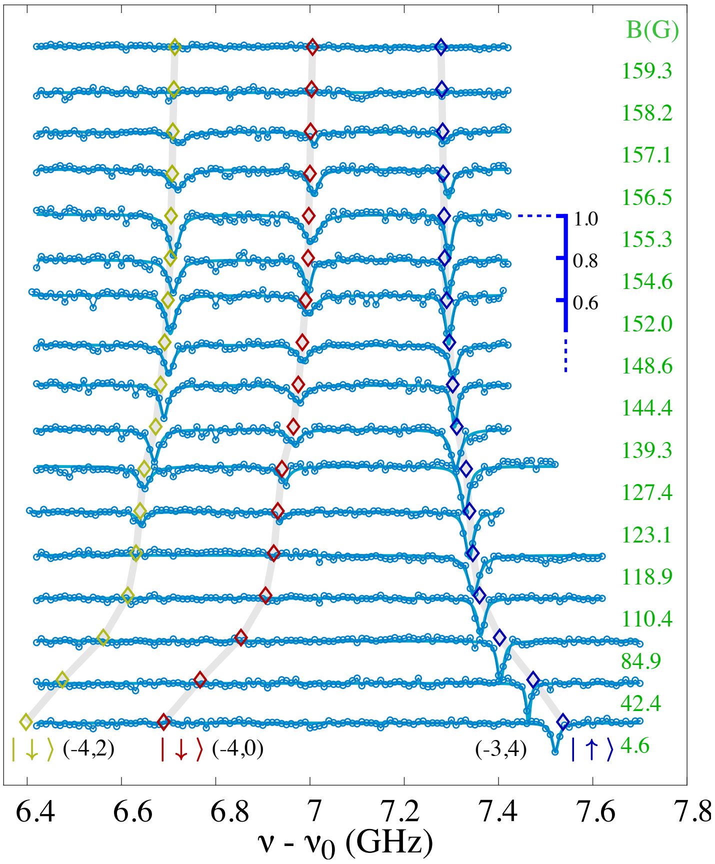

FIGURE 7.2: Observation of $|\uparrow\rangle$ and $|\downarrow\rangle$ molecules. Shown are REMPI spectra as a function of the REMPI laser frequency ν for various magnetic fields B. Here, $\nu_0 = 497603.591$ GHz. Each dip in a trace corresponds to a signal from a distinct molecular level. The REMPI signals are normalized, ranging from 0 to 1, as indicated by the vertical bar. The bar is valid for all data traces. The diamonds mark the theoretical positions of possible molecular signals and the colors indicate the spin state as well as the vibrational and rotational level (v, L_R). The faint color bands connecting the diamonds are guides to the eye. We note that the binding energy of the $|\uparrow\rangle$ level is smaller than that of the two $|\downarrow\rangle$ levels. In the shown spectra, however, the signal for $|\uparrow\rangle$ is at higher frequency ν since the intermediate rotational level for the REMPI is different, see also Methods.

recombination rate towards each respective state. In the magnetic field range up to about 120 G each REMPI spectrum exhibits only a single resonance dip which can be unambiguously assigned to the state $|\uparrow\rangle$. At about 120 G, two additional molecular signals start to appear stemming from molecular states in the spin state $|\downarrow\rangle$. The strengths of the signals of these states become similar to the $|\uparrow\rangle$ signals when approaching the Feshbach resonance at 155 G. For magnetic fields above the Feshbach resonance, all signals decrease very quickly within a few Gauss.

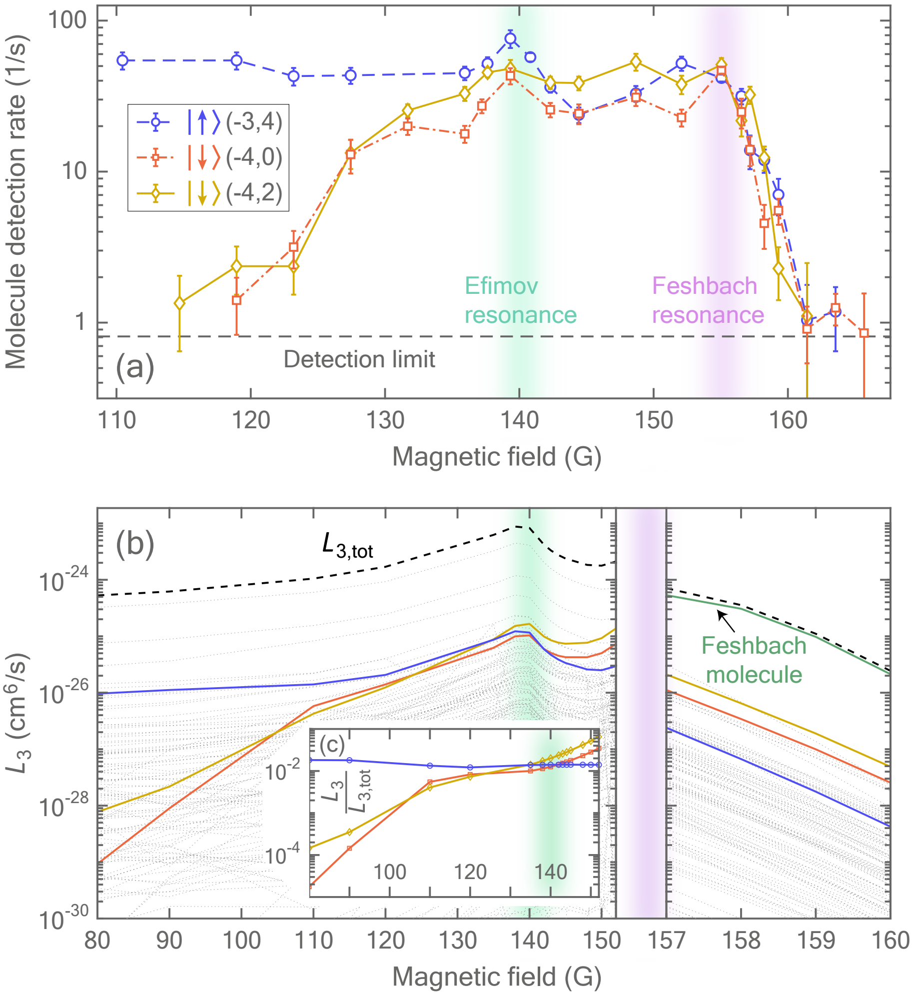

Figure 7.3: Opening up a product spin channel. (a) Molecule detection rates for three product states for which the quantum numbers $|\uparrow / \downarrow\rangle(\mathrm{v}, L_R)$ are given in the legend. The gray dashed line marks the experimental detection limit and the light-green and purple shaded areas indicate the position of the Efimov and Feshbach resonance, respectively. The error bars in the plot indicate one standard deviation (1σ). (b) Calculated three-body recombination rate coefficients. The black dashed line is the total rate coefficient $L_{3,\mathrm{tot}}$. Solid colored lines correspond to partial rates for the states under discussion. Gray lines correspond to other molecular states. No calculations are shown for $152\,\mathrm{G} \leq B \leq 157\,\mathrm{G}$, see text. We expect theoretical errors up to a few tens of percent for the partial rate for vibrational levels down to $\mathrm{v} = -4$, judging from when more vibrational states are included in our effective potentials [56]. (c) The normalized reaction rate coefficients $L_3/L_{3,\mathrm{tot}}$ do not exhibit a maximum at the Efimov resonance.

From our REMPI spectra, molecule detection rates for each observed molecular state are extracted. These rates are roughly proportional to the partial three-body recombination rates for the flux into individual product channels (see [56] and Methods). The obtained rates for the states in Fig. 7.2 are shown in Fig. 7.3(a) for the magnetic field region in the vicinity of the Efimov and Feshbach resonances, located at 140 G and 155 G, respectively.

The data show that the rates for the $|\downarrow\rangle$ states indeed strongly increase from below the detection limit (gray dashed line) to about a factor of 50 above the detection limit as the magnetic field is increased from $B < 115\,\mathrm{G}$ towards the Efimov resonance. The detection limit is mainly determined by the background noise of our REMPI scheme. By contrast, the rate for the $|\uparrow\rangle$ state is rather constant for all B-fields below the Efimov resonance. At the position of the Efimov resonance at 140 G we observe a clear enhancement of the rates for all molecular states. In fact, the signals for all three states attain similar strength, which demonstrates the large relative tuning range of our scheme. At this point the spin product channel $|\downarrow\rangle$ has been fully opened up for the reaction flux.

The relatively constant production rate for the $|\uparrow\rangle$ state below the Efimov resonance might be unexpected at first in view of the known a^4 scaling of the recombination rate in the limit of zero temperature [41, 153], where a is the scattering length. It can, however, be explained to a large extent as an effect of our finite temperature of 860 nK [28, 117], as further discussed below.

We carried out numerical model calculations for the partial rate coefficients L_3 for each molecular quantum state, using the adiabatic hyperspherical representation [21, 149, 160] (see Methods). This determines the partial recombination rate, $L_3(f) \cdot \int n^3 d^3r\,/3$, into a molecular state f, where n is the atomic density distribution. The calculations take into account thermal averaging of the partial rate constants. The results are shown in Fig. 7.3(b). The region from 152 to 157 G, i.e., the direct vicinity of the Feshbach resonance is excluded since the numerical calculations quickly become computationally highly demanding in this resonant regime.

Among all the possible molecular states produced by recombination (gray dotted lines), we highlight in color the molecular states under discussion. In addition, we present the total three-body recombination rate coefficient (dashed black lines).

Our calculations show that due to thermal averaging, the calculated recombination rate coefficient for the probed $|\uparrow\rangle$ state increases only moderately towards the Efimov resonance. For more details on how finite temperature affects the recombination rate coefficient, see Supplemental Materials. The increase of the theoretical curves is still faster than for the experimental data. This may be mainly explained by imperfections of the experiment. During the B-field ramp atoms are already lost due to three-body recombination and the sample slightly heats up. As a consequence, the density of the atom cloud sinks. In addition, the B-field ramp is not perfect, but tends to lag behind and to overshoot, which can lead to averaging out of signals. Furthermore, there could be a small variation in the REMPI efficiency as a function of magnetic field. These variations hamper a direct comparison between ion rates and L_3 coefficients.

Nevertheless, the main characteristics of the experimental data are qualitatively well described. For example, the observed sharp drop of the recombination rate above the Feshbach resonance is also clearly reproduced by the theory. The reason for this drop is the rapid decrease of the scattering length towards its zero crossing near $B = 166\,\mathrm{G}$ and the close-by minimum in L_3 due to Efimov physics [160, 168]. We note that above the Feshbach resonance the Feshbach molecular state appears (see dark-green solid line in Fig. 7.3(b)), and takes the main fraction of the total reaction flux.

Our calculations show that the effect of the Efimov resonance is to increase the partial three-body recombination rate coefficients with the same overall factor, not favoring particular product channels. This is evident from Fig. 7.3(b) where all partial rate coefficients exhibit a similar maximum at the location of the Efimov resonance. It also becomes manifest when normalizing the partial rate coefficients to the total rate coefficient (see Fig. 7.3(c)), as each maximum at the Efimov resonance disappears. The global enhancement is due to the fact that the Efimov resonance is a shape resonance which occurs in a single three-body adiabatic channel. As such, approaching the resonance increases the overall amplitude of the three-body scattering wavefunction at short distances where the reaction takes place, therefore, enhancing all the partial rates by the same factor [29]. Remarkably, near the Feshbach resonance we also find, both experimentally and theoretically, molecular products in spin states other than $|\uparrow\rangle$ and $|\downarrow\rangle$, as shown in Fig. 7.4. This points towards physics beyond the $|\uparrow\rangle$-$|\downarrow\rangle$ Feshbach mixing. In the experiments, these are molecular products with spins $(F, f_a, f_b) = (4,3,2)$ and $(5,3,2)$. In this notation, we omit m_F, as it is always $m_F = -4$. Thus, we observe product states where only one of the f_i has flipped, and where even the total angular momentum F can change. Following a similar analysis as used in Refs. [56, 57], the observation of such states can be understood as follows in terms of two-body physics. The spin state $(4,3,2)$ can be produced via two-body spin-exchange interaction at short distances, starting either from state $|\uparrow\rangle \equiv (4,2,2)$ or from $|\downarrow\rangle \equiv (4,3,3)$. Close to the Feshbach resonance the scattering wavefunction amplitude is strongly enhanced at short range and with it also the rate for spin-exchange. Producing the spin state $(5,3,2)$ is possible due to the presence of a finite B-field which breaks global rotational symmetry and couples different F quantum numbers. A $(5,3,2)$ state is typically energetically close to a corresponding $(4,3,2)$ state, such that coupling between them is resonantly enhanced.

In Fig. 7.4(a) and (b) REMPI spectra at magnetic fields of $B = 4.6\,\mathrm{G}$ and $B = 155\,\mathrm{G}$, respectively, are compared. The spectrum at high magnetic field exhibits many more resonance lines than the spectrum at low field. In a thorough analysis of the spectra, similarly as in Ref. [158], we identified a total

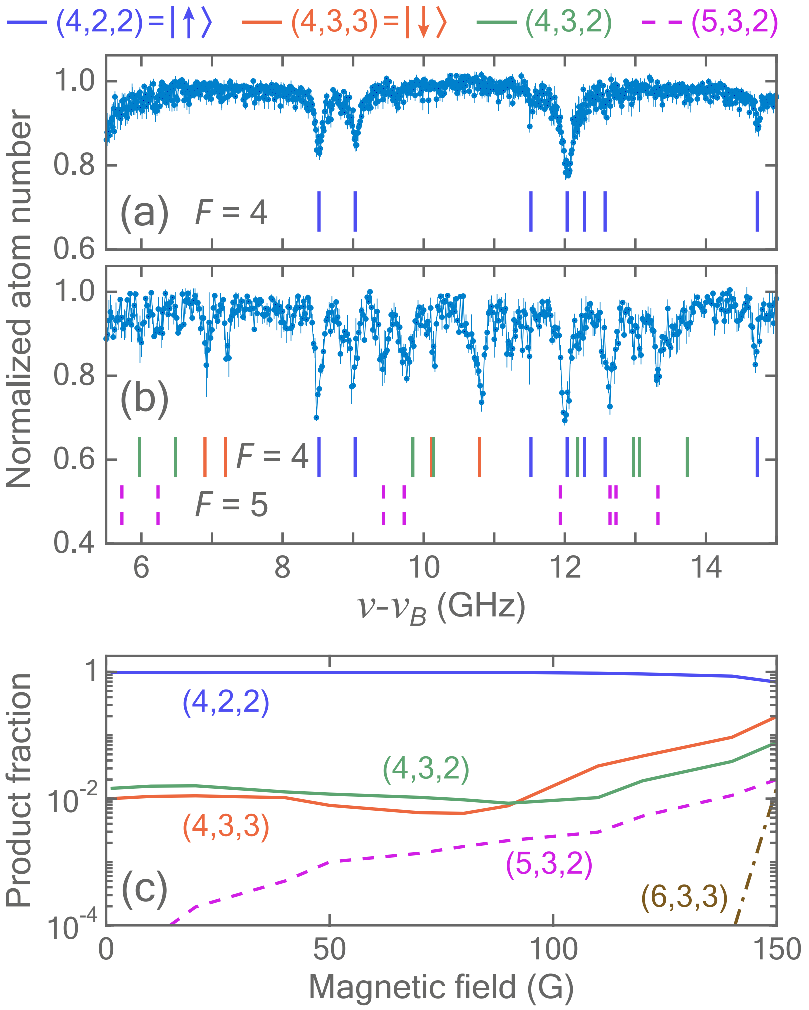

FIGURE 7.4: Spin families of molecular products. (a) and (b) Detection signals of product molecules of various spin families by REMPI spectroscopy at a magnetic field of $B = 4.6\,\mathrm{G}$ and $B = 155\,\mathrm{G}$, respectively. Vertical lines correspond to calculated resonance positions for molecular states assigned to spin families (F, f_a, f_b) according to the legend on top of the figure. The marked individual states have vibrational quantum numbers in the range from $\mathrm{v} = -1$ to -7 and rotational quantum numbers $L_R = 0, 2, 4$ or 6. The REMPI path is via a ${}^3\Pi_g$ intermediate state, see Methods. We have $\nu_B = \nu_0 = 497831.928$ GHz for (a) and $\nu_B = \nu_0 - 228$ MHz for (b). The 228 MHz shift compensates for the Zeeman shift, allowing for a better comparison of the two spectra. (c) Calculated, summed-up molecular product fraction for each spin family (F, f_a, f_b) as indicated next to the curves.

of four spin families for $B = 155\,\mathrm{G}$ and only a single one for $B = 4.6\,\mathrm{G}$. The individual spin states are marked with colored bars in Fig. 7.4(a) and (b).

Figure 7.4(c) shows our numerical calculations for the product fractions of the molecules in the different spin families (F, f_a, f_b) as a function of the external magnetic field B. Here, for each individual family we sum up the populations for all corresponding molecular states having the same spin characteristics. In agreement with our previous discussion, spin-exchange is strongly enhanced when approaching the Feshbach resonance. Furthermore, Fig. 7.4(c) reveals a hierarchy in the propensity for the production of spin states. Changing the total angular momentum F is more strongly suppressed than changing an atomic f quantum number, see also [90].

In summary, we have demonstrated a powerful scheme to control the reaction pathway in a three-body recombination process of ultracold atoms. Using a magnetically tunable Feshbach resonance we admixed a well-defined spin state to the reaction complex of three atoms and by this steered the reaction flux between the corresponding spin channels. We find that a large fraction of the total reaction flux can be redirected in this way. Furthermore, we show that in contrast to the Feshbach resonance an Efimov resonance only enhances globally the reaction rate, while maintaining the relative flux between reaction channels. We investigated our control scheme both experimentally and theoretically, using high-resolution state-to-state measurements and state-of-the-art numerical three-body scattering calculations, respectively.

The demonstrated reaction control holds large promise for general few-body reactions, as it is simple and can easily be extended. Feshbach resonances are ubiquitous in cold atomic and molecular gases. The scheme is fully coherent and can thus be used as a central building block in interferometric control, where the Feshbach resonance functions as a beam splitter for the incoming wave function. The split up parts can then potentially follow different pathways towards the same final product state where they interfere. For example, the final product state could have tunable spin-mixed character which can be set by further control methods such as state dressing with optical or microwave fields. In this way, additional tuning of the interference can be achieved.

Acknowledgements

This work was financed by the Baden-Württemberg Stiftung through the Internationale Spitzenforschung program (contract BWST ISF2017-061) and by the German Research Foundation (DFG, Deutsche Forschungsgemeinschaft) within contract 399903135. We acknowledge support from bwFor-Cluster JUSTUS 2 for high performance computing. J. P. D. also acknowledges partial support from the U.S. National Science Foundation, Grant No. PHY-2012125 and PHY-2308791, and NASA/JPL 1502690. S.H. also acknowledges support from Japan Science and Technology Agency Moonshot R&D Grant No. JPMJMS2063 and ASPIRE Grant No. JPMJAP2319.

Author contributions

S.H. and D.D. have carried out the experiments. J.L. and J.P.D. calculated the three-body recombination rate coefficients. J.H.D. supervised the project. All authors have contributed to the analysis of the experiment and to the writing of the manuscript.

Competing interests

The authors declare no competing interests.

7.3 Methods

Preparation of ultracold atomic sample

The experimental sequence starts with capturing ^{85}Rb atoms in a magneto-optical trap. After a magnetic transport over 40cm the atoms are subsequently loaded into an optical dipole trap where evaporative cooling is performed. They are then transported to the center of the Paul trap via a moving 1D-optical lattice. At the final stage of the sample preparation, the atoms are confined in a far-detuned crossed-dipole trap formed by 1064 nm lasers. The trapping frequency is $\omega_{x,y,z} = 2\pi \times (156, 148, 18)$ Hz. The resulting atom cloud consists of a pure sample in $(f_i, m_{f_i}) = (2, -2)$ hyperfine spin state with the typical particle number of 2.5×10^5. The temperature of atoms is 860 nK. This temperature was chosen as it provided the strongest recombination signals at a reasonably cold temperature.

REMPI detection

In order to state-selectively detect the product molecules, we apply two-step resonance-enhanced multiphoton ionization (REMPI) with a cw-laser which has a linewidth of ≈ 1 MHz. The laser beam is roughly an equal mixture of σ- and π-polarized light. It has a power of 100 mW and a beam waist ($1/e^2$ radius) of 0.1mm at the location of the atom cloud. We use identical photons for the two REMPI steps at a wavelength around 602 nm. For Figs. 7.2 and 7.3 the intermediate REMPI states are levels of $(2)^1\Sigma_u^+$ with $J' = 3$ for $|\uparrow\rangle$ states and $J' = 1$ for $|\downarrow\rangle$ states [57], where J' represents the total angular momentum excluding nuclear spin. The $J' = 1$ and $J' = 3$ levels are split by 2.9 GHz. The photoassociation laser frequency towards the intermediate level $J' = 1$ is $\nu_0 = 497603.591$ GHz at $B = 4.6$ G. The binding energies of the experimentally observed molecular states in Figs. 7.2 and 7.3 are $4.7\,\text{GHz} \times h$ for $|\uparrow\rangle$, and span a range between 6.4 to $7.3\,\text{GHz} \times h$ for $|\downarrow\rangle$. Here, the binding energy is determined relative to the B-field dependent (4,2,2) threshold. For Fig. 7.4, the intermediate REMPI states are deeply-bound levels of

$(2)^3\Pi\ 0_g^+$ with $J' = 1, 3, 5$ [57]. Here, $\nu_0 = 497831.928$ GHz is the photoassociation frequency towards $J' = 1$ at $B = 4.6$ G. The binding energies of the molecular states observed in Figs. 7.4 (a) and (b) span a range between 0.6 and 12.6 GHz × h. Again, the binding energy is determined relative to the (4,2,2) threshold. In general, the Zeeman effects of our intermediate states are negligible compared to the ones of the ground state. We make an effort to ensure that the REMPI efficiencies are similar for the states that we probe, also at various magnetic fields, but a precise calibration of the REMPI efficiency has not been done yet. We note that the first REMPI step is generally not saturated.

When ions are produced via REMPI, they are directly trapped and detected in an eV-deep Paul trap which is centered on the atom cloud. Elastic atom-ion collisions inflict tell-tale atom loss while the ions remain trapped. From the atom loss which is measured via absorption imaging of the atom cloud the ion number can be inferred, for details see [57]. From the ion numbers and the interaction time we obtain an ion production rate (i.e. the molecular detection rate) which is generally proportional to the state-selective molecular production rate and the three-body recombination loss rate constant.

Model calculations

Our numerical simulations use the adiabatic hyperspherical representation approach where the coordinates of three particles are given in terms of the hyperradius R for the overall size of the system and a set of hyperangles Ω for the internal motion [21, 140, 149, 160]. The three-body Schrödinger equation is solved by adiabatically separating the hyperradial motion

$$\begin{aligned}\left[-\frac{\hbar^2}{2\mu}\frac{d^2}{dR^2} + U_\nu(R)\right] F_\nu(R)\\ + \sum_{\nu'} W_{\nu\nu'}(R)F_{\nu'}(R) = EF_\nu(R),\end{aligned} \tag{7.1}$$

from the internal motion

$$\hat{H}_{\text{ad}}\Phi_\nu(R;\Omega) = U_\nu(R)\Phi_\nu(R;\Omega), \tag{7.2}$$

where the hyperradius R appears only as a parameter. The diagonalization of the hyperangular adiabatic Hamiltonian $\hat{H}_{\text{ad}}$ gives the three-body potentials U_ν and the channel functions Φ_ν, which are also used for computing the nonadiabatic couplings $W_{\nu\nu'}$, for the hyperradial equation.

In our model, the hyperangular adiabatic Hamiltonian reads

$$\hat{H}_{\mathrm{ad}} = \frac{\hat{\Lambda}^2(\Omega) + 15/4}{2\mu R^2}\hbar^2 + \sum_{\substack{i,j=a,b,c\\ i\neq j}} \hat{V}_{ab}(R,\Omega) + \sum_{i=a,b,c} \hat{H}_i^{\mathrm{sp}}(B), \tag{7.3}$$

where $\hat{\Lambda}$ denotes the hyperangular momentum operator [140, 149] and $\mu = m/\sqrt{3}$ is the reduced mass of three identical atoms of mass m. The atomic spin Hamiltonian $\hat{H}_i^{\mathrm{sp}}$ for atom i contains the hyperfine and Zeeman interaction, and to a very good approximation within the present work its eigenstates are $|f_i, m_{f_i}\rangle$. For two Rb atoms (e.g., i and j) of the $5S_{1/2} + 5S_{1/2}$ asymptote, the pairwise interaction $\hat{V}_{ij}$ can be expressed in terms of the electronic singlet and triplet Born-Oppenheimer potentials. We use the potentials from Ref. [139] with an additional repulsive term C/r_{ij}^{12} to reduce the number of bound states in our simulation. Here, r_{ij} is the interatomic distance. Removing deeply bound states mitigates the computational hardship without affecting too much the results, as generally more deeply bound states play a less important role in the three-body recombination process [56]. The truncation of the potentials shall be explained in more detail in a separate publication [91]. In brief, two parameters C (C_{s} and C_{t}) are adjusted individually for the truncated singlet and triplet potentials so that they contain 6 and 5 s-wave bound states, respectively, and so that the known singlet and triplet scattering lengths are reproduced. Additional fine-tuning of the two C parameters together with the atomic hyperfine splitting aims at reproducing the Feshbach resonance at about 155 G. As a result, the atomic hyperfine splitting is reduced by about 5% compared to the literature value. We use $C_{\mathrm{s}} = (0.3242030\, r_{\mathrm{vdw}})^6 \cdot C_6$ and $C_{\mathrm{t}} = (0.3258900\, r_{\mathrm{vdw}})^6 \cdot C_6$, where $r_{\mathrm{vdw}} = \frac{1}{2}(\frac{mC_6}{\hbar^2})^{1/4}$ is the van der Waals length and C_6 is the van der Waals coefficient.

Interactions between the particles and with the external magnetic field B couple various angular momenta. Therefore, the incoming spin channel $|2,-2\rangle|2,-2\rangle|2,-2\rangle$ can in principle be coupled to a range of spin channels $|f_a, m_{f_a}\rangle|f_b, m_{f_b}\rangle|f_c, m_{f_c}\rangle$, where f_i can be 2 or 3. We essentially only have the restriction that $M_{\mathrm{tot}} = m_{f_a} + m_{f_b} + m_{f_c}$ is conserved, as long as spin-spin interaction can be neglected. However, motivated by previous work [57], where we found a spin conservation propensity rule in three-body recombination of Rb atoms we restrict the spin of the third atom to be $|f_c, m_{f_c}\rangle = |2,-2\rangle$ in our calculations. One reason for this restriction could be that the third atom (c) interacts mainly mechanically with the other two, (a, b), while they are forming a molecule. This approximation leads to a model of five coupled three-body channels with the quantum numbers (F, f_a, f_b) = (4, 2, 2), (4, 3, 2), (4, 3, 3), (5, 3, 2), and (6, 3, 3).

7.4 Supplemental Materials

Feshbach resonance at 155 Gauss

The s-wave Feshbach resonance used in this work is located at 155.3 G. It couples the incoming $(F, f_a, f_b, m_F) = (4, 2, 2, -4)$ state and the closed-channel bound state $(F, f_a, f_b, m_F) = (4, 3, 3, -4)$. The scattering length across the Feshbach resonance is well characterized by the relation $a(B) = a_{\mathrm{bg}}(1 - \frac{\Delta B}{B - B_0})$. Here, $a_{\mathrm{bg}} = -443a_0$, $\Delta B = 10.9\,\mathrm{G}$, $B_0 = 155.3\,\mathrm{G}$ is the background scattering length, the width and the position of the resonance [13]. The scattering length is shown in Fig. 7.5.

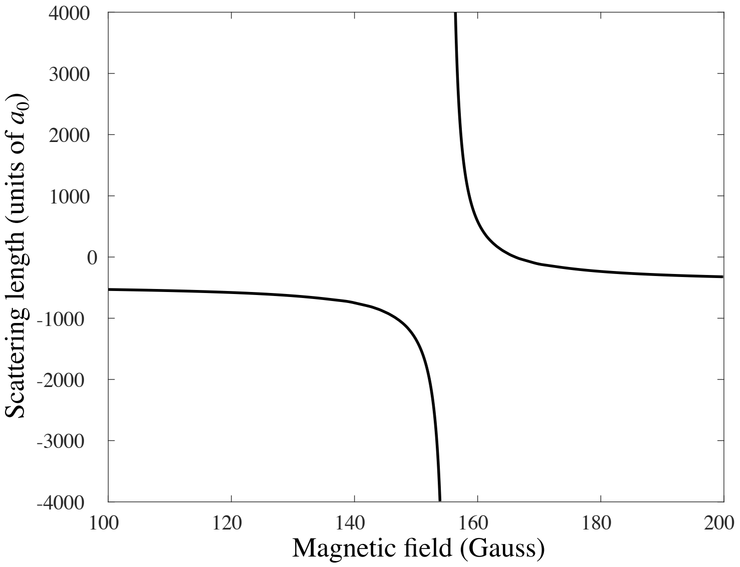

FIGURE 7.5: Scattering length in the vicinity of the s-wave Feshbach resonance. The scattering length in units of Bohr radius is plotted as a function of magnetic field.

Temperature dependence of L_3

The scaling of $L_3 \propto a^4$ is better perceivable at lower temperatures. In Fig. 7.6, we compare the L_3 for the $|\uparrow\rangle(-3, 4)$ state at 80 nK with the 860 nK result presented in the main manuscript. The Efimov resonance at about 140 G perturbs the overall scaling. At 150 G the L_3 value for 80 nK is again close to the a^4 prediction.

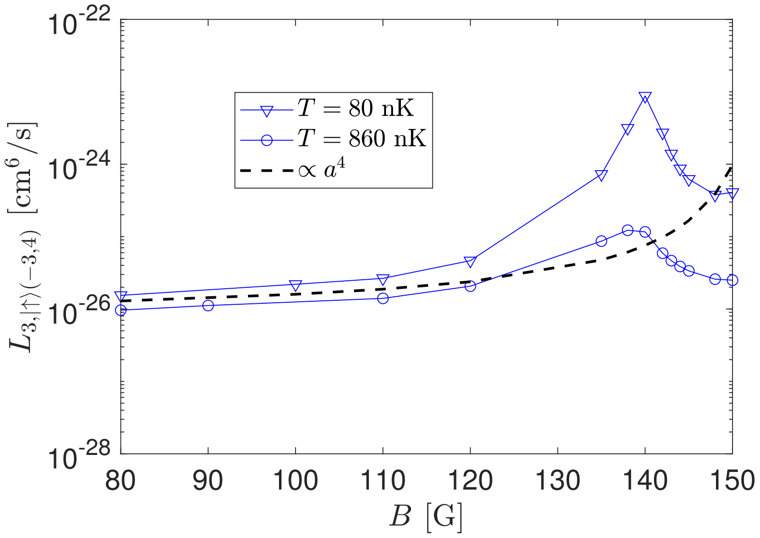

FIGURE 7.6: The three-body recombination rate constant L_3 for the $|\uparrow\rangle(-3,4)$ state at 80 nK is compared to that at 860 nK. The dashed line indicates the $L_3 \propto a^4$ scaling.

Chapter 8

Hollow-core fiber for single-mode, low loss transmission of broadband UV light

The content of this chapter is published in Ref. [36]. My contribution to this work was the experimental investigation of the fiber samples and characterizing them as well as contributions to the writing of the manuscript.

Dorer, D. and Frosz, M. H. and Haze, S. and Deiß, M. and Schoch, W. and
Hecker Denschlag, J.
"Hollow-Core Fiber for Single-Mode, Low Loss Transmission of Broadband
UV Light",
IEEE Journal of Selected Topics in Quantum Electronics **30** (6) 4300106 (2024).
DOI: `10.1109/JSTQE.2023.3299158`

We report on an anti-resonant hollow-core fiber (AR-HCF) designed for stable transmission of laser light in a broad wavelength range of 250 nm to 450 nm. We tested for wavelengths of 300 nm and 320 nm. The characterized fiber shows a low transmission power attenuation of 0.13 dB/m and an excellent single-mode profile. The fiber maintains stable transmission after an exposure of tens of hours with up to 60 mW CW-laser light and shows no indication of solarization effects. We further tested its performance under bending and observed a small critical bending radius of about 6 cm. These characteristics make the presented fiber a useful tool for many applications, especially in quantum optics labs where it may be instrumental to improve on stability and compactness.

8.1 Introduction

Optical fibers are well-established tools for stable transmission of laser light. For the visible to infrared wavelength range, silica-based optical fibers with a solid-core are routinely used for low-loss delivery of single-transverse-mode beams of high quality [141]. However, the applicability of solid-core fibers is severely compromised in the ultraviolet spectral range as they suffer irreversible degradation after even short periods of exposure to UV light [162]. This behavior is caused by UV-induced damage in the silica material - often referred to as solarization [37, 81, 133]. On the other hand, for example, in atomic, molecular and optical physics, there is a vastly growing number of applications involving UV light, and particularly at a wavelength around 300 nm. As an example, Rydberg states of Cs, Rb, and K atoms (see, e.g. [32]) can be excited with such wavelengths in a single-photon excitation from the ground state. As another example, Doppler cooling and state readout of the trapped ions Be^+, Mg^+, and Yb^+ works at the wavelengths 313 nm, 280 nm and 369 nm, respectively. Such platforms have a large potential for applications regarding, e.g., quantum computing, quantum simulation and metrology (see, e.g. [14, 86, 107, 128, 144, 155, 169]). Therefore, a good solution for stable and efficient, single-mode transmission of UV laser light could be very useful for such platforms and their applications.

One approach to overcome the solarization problem relies on hydrogen passivation [26, 97]. In another approach, hollow-core fibers are used to transmit light having negligible overlap with the silica glass. The structures of such hollow-core fibers can be tailored to achieve single-mode delivery of UV light. An example of such a structure is the Kagomé type [48]. Recently, single-ring structures formed by capillaries surrounding the hollow-core have gained increasing interest because of both low-loss transmission and high-quality single-mode transmission achieved by modal filtering when the fiber structure is suitably designed [47, 147]. An approach which targets a wavelength range around 300 nm and demonstrates low attenuation is reported in [47] where a single-ring structure with six capillaries and a ratio between core diameter D and capillary diameter d of $d/D = 0.51$ is used. We employ a similar design, however, our wall thickness of the ring capillaries $t \sim 220$ nm is about three times smaller, see Fig. 8.1(a). The wall thickness of the ring capillaries, which we call in the following core-wall thickness, is crucial because it determines the wavelength of the loss resonances according to $\lambda_q = 2t\sqrt{n^2 - 1}/q$ [3], where n is the index of the glass and q is the order of the resonance. Therefore, our fiber has a broad resonance-free zone from 250 nm to 450 nm in the UV. It is also of further advantage that the thin core-walls cause our fiber to operate in the second anti-resonance window ($1 < 2t\sqrt{n^2 - 1}/\lambda < 2$), since this is known to lead to higher coupling efficiency [43, 170]. Achieving such thin core-walls is still a significant fabrication challenge. In this article we report the fabrication and characterization of a hollow-core fiber (HCF) with a core-wall thickness of 220 nm for a targeted optimal guidance wavelength range of 300 nm to 320 nm. We evaluate the output beam quality by measuring the beam propagation ratio and investigate how bending the fiber impacts its transmission. Using the cutback-technique, we measured transmission loss of 0.13 dB/m at 320 nm and in addition we do not find an indication of fiber degradation when exposing the fiber to powers of up to 60 mW of UV light over tens of hours. The low measured loss is state of the art for the given spectral range.

8.2 Fiber fabrication

The fiber was fabricated in a stack-and-draw process (for an overview, see [123]). By adjustment of process parameters such as air-pressure applied inside the capillaries, furnace temperature and draw velocity, properties such as core diameter and wall thickness could be precisely controlled. We carefully chose materials for the fiber production. In a previous study [119], unwanted residues of ammonium chloride were found on surfaces of fibers made from glass containing a high concentration of chlorine. These residues drastically reduce the fiber coupling efficiency. For the cladding capillaries we used Suprasil F310 with < 0.2 ppm chlorine and ~ 200 ppm hydroxyl content to prevent crystal growth on the surface of the fiber ends. High concentration of hydroxyl groups in the glass is known to improve the long-term transmission of light in the UV and VIS spectral range. The tube to which the capillaries were directly fused was made of HSQ100 fused silica with less than 20 ppm hydroxyl content. The outermost part of the fiber was Suprasil F300 which features a low amount of hydroxyl groups (< 0.2 ppm) but a high amount of chlorine (typically between 800 and 2000 ppm). Since all glass structures except for the capillaries are far away from the relevant core structure, the high amount of chlorine seems to not play any role and we did not observe unwanted residues. A strong suppression of higher-order modes (HOMs) to ensure single-mode transmission while simultaneously having relatively low bend losses was our primary target in designing the fiber. While optimal HOM-suppression requires a ratio between capillary diameter d and core diameter D of $d/D = 0.68$ [147], the critical bend radius scales as $R_{cr} \sim \frac{(d/D)^2}{1-d/D}$ [45], therefore we aimed for a d/D value somewhat smaller than 0.68. For the presented fiber, the core diameter D is about 18 µm and the capillary diameter d is ~ 9 µm, resulting in a d/D-ratio of 0.5. The core-wall thickness of the capillaries is around 220 nm. Therefore, the first and second-order resonances can be expected at ~ 450 nm and ~ 250 nm with a broad transmission band in-between suitable for many applications in quantum labs.

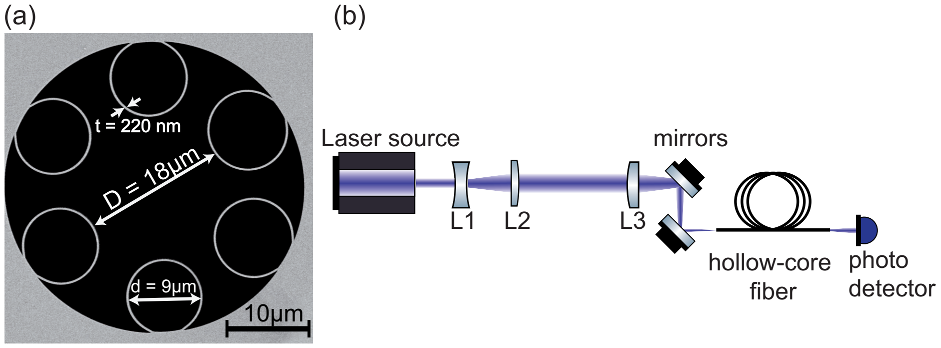

FIGURE 8.1: (a) Scanning electron microscopy image of the fiber cross-section. The structure consists of a hollow-core diameter $D \sim 18$ µm diameter and six hollow capillaries with a diameter $d \sim 9$ µm each. The core wall thickness t is ∼ 220 nm. (b) Setup for fiber-coupling. The output beam from the laser source is expanded by lenses L_1 and L_2 to a waist of 1.9 mm and then subsequently focused down with lens L_3 with a focal length of 125 mm. With two highly-reflective mirrors, the beam is coupled into the fiber. The transmitted light is measured by a photodetector and converted into a laserpower signal. Alternatively, a camera is used for beam shape analysis.

8.3 Experimental results

We used two different laser sources to carry out the experiments. The measurement described in Sec. 8.3.2 was performed with a Diode Pumped Solid-State laser (DPSS, model: 4136) from the company LASOS. It emits 10 mW of CW power at a wavelength of 320 nm and the beam profile has a Gaussian shape with $M^2 = 1.04 \pm 0.03$. For the measurements in Secs. 8.3.3 and 8.3.4, a frequency doubled dye laser system (Matisse 2DX, Sirah Lasertechnik GmbH) was used. We operated this setup at a wavelength of 302 nm and an optical power between 30 and 60 mW for degradation characterization of the fiber. The beam profile was elliptical with a ratio of 1:2. In both setups, no further spatial cleaning or filtering of the beams was done prior to fiber-coupling. To match the predicted mode diameter of the fiber, the waist of the collimated beam was enlarged by a factor of 7 (DPSS laser) or 10 (dye laser) to about 1.9 mm and then focused down to a beam diameter of $2\tilde{w}_0 = 12$ µm using a lens with a focal length of 125 mm where $\tilde{w}_0$ is the beam waist at the fiber facet. It is known that the coupling efficiency is maximized at all guided wavelengths when the beam diameter for fiber coupling is approximately 70% of the core diameter [43]. We used two flat mirrors to align the beam and optimize the transmission through the fiber (see Fig. 8.1(b)).

8.3.1 Output beam quality

We confirmed single-mode guidance by monitoring intensity profiles of the output beam with a CCD camera. In previous work [166], a HCF with $d/D \sim$

0.43 showed a somewhat asymmetric mode profile and higher transmission loss at a wavelength of 355 nm. Figure 8.2 (a) shows the near-field beam profile for the tested fiber. For this we used the DPSS system, but we were able to achieve equal results with the dye laser. The beam has a highly symmetric profile. The ratio of the diameters between the two main axes (y/x) is 0.98 which indicates a high quality circular shape. To further characterize the quality of the output beam, we measured the beam propagation ratio M^2. For this, we focused the collimated beam of a diameter of 2 mm with a lens of 300 mm focal length and measured the radius of the beam at various axial distances near the focal point, see Fig. 8.2(b). Then, we used Gaussian beam fitting according to

$$w(z) = w_0 \sqrt{\left(M^2 + M^2 \left(\frac{\lambda}{\pi w_0^2} \right)^2 (z - z_0)^2 \right)} \tag{8.1}$$

with w as the measured radius at a position z and the wavelength λ = 320 nm. The beam waist w_0 and a position offset z_0 are free fitting parameters. We extracted $M^2 = 1.03 \pm 0.04$. Note that for a single-mode TEM_{00} (Gaussian) laser beam, $M^2 = 1$. Higher-order modes are suppressed by large propagation losses, so that the mode is cleaned by the fiber after approximately 1 m. We noticed that fixation of the fiber end plays an essential role for optimal fiber coupling. In order to avoid mechanical stress on the fiber, we used a low expansion glue for fixation of the fiber on a V-groove holder. We could not find differences regarding the output beam quality between the two used laser sources within our measurement uncertainty. This additionally confirms the mode cleaning behavior of our HCF.

8.3.2 Cutback-method

The propagation loss was measured using the multiple-cutback method without changing the coupling into the fiber. After the front facet, we kept the fiber straight for 30 cm in order to minimize stress in the fiber which is helpful for controlled and reproducible in-coupling of the laser beam. The remaining length of the fiber is wound on a coil with 20 cm radius. As we show later in Sec.8.3.3, this bend radius leads to no additional bending losses. Once the transmission was maximized by adjusting the fiber coupling optics, the alignment was fixed. The results of the cutback-measurement are shown in Fig. 8.3. We measured a transmission power loss of 0.13 dB/m with an in-coupling loss of about 6% extracted from a linear fit. We note that a 94% coupling efficiency was also reported in Ref. [170]. Our results for transmission loss for a wavelength around 320 nm are very similar to the findings of [47] and are significantly better than the ones of [166] (∼ 0.6 dB/m) and of [53] (∼ 3 dB/m). Osorio et al. [106] reported a fiber with loss as low as ∼ 0.05 - 0.08 dB/m around 280 nm, but as their core-wall thickness was 0.6 µm (2.7 times thicker than in our case) that fiber was operating in the fifth

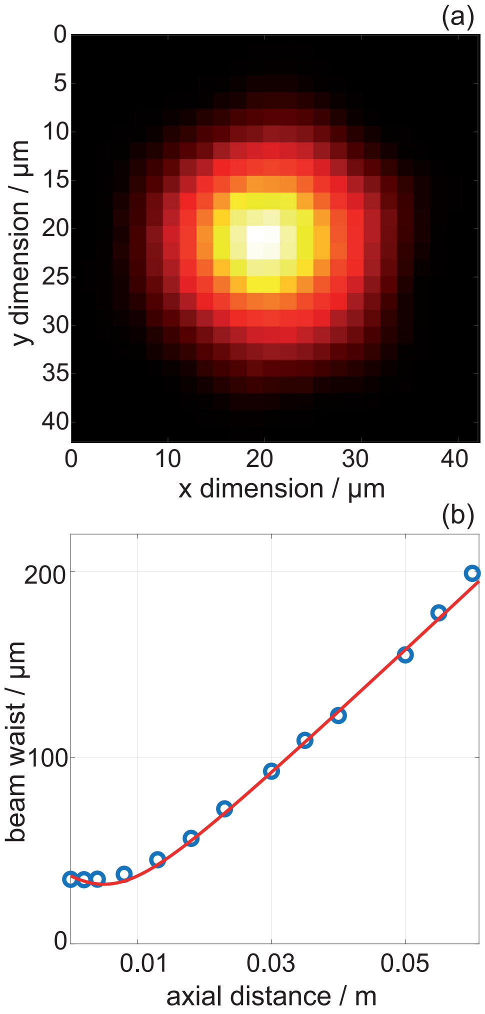

FIGURE 8.2: (a) Image of the near-field intensity profile of the output beam. It shows a nearly symmetric beam shape. (b) In order to characterize the transverse mode properties of the output beam we perform beam waist measurements on the beam which has been focused to a waist of 30 µm. The plot shows the beam waist as a function of axial distance to the position of the focusing lens (blue dots). The red curve is a fit to the data and is used to extract the beam propagation ratio $M^2 = 1.03 \pm 0.04$.

anti-resonance window, leading to a narrow transmission window ($\sim$ 270 - 290 nm) as well as to an expected reduced coupling efficiency. The d/D ratio of their fiber was 0.41, smaller than the value 0.51 of our fiber and thus further away from the optimum value of 0.68 for higher-order mode suppression. Despite the lower d/D value, due to the larger core size (critical bend radius scales with D^3 [45]), that fiber is also expected to have a higher critical bend-radius of $\sim$11 cm. Still, our measured loss at 320 nm is found to be about an order of magnitude higher than predicted by finite element modelling (FEM), which considers only confinement and bend loss, see Fig. 8.3(b). The additional loss observed in the measurement is most likely due

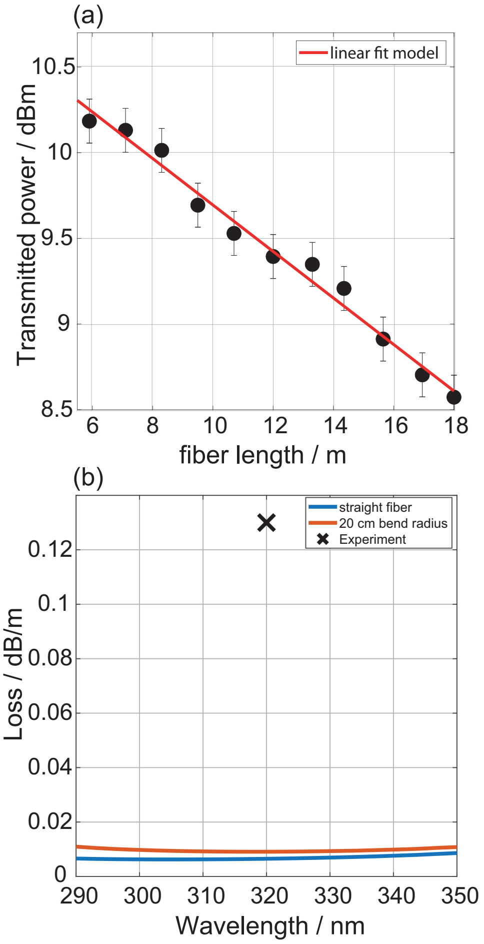

FIGURE 8.3: (a) Cutback loss measurement at a wavelength of 320 nm. Shown is the measured transmission power as a function of the fiber length. The error bars of the data points result from the uncertainty of the power measurement by a silicon photo detector. From a linear fit (red line), a transmission loss of 0.13 dB/m is obtained and an in-coupling loss of only 6 %. (b) Calculation of the transmission loss for a straight fiber (blue) and a fiber with a bend radius of 20 cm (red) which is typical for our experiments. The experimentally observed loss (black cross) is a factor of ~ 10 larger than the calculation.

to surface scattering and microbending. Microbending is an effect which occurs due to small perturbations along the fiber whereas surface scattering arises from a thermodynamically unavoidable surface roughness [106]. Both effects increase significantly towards shorter wavelengths [44, 106] (surface scattering scales $\propto \lambda^{-3}$ and microbending scales $\propto \lambda^{-6}$). Within the fabrication process azimuthal asymmetries in the cladding capillaries occur along the fibre and FEM simulations show a strong sensitivity of loss resonances to the core-wall thickness.

8.3.3 Performance under bending

For practical applications, an important requirement for the fabricated fibers is to be bending insensitive at bend radii relevant for laboratory experiments. Below a certain critical bend radius, single-ring fibers and similar fiber types exhibit a strong drop in transmission due to bend-loss [45] and also the shape of the outgoing mode changes. At the critical radius, the fundamental core mode couples to the fundamental mode inside one of the cladding tubes, thereby experiencing high loss. We give an upper estimate for the critical bend radius using the simplified expression from [45]

$$\frac{R_{cr}}{D} = \frac{D^2}{\lambda^2} \cdot \frac{\pi^2}{u_{01}^2} \frac{(d/D)^2}{1 - d/D}, \tag{8.2}$$

where the value u_{01} depends on the specific core mode. For the fundamental mode $u_{01} = 2.405$. In the original expression, there is an angular dependence which is neglected here. In practical lab situations it is not desirable to have to control the twist of the fiber carefully. Furthermore we see that bend-sensitivity can be reduced by choosing suitably small values of D and d/D. However, d/D should also not be chosen much smaller than $d/D = 0.68$ in order not to lose some suppression of higher-order modes [147]. For our design parameters $d/D = 0.5$, the critical bend radius is calculated to be $R_{cr} \approx 5.5$ cm at $\lambda = 300$ nm. The bending properties were measured with the remaining 5 m long piece of the same sample used for the cutback-method. For this, the initial part of the fiber is kept straight for 30 cm to not change the fiber coupling efficiency by later adjustments of the bend radius. In the further course of the fiber, this is followed by a single loop the radius of which is varied and a further straight part of the fiber of about 1 m. In Fig. 8.4 we show the transmission through the fiber for various bend radii. For bend radii above 7 cm, the transmitted power is not affected by the loop and it is similar to a straight fiber. At a bend radius of about 6 cm, the transmission drops rather abruptly by more than 8 dB. The transmission is minimal at the critical bend radius, because light can then couple best from the core mode to the outer capillary mode which leaks out. This mechanism is described in more detail in [45]. Our calculations and experiments show that the mode profile in the fiber can be strongly distorted for bending radii close to the critical value. The distortion is quite sensitive to the details of the stress applied to the fiber. After propagating through > 1.5 m of straight fiber the higher order modes have been cleaned out and only the fundamental mode remains.

8.3.4 Lifetime investigation

When exposed to UV light solid-core fibers exhibit a degradation of their transmission properties, a process which is known as solarization. Often this degradation already occurs within a few hours of exposure. We tested for

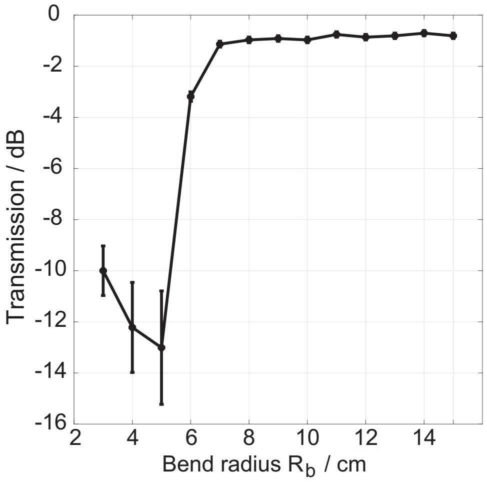

FIGURE 8.4: Power transmission measurement of a 5 m long fiber as a function of the bend radius R_b of a single winding. The calculated critical bend radius R_{cr} is approximately 5.5 cm. When decreasing the bend radius to the critical value, the transmission drops abruptly by more than 8 dB at a bend radius of 6 cm. The error bars correspond to the noise of the detector setup for the transmission measurement. © 2023 IEEE

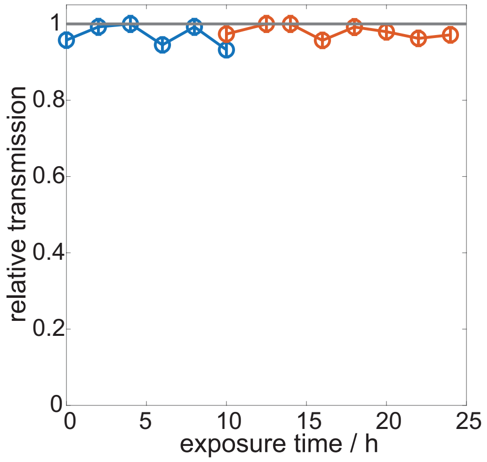

FIGURE 8.5: Longterm exposure of the fiber at 302 nm with the dye laser system. We show relative transmissions over several hours of exposure for two different power levels. We normalized the transmission to the maximal observed transmission for each power level. Blue (red) data points correspond to 30 (60) mW of laser power prior to the fiber coupling, respectively. Due to imperfections in the transverse mode, coupling was limited to about 65%.

solarization using laser powers of up to 60 mW. Figure 8.5 shows the transmission of UV laser light during the course of one day. No degradation of the fiber transmission is observable. We also performed a 10 mW UV-light exposure of the fiber over several weeks, the data of which are not shown here. Again, no degradation was observable.

8.4 Summary

We characterized the transmission of UV laser light through a single-ring hollow-core optical fiber which is designed for low-loss, single-mode transmission over a wavelength range of 250 nm to 450 nm. Using wavelengths of 302 nm and 320 nm we found single-mode transmission with a mode quality of $M^2 = 1.03$ and a loss of 0.13 dB/m using the cutback method. Our designed fiber has a transmission attenuation similar to other fiber types recently reported for UV guidance [47] but operates in a much broader spectral range of 250 to 450 nm due to very thin core-walls of 220 nm. Furthermore, it operates in the second anti-resonant window leading to high fiber coupling efficiency. As the fiber has a critical bend radius of about 6 cm, it can be conveniently used in compact laboratory environments that are typical for atom or ion traps. The fiber shows no effects of degradation over tens of hours of effective exposure time with a power up to 60 mW. In principle, it should be possible to fabricate similar fibers but with additional polarization-maintaining properties (see [121] for circular polarization for 1593 nm laser light). Such fibers are of high interest for applications e.g. in quantum optics labs where polarization stability is crucial.

Chapter 9

Conclusion and outlook

Conclusion

In my doctoral research, I focused intensively on the following topics and conducted in-depth investigations:

- Three-body recombination in an ultracold gas of rubidium
- High-resolution molecular spectroscopy of states near the 5s + 4d asymptote
- Characterization of a novel hollow-core fiber for transmitting ultraviolet light.

For these studies, I utilized a hybrid apparatus capable of trapping and preparing both neutral and charged atoms in well-defined quantum states. The main focus of my work was on investigating three-body recombination, with a particular emphasis on exploring methods to control the chemical reaction. To detect the resulting product molecules, we used resonant multiphoton ionization (REMPI) in the laboratory.

As a first step, I identified REMPI pathways that increase the molecule detection efficiency. For this purpose, I conducted high-resolution molecular spectroscopy of the electronic states $(2)^1\Sigma_u^+$ and $(2)^3\Pi_g$ which correlate with the 5s + 4d asymptote in the frequency range of 493 to 503 THz $\times h$. A key result of this work was achieving an ionization efficiency for the molecules that is nearly two orders of magnitude higher than previous methods in our laboratory. Furthermore, this research provided deeper insights into the molecular structure of the investigated states. In particular, we determined in collaboration with Prof. E. Tiemann from the University of Hannover the spin-orbit coupling in the $(2)^3\Pi_g$ system to be $55 \pm 10\,\mathrm{cm}^{-1}$, a value that significantly deviates from previously published results.

With this improved molecule detection method, we analyzed the molecular product distributions in greater detail and detected significantly more molecular product states than before. Our findings revealed that the three-body recombination reaction in rubidium tends to follow specific reaction pathways: the spin states of the two atoms which form a molecule exhibit a tendency to remain conserved throughout the reaction, thereby determining the spin character of the reaction products at the exit of the reaction. Furthermore, we utilized this spin conservation rule to demonstrate control of the reaction flux across different reaction pathways. We explored two methods based on the principle of using magnetic fields to control spin composition. These methods target either the entrance channel of the reaction (atomic scattering state) or the molecular product states at the reaction's exit.

We showed that controlling the spin composition of a reaction channel at the reaction's exit enables precise manipulation of the reaction flux into that channel. To achieve this, we utilized two molecular states featuring an avoided energy-level crossing. By applying an external magnetic field, we were able to adjust the spin composition of the two molecular product states, thereby selectively steering the reaction flux between the involved reaction channels. This type of control only affects the two product states exhibiting the avoided energy level crossing and, as observed in the experiment, does essentially not affect the distribution of the remaining reaction products.

In another experiment, we found a different method for control of the chemical reaction that utilizes a magnetically tunable Feshbach resonance to selectively mix a specific spin state into the entrance channel of the reaction. The experiment showed that this opens up reaction channels towards molecules belonging to various spin families. We observed a significant effect on the whole product distribution using the Feshbach control.

In the third project, although it was not the main focus of my thesis, I collaborated with the Max Planck Institute for the Science of Light in Erlangen to develop and test a hollow-core single-mode fiber for its suitability in the 300–320 nm wavelength range. In this range, the photon energy is already high enough to irreversibly damage conventional solid-core fibers after prolonged exposure, causing them to lose their ability to guide light efficiently. Motivated by this, we developed and characterized a fiber with a transmission efficiency exceeding 70% over a length of 10 m. Remarkably, this fiber showed no signs of degradation even after several days of continuous exposure. This type of fiber holds significant potential for future applications. In our group, we will use it particularly for the spectroscopy of Rydberg molecules using highly energetic photons.

Outlook

In the following, I will give an outlook for possible future experiments in our laboratory connected to my research.

Theoretically, the conservation of spin in the reaction which we experimentally found could have limitations. In fact, by approaching molecular product states with large enough binding energy, the expectation is that the spin conservation rule does not apply anymore in rubidium. By advancing into regions of deeper molecular binding energies, we could potentially observe the breakdown of the spin conservation propensity and learn more about the chemical reactions in general. For ^{87}Rb, we expect to observe deviations for binding energies larger than 120 GHz x h. Currently, we achieved to observe molecules with binding energies up to 77 GHz x h. Further improvements in the ionization efficiency could help to detect more deeply-bound molecular product states and therefore closing the gap. Currently, a two-photon-one-color scheme for molecule detection is used. This could be further optimized by switching to a two-photon-two-color scheme. This would enable us to optimize the optical transition to the intermediate states and the subsequent ionization step independently of each other. This could ultimately lead to an improved overall ionization efficiency.

The methods developed for controlling chemical reactions now open up the possibility of combining various control schemes and finding ways to manipulate both the entrance and exit channels of the reaction. Both control schemes that we developed and that are based on spin-mixing can be though of as beam splitters for reaction flux. This can be thought of as analogous to a beam splitter. Just as a beam splitter coherently divides an incoming beam into two beams, we can apply similar principles to split the incoming reaction channel into different outgoing reaction channels. By combining two beam splitters, we could investigate coherence effects in the reaction pathways. Just like beam splitter cube in optics, where we could split in different paths, recombine it and investigate interference between them. The analogy in the chemical reaction would be the Feshbach resonance which functions as one beam splitter for the incoming reaction channel. The split up parts can potentially take different pathways to reach the same final product state, where they interfere. For instance, the final product state might exhibit tunable spin-mixed characteristics, adjustable through additional control methods like state dressing with an optical field. Applying and demonstrating this general concept would cause a great step towards full control of chemical reactions.

On the technological side, I highly recommend to install and operate an channel electron multiplier (CEM) for our three-body recombination experiments. A channeltron is a compact electron multiplier that amplifies and detects charged particles or photons by generating a cascade of secondary electrons. It would allow us to directly detect produced ions in our experiments instead of counting the ions via atom loss.

Appendix A

Further projects in the laboratory

A.1 H-Bridge for Stern-Gerlach experiments

In this doctoral thesis, a measurement technique for the detection of hyperfine magnetic quantum number m_f was employed and evaluated. There are a variety of applications [98, 132, 159] which make use of the Stern-Gerlach method but we will mentioned just one typical application here. In [132], the Stern-Gerlach method was used for efficient quantum state preparation. Here, optical pumping is used for preparing the quantum state $f = 2, m_f = +2$ of ^{87}Rb and it was optimized by using the Stern-Gerlach method. Finally, they could optically pump 92% of their atoms in the desired quantum state. In our typical measurements, we work with spin-polarized samples of ^{87}Rb $(f = 1, m_f = -1)$ or ^{85}Rb $(f = 2, m_f = -2)$. For future experiments, however, one could change the setup from using a spin-polarized atomic cloud and conduct research requiring atoms in different hyperfine magnetic substates. Similar than the approach in [132], we could make use of the Stern-Gerlach measurement to optimize the spin preparation of the experiments.

The Stern-Gerlach method takes advantage of the fact that particles experience a force in a magnetic field gradient, with this force being dependent on the particle's magnetic moment. To implement this experimental method in our lab, we needed to generate a magnetic field gradient at the center of the science chamber. Typically, our Feshbach coils are operated in a Helmholtz configuration, producing an approximately homogeneous magnetic field. To enable dynamic control over the magnetic field, we designed an H-bridge circuit that allows switching between Helmholtz and Anti-Helmholtz configuration without altering the wiring or connections. The current flow through the coils is controlled by two IGBT half-bridge modules (Vishay VS-GA100 TS60SFPbF) which are self-locking, meaning no current flows through the coils when the control is off. Each module is operated by a half-bridge driver (IRF IR21844). It is crucial that upon system restart, the bridge circuit does not appear to be in a defined state and only a change of polarity leads to a defined state and no current should be applied by the power supply units, potentially damaging the bridge modules. This remains a known issue that requires a future, secure solution. Additionally, the module should never be switched while current is flowing through the coils because it can easily damage the bridge modules aswell due to high inductance voltages.

First measurements with Rb atoms

Initial test measurements in the laboratory successfully demonstrated that spin-resolved detection of the atomic cloud can be achieved using a magnetic field gradient. First, the initially prepared ^{87}Rb sample in the quantum state $f = 1, m_f = -1$ was transformed in a mixed spin state (the m_f magnetic quantum numbers were mixed). This was done by compensating the background magnetic field with the compensation coils, followed by reapplying a quantization axis. We repeatedly crossed the system through zero-field conditions to induce spin mixing. Then, the optical dipole trap was turned off and the atoms could fall free due to gravity. The atomic cloud was then imaged in a gradient field using time-of-flight absorption imaging. The result was three spatially separated clouds, as the mixtures of $m_f = -1, 0, +1$ responded differently to the gradient - one accelerated, one remained unaffected, and one decelerated.

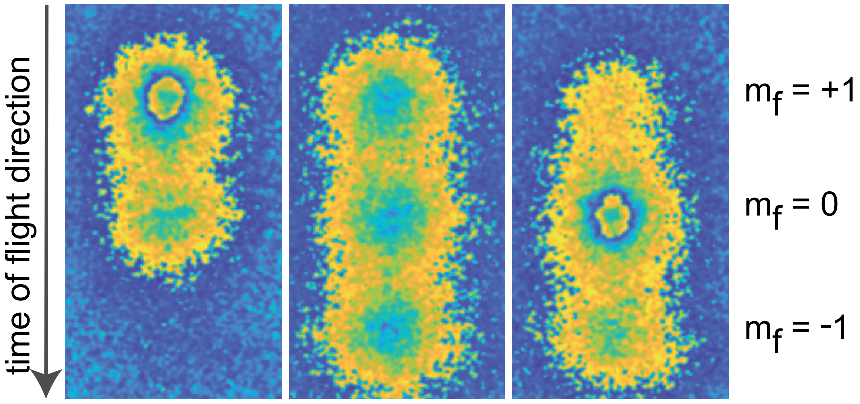

FIGURE A.1: Stern-Gerlach experiment in the science chamber with three different spin mixtures for ^{87}Rb. The corresponding m_f-components are labeled on the right.

A.2 Long-range molecular Rydberg spectroscopy

One of the research areas recently investigated in our laboratory are neutral or charged long-range Rydberg molecules [31, 32, 58]. A single photon excitation scheme is used to photoassociate atoms to a molecular Rydberg state or photo-excite molecules to a molecular Rydberg state. The detection of the molecules is very similar to the scheme described in Chapter 4.2 and they mainly differ in the used REMPI pathway. In the course of the Rydberg projects, technical difficulties were identified. It turned out that the Rydberg experiments are heavily affected by the linear Paul trap. The strong inhomogeneous electric fields $> 300\,\mathrm{V/cm}$ required for confining the charged particles in the trap affect the optical transitions to the Rydberg states. This leads to a massive broadening of the transitions in the recorded spectra which is a consequence of the Stark effect that Rydberg states exhibit due to their very large electric dipole moment.

There are two possible approaches that could solve the problem of high electric fields during optical excitation. One approach would be to operate the linear Paul trap in a digital way [7, 11, 34]. Since this approach would require massive reconstruction of the setup, we decided to follow another approach first. We generate very short cw laser pulses and synchronize them with the drive frequency of the linear Paul trap. So whenever the applied voltage of the linear Paul trap crosses the 0 V level, a laser pulse is sent into the science chamber. In the following, we present and discuss two methods for the generation of nanosecond short cw laser pulses.

A.2.1 Short cw laser pulses

For switching the excitation laser very fast, two different techniques have been tested.

A Pockels cell is an electro-optic device that is used to control the polarization state of light passing through it. It exploits the Pockels effect, which is the change in the refractive index of a material in response to an applied electric field. This change in refractive index alters the polarization of the light, which can be used to rapidly switch or modulate laser beams. The technical challenge here is to apply high voltage pulses (typically 250-400 V) within a few ns to the crystal. We had the electronics for this fast circuit developed by the company Alphanov and then used it in the laboratory. Fig.A.2(a) shows the optical setup used for testing and characterizing the fast on-and off-switching. The Pockels cell tested is named LM0202 by QiOptics and it is made of KD*P (Deuterated potassium dihydrogen phosphate). Half-wave plates are used to adjust the polarization of the light. In order to achieve the highest possible extinction ratio, we used Glan-Taylor polarizers, which can theoretically achieve an extinction ratio of up to 100000:1. The clear advantage of this method is the generation of very short switching times of less than 10 ns. The experimentally determined full width at half maximum of the generated pulse is about 9.6 ns, see Fig. A.2(b). However, it turned out to be unsuitable for our experiments. The device's repetition rate, particularly that of the crystal was limited to approximately 10 kHz due to thermal heating and degradation. The optimal repetition rate would be around 4.2 MHz which is the drive frequency of the linear Paul trap. An alternative would be another crystal (Beta barium borate - BBO) which would require significantly higher voltages for altering the polarization (in the kV range) to switch the laser on and off and also active temperature-stabilization by a water-cooling system.

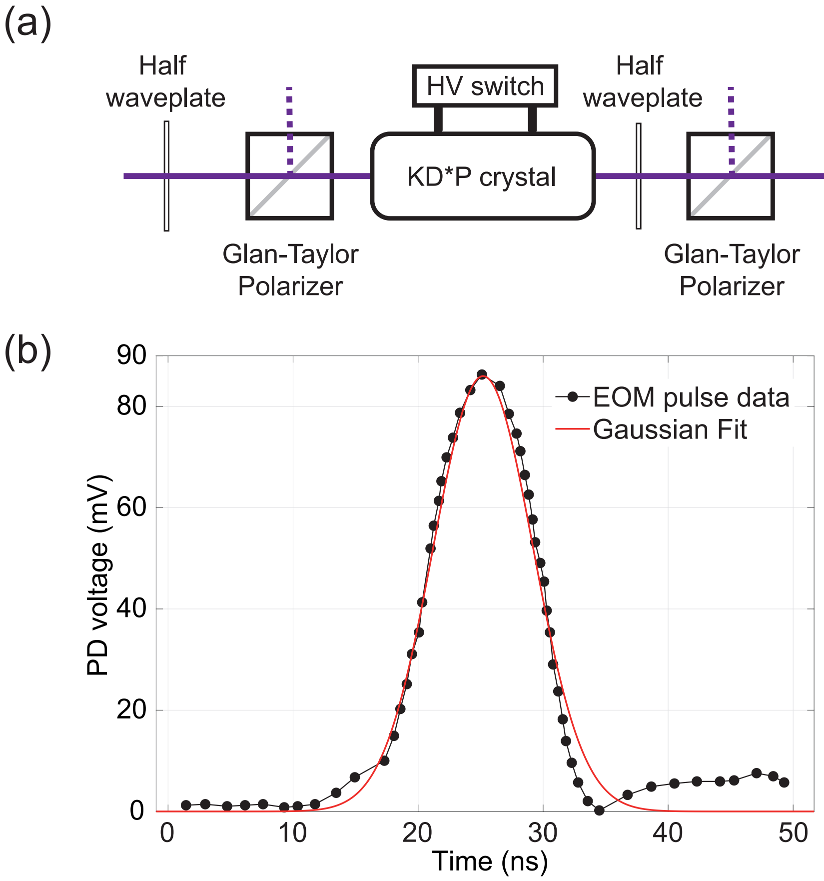

FIGURE A.2: Setup (a) and experimental results (b) for fast laser pulse switching using a Pockels cell. For adjusting the polarization of the light, we use half-wave plates and Glan-Taylor polarizers. The achievable full width at half maximum value for repetition rates below 10 kHz is around 10.6 ns limited by the electronics.

Acousto-optical modulators (AOMs) are a possible alternative to switch the cw laser on and off. An AOM is a device that uses sound waves to modulate light. It is based on the acousto-optic effect, where an acoustic wave propagating through a transparent medium creates a periodic variation in the refractive index. This variation acts as a diffraction grating for light passing through the medium, allowing the intensity, frequency and even the direction of the light to be controlled. A review about AOMs used for modulation of light is given in [109]. For our application, it is crucial to focus the laser beam as tightly as possible through the crystal medium. This ensures that turning the acoustic waves on and off results in very fast switching behavior of the diffracted light. However, a drawback of this focusing is that the diffraction efficiency decreases. The optical setup is simple, see Fig. A.3(a): only two lenses for focusing and collimation of the laser beams are required. The first diffraction order is used for testing the switching behavior and we achieved a full width at half maximum value of 18 ns depending on the waist of the beam inside the AOM crystal. Repetition rates of more than 4 MHz are also possible with this technique. The downside of the AOM switching is its relatively low efficiency: we ultimately could achieve a diffraction efficiency of only 50% in the first order because of the relatively small beam waist inside the crystal. The pulse itself is not perfectly clean as further oscillations appear after switching it off.

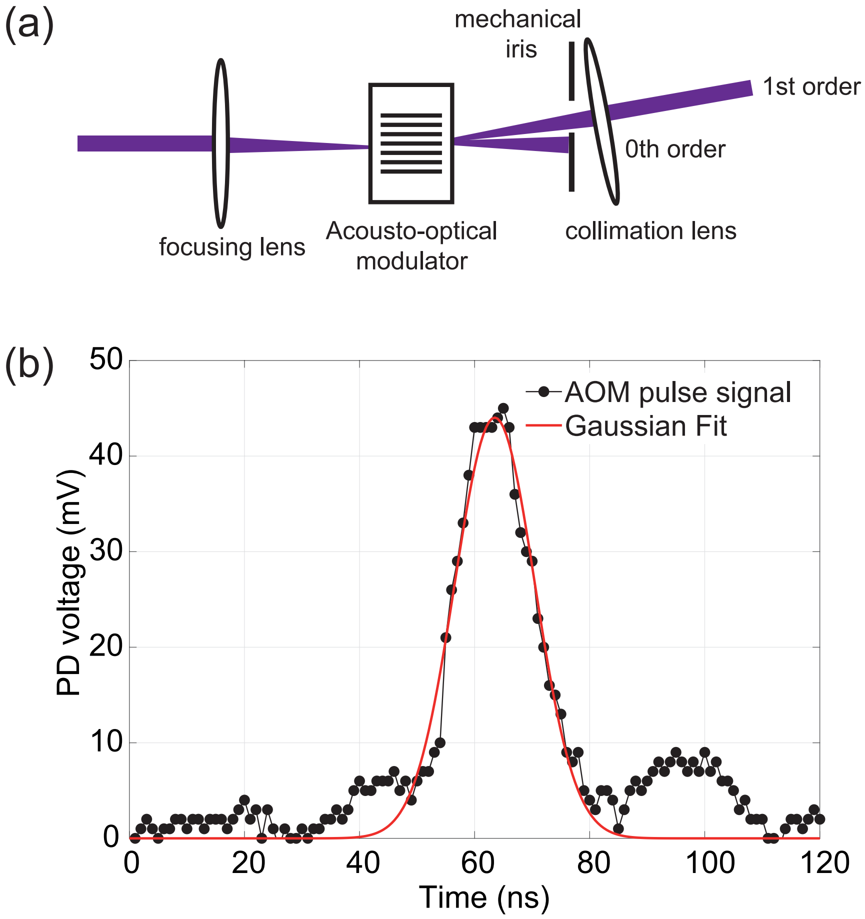

FIGURE A.3: Setup (a) and experimental results (b) for fast laser pulse switching using an acousto-optical modulator (AOM). In order to shorten switching times, we focus the laser beam through the AOM. We could achieve 18 ns of full-width half maximum pulse length at a repetition rate of 4.214 MHz. The pulse is not as clean as for the EOM pulse scheme as further oscillations appear after switching off the RF power.

A.2.2 Rydberg spectroscopy with cw laser pulses

To synchronize the laser pulses with the driving frequency of the linear Paul trap, we employed an Agilent 33522A radiofrequency (RF) generator. This generator offers two channels that can be synchronized in both time and phase. Channel 1 was utilized to drive the RF amplifier connected to the Paul trap, while Channel 2 was connected to a Mini-Circuits ZYSWA-2-50-DR RF switch. The RF switch connects the input to the RF amplifier for the acousto-optical modulator which then diffracts the light and generates a short pulse. To test the new scheme, we used an excitation to the atomic Rydberg states $32P_{1/2}$ and $32P_{3/2}$ which are separated by only a few GHz, see Fig. A.5(a). The orange curve shows the particle number as a function of the relative laser frequency $\nu - \nu_0$ without using a pulsed scheme and synchronization. The larger the particle number loss, the larger the number of Rydberg atoms and ions that have been created. We clearly observe two loss features from the $32P_{1/2}$ and $32P_{3/2}$ Rydberg resonances corresponding to a excitation at zero electric field. For lower relative laser frequencies the atomic loss signal decreases gradually. The behavior of the excitation signal strongly depends on the distribution of the electric field within the Paul trap. To effectively excite the atoms with a detuned laser (with respect to the resonance at zero electric field), a sufficiently strong electric field is required. Due to the resulting Stark shift, resonant excitation becomes more likely. However, such intense fields typically occur near the edges of the trap, where the field strength is larger due to the geometry of the trap. Since fewer atoms are concentrated in these regions, fewer particles are exposed to the high electric fields. This leads to a gradual decrease in the excitation signal over time. At relative laser frequencies of around 185 - 198 GHz, the orange curve exhibits interesting, almost step-like features. Currently, we interpret these signals as avoided crossings between the observed P-levels and the hydrogenic manifold. This becomes more clear in Fig. A.4 where a typical Stark map is shown. With aid of the calculated Stark map, it is possible to connect the avoided crossing signals to an electric field present in the experiment. A precise analysis of the spectra remains an unsolved problem, which has been discussed in more detail in [58]. In this context here, we use the measurements solely to assess whether the suppression of the electric fields is effective. The spectra in Fig. A.5 clearly show a distinct difference between the synchronized (blue) and unsynchronized (orange) conditions. In the following, we provide a rough estimate of the effectiveness of the electric field suppression. To do this, we use the Alkali-Rydberg Calculator (ARC) [131], an open-source Python-based program, to calculate a Stark map. The Stark map displays the energy levels as a function of the electric field. Fig. A.4 shows a comparison between the recorded spectra (right) and the calculated Stark map for $32P_{3/2}$. Avoided level crossings are clearly visible in the recorded spectrum (orange) without pulse synchronization [58]. These structures are observable to corresponding electrical fields of 250 V/cm. In the blue data set, however, these spectroscopic structures almost entirely vanish. The grey dashed line is a guide to the eye indicating that still electric fields up to 50 V/cm are present in the synchronized scheme. The tests clearly demonstrate that synchronization of the laser pulses with a classical (sinusoidal) Paul trap leads to a suppression of the electric field. The limitation here is the pulse duration, which, at approximately 18 ns, corresponds to about 8% of the driving frequency's period.

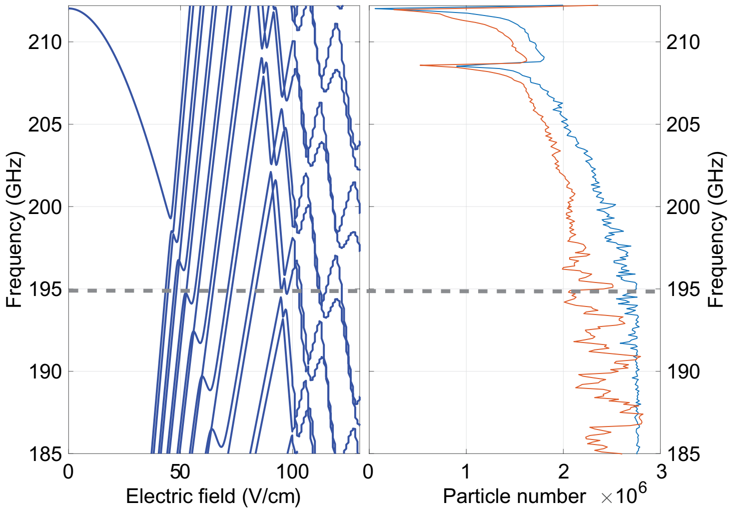

FIGURE A.4: A calculated Stark Map for the Rydberg state $32P_{3/2}$ (left). Experimental recordings with and without laser pulse synchronization (right). In the recorded spectra, a clear effect of the synchronization is observable which could be connected to a suppressed electrical field when exciting the atoms by a sychronized laser pulse. A clear quantitative statement is difficult but signals which appear for electrical fields > 50 V/cm are strongly suppressed (see missing avoided crossing signals below 195 GHz in frequency).

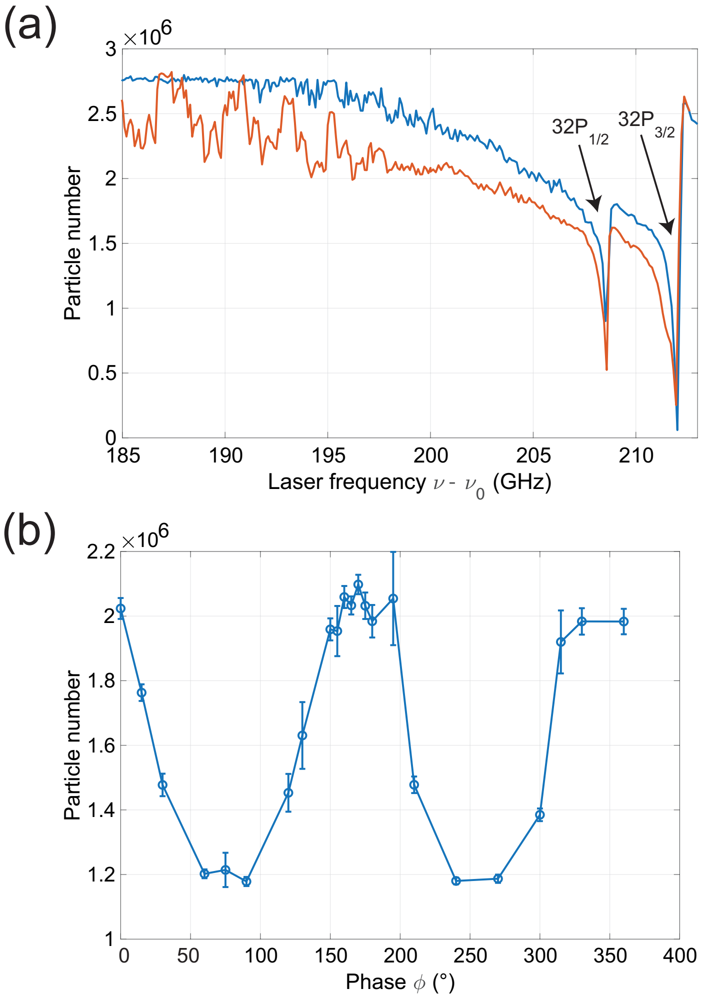

FIGURE A.5: (a) Rydberg spectroscopy with (blue) and without (orange) synchronization. The transition used is a single photon transition from atomic hyperfine level $f = 1, m_f = -1$ to the excited Rydberg state $32P_{1/2}$ and $32P_{3/2}$. We use the Matisse dye laser system together with a SHG to generate laser light at around 300 nm. ν_0 = 1006 THz is an arbitrary frequency reference. (b) Particle number as a function of the phase between Paul trap drive and laser pulse. The minima correspond to laser pulses when the applied rf power to the Paul trap has a maximum and the particle number maximum correspond to a rf minimum. The phase setting for the measurement in (a) is ϕ = 161 degree.

Appendix B

Additional recorded data near the 5s + 4d asymptote

This chapter aligns with Chapter 4. Here, we focus on two aspects: first, we compare pulsed and continuous-wave (cw) measurements for selected signals, and second, we compare the recorded signals associated with atomic Rydberg excitations with calculations performed using the ARC calculator [131]. For a comprehensive overview of the entire range of recorded spectra, please refer to Section 4.3. Additionally, we discuss signals which could not be assigned by the methods used in Section 4.4.1. The laser systems used have already been described in Chapter 2.4.

B.1 Comparison between pulsed and cw recordings

In the following section, the pulsed recordings are compared with more precise cw measurements. Fig. B.1 illustrates the comparison using several rotational transitions to $(2)^3\Pi_g$ $\Omega = 0^+$ and $\Omega = 0^-$ for $\nu = 13$. The data obtained with the pulsed system is shown in blue, with a frequency scan step size of 1 GHz. The cw recordings, displayed in green color, were taken with a much finer step size of 10 MHz. In the cw data set, transitions to various rotational states J' were observed and are marked with vertical lines: green lines indicate transitions to $\Omega = 0^+$, while orange lines mark transitions to $\Omega = 0^-$. A direct comparison clearly shows that significantly fewer structural details can be resolved in the pulsed data set, which is attributed to the broader linewidth of the laser system. Interestingly, there are even regions where no signals appear at all in the pulsed data. Only a more precise cw scan revealed the complete rotational structure, allowing for a definitive assignment of quantum numbers. This indicates that further investigation is needed for a more precise interpretation of the pulsed dataset.

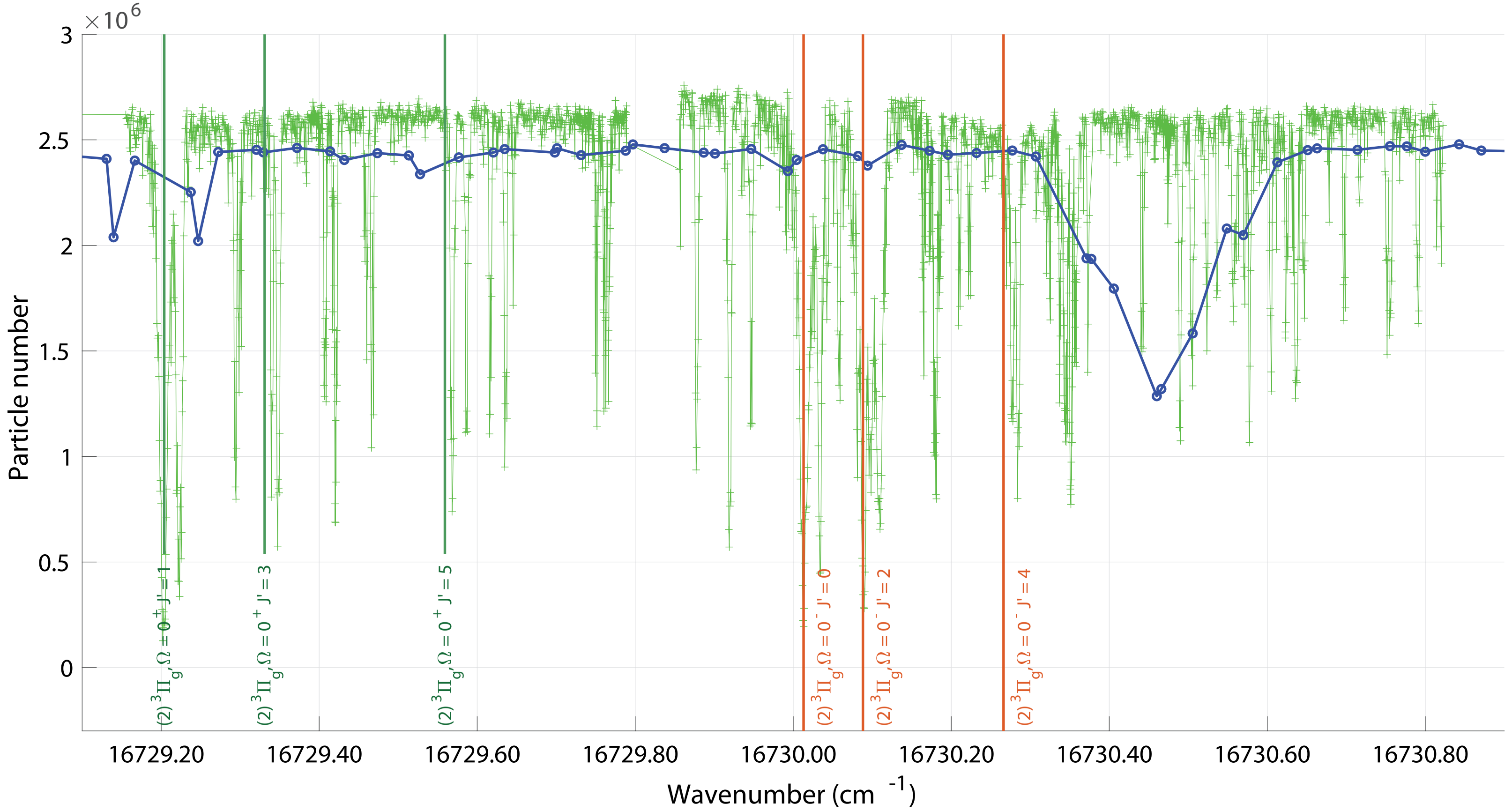

FIGURE B.1: Comparison between cw (green) and pulsed laser (blue) spectroscopy. The step size for the pulsed measurement is 1 GHz and 10 MHz for the cw measurements. It shows that the pulsed spectroscopy can not resolve rotational structure and additionally that signal strengths also deviate a lot. For example in the region between 16729.4 and 16730cm^{-1}, the cw recordings reveal lots of signals corresponding to molecular transitions while the pulsed recordings show very signals comparable to the noise level.

B.1.1 Further investigation of unassigned lines

The pulsed spectrum contains lines that are neither found in Ascoli's dataset nor identified through high-resolution spectroscopy in Ulm. These lines have been numbered as <unassigned> in Figures 4.5 and 4.4.
All lines except for line (6) for ^{87}Rb could not be observed and confirmed using cw spectroscopy. This particular signal is characterized by three sharp features, visible in both REMPI and photoassociation spectroscopy, with splittings of 380 MHz and 560 MHz. We further investigated the influence of an external magnetic field and observed shifts in the corresponding lines, see Fig. B.2 (b) and (c). We included a frequency shift due to the Zeeman effect with respect to $F_{f_a f_b} = 211, m_{f_{a,b}} = -1$, see Fig. B.2. The three red vertical lines in Fig. B.2 (a) have been recorded in a photoassociation spectroscopy as well. Compared to typical signal strength belonging to $(2)^1\Sigma_u^+$ or $(2)^3\Pi_g$, the signals shown here appear to be significantly stronger which might indicate that their origin is not related to the 5s + 4d asymptote.

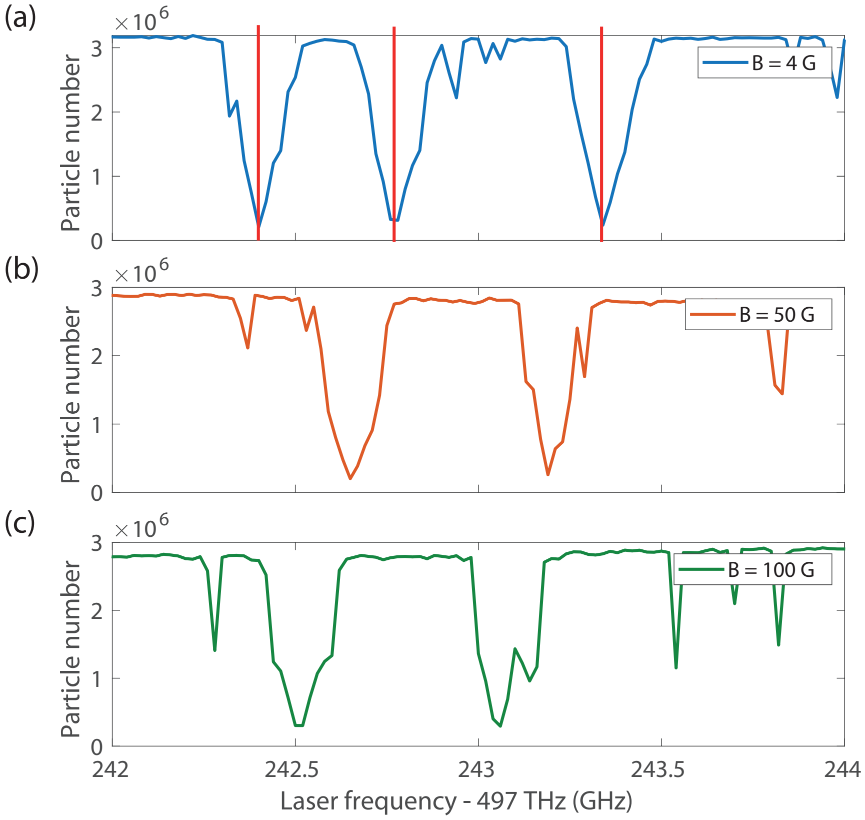

FIGURE B.2: High resolution recordings around 16585 cm^{-1} for ^{87}Rb. For a more detailed discussion, see text. The origin of the signals is still an open question which has to be clarified in the future.

For ^{85}Rb, it was also not possible to confirm the unassigned lines through cw spectroscopy, as no signal was detected in these regions. However, additional signals were found very close to predictions for Rydberg transitions in the cw recordings. Besides that, we could not detect further signals near other predictions of Rydberg lines in cw spectroscopy, which suggests that the observed lines may have a different origin. These signals also stand out due to three sharp features, which show splittings of a few hundred MHz, as seen in Fig. B.3 (a) to (c). The observed signal in Fig. B.3 (b) is close to a (two-photon) Rydberg transition to the atomic 17D state whereas the signal in Fig. B.3 (c) is close to 18D. Interestingly, the signal in Fig. B.3 (a) appears very close to a $(2)^1\Sigma_u^+$ state with only a separation of $0.43\,\mathrm{cm}^{-1}$.

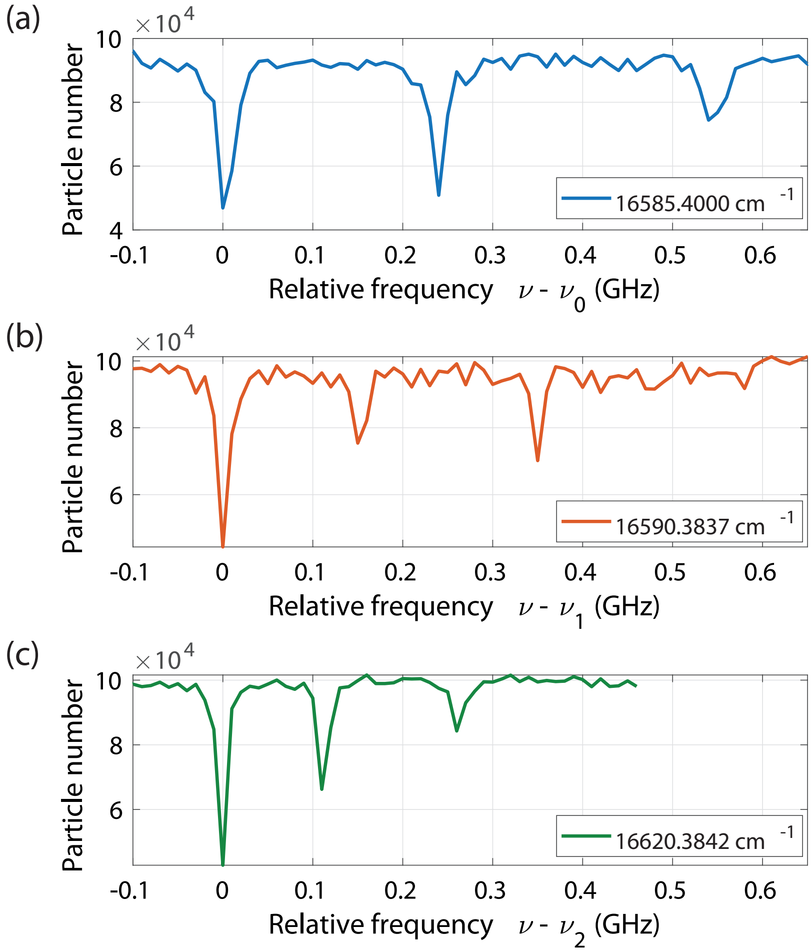

FIGURE B.3: High resolution recordings of unassigned lines for ^{85}Rb. For a more detailed discussion, see text. The origin of the signals is still an open question which has to be clarified in the future.

Another intriguing signal was found at 16782 cm^{-1} for ^{85}Rb. This signal is characterized by three photoassociation lines and several additional transitions observed in REMPI spectroscopy. Based on the positions of these additional signals, it could be that the excitation involves molecules produced via three-body recombination (TBR) which makes this observation very interesting. However, a definitive identification of this signal has not yet been achieved using possible rotational splittings of the excited state.

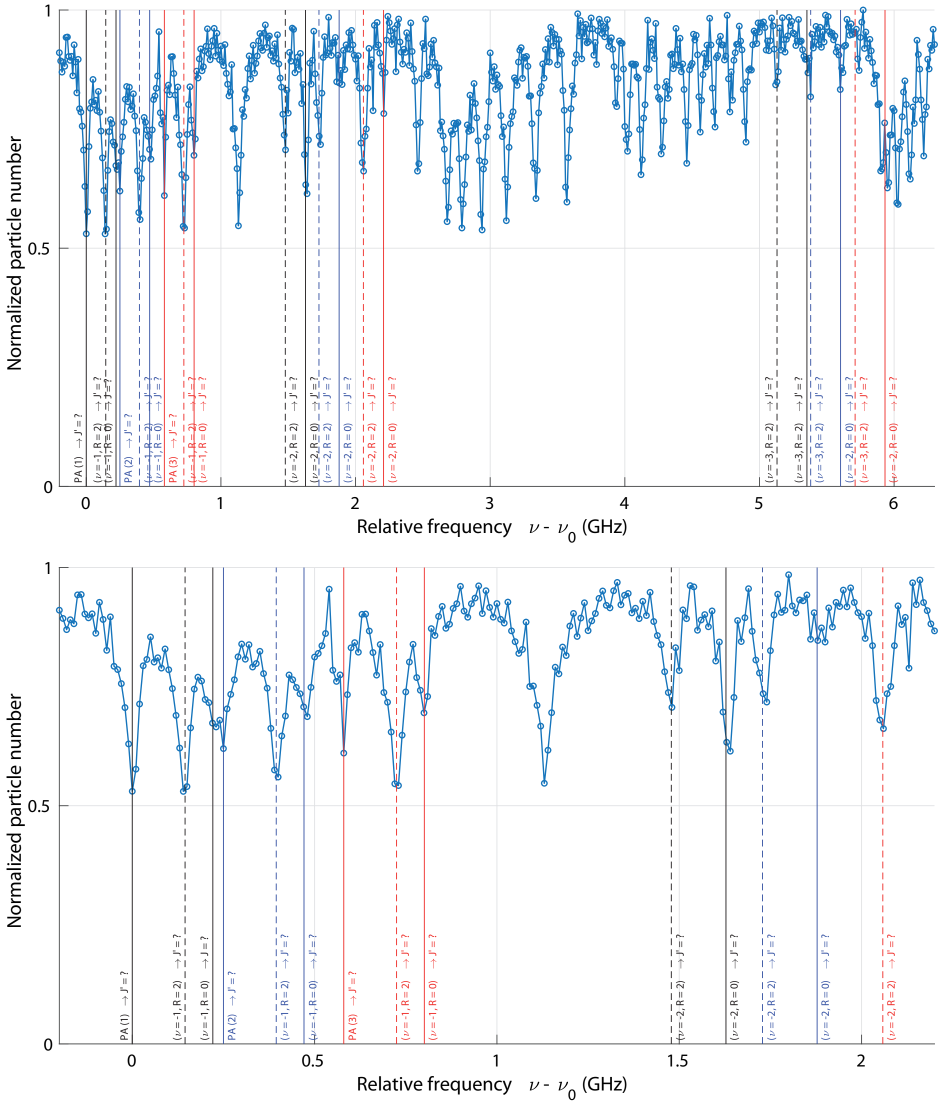

FIGURE B.4: High resolution recordings around 16782 cm^{-1} for ^{85}Rb. For a more detailed discussion, see text. The origin of the signals is still an open question which has to be clarified in the future.

B.2 Recorded atomic Rydberg excitations

The following sections discusses the strong signals in the pulsed spectrum (Figs. 4.5 and 4.4) that could not be attributed to any molecular transitions. We found that the pulsed system can also excite atoms into a Rydberg state. It became particularly apparent when signals with increasingly smaller intervals were detected in the ^{85}Rb data set, which could not be explained by a vibrational progression of the molecules. This process is energetically only possible if two identical photons from the pulsed laser are involved.
We used the Alkali-Rydberg-Calculator [131] to compute Rydberg transitions for the atoms. We started from the ground state of the Rb atoms $n = 5, l = 0$

TABLE B.1: Comparison of experimental observations and calculations for selected atomic Rydberg transitions for ^{87}Rb. For excited S states, principle quantum numbers n = 15 to 29 have been observed and for D states, n goes from 13 to 27. The experimental uncertainty is about 0.1 cm^{-1} due to the linewidth of the pulsed laser system.

Principal quantum number n	Experimental obs. (cm^{-1})	Calculation (cm^{-1})	Experimental obs. (cm^{-1})	Calculation (cm^{-1})
	S (J = 1/2)		D (J = 3/2)	
13	-	-	16441.68	16441.5738
14	-	-	16502.91	16502.8306
15	16455.81	16455.8196	16551.21	16551.1434
16	16514.02	16514.0291	16589.97	16589.9161
17	16560.10	16560.1026	16621.54	16621.5038
18	16597.19	16597.1939	16647.61	16647.5774
19	16627.49	16627.4949	16669.38	16669.3491
20	16652.56	16652.5675	16687.74	16687.7155
21	16673.54	16673.5490	16703.37	16703.3513
22	16691.28	16691.2833	16716.79	16716.7721
23	16706.40	16706.4075	16728.39	16728.3772
24	16719.40	16719.4099	16738.49	16738.4800
25	16730.66	16730.6696	16747.34	16747.3289
26	16740.48	16740.4846	16755.13	16755.1232
27	16749.09	16749.0920	16762.03	16762.0240
28	16756.68	16756.6820	-	-
29	16763.40	16763.4088	-	-

(S) and calculated transitions to (n', S') or (n', D') where n (n') represents the principle quantum number of the ground state (excited state) and S (S') or $D(D')$ the angular momentum quantum number of the ground state (excited state). In our calculations, hyperfine splitting was initially neglected but later added to allow comparison with the experimental data. The factor that needs to be added depends on the isotope: -0.28497 cm^{-1} for ^{87}Rb and -0.1181379 cm^{-1} for ^{85}Rb.

According to the selection rule for dipole transitions $\Delta l = \pm 1$, it becomes clear that, starting from an $l = 0$ (S) state, only transitions to $l' = 0$ (S') or $l' = 2$ (D') are possible with two photons involved. This was confirmed by the spectroscopic observations, as no transitions to $l' = 1$ (P') could be observed. Tables B.2 and B.1 show the comparison between experimental observations and calculations using ARC. For both isotopes, there is a good agreement between theory and experiment within the experimental uncertainty.

TABLE B.2: Comparison of experimental observations and calculations for selected atomic Rydberg transitions for ^{85}Rb. For excited S states, principle quantum numbers n = 15 to 29 have been observed and for D states, n goes from 13 to 27. The experimental uncertainty is about 0.1 cm^{-1} due to the linewidth of the pulsed laser system.

Principal quantum number n	Experimental obs. (cm^{-1})	Calculation (cm^{-1})	Experimental obs. (cm^{-1})	Calculation (cm^{-1})
	S (J = 1/2)		D (J = 3/2)	
13	-	-	16441.47	16441.5707
14	-	-	16502.79	16502.8274
15	16455.71	16455.8165	-	16551.1402
16	16513.92	16514.0259	16589.86	16589.9130
17	16559.99	16560.0995	16621.36	16621.5006
18	16597.15	16597.1908	16647.55	16647.5742
19	16627.41	16627.4918	16669.27	16669.3459
20	16652.47	16652.5643	16687.74	16687.7123
21	16673.54	16673.5458	16703.25	16703.3481
22	16691.28	16691.2801	16716.69	16716.7689
23	16706.42	16706.4044	16728.26	16728.3740
24	16719.38	16719.4068	16738.43	16738.4767
25	16730.65	16730.6664	16747.24	16747.3257
26	16740.40	16740.4814	16755.12	16755.1200
27	16749.01	16749.0888	16761.97	16762.0208
28	16756.65	16756.6788	16768.08	16768.1596
29	16763.27	16763.4056	16773.56	16773.6446
30	16769.32	16769.3954	16778.46	16778.5655
31	16774.68	16774.7521	16782.97	16782.9970
32	16779.49	16779.5617	-	-
33	16783.97	16783.8964	-	-

Appendix C

Energy-scaling of the product state distribution for three-body recombination of ultracold atoms

This appendix contains an original reprint of a publication to which I contributed during my doctoral thesis. The content of this chapter is published in Ref. [56]. The experimental part of this work was conducted in the BaRbIE lab under the supervision of postdoctoral researcher Shinsuke Haze. My contribution to this publication involved supporting lab work and assisting in the execution of the experiments.

Shinsuke Haze, Jinglun Li, Dominik Dorer, José P. D'Incao, Paul S. Julienne, Eberhard Tiemann, Markus Deiß and Johannes Hecker Denschlag

"Energy-scaling of the product state distribution for three-body recombination of ultracold atoms", *Phys. Rev. Res.* **5**, 013161 (2023).
DOI: `https://doi.org/10.1103/PhysRevResearch.5.013161`

PHYSICAL REVIEW RESEARCH **5**, 013161 (2023)

Energy scaling of the product state distribution for three-body recombination of ultracold atoms

Shinsuke Haze,[1,*] José P. D'Incao,[1,2] Dominik Dorer,[1] Jinglun Li,[1] Markus Deiß,[1] Eberhard Tiemann,[3]
Paul S. Julienne,[4] and Johannes Hecker Denschlag[1,†]
[1]*Institut für Quantenmaterie and Center for Integrated Quantum Science and Technology (IQ^{ST}), Universität Ulm, 89069 Ulm, Germany*
[2]*JILA, NIST, and Department of Physics, University of Colorado, Boulder, Colorado 80309, USA*
[3]*Institut für Quantenoptik, Leibniz Universität Hannover, 30167 Hannover, Germany*
[4]*Joint Quantum Institute, University of Maryland and National Institute of Standards and Technology (NIST), College Park, Maryland 20742, USA*

(Received 8 November 2022; accepted 2 February 2023; published 3 March 2023)

Three-body recombination is a chemical reaction where the collision of three atoms leads to the formation of a diatomic molecule. In the ultracold regime it is expected that the production rate of a molecule generally decreases with its binding energy E_b, however, its precise dependence and the physics governing it have been left unclear so far. Here we present a comprehensive experimental and theoretical study of the energy dependency for three-body recombination of ultracold Rb. For this, we determine production rates for molecules in a state-to-state resolved manner, with the binding energies E_b ranging from 0.02 to 77 GHz × h. We find that the formation rate approximately scales as $E_b^{-\alpha}$, where α is in the vicinity of 1. The formation rate typically varies only within a factor of two for different rotational angular momenta of the molecular product, apart from a possible centrifugal barrier suppression for low binding energies. In addition to numerical three-body calculations we present a perturbative model which reveals the physical origin of the energy scaling of the formation rate. Furthermore, we show that the scaling law potentially holds universally for a broad range of interaction potentials.

DOI: 10.1103/PhysRevResearch.5.013161

I. INTRODUCTION

When a molecule is formed in a chemical reaction there are often thousands of quantum states it can end up in, due to the various electronic, vibrational, rotational, and spin degrees of freedom. Generally, the product population is not uniformly distributed over these possible product states, but rather follows characteristic propensity rules. Finding and identifying propensity rules can provide deep insights on the basic principles which drive and govern specific reactions. Furthermore, the propensity rules can be used to develop predictions and approximations, especially when full detailed calculations are highly complex, such as, e.g., for reactions involving more than two atoms.

Propensity rules can be extracted experimentally from state-to-state measurements where the reactants are prepared in well defined quantum states and product states are detected in a quantum state resolved way. In recent years, there has been rapid progress in the methodology of state-to-state chemistry using atomic and molecular beams [1–4] or ultracold samples [5,6]. Individual partial waves of product states have been resolved (see, e.g., [7–9]) and spin conservation propensity rules have been observed with hyperfine and rotational states [10–14].

Three-body recombination is one of the most fundamental and ubiquitous chemical reactions. In a collision of three atoms, two combine to form a molecule and the third atom enables the dissipation of the released energy. The released energy consists of the initial collision energy plus the molecular binding energy E_b and is converted into relative motion between the molecule and the third atom. Experiments have shown that three-body recombination at ultracold temperatures generally produces the most weakly bound molecular state (see, e.g. [11,15–17]). Semiclassical and fully quantum mechanical treatments have been carried out. They generally indicate that there is a propensity towards weakly bound molecular product states [11,18–20]. However, precisely how the molecular production rate decreases with the binding energy has not been clarified yet. Reference [21], e.g., suggested the suppression to be exponential in triatomic reactions. A recent calculation of three-body recombination of hydrogen atoms at room temperature predicted a molecular production rate $\propto E_b^{-1.5}$ for recombination towards deeply bound molecules, which was enhanced by the Jahn-Teller effect [20].

Here we investigate the rate decrease both experimentally as well as theoretically by studying three-body recombination of ^{87}Rb atoms at ultralow collision energies. We find a $E_b^{-\alpha}$ power law for the molecular production rate where the exponent α is close to 1. This result differs from a previous scaling estimate of $\alpha = 1/2$ which was based on studying bound states in a limited range of binding energies [11]. We have

---

[*] shinsuke.haze.qiqb@osaka-u.ac.jp
[†] johannes.denschlag@uni-ulm.de

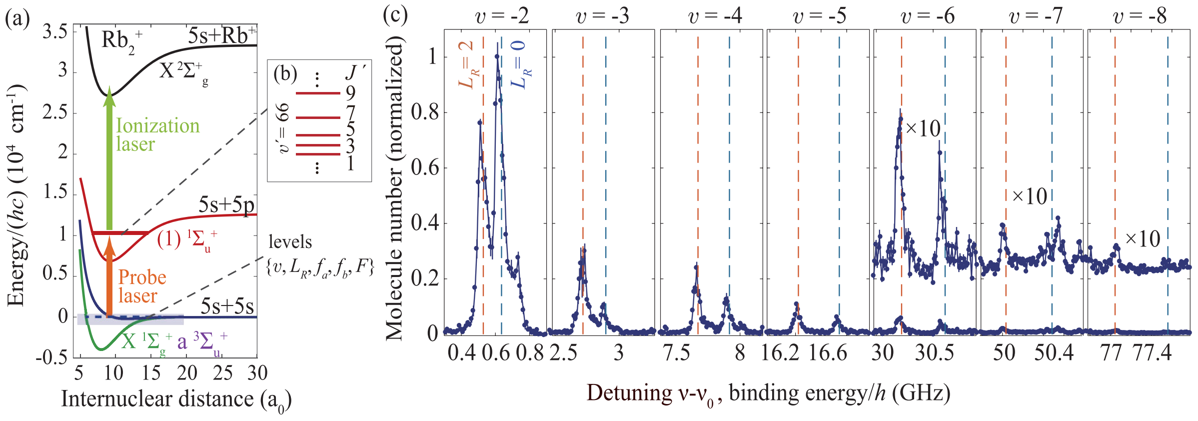

FIG. 1. (a) Two-color REMPI scheme for state-selective detection of molecules. Probe and ionization lasers have a wavelength of 1065 nm and 544 nm, respectively. (b) Rotational level structure of the relevant molecular states with negative parity. (c) Various segments of REMPI detection signals of $(\upsilon, L_R = 0, 2)$ product molecules as a function of the probe laser frequency ν. Here $\nu_0 = 281445.045$ GHz, corresponding to the transition from the $5s + 5s$ asymptote to $\upsilon' = 66,\ J' = 1$. The vibrational quantum numbers υ are given on the top of the figure and the rotational quantum numbers L_R are indicated by the color coding of the dashed vertical lines ($L_R = 0$ and 2 in blue and red, respectively). These dashed lines are expected frequency positions for the given states obtained from coupled-channel calculations. For smaller signals ($\upsilon = -6, -7, -8$) magnifications by a factor of 10 are also shown. The data for the most weakly bound state $\upsilon = -1,\ L_R = 0$ are not presented, because the corresponding line is largely drowned by a neighboring photoassociation line [11].

now extended this range by roughly a factor of ten, on both the experimental and theoretical side. Our experimental data comprise 30 final quantum channels of detected molecules with binding energies of up to $E_b = 77$ GHz $\times\, h$.

Our numerical calculations for the three-body recombination rates $L_3(E_b)$ are in remarkable agreement with our measurements, especially for those product channels where molecules with low rotational angular momentum L_R are formed. Besides the general $E_b^{-\alpha}$ trend of $L_3(E_b)$ the calculations also reproduce prominent deviations from this trend at particular binding energies E_b. These deviations might be interpreted as interference effects of various kinds.

Our perturbative model indicates that for each angular momentum $L_R > 0$ there is a critical binding energy $E_c(L_R)$ so that for $E_b > E_c(L_R)$ the trend of the partial recombination rate will be described by $L_3(E_b, L_R) = cE_b^{-\alpha}$, where c is a constant. We find that the factor c is roughly independent of L_R. For $E_b < E_c(L_R)$ there is a suppression of $L_3(E_b, L_R)$ which can be explained as the effect of an angular momentum barrier in the exit channel. As a result, this suggests that only molecular states with small L_R will significantly contribute to molecular production at low binding energies E_b.

Finally, we show that the $E_b^{-\alpha}$ scaling law can be also derived theoretically in an analytic, perturbative approach. We find that within this approach the $E_b^{-\alpha}$ scaling is quite independent on the long-range behavior of the interaction potential between two atoms. Specifically, potentials with a power-law tail $-C_n/r^n$ for $n = 3, 4$ or 6, or the Morse potential, as well as the contact potential have α values in the range [0.91, 1].

Within the framework of the perturbative calculations the scaling of the rate constant $L_3(E_b)$ is largely determined by $|\phi_d(\sqrt{E_b m/3})|^2$, where ϕ_d is the diatomic molecular wave function in momentum representation and m is the atomic mass. It turns out that this part of the momentum wave function is linked to the molecular wave function in real space in the vicinity of the classical outer turning point of the molecular potential (at energy $-E_b$). This indicates that the outer classical turning point marks a typical distance for the recombination to occur.

II. EXPERIMENT

In our experiments we prepare an ultracold cloud of 5×10^6 ^{87}Rb atoms in a far-detuned 1D optical lattice trap ($\lambda = 1064$ nm, trap depth $\approx 10\,\mu$K $\times\, k_B$) combined with an optical dipole trap so that we obtain a trap frequency of $2\pi \times 23$Hz in the transverse direction. The atoms are spin-polarized in the hyperfine state $f = 1,\ m_f = -1$ of the electronic ground state and have a temperature of about 750 nK. Our measurements are carried out at a low external magnetic field of about 4 G. We hold the atom cloud in the trap for a duration of 500 ms during which Rb$_2$ molecules are spontaneously produced via three-body recombination in the coupled $X^1\Sigma_g^+ - a^3\Sigma_u^+$ molecular complex, below the $5S_{1/2} + 5S_{1/2}$ atomic asymptote. The molecules are state-selectively ionized via resonance-enhanced multiphoton ionization [REMPI] [see Fig. 1(a) and Appendix A for details], and then trapped and detected as ions in a Paul trap at a distance of 50 μm (see Appendix B for details). In brief, a first REMPI laser (the probe laser) resonantly excites such a molecule to the intermediate level $\upsilon' = 66$, J' of the state $A^1\Sigma_u^+$ using a wavelength of about 1065 nm [22,23]. Here υ' is the vibrational quantum number and J' is the total angular momentum quantum number excluding nuclear spin. From the intermediate level a second laser (the ionization laser) at a wavelength of about 544 nm resonantly excites the molecule to a state above the Rb$_2^+$ ionization threshold, so that the molecule can autoionize. In one experimental run we can detect and count up to ≈ 70 ions in the Paul trap. The ion number scales linearly with the molecule number. The corresponding scaling factor

η is the detection efficiency of a molecule. As discussed in Appendixes A and C, η is roughly constant over the range of bound states investigated in this work, and its value is $\eta \approx 4.8 \times 10^{-3}$. A REMPI spectrum of a particular product state is obtained by scanning the probe laser frequency in steps of typically 5 MHz. Our setup features an improvement of the product state signals and the sensitivity by a factor of $\approx$25 as compared to previous work [11], extending our detection range of binding energies to about 80 GHz × h, which was instrumental for the present work (for details, see Appendix D).

In the following we specify molecular states by their vibrational quantum number υ and their rotational quantum number L_R only, which is sufficient due to the conservation of the hyperfine spin state in the reaction process [24]. Figure 1(c) shows product state spectra for molecules with $L_R = 0$ or 2, and with υ ranging from -2 to -8. We note that whenever υ is negative, it is counted downwards from the atomic $f_a = f_b = 1, m_{fa} = m_{fb} = -1$ asymptote, starting with $\upsilon = -1$ for the most weakly bound vibrational level. The most deeply bound state, $(\upsilon = -8, L_R = 0)$, has a binding energy of 77 GHz × h. Here all signals are obtained using the same intermediate state $J' = 1$ for REMPI. The frequency reference ν_0 corresponds to the photoassociation transition towards this intermediate state such that, at a resonance position, $(\nu - \nu_0) \times h$ directly represents the binding energy of the initially produced molecular state. Our data clearly show that the production rate of molecules for a given rotational level L_R generally drops with the binding energy E_b. The drop is significant over the investigated range of E_b. The relative strength of $L_R = 0$ and 2 signals, however, can vary for different vibrational levels υ. Large molecular signals such as, e.g., obtained for $\upsilon = -2$ correspond to 63(3) produced ions per run whereas typical background signals are 0.69(0.15) ions per run (see also Fig. 11 in Appendix D). In the measurements of Fig. 1(c) the number of repetitions of the experiment per data point was gradually increased from 5 to 40 for increasing binding energy, in order to improve the visibility of smaller signals. We assign the signals in our REMPI spectra by comparing their frequency positions to those obtained from close-coupled channel calculations (see, e.g., [10,11]) and by observing characteristic rotational ladders, since any molecular state with $L_R > 0$ can be detected via two different rotational states $J' = |L_R \pm 1|$ [see Appendix E, not shown in Fig. 1(c)]. The deviations between calculated [dashed vertical lines in Fig. 1(c)] and measured resonance frequency positions are typically smaller than ~30 MHz and arise mainly from daily drifts of our wavelength meter.

III. QUANTITATIVE ANALYSIS

We now carry out a quantitative analysis of the observed population distribution. Figure 2 shows measured (scaled) and calculated partial rate constants $L_3(E_b) \equiv L_3(\upsilon, L_R)$ for the production of $(\upsilon,\ L_R)$ molecules at a temperature of 0.8 μK. The experimental values for $L_3(\upsilon, L_R)$ were obtained by multiplying the measured ion numbers with a single calibration factor for all detected (υ, L_R) states. This factor was chosen to optimize the agreement between experiment and theory (Appendix C). As can be seen from Fig. 2, the theoretical predictions reproduce remarkably well the relative strengths of the state dependent rates $L_3(\upsilon, L_R)$ obtained from the experiments. The calculations are based on solving the three-body Schrödinger equation in an adiabatic hyperspherical representation [18,25], using a single-spin model as described in Appendix F (see also Ref. [11]). Within our model the ^{87}Rb atoms interact via pairwise additive long-range van der Waals potentials with a scattering length of 100.36 a_0 [26]. The potentials are truncated and support 15 $L_R = 0$ molecular bound states, and a total of 240 bound states. We calculated the theory data point for $L_R = 8$, $\upsilon = -3$ using a model potential with 12 s-wave bound states because for 15 s-wave bound states a numerical instability occurs specifically for this level.

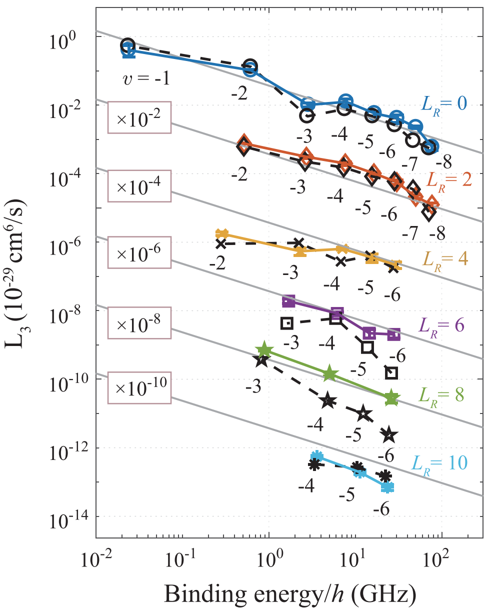

FIG. 2. Measured (scaled) and calculated rate constants $L_3(\upsilon, L_R)$ for product molecules (υ, L_R) as a function of their binding energy E_b. The rotational quantum numbers L_R are indicated by different plot symbols (black: calculations; colors: experiment). For each sequence of states with the same L_R the vibrational quantum number υ is given below the data points. For better visibility the data for each L_R are shifted in vertical direction by multiplying them with 10^{-L_R}. The gray solid lines show the energy scaling $(E_b/\mathrm{GHz} \times h)^{-0.8} \times 0.2 \times 10^{-29}$ cm^6/s.

Figure 2 reveals that the $L_3(\upsilon, L_R)$ rate roughly follows the overall scaling of $E_b^{-\alpha}$ for all rotational states. A fit analysis to the experimental data yields a scaling factor $\alpha = 0.80(\pm 0.14)$ (see gray solid lines), while the fit to the theoretical data yields $\alpha = 0.77(\pm 0.10)$. We point out that all gray solid lines in Fig. 2 correspond to exactly the same function, $(E_b/\mathrm{GHz} \times h)^{-0.8} \times 0.2 \times 10^{-29}$ cm^6/s. For better visibility these lines along with the respective data points have been shifted in vertical direction by multiplying them with 10^{-L_R}. We notice that the measured data for $L_R = 2$ are all located above the gray line while the data for $L_R = 4$ or 10 are all below the gray line. This indicates that there is a systematic dependence of $L_3(E_b)$ on L_R, as already discussed in [11]. Nevertheless, considering the overall range of L_3 and L_R in our data, this variation of $L_3(E_b)$ with L_R is still comparatively small, typically within a factor of 2. Therefore, to a first approximation, the production rate does seem to be quite independent of the molecular rotation L_R. This fact might be somewhat counterintuitive given that the atoms initially collide with vanishing angular momenta, and therefore products with small angular momenta would seem to be naturally preferable.

We note that there are considerable variations around the general $E_b^{-\alpha}$ scaling trend. For example, the rate for the state $\upsilon = -3, L_R = 0$ is significantly lower than the rate for the more-deeply bound state $\upsilon = -4, L_R = 0$. Remarkably, even such individual variations are largely reproduced by our numerical calculations. In general, the theoretical and experimental data curves are very similar, especially for the low rotational states $L_R = 0$ and $L_R = 2$. This suggests that our three-body model is quite accurate and that it should in principle be capable to track down how the deviations from the general scaling come about in individual cases. For example, we point to the experimental and theoretical data points for $\upsilon = -2$ and $L_R = 4$, which are located below the $E_b^{-\alpha}$ scaling trend. This suppression may be due to an angular momentum barrier effect which we will discuss in Sec. V B.

IV. PERTURBATIVE APPROACH

In order to gain a deeper insight into the observed energy scaling we discuss in the following a perturbative model for the partial three-body recombination rates $L_3(\upsilon, L_R)$. Generally, the rates $L_3(\upsilon, L_R)$ towards each specific molecular product $d = (\upsilon, L_R)$ are given by [27] (see also Appendix G)

$$L_3(\upsilon, L_R) = \frac{12\pi m}{\hbar}(2\pi\hbar)^6 q_d |\langle\psi_f|U_0(E)|\psi_{\text{in}}\rangle|^2, \qquad (1)$$

where m represents the mass of an atom. $|\psi_{\text{in}}\rangle$ is the initial state, consisting of three free atoms each propagating as a plane wave with essentially vanishing momentum. $|\psi_f\rangle$ is the final state of a free atom and a free molecule. Atom and molecule are asymptotically propagating as plane waves with relative momentum q_d which is fixed by the molecular binding energy E_b and the total energy E of the three-body system via $\frac{3q_d^2}{4m} - E_b = E$, where we use the center of mass system as a reference. In Eq. (1), $U_0(E)$ represents a three-body transition operator which describes the transition process between the states. It can be approximated by a perturbative expansion (Appendix G) derived from the Alt-Grassberger-Sandhas (AGS) equation [27–29]. To the leading order of the expansion, we have a process where atoms a and b of the three free atoms a, b, and c collide to exchange a momentum $\mathbf{q}_d$. During this collision atom b is scattered into a molecular bound state with atom c. This is shown schematically in the inset of Fig. 3. The initial momenta of the atoms are 0. After the collision atom a remains free and carries away the momentum $\mathbf{q}_d$ and a corresponding part of the released binding energy. The formed molecular bound state ϕ has a total momentum $-\mathbf{q}_d$ and the relative momentum between its atomic constituents is $(-\mathbf{q}_d/2)$. Apart from constants, the result of the calculation is

$$L_3(\upsilon, L_R) \propto q_d \left|\phi_d\left(\frac{1}{2}q_d\right)\right|^2 |t_{\text{h}}(q_d)|^2. \qquad (2)$$

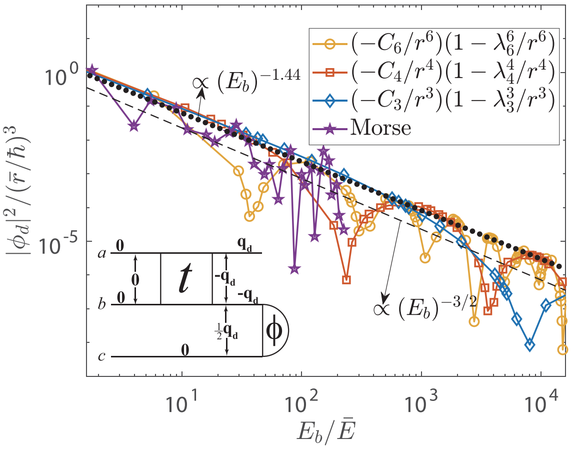

FIG. 3. Plot of $|\phi_d(\sqrt{E_b m/3})|^2 \propto L_3(E_b)/\sqrt{E_b}$ vs E_b for various two-body potentials. These are the potentials with the power-law tail, $\sim -C_n/r^n$ for $n = 3, 4$ or 6, and the Morse potential $D_e[e^{-2a(r-r_e)} - 2e^{-a(r-r_e)}]$ (see legend). We use $\bar{E} = \hbar/m\bar{r}^2$, with $\bar{r} = \frac{1}{2}(mC_n/\hbar^2)^{1/(n-2)}$ for the power-law potentials and $\bar{r} = a$ for the Morse potential, respectively. The values for λ_n and D_e are chosen such that the potentials have 14 or 15 s-wave bound states. The shown points correspond to bound states with $\upsilon \geqslant -13$. In order to map out the function $|\phi_d(\sqrt{E_b m/3})|^2$ better we show data points for four different values for λ_n (for each n) or for D_e (see text). The dotted line is a power-law fit to the upper envelope of the data points for the $-C_6/r^6$ potential as well as the other potentials. The dashed line represents the scaling for contact interactions. For $n = 6$ the energy range considered in this figure corresponds to [0.01 . . . 100] GHz × h for ^{87}Rb atoms. The inset describes the scattering process in the perturbative approximation (see Appendix G). Horizontal lines represent atoms and the numbers above these lines denote single-atom momenta. The relative momentum between two atoms is indicated by a number that connects to the corresponding horizontal lines by arrows.

Here $\phi_d(p = \frac{1}{2}q_d)$ corresponds to the radial part of the molecular wave function in momentum space. It is normalized according to $\int |\phi_d(p)|^2 p^2\, dp = 1$. The factor $t_{\text{h}}(p' = q_d) \equiv \langle p' = q_d|t^s(0)|p = 0\rangle$ is the matrix element of the s-wave component t^s of the two-body transition operator t for the two-body collision and we have set $E = 0$. Here p (p') represent the relative momenta of the incoming (outgoing) two colliding atoms, respectively. Within the perturbative approximation, the E_b scaling of $L_3(\upsilon, L_R)$ can result only from two-body quantities, i.e., E_b, ϕ_d and t_{h}. Since $E \approx 0$, one obtains $q_d \approx 2\sqrt{E_b m/3}$.

In order to analyze the scaling of $L_3(\upsilon, L_R)$ with the molecular binding energy E_b, we discuss $\phi_d(\sqrt{E_b m/3})$ and $t_{\text{h}}(2\sqrt{E_b m/3})$ separately. We find that $t_{\text{h}}(p)$ oscillates but its amplitude varies only gently with p until the deeply bound states are reached [see Fig. 13(a) in Appendix G]. Therefore, $t_{\text{h}}(2\sqrt{E_b m/3})$ cannot strongly contribute to an overall scaling with E_b for the three-body recombination rate. In contrast to that, $\phi_d(\sqrt{E_b m/3})$ which is obtained from two-body bound state calculations, vanishes quickly with increasing E_b. This is shown in Fig. 3 (yellow data points) for atoms interacting via the van der Waals potential. Besides the overall decrease of $|\phi_d(\sqrt{E_b\, m/3})|^2$ for growing E_b, there are also oscillations. The sharp drops in these oscillations correspond to the nodes of the various momentum wave functions ϕ_d for the bound states with energy E_b. While the oscillations lead to some scatter of the data, the upper envelope of the data points indicates an overall power-law scaling of the amplitude. A fit to this envelope (dotted line in Fig. 3) gives $|\phi_d(\sqrt{E_b\, m/3})|^2 \propto E_b^{-1.44\pm0.03}$ which yields $L_3 \propto E_b^{-0.94\pm0.03}$. This result agrees quite well with our full calculations from Fig. 2. We note that in the shown energy range there are only 13 bound states in the van der Waals potential, resulting in 13 data points. In order to map out in more detail the functional form of $|\phi_d(\sqrt{E_b\, m/3})|^2$ in Fig. 3 we have slightly varied λ_6 over four different values (while keeping the number of bound states in the potential constant). The variation in λ_6 leads to variations of E_b and therefore also of ϕ_d and the scattering length a. When we present all these data points together, a quasicontinuous curve is obtained. We note that the oscillating amplitude of $t_{\mathrm{h}}(p)$, which is nearly constant for a fixed scattering length a, can depend on a.

V. ENERGY SCALING FOR GENERAL LONG-RANGE POTENTIALS

Remarkably, we find that the scaling law is similar for a range of different two-body interaction potentials, such as the Morse potential and potentials of the form $V(r) = -C_n/r^n(1-\lambda_n^n/r^n)$. Here the parameter n is typically $n = 3, 4$ or 6, and λ_n is a short-range parameter which defines the inner barrier. The case $n = 6$ corresponds to the Lennard-Jones potential which was already discussed in the previous section. The corresponding functions $|\phi_d(\sqrt{E_b\, m/3})|^2$ are shown in Fig. 3. Clearly, their envelopes roughly decrease in a similar manner, i.e., $\approx E_b^{-1.44\pm0.03}$. Furthermore, we also consider contact interactions between the atoms. For these we use $\phi_d(p) = \frac{2}{\sqrt{\pi}}\frac{(m\,E_b)^{1/4}}{p^2+m\,E_b}$ and analytically obtain from Eq. (2) the scaling to be exactly $|\phi_d(\sqrt{E_b\, m/3})|^2 \propto 1/E_b^{3/2}$ (see black dashed line in Fig. 3), corresponding to $L_3(E_b) \propto 1/E_b$. Therefore, even the results for contact interaction are in relatively good agreement with our other numerical and the experimental results.

In the following we discuss how this similar scaling for the different long-range potentials can be explained. We make use of approximate analytical wave functions for the molecular bound state. Let $\psi(r) = u(r)/r$ be the radial part of the molecular wave function with rotational angular momentum L_R. Here r is the internuclear distance between the two atoms. A typical example of the reduced radial wave function $u(r)$ is shown in Fig. 4(a). The Fourier transform of $u(r)/r$ generates the molecular wave function in momentum space

$$\phi_d(p) = \sqrt{\frac{2}{\pi}}\int_0^\infty r\, j_{L_R}(pr/\hbar)u(r)\,dr, \tag{3}$$

where j_{L_R} is the spherical Bessel function of the first kind of order L_R. A numerical analysis shows that the dominant contribution to $\phi_d(\sqrt{E_b m/3})$ comes from the last lobe of $u(r)$, which is located around the classical outer turning point r_0. In Fig. 4(b) we show the Fourier integral for the case $L_R = 0$ in an accumulated fashion $\phi^{\mathrm{acc}}(p;r) = \int_0^r \sin(pr/\hbar)u(r)\,dr/\int_0^\infty \sin(pr/\hbar)u(r)\,dr$, which verifies the dominant contribution of the last lobe. The turning point of the level [blue circle in Fig. 4(a)] is determined by $\tilde V(r_0) + E_b = 0$, where $\tilde V(r) = V(r) + \hbar^2 L_R(L_R+1)/(mr^2)$. The reduced radial wave function $u(r) = r\psi(r)$ in this region is approximated by $\tilde u(r) = \mathcal{N}^{1/2}\mathrm{Ai}[s(r-r_0)]$, where $\mathrm{Ai}(x)$ is the Airy function, $s = (mD/\hbar^2)^{1/3}$, $D = d\tilde V(r)/dr|_{r=r_0}$, and $\mathcal{N}$ is a normalization factor that ensures that $\tilde u(r)$ best matches $u(r)$ in the region. It turns out that to a good approximation $\mathcal{N} = sN$, where N is a constant independent of E_b [30]. We Fourier transform $\tilde u(r)$ and obtain

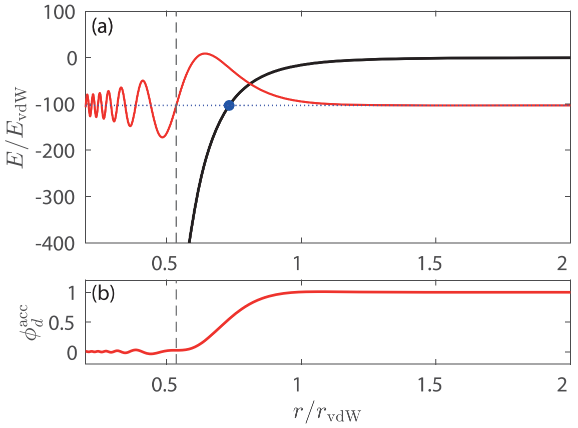

FIG. 4. (a) Typical example for a molecular wave function (red solid line) located in the $-C_6/r^6$ van der Waals potential (black solid line). The blue horizontal dotted line and the blue circle indicate the molecular level position $-E_b$ and the corresponding classical outer turning point, respectively. The vertical dashed line shows the starting position of the last lobe of the molecular wave function. (b) The accumulated Fourier integral $\phi_d^{\mathrm{acc}}(\sqrt{mE_b/3};r)$; see text. $E_{\mathrm{vdW}} = \hbar^2/mr_{\mathrm{vdW}}^2$ is the van der Waals energy, and $r_{\mathrm{vdW}} = \frac{1}{2}(mC_6/\hbar^2)^{1/4}$ is the van der Waals length.

$$\tilde\phi_d(p) = \sqrt{\frac{2N\hbar^2}{\pi s p^2}}\,g_d(p), \tag{4}$$

where

$$g_d(p) = \int_0^\infty \frac{p\tilde r}{s\hbar}\, j_{L_R}(p\tilde r/s\hbar)\mathrm{Ai}(\tilde r - \tilde r_0)\,d\tilde r. \tag{5}$$

Here $\tilde r = sr$, $\tilde r_0 = sr_0$. At $p = \sqrt{E_b m/3}$, we get

$$|\tilde\phi_d(\sqrt{E_b m/3})|^2 = \frac{6N\hbar^2}{\pi\, s m E_b}\,g_d^2(\sqrt{E_b m/3}), \tag{6}$$

which approximates $|\phi_d(\sqrt{E_b m/3})|^2$.

After this general discussion we now discuss the cases for $L_R = 0$ and $L_R > 0$.

A. Case: $L_R = 0$

For a $L_R = 0$ molecular state and $\tilde V(r) = -C_n/r^n$ the classical outer turning point is given by $r_0 = (C_n/E_b)^{1/n}$. From the derivative of the potential $\tilde V(r)$ we obtain for the parameter s (which we defined earlier in connection with the Airy

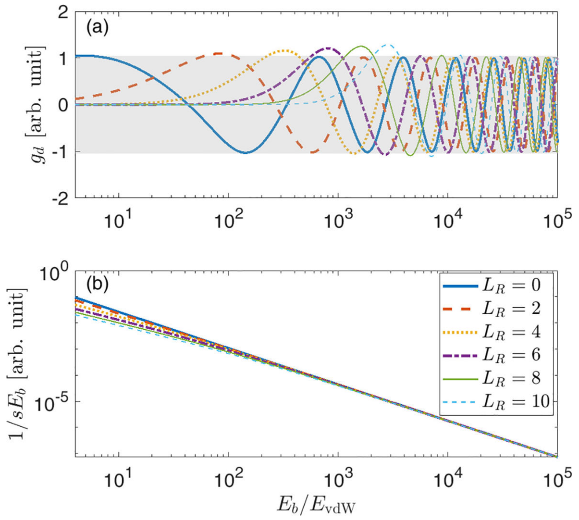

FIG. 5. (a) Plot of $g_d(\sqrt{E_b m/3})$ as a function of E_b for the partial waves $L_R \leqslant 10$ [see legend in (b)]. The gray area highlights the range of the oscillation for $L_R = 0$. (b) Plot of $1/(sE_b)$. For both (a) and (b) we use the $-C_6/r^6$ potential.

function)

$$s = (mn/\hbar^2)^{1/3} E_b^{(n+1)/3n} C_n^{-1/3n}. \tag{7}$$

Thus, the factor $6N\hbar^2/(\pi s m E_b)$ in Eq. (6) scales as $E_b^{-(4n+1)/3n}$. The other factor in Eq. (6), $g_d(\sqrt{E_b m/3})$, is plotted in Fig. 5(a) for $n = 6$, (blue line). $g_d(\sqrt{E_b m/3})$ oscillates between 1 and -1 with a constant amplitude, as indicated by the gray area. Therefore, $g_d(\sqrt{E_b m/3})$ does not contribute to an overall scaling of $|\phi_d(\sqrt{E_b m/3})|^2$ with E_b. This is similar as for $t_{\text{h}}(q_d)$ as mentioned in Sec. IV. The variation of $g_d(\sqrt{E_b m/3})$ merely leads to some scatter of L_3. Therefore, we ignore $g_d(\sqrt{E_b m/3})$ in the following discussion on scaling and obtain

$$|\phi_d(\sqrt{E_b m/3})|^2 \propto E_b^{-(4n+1)/3n} = E_b^{-\beta}. \tag{8}$$

For $n = 3, 4$ and 6, the exponent $\beta = (4n+1)/3n$ takes the values of 1.44, 1.42, and 1.39, which agree very well with our numerical results in the perturbative approach. For the scaling of L_3 we have $L_3 \propto E_b^{-\alpha}$, where $\alpha = \beta - 0.5$. It is remarkable that for any positive integer n the exponents are constrained to a narrow range, i.e., $\beta \in [1.33, 1.67]$ and $\alpha \in [0.83, 1.17]$. Considering that a real interaction potential can typically be expanded in terms of the $-C_n/r^n$ functions, these ranges should be valid quite generally. In fact, the range of $\alpha \in [0.83, 1.17]$ agrees with the exponent $\alpha = 0.8 \pm 0.14$ extracted from our experimental measurements within the range of uncertainty.

B. Case: $L_R > 0$

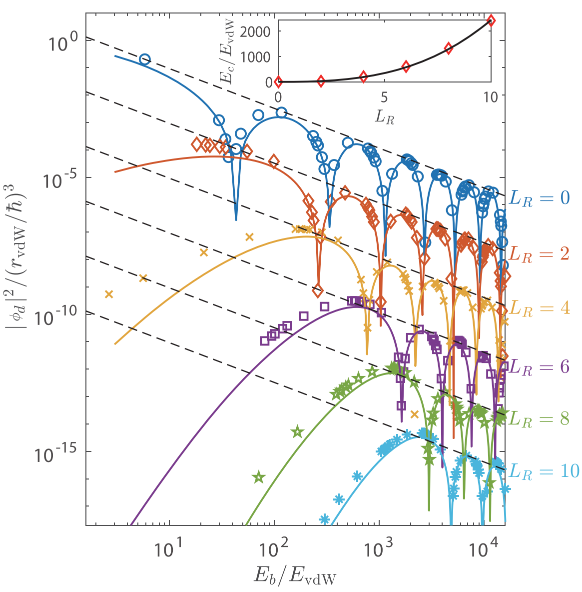

FIG. 6. Power-law scaling of $|\phi_d(\sqrt{E_b\, m/3})|^2 \propto L_3(E_b)/\sqrt{E_b}$ for various rotational angular momenta L_R. The data points are a full calculation for the Lennard-Jones potential $(-C_6/r^6)(1 - \lambda_6^6/r^6)$. As in Fig. 3 and Sec. IV, we have slightly varied λ_6 over seven different values while keeping the number of bound states in the potential constant. This helps to map out $|\phi_d(\sqrt{E_b\, m/3})|^2$ in detail. Therefore, although there are only eight bound states in the shown energy range, we obtain 55 data points. The solid lines are calculations for the Lennard-Jones potential using Eq. (6). The dashed lines show the $E_b^{-1.45}$ energy scaling for $|\phi_d|^2$, as determined by a fit to the upper envelope of the data set. For better visibility the data for $L_R > 0$ are shifted in vertical direction by multiplying them with 10^{-L_R}. We define E_c to be the energy at which the curve $|\phi_d|^2$ (for a given L_R) has its first maximum (coming from low energy). The inset shows E_c as a function of L_R (diamonds). The data are well described by Eq. (9) (solid line).

We now consider the case of rotational angular momentum $L_R > 0$. Because for this case we do not obtain a simple analytical expression for s as in Eq. (7), we present only numerical results. Figure 5(b) shows a plot of $1/(sE_b)$ for various L_R (and using the $-C_6/r^6$ potential as a typical example). Clearly, all curves are quite similar, especially for large E_b. The functions $g_d(\sqrt{E_b m/3})$ are shown in Fig. 5(a), as discussed before. They oscillate with a constant amplitude and therefore do not contribute to the energy scaling for large energies E_b. As a consequence, the energy scaling is quite independent on the rotational state L_R of the molecule. Figure 6 shows calculations for $|\phi_d(\sqrt{E_b\, m/3})|^2$ for various rotational angular momenta of the molecule. As a typical example we use the Lennard-Jones potential. Similar as for Fig. 3 we have slightly varied λ_6 over four different values in order to increase the number of data points and to better map out $|\phi_d(\sqrt{E_b\, m/3})|^2$. The sudden drops in $|\phi_d(\sqrt{E_b\, m/3})|^2$ reflect nodes of the molecular wave function. For large enough binding energy E_b all curves for the different values of L_R follow the same power law $E_b^{-1.45}$ corresponding to an energy scaling of the partial rate constants (for fixed L_R) of $L_3(E_b) \propto E_b^{-0.95}$.

We note, however, that for $L_R > 0$ and small enough binding energies, our calculations in Fig. 6 reveal a strong suppression of $|\phi_d|^2$ and therefore of $L_3(E_b)$. This effect is due to the function $g_d(\sqrt{E_b m/3})$. As shown in Fig. 5(a), for $L_R > 0$, $g_d(\sqrt{E_b m/3})$ increases gradually with E_b starting from 0. When it reaches its first maximum, it goes over to the previously discussed oscillatory behavior in the gray area, similar to the case of $L_R = 0$. As a consequence, $|\phi_d(\sqrt{E_b m/3})|^2$ is increasingly suppressed for $E_b \to 0$, as observed in our numerical results. This suppression can be understood as an effect of the angular momentum barrier. In a simple picture, in order to create a molecule rotating with angular momentum L_R at interparticle distance r_0 of the outer turning point, a minimal momentum p_c needs to be supplied of the order $p_c \approx \hbar L_R/r_0$. The minimal momentum p_c translates into a minimal binding energy $E_c = 3p_c^2/m \approx \hbar^2 L_R(L_R+1)/(mr_0^2)$. At the same time we have $E_c \approx C_6/r_0^6 - \hbar^2 L_R(L_R+1)/(mr_0^2)$. Combining these two equations to eliminate r_0 one can estimate the critical energy E_c to be

$$E_c/E_{\mathrm{vdW}} \approx c_c[L_R(L_R+1)]^{3/2}, \qquad (9)$$

where $c_c = 1.5$ and $E_{\mathrm{vdW}} = 4\hbar^3/(m^{3/2}C_6^{1/2})$ is the van der Waals energy. Reading off $E_c(L_R)$ from our numerical results in Fig. 6 as the first maximum of $|\phi_d(\sqrt{E_b m/3})|^2$ we find that the data points are well described by Eq. (9) when we use $c_c = 2.12$; see inset of Fig. 6. This validates our simple interpretation of the angular momentum suppression.

VI. DISCUSSION

We now compare and discuss the results of our theoretical and experimental approaches. The suppression effect for large L_R and small E_b, which is so clearly visible in Fig. 6 is not so obvious in Fig. 2 where we present our experimental data and our full coupled channel calculations. A small suppression effect might only be recognizable for the state $\upsilon = -2, L_R = 4$ in Fig. 2. In practice, the observation of suppressed low-energy high-L_R molecular signals can be hampered by various issues. By accident it can occur that no weakly bound molecular level with $E_b < E_c$ exists for a given rotational angular momentum L_R. In fact, quantum defect theory predicts for a van der Waals potential that if the most weakly bound state for a partial wave L_R is not close to threshold, then also the most weakly bound state for the partial wave $L_R + 4$ will not [31]. Alternatively, the level can be overlooked experimentally, if its signal is too weak. It will be overlooked theoretically if the level has a vibrational quantum number beyond the limits of the model potential. It should be, however, clear that the suppression mechanism must exist. Indeed, in a recent experiment on diatomic molecular reactions, a similar suppression mechanism has been identified [14].

When comparing Fig. 6 with Fig. 2 it is evident that the distinct drops of $|\phi_d(\sqrt{E_b m/3})|^2$ in Fig. 6 do not clearly appear in Fig. 2. There are several possible explanations for this. First, the data sampling in Fig. 2 is seven times smaller than for Fig. 6. Therefore, it is likely that a narrow drop is not encountered in Fig. 2. Second, the calculations in Fig. 6 correspond to the leading order of an expansion. Including higher orders might wash out the sudden drops, as other pathways for the molecular formation can be taken.

Concerning the full model and the experiment, we expect that the scaling exponent α of the $E_b^{-\alpha}$ scaling law is prone to changes for deeper binding energies than the ones considered here. As recently discussed in [10], for ^{87}Rb and $E_b > 150$ GHz × h the spin conservation propensity rule which allows for working with a single spin channel should break down, affecting the scaling law. In addition, the short-range three-body interaction, which is ignored so far in our treatment, should play an increasingly important role when forming more tightly bound molecular states. Recent work on three-body recombination of hydrogen [20] has already found evidence for this, as the Jahn-Teller effect substantially enhances recombination rates into tightly bound molecular states.

VII. SUMMARY AND OUTLOOK

To summarize, we have experimentally and theoretically investigated how the three-body recombination of an ultracold gas scales with the molecular binding energy E_b, detecting bound levels from 0.02 to 77 GHz×h, thus spanning an energy range of more than three orders of magnitude. This became possible by applying improved experimental schemes for the state-to-state detection of molecules and by carrying out large scale numerical calculations. Besides these numerical calculations an analytical perturbative model was developed which gives deep physical insights into the recombination process and can explain the observed scaling law. In particular, the perturbative model shows that to a large part the scaling law can be extracted from two-body quantities such as the molecular wave function. Our experimental and theoretical approaches show that the three-body recombination exhibits a propensity towards weakly bound product molecules. The recombination rate follows a $E_b^{-\alpha}$ scaling law where α is in the vicinity of 1. Remarkably, we find that this scaling law is quite universal as it should hold for a range of different potentials such as the Morse potential, potentials of type $-C_n/r^n$ with $n = 3, 4, 6$, as well as the contact potential. In addition, apart from a centrifugal barrier suppression at low enough binding energies, our results indicate that the three-body recombination populates molecular quantum states with different rotational angular momenta quite evenly, within about a factor of two.

In the future it will be interesting to explore how the scaling law evolves for deeper binding energies and what physical mechanisms will lead to its breakdown. On the experimental side, the detection sensitivity must be enhanced and the spectroscopic data will be expanded for reliable quantum state identification. On the theory side, short-range three-body interactions which are ignored so far in our treatment will be taken into account.

Moreover, it will be insightful to explore how deviations of individual reaction channels from the $E_b^{-\alpha}$ scaling law can be explained on a microscopic level, e.g., as interference effects of collision pathways. In fact, our perturbative calculations already produce tell-tale oscillations, and it will be interesting whether we can match up these oscillations with the ones from the hyperspherical approach. This might give deeper insights into the reaction process.

We expect that our results on the scaling of the reaction rate with energy are not restricted to the recombination process of neutral atoms alone, but they can also be applied to other systems and processes. For example, these systems could involve molecules or ions as collision partners and they might also comprise a range of collisional relaxation processes. We expect these process rates to be governed by a $E_b^{-\alpha}$ scaling law, where α should always be in the vicinity of unity.w

ACKNOWLEDGMENTS

This work was financed by the Baden-Württemberg Stiftung through the Internationale Spitzenforschung program (Contract No. BWST ISF2017-061) and by the German Research Foundation (DFG, Deutsche Forschungsgemeinschaft) within Contract No. 399903135. We acknowledge support from bwForCluster JUSTUS 2 for high performance computing. J.P.D. also acknowledges partial support from the U.S. National Science Foundation (PHY-2012125) and NASA/JPL (1502690).

APPENDIX A: THE (1,1) REMPI

Our (1,1) REMPI scheme consists of two excitation steps which are described in the following. The overall ionization efficiency η is given by the product of the efficiencies of the first and the second (1,1) REMPI step. We achieve $\eta \approx 4.8 \times 10^{-3}$ (see also Appendix C) for all (υ, L_R) product molecules that we probe in the experiment. This is about an order of magnitude larger as compared to our previous work [11,12].

1. First REMPI step

The first REMPI step resonantly excites a molecule towards the intermediate level $\upsilon' = 66$, J' of the state $A^1\Sigma_u^+$ using a wavelength of about 1065 nm [22,23]. For this excitation we use a cw external-cavity diode laser with a short-term linewidth of about 100 kHz. It has a waist ($1/e^2$-radius) of ≈280 μm and an intensity of ≈12 W cm^{-2} at the position of the atomic cloud. The laser is frequency-stabilized to a wavelength meter achieving a shot-to-shot and long-term stability of a few megahertz. The laser beam polarization has an angle of about 45° with respect to the B field and can therefore drive σ and π transitions.

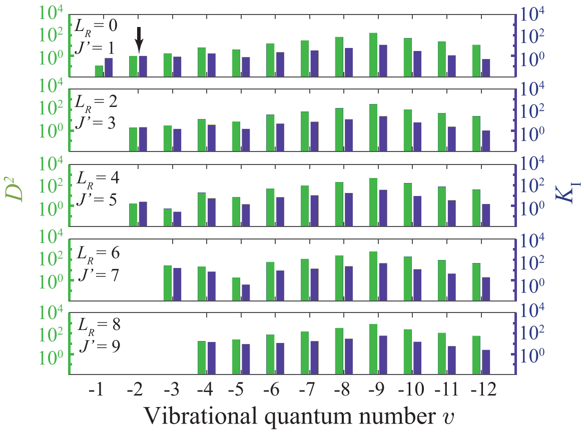

FIG. 7. Calculations for the squared reduced transition electric dipole moment D^2 and relative transition probability $K_I \propto D^2 f_D / E_b^{1/2}$ for the transitions from the product states (υ, L_R) towards the intermediate states J', $\upsilon' = 66$ of $A^1\Sigma_u^+$. Both, D^2 and K_I are normalized by a global factor, respectively, so that their values for the state $\upsilon = -2$, $L_R = 0$ are 1 (see arrow). The plot is logarithmic.

We estimate that the first REMPI step is saturated for the molecular states considered in this work. This means a molecule is resonantly excited to the intermediate level J' with nearly unit probability when probed. In order to derive this we consider the following quantities: The transition electric dipole moment, the limited time to optically excite the product molecule, and a detuning due to the Doppler shift. In Fig. 7 we show calculated squared reduced transition electric dipole moments D^2 for transitions from (υ, L_R) product states towards the vibrational level $\upsilon' = 66$ within $A^1\Sigma_u^+$ (green columns). For convenience, D^2 is normalized by a global factor so that its value for $(\upsilon = -2, L_R = 0)$ equals to 1. As a general pattern, D^2 increases with binding energy in the range between the threshold and the vibrational quantum number $\upsilon = -9$. This is, however, partially compensated by the following kinetic effects. In the formation of the molecule by three-body recombination the binding energy is converted into kinetic energy of the products. Neglecting the energy of the ultracold atoms, the velocity υ_{Rb2} of the molecule is $\propto E_b^{1/2}$. This velocity has two effects. First, it limits the time scale $\propto 1/E_b^{1/2}$ for the molecule to be located in the detection region, as determined by the size of the REMPI laser beams. Second, the velocity will on average lead to Doppler-broadening and to a reduction of the on-resonance photoexcitation rate by a factor given by $f_D = (2\upsilon_{\mathrm{Rb2}}/(\lambda\gamma))^{-1} \arctan(2\upsilon_{\mathrm{Rb2}}/(\lambda\gamma))$, where λ is the transition wavelength and $\gamma \approx 2\pi \times 15$ MHz is the linewidth of the excited state. Therefore, the optical excitation probability K_I of the molecules approximately scales as $K_I \propto D^2 f_D / E_b^{1/2}$. In Fig. 7 we plot K_I, which is also normalized so that for $(\upsilon = -2, L_R = 0)$ it equals to 1 (blue columns). Again, down to $\upsilon = -9$ there is a tendency that the ionization efficiency increases for increasing binding energy. In [11] we have found that for the given parameters of the probe laser beam the transitions from $\upsilon = -2$, $L_R = 0$, 2 towards the intermediate state are driven in a strongly saturated regime. Since all transitions for the product molecules in Fig. 7 have a K_I close or larger than the ones for $\upsilon = -2$, $L_R = 0$, 2, we can expect saturation of the first step of the (1,1) REMPI for all considered product levels.

2. Second REMPI step

For the second step of the REMPI we use the ionization laser at 544 nm to resonantly drive a transition from the intermediate state to a probably autoionizing molecular Rb$_2$ level [see Fig. 1(a)]. The laser is a cw, frequency-doubled OPO system from Hübner Photonics. It has a short-term linewidth on the order of 1 MHz. At the position of the atomic cloud the beam waist is 240 μm, and we typically work with an intensity of 110 W cm^{-2}. As the probe laser, it is frequency-stabilized to a wavelength meter achieving a shot-to-shot and long-term stability of a few megahertz. The laser polarization is at an angle of about 45° with respect to the B field and can therefore drive σ and π transitions. When the excited Rb$_2$ molecule autoionizes it produces a deeply bound Rb$_2^+$ molecular ion. Figure 8 shows resonance lines when scanning the frequency ν_I of the ionization laser and starting from the intermediate state $A^1\Sigma_u^+$, $\upsilon' = 66$, $J' = 1$ which has been populated via photoassociation. These lines are spectroscopically not

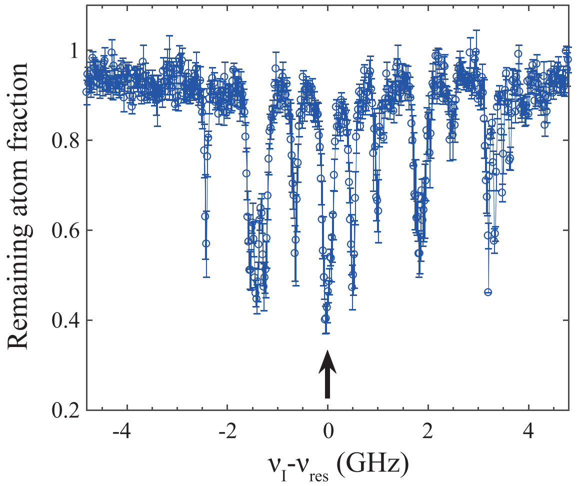

FIG. 8. Resonance spectrum when scanning the frequency ν_I of the ionization laser, starting from the intermediate level $A^1\Sigma_u^+$, $\upsilon' = 66$, $J' = 1$. Here produced ions are detected by induced loss in an atom cloud (see Appendix B). The strongest line is marked by an arrow and has the center frequency $\nu_{\mathrm{res}} = 551\,422.660$ GHz.

yet assigned. For REMPI via $J' = 1$ we use the resonance line centered at $\nu_I = \nu_{\mathrm{res}} = 551\,422.660$ GHz (marked by an arrow).

Regarding the intermediate states with $J' > 1$, we carry out similar spectroscopy as for Fig. 8 and identify the strongest resonance, respectively, which is then used for REMPI. Since photoassociation cannot produce a molecule with $J' > 1$ in our cold sample, we instead populate such a state by resonantly exciting suitable product molecules (υ, L_R) after three-body recombination with the probe laser. Table I lists the optimal ionization laser frequencies for various rotational levels J' of the intermediate state $\upsilon' = 66$. From additional spectroscopic measurements we extract a rotational constant $B_{\upsilon'=66} = 443(2)$ MHz $\times h$, in agreement with the value reported in [23]. For completeness, we present in Table I also the measured level energies $E_{J'}$ for the various detected rotational states J' within $\upsilon' = 66$ of $A^1\Sigma_u^+$.

The second REMPI step is generally not saturated in our experiment. This is shown in Fig. 9 for the case of initial $(\upsilon = -2, L_R = 2)$ molecules and the intermediate level $J' = 1$, $\upsilon' = 66$ of $A^1\Sigma_u^+$. The detected number of ions increases linearly with laser intensity. We have, however, verified that ionization of a given initial state via different intermediate rotational states $J' = L_R \pm 1$ provides similar ion signal strengths. Furthermore, the reduction f_D due to the Doppler effect (as discussed for the REMPI step 1) should be negligible here, since the linewidth γ is about 200 MHz according to Fig. 8. We note that γ corresponds to an approximate measure of the autoionization width.

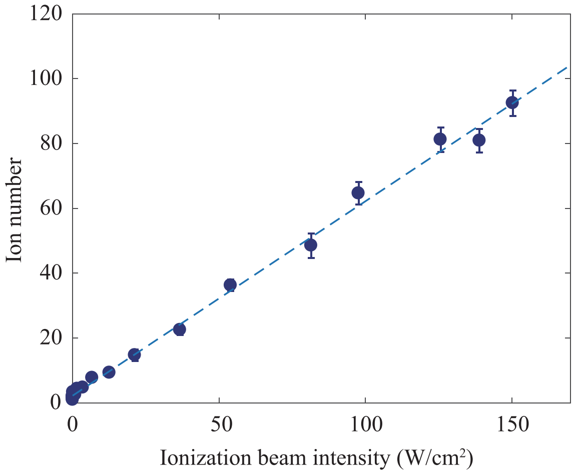

FIG. 9. Ion number as a function of the intensity of the ionization laser beam in the (1,1) REMPI scheme. These data are obtained for $(\upsilon = -2, L_R = 2)$ molecules which are ionized via the intermediate state $J' = 1$. Here $\nu_I = 551422.66$ GHz, see Table I. The dashed blue line is a linear fit to the data.

TABLE I. REMPI paths. Column 2 lists the energies $E_{J'}$ of the intermediate levels J' in the state $\upsilon' = 66$ of $A^1\Sigma_u^+$, with respect to the $(5s, f = 1) + (5s, f = 1)$ atomic asymptote. In the third column we list the frequencies ν_{res} of the ionization laser which are used in the (1,1) REMPI scheme for the second transition starting from the intermediate levels $J' = 1, 3, 5, 7, 9$ in the state $\upsilon' = 66$ of $A^1\Sigma_u^+$.

J'	$E_{J'}$ GHz × h	ν_{res} GHz
1	281 445.045	551 422.66
3	281 449.481	551 420.70
5	281 457.442	551 419.30
7	281 468.987	551 423.10
9	281 484.065	551 421.60

APPENDIX B: COUNTING REMPI IONS VIA ATOM LOSS

We detect and count ions in the Paul trap via atom loss which the ions inflict on neutral atoms due to elastic atom-ion collisions. The basic method has been developed in previous work [6,11,32]. Here we use a modified scheme, which is described in the following.

Ion-inflicted atom loss: After the 500 ms phase of three-body recombination, the REMPI lasers are switched off and the optical lattice trap with the atom cloud is adiabatically moved over a distance of 50 μm to the center of the Paul trap, in order to immerse the ions which have been produced during the 500ms time into the atom cloud. At the same time the optical lattice trap is adiabatically converted into a crossed dipole trap, by turning off one of the 1D lattice beams. The trap frequencies of the crossed optical dipole trap are $\omega_{x,y,z} = 2\pi \times (23,\ 180,\ 178)$ Hz, where z represents the vertical direction. In this trap the atom cloud is Gaussian-shaped with widths of $\sigma_{x,y,z} \approx (58.6,\ 7.5,\ 7.5)$ μm, and it still consists of about 4×10^6 atoms, corresponding to a peak atomic density of about $n_0 = 0.9 \times 10^{14}$ cm^{-3}. In the Paul trap the ions have typical kinetic energies on the order of mK × k_B or larger as a result of, e.g., excess micromotion. Therefore, in elastic atom-ion collisions one atom after the next is kicked out of the

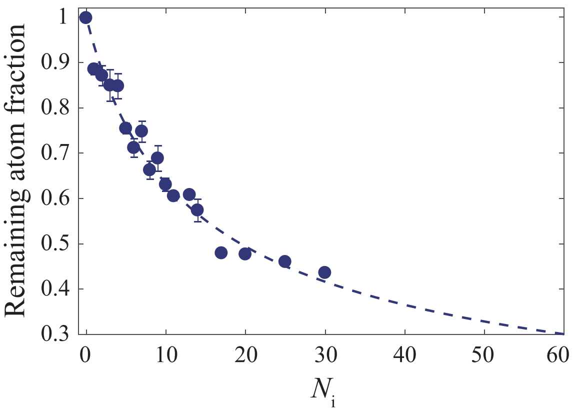

FIG. 10. Remaining atom fraction as a function of the initially prepared number of ions N_i (Rb^+ and Rb_2^+) after an interaction time of 500 ms. The dashed line is a fit of the function $(\frac{N_i}{c_1}+1)^{c_2}$ to the data (see text).

comparatively shallow (9 μK × k_B) optical dipole trap while the ions remain confined in the 2.5 eV deep Paul trap.

Converting atom loss signals into ion numbers: In order to extract ion numbers from atom loss signals we carry out the following, independent calibration. We start using a configuration where the ion trap and the optical dipole trap are spatially separated from each other so that atoms and ions cannot collide. We prepare a well-defined number of laser-cooled $^{138}Ba^+$ ions forming an ion crystal in the Paul trap. Using fluorescence imaging the number of ions in the crystal is counted. In parallel, we prepare a dense Rb atom cloud in the optical dipole trap. Afterwards, the centers of the ion trap and the optical dipole trap are quickly overlaid so that the Ba^+ ions are immersed into the atom cloud, where they undergo chemical reactions. This leads almost exclusively to the formation of Rb^+ and Rb_2^+ ions [33]. The number of ions remains constant because of the large depth of the Paul trap. Subsequently the traps are again separated from each other and a new atom cloud is prepared in the optical dipole trap, while the ions remain confined in the Paul trap. The properties of this new atom cloud are adjusted to match the cloud that was used for atom loss measurements as described in the previous paragraph. Once again the ions are immersed into the atom cloud by overlapping the traps. After an atom-ion interaction time of 500 ms the remaining number of atoms is measured. In Fig. 10 we show data for different numbers N_i of prepared ions. The blue dashed line represents a fit using the empirical function $(\frac{N_i}{c_1}+1)^{c_2}$, where the fit parameters are $c_1 = 8.6$ and $c_2 = -1.6$. This function serves as reference to convert measured atom loss in the three-body recombination experiment into ion numbers.

APPENDIX C: CONVERSION OF REMPI ION NUMBERS TO MOLECULE NUMBERS AND L_3 RATE COEFFICIENTS

As discussed in Appendix A, the number of formed molecules in a final channel is given by the measured ion number N_{Ion} after REMPI divided by a global ionization efficiency factor η. Similarly, the $L_3(\upsilon, L_R)$ rate coefficients are given by the measured ion numbers multiplied with a proportionality factor κ. We note that each three-body recombination experiment has a run time of 500 ms, and after this time the atomic density of the sample has dropped by 13% due to collisional and reactive loss. Taking this loss into account we estimate the ion number $N^*_{\text{Ion}} = N_{\text{Ion}} \times 1.22$ for the case that the density stayed constant. To determine the proportionality factor κ, we sum over all channels according to $\kappa \sum_{\upsilon,L_R} N^*_{\text{Ion}}(\upsilon, L_R) = \sum_{\upsilon,L_R} L_3(\upsilon, L_R) = L_3$, where $L_3(\upsilon, L_R)$ and L_3 are the calculated partial and total recombination rate constants, respectively. We obtained $\kappa = 1.92 \times 10^{-32}$ cm^6 s^{-1}. From an additional measurement of the initial atom number and the temperature of the atom cloud and using the molecular production rate

$$\dot{M} = \frac{L_3}{3\sqrt{27}}\left(\frac{m\bar{\omega}^2}{2\pi k_B}\right)^3 \frac{N^3}{T^3} \tag{C1}$$

we determined η to be $\eta \approx 4.8 \times 10^{-3}$. Here M is the number of produced molecules, m is the atomic mass, and $\bar{\omega} = (\omega_x\omega_y\omega_z)^{1/3}$ is the geometric mean of the trapping frequencies.

APPENDIX D: BOOSTING THE MOLECULE SIGNALS

Compared to our previous work [11,12] the product state signals and the sensitivity were boosted by a factor of ≈25 as a result of two improvement steps.

The first improvement step is working with an optical lattice trap instead of a plain crossed dipole trap. This increases the atomic density n and therefore improves the signal compared to the background since the three-body recombination rate scales nonlinearly with n as $\dot{N}_{\text{at}} = \int \dot{n}\, d^3r = -L_3 \int n^3\, d^3r$, whereas background signals scale less strongly with n. In total, switching to the optical lattice configuration in our set up increased the signal by a factor of 2.5. This improvement is shown in Fig. 11 for the detection signals of the $\upsilon = -2$, $L_R = 0$, 2 product molecules when using the intermediate state $J' = 1$. We plot the ion number (i.e., the molecular (1,2) REMPI signal) as a function of the probe laser frequency ν for different experimental settings. The black data points are the signals for the settings in [11]. For the green data points we have replaced the crossed dipole trap as used in [11] by the optical lattice.

The second improvement step is an enhancement of the REMPI efficiency. In [11,12] only the first REMPI step in a (1,2) REMPI configuration was resonantly driven. In our new (1,1) scheme [see Fig. 1(a) and Appendix A] both REMPI steps are resonantly driven and the last excitation step is resulting in a molecular state which is probably autoionizing. Switching to the (1,1) REMPI increased the signals by a factor of 10. For comparison, in Fig. 11, the blue and orange data give the signals for (1,1) REMPI with and without lattice, respectively.

In order to optimize REMPI we have also experimentally tested several vibrational levels around $\upsilon' = 66$ within $A^1\Sigma_u^+$ as intermediate level, but obtained the best results for $\upsilon' = 66$ in terms of efficiency and suppressing background signals. The level $\upsilon' = 66$ has essentially a simple rotational ladder structure, as it has unresolved hyperfine splittings of less than 3 MHz × h [22,23].

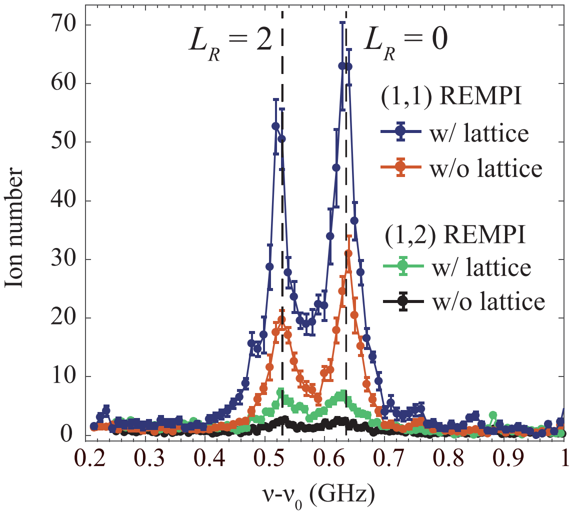

FIG. 11. Boost of the molecular detection signal. Shown are measured ion numbers after REMPI of ($\upsilon = -2, L_R = 0, 2$) product molecules as a function of the probe laser frequency ν. $\nu_0 = 281\,445.045$ GHz is the resonance frequency for photoassociation towards the $J' = 1$ intermediate state. The different colors indicate different measurement configurations as detailed in the legend.

APPENDIX E: CONSISTENCY CHECKS FOR LINE ASSIGNMENTS

In general, we observe each molecular level with $L_R > 0$ in terms of two transition lines, $L_R \to J' = L_R \pm 1$. This greatly helps to verify the consistency of the line assignment. As an example, we provide in Fig. 12 the collection of REMPI detection signals for $\upsilon = -4$ molecules with rotational states L_R ranging from $L_R = 0$ to 10.

APPENDIX F: THREE-BODY MODEL FOR ^{87}Rb ATOMS

Our three-body calculations for ^{87}Rb atoms were performed using the adiabatic hyperspherical representation [18,25] where the hyperradius R determines the overall size of the system, while all other degrees of freedom are represented by a set of hyperangles Ω. Within this framework, the three-body adiabatic potentials U_α and channel functions Φ_α are determined from the solutions of the hyperangular adiabatic equation

$$\left[\frac{\Lambda^2(\Omega)+15/4}{2\mu R^2}\hbar^2+\sum_{i<j}V(r_{ij})\right]\Phi_\alpha(R;\Omega) = U_\alpha(R)\Phi_\alpha(R;\Omega), \qquad \text{(F1)}$$

which contains the hyperangular part of the kinetic energy, via the grand-angular momentum operator Λ^2, and the three-body reduced mass $\mu = m/\sqrt{3}$. To calculate the three-body recombination rate we solve the hyperradial Schrödinger equation,

$$\left[-\frac{\hbar^2}{2\mu}\frac{d^2}{dR^2}+U_\alpha(R)\right]F_\alpha(R)+\sum_{\alpha'}W_{\alpha\alpha'}(R)F_{\alpha'}(R) = EF_\alpha(R), \qquad \text{(F2)}$$

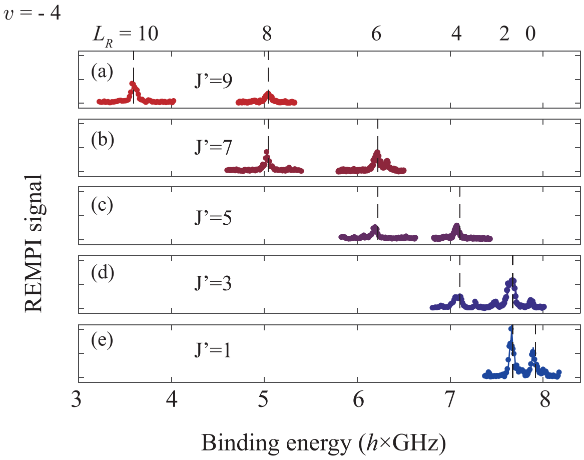

FIG. 12. Consistency of assignments of product molecular states to REMPI detection signals. The vertical dashed lines mark the binding energies of the molecules with quantum numbers $\upsilon = -4, L_R$ as obtained from coupled channel calculations. The rotational quantum number L_R is shown on top of the figure. For each level with $L_R > 0$ we observe two resonance lines, corresponding to REMPI via the intermediate levels $J' = L_R \pm 1$. The resonance lines are plotted as a function of the probe laser frequency and are arranged such that the frequency position of each resonance peak is given by $\nu - \nu_0 - B_{\upsilon'=66} \times [J'(J'+1) - 2]$, ideally corresponding to the molecular binding energy. The rotational constant is $B_{\upsilon'=66} = 443$ MHz. ν_0 is the photoassociation resonance frequency towards $J' = 1$. In vertical direction the lines are arranged according to J'. The match in frequency position of the two measured resonance lines and the calculated binding energy for a level indicates consistency of the assignment.

where α is an index that labels all necessary quantum numbers to characterize each channel, E is the total energy, and nonadiabatic couplings are given by

$$W_{\alpha\alpha'}(R) = -\frac{\hbar^2}{2\mu}\left(\left\langle\Phi_\alpha\middle|\frac{d^2}{dR^2}\Phi_{\alpha'}\right\rangle+2\left\langle\Phi_\alpha\middle|\frac{d}{dR}\Phi_{\alpha'}\right\rangle\frac{d}{dR}\right). \qquad \text{(F3)}$$

Solving Eq. (F2) numerically [18] we determine the S-matrix and the recombination rate L_3 via

$$L_3 = \sum_{f,i}\frac{96\pi^2(2J+1)\hbar}{\mu k_i^4}|S_{fi}|^2 = \sum_f L_3(f), \qquad \text{(F4)}$$

where i and $f \equiv (\upsilon, L_R)$ represent the initial and final states and $L_3(f)$ is the corresponding partial recombination rate for a given final state.

In this present study, the interaction between ^{87}Rb atoms is modeled by the same potential used in Ref. [11], and is given by the Lennard-Jones potential,

$$V(r) = -\frac{C_6}{r^6}\left(1-\frac{\lambda^6}{r^6}\right), \qquad \text{(F5)}$$

where $C_6 = 4710.431E_h a_0^6$ is the van der Waals dispersion coefficient from Ref. [26]. Here E_h denotes the Hartree energy. We adjust the value of λ to have different numbers of diatomic bound states supported by the interaction, while still reproducing the value of the scattering length for ^{87}Rb atoms, $a = 100.36a_0$ [26]. Our calculations were performed using $\lambda \approx 15.5943a_0$, producing 15 s-wave ($L_R = 0$) molecular bound states, and a total of 240 bound states including higher partial-wave states, $L_R > 0$.

Our numerical calculations for three-body recombination through the solutions of Eq. (F2) have included up to 300 hyperspherical channels leading to a total rate converged within a few percent. The calculated total recombination rate constant at 0.8 μK (including thermal averaging) is $L_3 \approx 0.91 \times 10^{-29}$ cm^6/s. We note that there is an unresolved discrepancy between this calculated total three-body recombination rate constant and the corresponding experimental value for Rb in the spin state $f = 1, m_f = -1$. The experimental value is $L_3 = (4.3 \pm 1.8) \times 10^{-29}$ cm^{6}s^{-1}, [34]. This discrepancy, however, does not affect the analysis of the overall scaling behavior of $L_3(\upsilon, L_R)$ with binding energy.

APPENDIX G: INTERPRETING THE 1/E_b SCALING LAW VIA A PERTURBATIVE APPROACH

The Alt-Grassberger-Sandhas (AGS) equation is an efficient approach for solving three-particle collision problems [28], and for identical particles it reads [27,29]

$$U_0(E) = \tfrac{1}{3}G_0^{-1}(E)[1 + P_+ + P_-] + [P_+ + P_-]\mathscr{T}(E)G_0(E)U_0(E). \qquad \text{(G1)}$$

Here the three-body transition operator U_0 describes the transition process from the initial state of three free, noninteracting atoms to product states of a molecule of the atom pair (a, b) plus a free atom c. E denotes the total energy of the three-body system, $G_0(E) = (E + i\epsilon - H_0)^{-1}$ is the free Green's operator corresponding to the noninteracting three-body Hamiltonian H_0, and ϵ is a small quantity to shift the energy away from the real axis. $\mathscr{T}(E) = \int d\mathbf{q}|\mathbf{q}\rangle t(E_{2b})\langle\mathbf{q}|$ represents the generalized two-body transition operator for the interacting pair (a, b) [27,29]. Here $t(E_{2b})$ is the pure two-body transition operator at two-body energy $E_{2b} = E - \frac{3q^2}{4m}$, $\mathbf{q}$ is the three-dimensional relative momentum between atom c and the center of mass of the pair (a, b), m is the mass of an atom and q is the absolute value of $\mathbf{q}$. $P_+ = P_{bc}P_{ab}$ and $P_- = P_{ac}P_{ab}$ denote the cyclic and anticyclic permutation operators for the atoms (a, b, c), respectively. The partial three-body recombination rate $L_3(\upsilon, L_R)$ towards each specific molecular product d is given by [27]

$$L_3(\upsilon, L_R) = \frac{12\pi m}{\hbar}(2\pi\hbar)^6 q_d|\langle\psi_f|U_0(E)|\psi_{\text{in}}\rangle|^2, \qquad \text{(G2)}$$

where $|\psi_{\text{in}}\rangle$ and $|\psi_f\rangle$ represent the initial and product states, respectively. Here q_d denotes the absolute value of the asymptotic momentum of the molecule which is fixed by the molecule binding energy E_b and the total energy E via $\frac{3q_d^2}{4m} - E_b = E$. Iteratively plugging Eq. (G1) into its right side, one gets a series expansion $U_0(E) = \sum_{n=0}^{\infty} U_0^{(n)}(E)$ with $U_0^{(n)}(E) = \{[P_+ + P_-]\mathscr{T}(E)G_0(E)\}^n \frac{1}{3}G_0^{-1}(E)[1 + P_+ + P_-]$. We assume that the three-body recombination process can be reasonably well described by the leading order contribution for U_0 [27]. Since $U_0^{(0)}(E)|\psi_{\text{in}}\rangle = \frac{1}{3}[1 + P_+ + P_-](E - H_0)|\psi_{\text{in}}\rangle = 0$ due to energy conservation, $U_0^{(0)}(E)$ has no contribution to the three-body recombination rate according to Eq. (G2). Therefore, we approximate $U_0(E)$ by $U_0^{(1)}(E)$

$$U_0(E) \approx [P_+ + P_-]\mathscr{T}(E)\tfrac{1}{3}[1 + P_+ + P_-]. \qquad \text{(G3)}$$

Since the three-body recombination rate is usually quite energy independent in the ultracold regime [35], we take the zero energy limit $E \to 0$ to simplify the derivation. In this limit, the initial free atom state is $|\psi_{\text{in}}\rangle = |\mathbf{p} = 0, \mathbf{q} = 0\rangle$, where $\mathbf{p}$ describes the relative momentum between atoms a and b. We note that, for identical particles, neither the result of $L_3(\upsilon, L_R)$ nor the derivation procedure associated to this quantity should depend on the choice of pair (a, b). Plugging the expression of Eq. (G3) into Eq. (G2) we obtain

$$\begin{aligned} L_3(\upsilon, L_R) &\approx \frac{12\pi m}{\hbar}(2\pi\hbar)^6 q_d|\langle\psi_f|[P_+ + P_-]\mathscr{T}(E) \\ &\quad \times \frac{1}{3}[1 + P_+ + P_-]|\psi_{\text{in}}\rangle|^2 &\text{(G4)} \\ &= \frac{12\pi m}{\hbar}(2\pi\hbar)^6 q_d|\langle\psi_f|2P_+\mathscr{T}(E)|\psi_{\text{in}}\rangle|^2, &\text{(G5)} \end{aligned}$$

where we have replaced $P_+ + P_-$ by $2P_+$ because the term of P_+ will contribute equally as the term of P_- to $L_3(\upsilon, L_R)$, [29,36]. For similar reasons $[1 + P_+ + P_-]/3$ is replaced by 1. In the plane wave basis, P_+ is given by

$$P_+ = \int d\mathbf{q}' \int d\mathbf{q}''|\mathbf{p}', \mathbf{q}'\rangle\langle\mathbf{p}'', \mathbf{q}''|, \qquad \text{(G6)}$$

where $\mathbf{p}' = \mathbf{q}'' + \frac{1}{2}\mathbf{q}'$ and $\mathbf{p}'' = -\mathbf{q}' - \frac{1}{2}\mathbf{q}''$. To derive Eq. (G6), we let the single atom momenta be $\{\mathbf{k}_a'' = \mathbf{k}_1, \mathbf{k}_b'' = \mathbf{k}_2, \mathbf{k}_c'' = \mathbf{k}_3\}$ and by definition we have $\{\mathbf{p}'' = (\mathbf{k}_2 - \mathbf{k}_1)/2, \mathbf{q}'' = 2\mathbf{k}_3/3 - \mathbf{k}_1/3 - \mathbf{k}_2/3\}$. The permutation operator P_+ changes the atom indices according to $(a, b, c) \to (c, a, b)$ and therefore $\{\mathbf{k}_a'' = \mathbf{k}_1,\ \mathbf{k}_b'' = \mathbf{k}_2,\ \mathbf{k}_c'' = \mathbf{k}_3\} \to \{\mathbf{k}_a' = \mathbf{k}_2, \mathbf{k}_b' = \mathbf{k}_3, \mathbf{k}_c' = \mathbf{k}_1\}$, which leads to $\{\mathbf{p}'' = (\mathbf{k}_2 - \mathbf{k}_1)/2, \mathbf{q}'' = 2\mathbf{k}_3/3 - \mathbf{k}_1/3 - \mathbf{k}_2/3\} \to \{\mathbf{p}' = (\mathbf{k}_3 - \mathbf{k}_2)/2, \mathbf{q}' = 2\mathbf{k}_1/3 - \mathbf{k}_2/3 - \mathbf{k}_3/3\}$, or equivalently, $\{\mathbf{p}'' = -\mathbf{q}''/2 - \mathbf{q}',\ \mathbf{q}''\} \to \{\mathbf{p}' = \mathbf{q}'/2 + \mathbf{q}'',\ \mathbf{q}'\}$. It is then straightforward that $P_+ = \int d\mathbf{q}' \int d\mathbf{q}''|\mathbf{p}' = \mathbf{q}'/2 + \mathbf{q}'', \mathbf{q}'\rangle\langle\mathbf{p}'' = -\mathbf{q}''/2 - \mathbf{q}', \mathbf{q}''|$. Using the previous expressions for P_+ and $\mathscr{T}(E)$, and $|\psi_{\text{in}}\rangle = |\mathbf{p} = \mathbf{0}, \mathbf{q} = \mathbf{0}\rangle$, we find

$$\begin{aligned} \langle\psi_f|P_+\mathscr{T}(E)|\psi_{\text{in}}\rangle &= \langle\psi_f| \int d\mathbf{q}' \int d\mathbf{q}''|\mathbf{p}', \mathbf{q}'\rangle\langle\mathbf{p}'', \mathbf{q}''| \\ &\quad \times \int d\tilde{\mathbf{q}}|\tilde{\mathbf{q}}\rangle t\left(E - \frac{3\tilde{q}^2}{4m}\right)\langle\tilde{\mathbf{q}}|\psi_{\text{in}}\rangle \\ &= \langle\psi_f| \int d\mathbf{q}' \int d\mathbf{q}''|\mathbf{p}', \mathbf{q}'\rangle \\ &\quad \times \langle\mathbf{q}''|0\rangle\langle\mathbf{p}''|t(0)|\mathbf{p} = 0\rangle \\ &= \int d\mathbf{q}'\langle\psi_f|\mathbf{p}', \mathbf{q}'\rangle\langle\mathbf{p}''|t(0)|\mathbf{p} = 0\rangle, \end{aligned} \qquad \text{(G7)}$$

where we have used $\langle \mathbf{q}'|\tilde{\mathbf{q}}\rangle = \delta(\mathbf{q}' - \tilde{\mathbf{q}})$, and in the last line we have $\mathbf{p}' = \frac{1}{2}\mathbf{q}'$ and $\mathbf{p}'' = -\mathbf{q}'$. We now switch from the plane wave basis to a partial wave basis by using

$$|\mathbf{p}\rangle = |p\rangle \sum_{l,m} Y^*_{l,m}(\mathbf{e_p})|l, m\rangle, \tag{G8}$$

where $p = |\mathbf{p}|$, $\mathbf{e_p} = \mathbf{p}/p$ and the normalization of $|p\rangle$ is given by $\langle p'|p\rangle = \frac{\delta(p-p')}{p^2}$. The expression $\langle \mathbf{p}''|t(0)|\mathbf{p} = 0\rangle$ in the last line of Eq. (G7) can be expressed as

$$\langle -\mathbf{q}'|t(0)|\mathbf{p} = 0\rangle = \tfrac{1}{4\pi}\langle q'|t^s(0)|p = 0\rangle, \tag{G9}$$

where t^s is the s-wave component of the two-body transition operator t. Here we have used that according to the Wigner threshold law at low collision energies only s-wave collisions can contribute. Furthermore, we assume that the interaction between two atoms conserves angular momentum.

Next we consider the expression $\langle \psi_f|\mathbf{p}' = \frac{1}{2}\mathbf{q}', \mathbf{q}'\rangle$. For $|\psi_f\rangle$ we make the ansatz $|\psi_f\rangle = |\phi_d\rangle|q_d, \hat{l}, \hat{m}\rangle$. Here $|\phi_d\rangle = |L_R, m_{L_R}\rangle \int dp\, p^2\phi_d(p)|p\rangle$ is the internal wave function of the molecule with rotational angular momentum quantum numbers L_R, m_{L_R}. $\phi_d(p)$ is normalized via $\int |\phi_d(p)|^2 p^2 dp = 1$. The state $|q_d, \hat{l}, \hat{m}\rangle \equiv |q_d\rangle|\hat{l}, \hat{m}\rangle$ describes the relative motion between molecule and atom. It corresponds to a partial wave with rotational quantum numbers $\hat{l}$, $\hat{m}$. Next, we calculate that

$$\left\langle \phi_d \middle| \frac{1}{2}\mathbf{q}' \right\rangle = \phi^*_d\left(\frac{1}{2}q'\right)\, Y^*_{L_R,m_{L_R}}(\mathbf{e}_{\mathbf{q}'}), \tag{G10}$$

$$\langle q_d, \hat{l}, \hat{m}|\mathbf{q}'\rangle = \frac{\delta(q_d - q')}{q^2}\, Y^*_{\hat{l},\hat{m}}(\mathbf{e}_{\mathbf{q}'}). \tag{G11}$$

Plugging the results of Eqs. (G9) to (G11) into Eq. (G7) and carrying out the integration over $\mathbf{q}'$ we obtain

$$\begin{aligned}\langle \psi_f|P_+\mathscr{T}(E)|\psi_{\text{in}}\rangle =& \frac{(-1)^m}{4\pi}\phi^*_d\left(\frac{1}{2}q_d\right)\langle q_d|t^s(0)|p = 0\rangle \\ &\times\ \delta_{L_R,\hat{l}}\delta_{m_{L_R},-\hat{m}},\end{aligned} \tag{G12}$$

where we have used $\int d\Omega_q Y^*_{lm}(\mathbf{e_q})Y^*_{l'm'}(\mathbf{e_q}) = (-1)^m\delta_{l,l'}\delta_{m,-m'}$. We then define

$$t_{\text{h}}(q_d) = \langle q_d|t^s(0)|p = 0\rangle \tag{G13}$$

and use Eq. (G12) to rewrite Eq. (G4) as

$$\begin{aligned}L_3(\upsilon, L_R) \approx& \frac{12\pi m}{\hbar}(2\pi\hbar)^6 q_d(2L_R + 1) \\ &\times \left|\frac{1}{2\pi}\phi_d\left(\frac{1}{2}q_d\right)t_{\text{h}}(q_d)\right|^2.\end{aligned} \tag{G14}$$

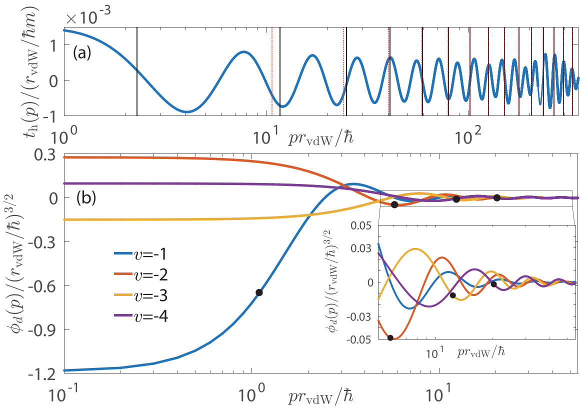

FIG. 13. (a) Two-body half-shell t-matrix t_{h} as a function of the relative two-body momentum p. The vertical lines indicate the momentum values $2\sqrt{mE_b/3}$ corresponding to s-wave (black solid) and d-wave (red dotted) molecules where t_{h} needs to be evaluated. (b) Momentum space wave functions of the four most shallow s-wave molecules. The dots indicate the momentum values $\sqrt{mE_b/3}$ where ϕ_d needs to be evaluated. These results are obtained from a Lennard-Jones potential with 15 s-wave molecular states and a scattering length $a = 1.21\ r_{\text{vdW}}$. Here $r_{\text{vdW}} = \frac{1}{2}(mC_6/\hbar^2)^{1/4}$ is the characteristic length scale of the van der Waals interaction. Given $r_{\text{vdW}} = 82.64\ \text{a}_0$ for ^{87}Rb, this scattering length corresponds to $a = 100.36\ \text{a}_0$.

Here we have summed over the $2L_R + 1$ equal contributions corresponding to the available m_d-channels for a given L_R quantum number. $t_{\text{h}}(q_d)$ has momentum $p = 0$ fixed on the energy shell $p^2/m = E_{2b} = 0$, and is commonly referred to as half-shell t-matrix in nuclear physics [37,38].

In order to analyze the scaling of $L_3(\upsilon, L_R)$ with the molecular binding energy E_b, we use the relation $\frac{3q_d^2}{4m} - E_b = 0$ and ignore all coefficients independent on q_d in Eq. (G14) to obtain

$$L_3(\upsilon, L_R) \propto (E_b)^{1/2}|\phi_d(\sqrt{mE_b/3})|^2|t_{\text{h}}(2\sqrt{mE_b/3})|^2. \tag{G15}$$

In Fig. 13(a) we show $t_{\text{h}}(p)$. It oscillates but the amplitude varies only slowly with the two-body momentum p. Of course, this holds only until the bottom of the interaction potential (corresponding to the most deeply bound states) is reached, as the bottom leads to a momentum cutoff. Figure 13(b) shows $\phi_d(p)$, which is discussed in the main text.

---

[1] X. Yang, State-to-state dynamics of elementary bimolecular reactions, Annu. Rev. Phys. Chem. **58**, 433 (2007).

[2] H. Pan, K. Liu, A. Caracciolo, and P. Casavecchia, Crossed beam polyatomic reaction dynamics: Recent advances and new insights, Chem. Soc. Rev. **46**, 7517 (2017).

[3] J. Jankunas and A. Osterwalder, Cold and controlled molecular beams: Production and applications, Annu. Rev. Phys. Chem. **66**, 241 (2015).

[4] S. Y. T. van de Meerakker, H. L. Bethlem, N. Vanhaecke, and G. Meijer, Manipulation and control of molecular beams, Chem. Rev. **112**, 4828 (2012).

[5] Y. Liu, D. D. Grimes, M.-G. Hu, and K.-K. Ni, Probing ultracold chemistry using ion spectrometry, Phys. Chem. Chem. Phys. **22**, 4861 (2020).

[6] A. Härter, A. Krükow, M. Deiß, B. Drews, E. Tiemann, and J. Hecker Denschlag, Population distribution of product states

following three-body recombination in an ultracold atomic gas, Nat. Phys. **9**, 512 (2013).

[7] P. Paliwal, N. Deb, D. M. Reich, A. van der Avoird, C. P. Koch, and E. Narevicius, Determining the nature of quantum resonances by probing elastic and reactive scattering in cold collisions, Nat. Chem. **13**, 94 (2021).

[8] T. de Jongh, M. Besemer, Q. Shuai, T. Karman, A. van der Avoird, G. C. Groenenboom, and S. Y. T. van de Meerakker, Imaging the onset of the resonance regime in low-energy NO-He collisions, Science **368**, 626 (2020).

[9] M. Beyer and F. Merkt, Half-Collision Approach to Cold Chemistry: Shape Resonances, Elastic Scattering, and Radiative Association in the $H^+ + H$ and $D^+ + D$ Collision Systems, Phys. Rev. X **8**, 031085 (2018).

[10] S. Haze, J. P. D'Incao, D. Dorer, M. Deiß, E. Tiemann, P. S. Julienne, and J. Hecker Denschlag, Spin-Conservation Propensity Rule for Three-Body Recombination of Ultracold Rb Atoms, Phys. Rev. Lett. **128**, 133401 (2022).

[11] J. Wolf, M. Deiß, A. Krükow, E. Tiemann, B. P. Ruzic, Y. Wang, J. P. D'Incao, P. S. Julienne, and J. Hecker Denschlag, State-to-state chemistry for three-body recombination in an ultracold rubidium gas, Science **358**, 921 (2017).

[12] J. Wolf, M. Deiß, and J. Hecker Denschlag, Hyperfine Magnetic Substate Resolved State-to-State Chemistry, Phys. Rev. Lett. **123**, 253401 (2019).

[13] M.-G. Hu, Y. Liu, M. A. Nichols, L. Zhu, G. Quéméner, O. Dulieu, and K.-K. Ni, Nuclear spin conservation enables state-to-state control of ultracold molecular reactions, Nat. Chem. **13**, 435 (2021).

[14] Y. Liu, M.-G. Hu, M. A. Nichols, D. Yang, D. Xie, H. Guo, and K.-K. Ni, Precision test of statistical dynamics with state-to-state ultracold chemistry, Nature (London) **593**, 379 (2021).

[15] T. Weber, J. Herbig, M. Mark, H.-C. Nägerl, and R. Grimm, Three-Body Recombination at Large Scattering Lengths in an Ultracold Atomic Gas, Phys. Rev. Lett. **91**, 123201 (2003).

[16] S. Jochim, M. Bartenstein, A. Altmeyer, G. Hendl, C. Chin, J. Hecker Denschlag, and R. Grimm, Pure Gas of Optically Trapped Molecules Created from Fermionic Atoms, Phys. Rev. Lett. **91**, 240402 (2003).

[17] B.-B. Wang, M. Zhang, and Y.-C. Han, Ultracold state-to-state chemistry for three-body recombination in realistic $^3He_2$-alkaline-earth-metal systems, J. Chem. Phys. **157**, 014305 (2022).

[18] J. Wang, J. P. D'Incao, and C. H. Greene, Numerical study of three-body recombination for systems with many bound states, Phys. Rev. A **84**, 052721 (2011).

[19] J. Pérez-Ríos, S. Ragole, J. Wang, and C. H. Greene, Comparison of classical and quantal calculations of helium three-body recombination, J. Chem. Phys. **140**, 044307 (2014).

[20] C. H. Yuen and V. Kokoouline, Jahn-Teller effect in three-body recombination of hydrogen atoms, Phys. Rev. A **101**, 042709 (2020).

[21] D. J. Nesbitt, Toward state-to-state dynamics in ultracold collisions: Lessons from high-resolution spectroscopy of weakly bound molecular complexes, Chem. Rev. **112**, 5062 (2012).

[22] M. Deiß, B. Drews, J. Hecker Denschlag, and E. Tiemann, Mixing of 0^+ and 0^- observed in the hyperfine and Zeeman structure of ultracold Rb_2 molecules, New J. Phys. **17**, 083032 (2015).

[23] A. N. Drozdova, A. V. Stolyarov, M. Tamanis, R. Ferber, P. Crozet, and A. J. Ross, Fourier transform spectroscopy and extended deperturbation treatment of the spin-orbit-coupled $A^1\Sigma_u^+$ and $b^3\Pi_u$ states of the Rb_2 molecule, Phys. Rev. A **88**, 022504 (2013).

[24] Up to binding energies of 77 GHz × h our measurements confirm the previously found propensity rules for the conservation of the angular momentum quantum numbers $f_a; f_b; F; m_F = m_{f_a} + m_{f_b}$ in three-body recombination [10-12]. Here f_a, f_b, and F are the quantum numbers for the initial total angular momenta $\boldsymbol{f_a}$ and $\boldsymbol{f_b}$ of the two atoms that combine to form the molecule, and $\boldsymbol{F} = \boldsymbol{f_a} + \boldsymbol{f_b}$ with corresponding magnetic quantum number m_F.

[25] J. P. D'Incao, Few-body physics in resonantly interacting ultracold quantum gases, J. Phys. B: At. Mol. Opt. Phys. **51**, 043001 (2018).

[26] C. Strauss, T. Takekoshi, F. Lang, K. Winkler, R. Grimm, J. Hecker Denschlag, and E. Tiemann, Hyperfine, rotational, and vibrational structure of the $a^3\Sigma_u^+$ state of $^{87}Rb_2$, Phys. Rev. A **82**, 052514 (2010).

[27] J.-L. Li, T. Secker, P. M. A. Mestrom, and S. J. J. M. F. Kokkelmans, Strong spin-exchange recombination of three weakly interacting ^7Li atoms, Phys. Rev. Res. **4**, 023103 (2022).

[28] E. Alt, P. Grassberger, and W. Sandhas, Reduction of the three-particle collision problem to multi-channel two-particle Lippmann-Schwinger equations, Nucl. Phys. B **2**, 167 (1967).

[29] T. Secker, J.-L. Li, P. M. A. Mestrom, and S. J. J. M. F. Kokkelmans, Multichannel nature of three-body recombination for ultracold ^{39}K, Phys. Rev. A **103**, 022825 (2021).

[30] Technically, N depends on E_b. This dependence, however, is so weak that its effect on the scaling is negligible.

[31] C. Chin, R. Grimm, P. Julienne, and E. Tiesinga, Feshbach resonances in ultracold gases, Rev. Mod. Phys. **82**, 1225 (2010).

[32] A. Härter, A. Krükow, A. Brunner, and J. Hecker Denschlag, Minimization of ion micromotion using ultracold atomic probes, Appl. Phys. Lett. **102**, 221115 (2013).

[33] A. Mohammadi, A. Krükow, A. Mahdian, M. Deiß, J. Pérez-Ríos, H. da Silva, M. Raoult, O. Dulieu, and J. Hecker Denschlag, Life and death of a cold $BaRb^+$ molecule inside an ultracold cloud of Rb atoms, Phys. Rev. Res. **3**, 013196 (2021).

[34] E. A. Burt, R. W. Ghrist, C. J. Myatt, M. J. Holland, E. A. Cornell, and C. E. Wieman, Coherence, Correlations, and Collisions: What One Learns about Bose-Einstein Condensates from Their Decay, Phys. Rev. Lett. **79**, 337 (1997).

[35] H. Suno, B. D. Esry, C. H. Greene, and J. P. Burke, Three-body recombination of cold helium atoms, Phys. Rev. A **65**, 042725 (2002).

[36] W. Glöckle, *The Quantum Mechanical Few-Body Problem*, Texts and Monographs in Physics (Springer, Berlin, 1983).

[37] D. J. Ernst, C. M. Shakin, and R. M. Thaler, Separable representations of two-body interactions, Phys. Rev. C **8**, 46 (1973).

[38] L. Hlophe, C. Elster, R. C. Johnson, N. J. Upadhyay, F. M. Nunes, G. Arbanas, V. Eremenko, J. E. Escher, and I. J. Thompson (TORUS Collaboration), Separable representation of phenomenological optical potentials of Woods-Saxon type, Phys. Rev. C **88**, 064608 (2013).

Erklärung

Ich versichere hiermit, dass ich die Arbeit selbständig angefertigt habe und keine anderen als die angegebenen Quellen und Hilfsmittel benutzt sowie die wörtlich oder inhaltlich übernommenen Stellen als solche kenntlich gemacht habe.

Ulm, den 20.05.2025

Dominik Dorer

List of Figures

List of Tables

Bibliography

[1] C. Amiot. "Laser-induced fluorescence of Rb_2: The $(1)^1\Sigma_g^+$(X), $(2)^1\Sigma_g^+$, $(1)^1\Pi_u$(B), $(1)^1\Pi_g$, and $(2)^1\Pi_u$(C) electronic states". In: The Journal of Chemical Physics **93**, 12 (1990). DOI: `10.1063/1.459246`.

[2] Loïc Anderegg et al. "Observation of microwave shielding of ultracold molecules". In: Science **373**, 6556 (2021). DOI: `10.1126/science.abg9502`.

[3] J.-L. Archambault et al. "Loss calculations for antiresonant waveguides". In: Journal of Lightwave Technology **11**, 3 (1993). DOI: `10.1109/50.219574`.

[4] M. Ascoli. "Spectroscopy of States with Ion-Pair Character Near Rb(5s) + Rb(4d)". Doctoral dissertation. University of Connecticut, 2015.

[5] P.W. Atkins and R.S. Friedman. *Molecular Quantum Mechanics*. OUP Oxford, 2011.

[6] N. Balakrishnan. "Perspective: Ultracold molecules and the dawn of cold controlled chemistry". In: J. Chem. Phys. **145**, 15 (2016). DOI: `10.1063/1.4964096`.

[7] Steffi Bandelow, Gerrit Marx, and Lutz Schweikhard. "The stability diagram of the digital ion trap". In: International Journal of Mass Spectrometry **336** (2013). DOI: `https://doi.org/10.1016/j.ijms.2012.12.013`.

[8] M. A. Bellos et al. "Upper bound to the ionization energy of $^{85}Rb_2$". In: Phys. Rev. A **87**, 012508 (2013). DOI: `10.1103/PhysRevA.87.012508`.

[9] P.F. Bernath. *Spectra of Atoms and Molecules*. Oxford University Press, 2016.

[10] R. S. Berry. "Ionization of Molecules at Low Energies". In: J. Chem. Phys. **45**, 4 (1966). DOI: `10.1063/1.1727742`.

[11] Alberto Berton et al. "Mapping the Stability Diagram of a Digital Ion Trap (DIT) Mass Spectrometer Varying the Duty Cycle of the Trapping Rectangular Waveform". In: Journal of the American Society for Mass Spectrometry **19**, 4 (2008). DOI: `10.1016/j.jasms.2007.12.012`.

[12] N. Bigagli et al. "Collisionally stable gas of bosonic dipolar groundstate molecules". In: Nat. Phys. **19**, 11 (2023). DOI: `10.1038/s41567-023-02200-6`.

[13] Caroline L. Blackley et al. "Feshbach resonances in ultracold ^{85}Rb". In: Phys. Rev. A **87**, 033611 (2013). DOI: `10.1103/PhysRevA.87.033611`.

[14] D. Bluvstein et al. "A quantum processor based on coherent transport of entangled atom arrays". In: Nature **604**, 7906 (2022). DOI: 10.1038/s41586-022-04592-6.

[15] N. Bohr. "I. On the constitution of atoms and molecules". In: The London, Edinburgh, and Dublin Philosophical Magazine and Journal of Science **26**, 151 (1913), pp. 1–25. DOI: 10.1080/14786441308634955.

[16] Eric Braaten and H.-W. Hammer. "Universality in few-body systems with large scattering length". In: Physics Reports **428**, 5 (2006). DOI: https://doi.org/10.1016/j.physrep.2006.03.001.

[17] John M. Brown and Alan Carrington. *Rotational Spectroscopy of Diatomic Molecules*. Cambridge Molecular Science. Cambridge University Press, 2003.

[18] James P. Burke et al. "Impact of the ^{87}Rb singlet scattering length on suppressing inelastic collisions". In: Phys. Rev. A **55**, R2511(R) (1997). DOI: 10.1103/PhysRevA.55.R2511.

[19] E. A. Burt et al. "Coherence, Correlations, and Collisions: What One Learns about Bose-Einstein Condensates from Their Decay". In: Phys. Rev. Lett. **79**, 337 (1997). DOI: 10.1103/PhysRevLett.79.337.

[20] Lincoln D Carr et al. "Cold and ultracold molecules: science, technology and applications". In: New Journal of Physics **11**, 5 (2009). DOI: 10.1088/1367-2630/11/5/055049.

[21] Roman Chapurin et al. "Precision Test of the Limits to Universality in Few-Body Physics". In: Phys. Rev. Lett. **123**, 233402 (2019). DOI: 10.1103/PhysRevLett.123.233402.

[22] X.-Y. Chen et al. "Ultracold field-linked tetratomic molecules". In: Nature **626**, 7998 (2024). DOI: 10.1038/s41586-023-06986-6.

[23] Lawrence W. Cheuk et al. "Observation of Collisions between Two Ultracold Ground-State CaF Molecules". In: Phys. Rev. Lett. **125**, 043401 (2020). DOI: 10.1103/PhysRevLett.125.043401.

[24] Cheng Chin et al. "Feshbach resonances in ultracold gases". In: Rev. Mod. Phys. **82**, 2 (2010). DOI: 10.1103/RevModPhys.82.1225.

[25] N. R. Claussen et al. "Very-high-precision bound-state spectroscopy near a ^{85}Rb Feshbach resonance". In: Phys. Rev. A **67**, 060701 (2003). DOI: 10.1103/PhysRevA.67.060701.

[26] Yves Colombe et al. "Single-mode optical fiber for high-power, low-loss UV transmission". In: Opt. Express **22**, 16 (2014). DOI: 10.1364/OE.22.019783.

[27] J. P. D'Incao and B. D. Esry. "Manifestations of the Efimov effect for three identical bosons". In: Phys. Rev. A **72**, 032710 (2005). DOI: 10.1103/PhysRevA.72.032710.

[28] J. P. D'Incao, H. Suno, and B. D. Esry. "Limits on Universality in Ultracold Three-Boson Recombination". In: Phys. Rev. Lett. **93**, 123201 (2004). DOI: 10.1103/PhysRevLett.93.123201.

[29] José P D'Incao. "Few-body physics in resonantly interacting ultracold quantum gases". In: Journal of Physics B: Atomic, Molecular and Optical Physics **51**, 4 (2018). DOI: 10.1088/1361-6455/aaa116.

[30] J. Dalibard and C. Cohen-Tannoudji. “Laser cooling below the Doppler limit by polarization gradients: simple theoretical models”. In: J. Opt. Soc. Am. B **6**, 11 (1989). DOI: `10.1364/JOSAB.6.002023`.

[31] Markus Deiß, Shinsuke Haze, and Johannes Hecker Denschlag. “Long-Range Atom-Ion Rydberg Molecule: A Novel Molecular Binding Mechanism”. In: Atoms **9**, 2 (2021). DOI: `10.3390/atoms9020034`.

[32] Markus Deiß et al. “Observation of spin-orbit-dependent electron scattering using long-range Rydberg molecules”. In: Phys. Rev. Research **2**, 013047 (2020). DOI: `10.1103/PhysRevResearch.2.013047`.

[33] W. Demtröder. *Molecular Physics*. Wiley-Vch (D), 2017.

[34] L. Ding and S. Kumashiro. “Ion motion in the rectangular wave quadrupole field and digital operation mode of a quadrupole ion trap mass spectrometer”. In: Rapid Communications in Mass Spectrometry **20**, 1 (2006). DOI: `https://doi.org/10.1002/rcm.2253`.

[35] E. A. Donley et al. “Atom-molecule coherence in a Bose-Einstein condensate”. In: Nature **417**, 6888 (2002). DOI: `10.1038/417529a`.

[36] D. Dorer et al. “Hollow-Core Fiber for Single-Mode, Low Loss Transmission of Broadband UV Light”. In: IEEE Journal of Selected Topics in Quantum Electronics **30**, 6 (2024). DOI: `10.1109/JSTQE.2023.3299158`.

[37] Adrian Dragomir et al. “Two-photon absorption properties of commercial fused silica and germanosilicate glass at 264 nm”. In: Applied Physics Letters **80**, 1114-1116 (2002). DOI: `10.1063/1.1448387`.

[38] B. Drews et al. “Inelastic collisions of ultracold triplet Rb_2 molecules in the rovibrational ground state”. In: Nat. Commun. **8**, 14854 (2017). DOI: `10.1038/ncomms14854`.

[39] Stephan Dürr et al. “Observation of Molecules Produced from a Bose-Einstein Condensate”. In: Phys. Rev. Lett. **92**, 020406 (2004). DOI: `10.1103/PhysRevLett.92.020406`.

[40] U. Fano. “Propensity rules: An analytical approach”. In: Phys. Rev. A **32**, 617 (1985). DOI: `10.1103/PhysRevA.32.617`.

[41] P. O. Fedichev, M. W. Reynolds, and G. V. Shlyapnikov. “Three-Body Recombination of Ultracold Atoms to a Weakly Bound s Level”. In: Phys. Rev. Lett. **77**, 2921 (1996). DOI: `10.1103/PhysRevLett.77.2921`.

[42] F. Ferlaino et al. “Efimov Resonances in Ultracold Quantum Gases”. In: Few-Body Syst **51**, 2 (2011). DOI: `10.1007/s00601-011-0260-7`.

[43] Eric Numkam Fokoua et al. “Limits of Coupling Efficiency into Hollow-Core Antiresonant Fibers”. In: *2021 Conference on Lasers and Electro-Optics, CLEO 2021 - Proceedings*. IEEE, 2021.

[44] Eric Numkam Fokoua et al. “Loss in hollow-core optical fibers: mechanisms, scaling rules, and limits”. In: Adv. Opt. Photon. **15**, 1 (2023). DOI: `10.1364/AOP.470592`.

[45] Michael H. Frosz et al. “Analytical formulation for the bend loss in single-ring hollow-core photonic crystal fibers”. In: Photon. Res. **5**, 2 (2017). DOI: `10.1364/PRJ.5.000088`.

[46] C. Gabbanini et al. “Cold Rubidium Molecules Formed in a Magneto-Optical Trap”. In: Phys. Rev. Lett. **84**, 2814 (2000). DOI: `10.1103/PhysRevLett.84.2814`.

[47] Shou-Fei Gao et al. “Hollow-core negative-curvature fiber for UV guidance”. In: Opt. Lett. **43**, 6 (2018). DOI: `10.1364/OL.43.001347`.

[48] F. Gebert et al. “Damage-free single-mode transmission of deep-UV light in hollow-core PCF”. In: Opt. Express **22**, 13 (2014). DOI: `10.1364/OE.22.015388`.

[49] A Goban et al. “Emergence of multi-body interactions in a fermionic lattice clock”. In: Nature **563**, 7731 (2018). DOI: `10.1038/s41586-018-0661-6`.

[50] Y. Guan et al. “Updated potential energy function of the Rb_2 $a^3\Sigma_u^+$ state in the attractive and repulsive regions determined from its joint analysis with the $2^3\Pi_{0g}$ state”. In: J. Chem. Phys. **139**, 14 (2013), p. 144303. DOI: `10.1063/1.4823496`.

[51] A. Härter et al. “Population distribution of product states following three-body recombination in an ultracold atomic gas”. In: Nat. Phys. **9**, 512 - 517 (2013). DOI: `10.1038/nphys2661`.

[52] Arne Härter. “Two-Body and Three-Body Dynamics in Atom-Ion Experiments”. PhD thesis. Ulm University, 2013.

[53] Alexander Hartung et al. “Low-loss single-mode guidance in large-core antiresonant hollow-core fibers”. In: Opt. Lett. **40**, 14 (2015). DOI: `10.1364/OL.40.003432`.

[54] Shinsuke Haze et al. *Controlling few-body reaction pathways using a Feshbach resonance*. 2024. arXiv: `2408.14922`. URL: `https://arxiv.org/abs/2408.14922`.

[55] Shinsuke Haze et al. “Controlling few-body reaction pathways using a Feshbach resonance”. In: Nature Physics **21**, 2 (Feb. 2025), pp. 228–232. DOI: `10.1038/s41567-024-02726-3`. URL: `https://doi.org/10.1038/s41567-024-02726-3`.

[56] Shinsuke Haze et al. “Energy scaling of the product state distribution for three-body recombination of ultracold atoms”. In: Phys. Rev. Res. **5**, 013161 (2023). DOI: `10.1103/PhysRevResearch.5.013161`.

[57] Shinsuke Haze et al. “Spin-Conservation Propensity Rule for Three-Body Recombination of Ultracold Rb Atoms”. In: Phys. Rev. Lett. **128**, 133401 (2022). DOI: `10.1103/PhysRevLett.128.133401`.

[58] Shinsuke Haze et al. *Stark spectroscopy of Rydberg atoms in an atom-ion hybrid trap*. 2019. arXiv: `1901.11069 [physics.atom-ph]`.

[59] W. Heisenberg. “Über quantentheoretische Umdeutung kinematischer und mechanischer Beziehungen.” In: Zeitschrift für Physik **33**, 1 (1925). DOI: `10.1007/BF01328377`.

[60] Jens Herbig et al. “Preparation of a Pure Molecular Quantum Gas”. In: Science **301**, 5639 (2003). DOI: `10.1126/science.1088876`.

[61] Rebekah Hermsmeier et al. “Quantum Spin State Selectivity and Magnetic Tuning of Ultracold Chemical Reactions of Triplet Alkali-Metal

Dimers with Alkali-Metal Atoms”. In: Phys. Rev. Lett. **127**, 103402 (2021). DOI: `10.1103/PhysRevLett.127.103402`.

[62] D. R. Herschbach. “Molecular Dynamics of Chemical Reactions”. In: Pure and Applied Chemistry **47**, 1 (1976), pp. 61–73. DOI: `doi:10.1351/pac197647010061`.

[63] Gerhard Herzberg and J. W. T. Spinks. *Molecular spectra and molecular structure: I. Spectra of diatomic molecules; 2nd ed.* D.Van Nostrand Company Inc, 1950.

[64] D. K. Hoffmann et al. “Reaction kinetics of ultracold molecule-molecule collisions”. In: Nat. Commun. **9**, 5244 (2018). DOI: `10.1038/s41467-018-07576-1`.

[65] M.-G. Hu et al. “Nuclear spin conservation enables state-to-state control of ultracold molecular reactions”. In: Nat. Chem. **13**, 5 (2021). DOI: `10.1038/s41557-020-00610-0`.

[66] Y. Huang et al. “Formation, detection and spectroscopy of ultracold Rb_2 in the $X^1\Sigma_g^+$ state”. In: Journal of Physics B: Atomic, Molecular and Optical Physics **39**, 19 (2006). DOI: `10.1088/0953-4075/39/19/S04`.

[67] Klaus Hueck et al. “Calibrating high intensity absorption imaging of ultracold atoms”. In: Opt. Express **25**, 8 (2017). DOI: `10.1364/OE.25.008670`.

[68] Daniel Hummler. “Measurement of atom number of ultracold Rb-clouds using absorption imaging”. Master’s thesis. Ulm University, 2020.

[69] F. Hund. “Zur Deutung der Molekelspektren. I”. In: Zeitschrift für Physik **40**, 10 (1927). DOI: `10.1007/BF01400234`.

[70] F. Hund. “Zur Deutung der Molekelspektren. II”. In: Zeitschrift für Physik **42**, 2 (1927). DOI: `10.1007/BF01397124`.

[71] S. Jochim et al. “Pure Gas of Optically Trapped Molecules Created from Fermionic Atoms”. In: Phys. Rev. Lett. **91**, 240402 (2003). DOI: `10.1103/PhysRevLett.91.240402`.

[72] Kevin M. Jones et al. “Ultracold photoassociation spectroscopy: Long-range molecules and atomic scattering”. In: Rev. Mod. Phys. **78**, 483 (2006). DOI: `10.1103/RevModPhys.78.483`.

[73] P. S. Julienne. “Molecular States Near a Collision Threshold”. In: Chap. 6 in *Cold Molecules: Theory, Experiment, Applications*, edited by R. Krems, B. Friedrich, and W. C. Stwalley, CRC press (2009).

[74] P. S. Julienne. “Ultracold molecules from ultracold atoms: a case study with the KRb molecule”. In: Faraday Discuss. **142**, 361-388 (2009). DOI: `10.1039/B820917K`.

[75] P. S. Julienne et al. “Collisional Stability of Double Bose Condensates”. In: Phys. Rev. Lett. **78**, 1880 (1997). DOI: `10.1103/PhysRevLett.78.1880`.

[76] S. Jyothi et al. “Photodissociation of Trapped Rb_2^+: Implications for Simultaneous Trapping of Atoms and Molecular Ions”. In: Phys. Rev. Lett. **117**, 213002 (2016). DOI: `10.1103/PhysRevLett.117.213002`.

[77] Wolfgang Ketterle and N.J. Van Druten. "Evaporative Cooling of Trapped Atoms". In: ed. by Benjamin Bederson and Herbert Walther. Vol. 37. Advances In Atomic, Molecular, and Optical Physics. Academic Press, 1996, pp. 181–236. DOI: `https://doi.org/10.1016/S1049-250X(08)60101-9`.

[78] Thorsten Köhler, Krzysztof Góral, and Paul S. Julienne. "Production of cold molecules via magnetically tunable Feshbach resonances". In: Rev. Mod. Phys. **78**, 1311 (2006). DOI: `10.1103/RevModPhys.78.1311`.

[79] S. J. J. M. F. Kokkelmans, H. M. J. M. Boesten, and B. J. Verhaar. "Role of collisions in creation of overlapping Bose condensates". In: Phys. Rev. A **55**, R1589 (1997). DOI: `10.1103/PhysRevA.55.R1589`.

[80] Artjom Krükow et al. "Reactive two-body and three-body collisions of Ba^+ in an ultracold Rb gas". In: Phys. Rev. A **94**, 030701 (2016). DOI: `10.1103/PhysRevA.94.030701`.

[81] Matthieu Lancry and Bertrand Poumellec. "UV laser processing and multiphoton absorption processes in optical telecommunication fiber materials". In: Physics Reports **523**, 4 (2013). DOI: `https://doi.org/10.1016/j.physrep.2012.09.008`.

[82] A. R. Lee, C. S. Enos, and A. G. Brenton. "Collisional excitation of CO: a study of the Wigner spin rule". In: International Journal of Mass Spectrometry and Ion Processes **104**, 1 (1991). DOI: `https://doi.org/10.1016/0168-1176(91)85005-7`.

[83] Y. T. Lee et al. "Molecular Beam Reactive Scattering Apparatus with Electron Bombardment Detector". In: Review of Scientific Instruments **40**, 11 (1969), pp. 1402–1408. DOI: `10.1063/1.1683809`.

[84] Yoo Kyung Lee, Hanzhen Lin, and Wolfgang Ketterle. "Spin Dynamics Dominated by Resonant Tunneling into Molecular States". In: Phys. Rev. Lett. **131**, 213001 (2023). DOI: `10.1103/PhysRevLett.131.213001`.

[85] H. Lefebvre-Brion and R.W. Field. *The Spectra and Dynamics of Diatomic Molecules: Revised and Enlarged Edition*. Academic Press, 2004. ISBN: 9780080517506.

[86] D. Leibfried et al. "Experimental demonstration of a robust, high-fidelity geometric two ion-qubit phase gate". In: Nature **422** (2003). DOI: `10.1038/nature01492`.

[87] D. Leibfried et al. "Quantum dynamics of single trapped ions". In: Rev. Mod. Phys. **75**, 281 (2003). DOI: `10.1103/RevModPhys.75.281`.

[88] P. D. Lett et al. "Spectroscopy of Na_2 by photoassociation of laser-cooled Na". In: Phys. Rev. Lett. **71**, 2200 (1993). DOI: `10.1103/PhysRevLett.71.2200`.

[89] J.-L. Li et al. "Strong spin-exchange recombination of three weakly interacting ^{7}Li atoms". In: Phys. Rev. Research **4**, 023103 (2022). DOI: `10.1103/PhysRevResearch.4.023103`.

[90] Jing-Lun Li et al. *Spin hierarchy in van der Waals molecule formation via ultracold three-body recombination*. 2024. URL: `https://arxiv.org/abs/2407.18567`.

[91] Jing-Lun Li et al. *Spin structure of diatomic van der Waal molecules of alkali atoms*. 2024. URL: https://arxiv.org/abs/2411.14787.

[92] Junyu Lin et al. “Microwave Shielding of Bosonic NaRb Molecules”. In: Phys. Rev. X **13**, 031032 (2023). DOI: 10.1103/PhysRevX.13.031032.

[93] Yi-Xiang Liu et al. “Quantum interference in atom-exchange reactions”. In: Science **384**, 6700 (2024). DOI: 10.1126/science.adl6570.

[94] Y. Liu et al. “Precision test of statistical dynamics with state-to-state ultracold chemistry”. In: Nature **593**, 7859 (2021). DOI: 10.1038/s41586-021-03459-6.

[95] J. Lozeille et al. “Detection by two-photon ionization and magnetic trapping of cold Rb_2 triplet state molecules”. In: Eur. Phys. J. D **39**, 2 (2006). DOI: 10.1140/epjd/e2006-00084-4.

[96] M. W. Mancini et al. “Observation of Ultracold Ground-State Heteronuclear Molecules”. In: Phys. Rev. Lett. **92**, 133203 (2004). DOI: 10.1103/PhysRevLett.92.133203.

[97] Christian D. Marciniak et al. “Towards fully commercial, UV-compatible fiber patch cords”. In: Opt. Express **25**, 14 (2017). DOI: 10.1364/OE.25.015643.

[98] Javier Martínez-Cifuentes and K. M. Fonseca-Romero. “Spin-state estimation using the Stern-Gerlach experiment”. In: Phys. Rev. A **103**, 042202 (2021). DOI: 10.1103/PhysRevA.103.042202.

[99] Kyle Matsuda et al. “Resonant collisional shielding of reactive molecules using electric fields”. In: Science **370**, 6522 (2020). DOI: 10.1126/science.abe7370.

[100] Harold J. Metcalf and Peter van der Straten. *Laser Cooling and Trapping*. New York: Springer-Verlag, 1999.

[101] J. D. Miller, R. A. Cline, and D. J. Heinzen. “Photoassociation spectrum of ultracold Rb atoms”. In: Phys. Rev. Lett. **71**, 2204 (1993). DOI: 10.1103/PhysRevLett.71.2204.

[102] M. H. G. de Miranda et al. “Controlling the quantum stereodynamics of ultracold bimolecular reactions”. In: Nat. Phys. **7**, 502-507 (2011). DOI: 10.1038/nphys1939.

[103] A. J. Moerdijk, H. M. J. M. Boesten, and B. J. Verhaar. “Decay of trapped ultracold alkali atoms by recombination”. In: Phys. Rev. A **53**, 916 (1996). DOI: 10.1103/PhysRevA.53.916.

[104] Amir Mohammadi et al. “Life and death of a cold $BaRb^+$ molecule inside an ultracold cloud of Rb atoms”. In: Phys. Rev. Research **3**, 013196 (2021). DOI: 10.1103/PhysRevResearch.3.013196.

[105] John H. Moore. “Investigation of the Wigner Spin Rule in Collisions of N^+ with He, Ne, Ar, N_2, and O_2”. In: Phys. Rev. A **8**, 2359 (1973). DOI: 10.1103/PhysRevA.8.2359.

[106] J. H. Osório et al. “Hollow-core fibers with reduced surface roughness and ultralow loss in the short-wavelength range”. In: Nat. Commun. **3**, 1146 (2023). DOI: 10.1038/s41467-023-36785-6.

[107] C. Ospelkaus et al. “Microwave quantum logic gates for trapped ions”. In: Nature **476**, 7359 (2003). DOI: 10.1038/nature10290.

[108] S. Ospelkaus et al. “Controlling the Hyperfine State of Rovibronic Ground-State Polar Molecules”. In: Phys. Rev. Lett. **104** (3 Jan. 2010), p. 030402. DOI: `10.1103/PhysRevLett.104.030402`.

[109] Yajun Pang, Kai Zhang, and Liying Lang. “Review of acousto-optic spectral systems and applications”. In: Frontiers in Physics **10** (2022). DOI: `10.3389/fphy.2022.1102996`.

[110] J. J. Park et al. “A Feshbach resonance in collisions between triplet ground-state molecules”. In: Nature **614**, 7946 (2023). DOI: `10.1038/s41586-022-05635-8`.

[111] Su Jin Park et al. “Theoretical Study of the Electronic States of the Rb2 Molecule”. In: Journal of Molecular Spectroscopy **207**, 2 (2001). DOI: `https://doi.org/10.1006/jmsp.2001.8337`.

[112] Asen Pashov et al. “The $C(2)^1\Pi_u$ state in Rb2. Observation and deperturbation”. In: Spectrochimica Acta Part A: Molecular and Biomolecular Spectroscopy **281**, 121624 (2022). DOI: `https://doi.org/10.1016/j.saa.2022.121624`.

[113] Linus Pauling. “Quantum Mechanics and the Chemical Bond”. In: Phys. Rev. **37**, 1185 (1931). DOI: `10.1103/PhysRev.37.1185`.

[114] Elena A. Pazyuk, Elena I. Revina, and Andrey V. Stolyarov. “Theoretical study of spin–orbit and Coriolis coupling among the low-lying states of Rb2 and Cs2”. In: Chemical Physics **462**, 51-56 (2015). DOI: `https://doi.org/10.1016/j.chemphys.2015.07.018`.

[115] G Pichler et al. “Diffuse bands in the visible absorption spectra of dense alkali vapours”. In: J. Phys. B: Atom. Mol. Phys. **16**, 24 (1983). DOI: `10.1088/0022-3700/16/24/017`.

[116] G Reinaudi et al. “Strong saturation absorption imaging of dense clouds of ultracold atoms”. In: Optics letters **32** (Dec. 2007).

[117] B. S. Rem et al. “Lifetime of the Bose Gas with Resonant Interactions”. In: Phys. Rev. Lett. **110**, 163202 (2013). DOI: `10.1103/PhysRevLett.110.163202`.

[118] L. A. Reynolds et al. “Direct Measurements of Collisional Dynamics in Cold Atom Triads”. In: Phys. Rev. Lett. **124**, 073401 (2020). DOI: `10.1103/PhysRevLett.124.073401`.

[119] Shuichiro Rikimi et al. “Growth of Ammonium Chloride on Cleaved End-Facets of Hollow Core Fibers”. In: *2020 Conference on Lasers and Electro-Optics (CLEO)*. 2020.

[120] J. L. Roberts et al. “Magnetic Field Dependence of Ultracold Inelastic Collisions near a Feshbach Resonance”. In: Phys. Rev. Lett. **85**, 728 (2000). DOI: `10.1103/PhysRevLett.85.728`.

[121] P. Roth et al. “Strong circular dichroism for the HE_{11} mode in twisted single-ring hollow-core photonic crystal fiber”. In: Optica **5**, 10 (2018). DOI: `10.1364/OPTICA.5.001315`.

[122] J. Rui et al. “Controlled state-to-state atom-exchange reaction in an ultracold atom–dimer mixture”. In: Nat. Phys. **13**, 7 (2017). DOI: `10.1038/nphys4095`.

[123] Philip St.J. Russell. “Photonic-Crystal Fibers”. In: Journal of Lightwave Technology **24**, 12 (2006). DOI: `10.1109/JLT.2006.885258`.

[124] Daniel K. Ruttley et al. “Formation of Ultracold Molecules by Merging Optical Tweezers”. In: Phys. Rev. Lett. **130**, 223401 (2023). DOI: `10.1103/PhysRevLett.130.223401`.

[125] S. Sala et al. “Coherent Molecule Formation in Anharmonic Potentials Near Confinement-Induced Resonances”. In: Phys. Rev. Lett. **110**, 203202 (2013). DOI: `10.1103/PhysRevLett.110.203202`.

[126] Stefan Schmid. “Dynamics of a cold trapped ion in a Bose-Einstein condensate”. PhD thesis. Ulm University, 2012.

[127] Stefan Schmid et al. “An apparatus for immersing trapped ions into an ultracold gas of neutral atoms”. In: Review of Scientific Instruments **83**, 5 (2012). DOI: `10.1063/1.4718356`.

[128] P. Scholl et al. “Quantum simulation of 2D antiferromagnets with hundreds of Rydberg atoms”. In: Nature **595**, 7866 (2021). DOI: `10.1038/s41586-021-03585-1`.

[129] E. Schrödinger. “Quantisierung als Eigenwertproblem”. In: Annalen der Physik **385**, 13 (1926). DOI: `https://doi.org/10.1002/andp.19263851302`.

[130] T. Secker et al. “Multichannel nature of three-body recombination for ultracold ^{39}K”. In: Phys. Rev. A **103**, 022825 (2021). DOI: `10.1103/PhysRevA.103.022825`.

[131] N. Šibalić et al. “ARC: An open-source library for calculating properties of alkali Rydberg atoms”. In: Computer Physics Communications **220**, 319-331 (2017). DOI: `https://doi.org/10.1016/j.cpc.2017.06.015`.

[132] Vivek Singh, V B Tiwari, and S R Mishra. “Efficient quantum state preparation using Stern–Gerlach effect on cold atoms”. In: Measurement Science and Technology **33**, 095019 (2022). DOI: `10.1088/1361-6501/ac78c4`.

[133] Linards Skuja, Hideo Hosono, and Masahiro Hirano. “Laser-induced color centers in silica”. In: *Laser-Induced Damage in Optical Materials: 2000*. Vol. 4347. 2001. DOI: `10.1117/12.425020`.

[134] J. Söding et al. “Three-body decay of a rubidium Bose-Einstein condensate”. In: Applied Physics B: Lasers and Optics **69**, 4 (1999). DOI: `10.1007/s003400050805`.

[135] Hyungmok Son et al. “Control of reactive collisions by quantum interference”. In: Science **375**, 6584 (2022). DOI: `10.1126/science.abl7257`.

[136] Jaroslaw Sperling and Korbinian Hens. “Made Easy: CW Laser Light Widely Tunable Across the Visible”. In: Optik & Photonik **13**, 3 (2018). DOI: `https://doi.org/10.1002/opph.201800022`.

[137] Daniel A. Steck. *Rubidium 87 D Line Data*. Version 10 September 2023. URL: `http://steck.us/alkalidata`.

[138] Allied Vision. *Stingray Technical Manual V4.6.9. 2020.*

[139] C. Strauss et al. “Hyperfine, rotational, and vibrational structure of the $a^3\Sigma_u^+$ state of $^{87}Rb_2$”. In: Phys. Rev. A **82**, 052514 (2010). DOI: 10.1103/PhysRevA.82.052514.

[140] H. Suno et al. “Three-body recombination of cold helium atoms”. In: Phys. Rev. A **65**, 042725 (2002). DOI: 10.1103/PhysRevA.65.042725.

[141] Yoshiaki Tamura et al. “The First 0.14-dB/km Loss Optical Fiber and its Impact on Submarine Transmission”. In: J. Lightwave Technol. **36**, 1 (2018). DOI: 10.1109/JLT.2018.2796647.

[142] Ellison H. Taylor and Sheldon Datz. “Study of Chemical Reaction Mechanisms with Molecular Beams. The Reaction of K with HBr”. In: The Journal of Chemical Physics **23**, 9 (Sept. 1955), pp. 1711–1718. DOI: 10.1063/1.1742417.

[143] G. Thalhammer et al. “Long-Lived Feshbach Molecules in a Three-Dimensional Optical Lattice”. In: Phys. Rev. Lett. **96**, 050402 (2006). DOI: 10.1103/PhysRevLett.96.050402.

[144] N. Timoney et al. “Quantum gates and memory using microwave-dressed states”. In: Nature **476**, 7359 (2011). DOI: 10.1038/nature10319.

[145] William G. Tobias et al. “Reactions between layer-resolved molecules mediated by dipolar spin exchange”. In: Science **375**, 6586 (2022). DOI: 10.1126/science.abn8525.

[146] Timur V. Tscherbul and Roman V. Krems. “Tuning Bimolecular Chemical Reactions by Electric Fields”. In: Phys. Rev. Lett. **115**, 023201 (2015). DOI: 10.1103/PhysRevLett.115.023201.

[147] Patrick Uebel et al. “Broadband robustly single-mode hollow-core PCF by resonant filtering of higher-order modes”. In: Opt. Lett. **41**, 9 (2016). DOI: 10.1364/OL.41.001961.

[148] Romain Veyron et al. “Quantitative absorption imaging: The role of incoherent multiple scattering in the saturating regime”. In: Phys. Rev. Res. **4**, 033033 (2022). DOI: 10.1103/PhysRevResearch.4.033033.

[149] Jia Wang, J. P. D’Incao, and Chris H. Greene. “Numerical study of three-body recombination for systems with many bound states”. In: Phys. Rev. A **84**, 052721 (2011). DOI: 10.1103/PhysRevA.84.052721.

[150] Jia Wang et al. “Origin of the Three-Body Parameter Universality in Efimov Physics”. In: Phys. Rev. Lett. **108**, 263001 (2012). DOI: 10.1103/PhysRevLett.108.263001.

[151] Bo-Yang Wang et al. “Measurement of the three-body-recombination coefficient of ultracold lithium and strontium atoms”. In: Phys. Rev. A **110**, 013322 (2024). DOI: 10.1103/PhysRevA.110.013322.

[152] Tino Weber et al. “Bose-Einstein Condensation of Cesium”. In: Science **299**, 5604 (2003). DOI: 10.1126/science.1079699.

[153] Tino Weber et al. “Three-Body Recombination at Large Scattering Lengths in an Ultracold Atomic Gas”. In: Phys. Rev. Lett. **91**, 123201 (2003). DOI: 10.1103/PhysRevLett.91.123201.

[154] R. J. Wild et al. “Measurements of Tan’s Contact in an Atomic Bose-Einstein Condensate”. In: Phys. Rev. Lett. **108**, 145305 (2012). DOI: 10.1103/PhysRevLett.108.145305.

[155] F. Wolf et al. “Non-destructive state detection for quantum logic spectroscopy of molecular ions”. In: Nature **530**, 7591 (2016). DOI: `10.1038/nature16513`.

[156] Joschka Wolf. “Towards resolved sideband spectroscopy in an atom-ion hybrid trap”. Master’s thesis. Ulm University, 2014.

[157] Joschka Wolf, Markus Deiß, and Johannes Hecker Denschlag. “Hyperfine Magnetic Substate Resolved State-to-State Chemistry”. In: Phys. Rev. Lett. **123**, 253401 (2019). DOI: `10.1103/PhysRevLett.123.253401`.

[158] Joschka Wolf et al. “State-to-state chemistry for three-body recombination in an ultracold rubidium gas”. In: Science **358**, 6365 (2017). DOI: `10.1126/science.aan8721`.

[159] Tsung-Yao Wu et al. “Stern–Gerlach detection of neutral-atom qubits in a state-dependent optical lattice”. In: Nature Physics **15**, 6 (2019). DOI: `10.1038/s41567-019-0478-8`.

[160] Xin Xie et al. “Observation of Efimov Universality across a Nonuniversal Feshbach Resonance in ^{39}K”. In: Phys. Rev. Lett. **125**, 243401 (2020). DOI: `10.1103/PhysRevLett.125.243401`.

[161] K. Xu et al. “Formation of Quantum-Degenerate Sodium Molecules”. In: Phys. Rev. Lett. **91**, 210402 (2003). DOI: `10.1103/PhysRevLett.91.210402`.

[162] N. Yamamoto, L. Tao, and A.P. Yalin. “Single-mode delivery of 250 nm light using a large mode area photonic crystal fiber”. In: Opt. Express **17**, 19 (2009). DOI: `10.1364/OE.17.016933`.

[163] Zoe Z. Yan et al. “Resonant Dipolar Collisions of Ultracold Molecules Induced by Microwave Dressing”. In: Phys. Rev. Lett. **125**, 063401 (2020). DOI: `10.1103/PhysRevLett.125.063401`.

[164] Huan Yang et al. “Creation of an ultracold gas of triatomic molecules from an atom-diatomic molecule mixture”. In: Science **378**, 6623 (2022). DOI: `10.1126/science.ade6307`.

[165] Jinxin Yang et al. “Experimental study of the $b^3\Pi_{1u}$ and $2^3\Pi_{1g}$ states of ^{85}Rb$_2$”. In: J. Mol. Spectrosc. **336**, 36-41 (2017). DOI: `https://doi.org/10.1016/j.jms.2017.04.011`.

[166] Fei Yu et al. “Single-mode solarization-free hollow-core fiber for ultraviolet pulse delivery”. In: Opt. Express **26**, 8 (2018). DOI: `10.1364/OE.26.010879`.

[167] Yichao Yu et al. “Coherent Optical Creation of a Single Molecule”. In: Phys. Rev. X **11**, 3 (2021).

[168] M. Zaccanti et al. “Observation of an Efimov spectrum in an atomic system”. In: Nat. Phys. **5**, 8 (2009). DOI: `10.1038/nphys1334`.

[169] Chi Zhang et al. “Submicrosecond entangling gate between trapped ions via Rydberg interaction”. In: Nature **580**, 7803 (2020). DOI: `10.1038/s41586-020-2152-9`.

[170] Viktor Zuba et al. “Experimental Investigation into Optimum Laser Coupling Efficiency into Hollow-Core NANFs”. In: *2022 Conference on Lasers and Electro-Optics (CLEO)*.